JPL Quarterly Technical Review

Volume 1 April 1971 Number 1

Papers on:

Antennas
Biology
Chemistry
Computer Applications
Electronic Components
Lunar and Planetary Exploration
Materials
Power Sources
Propulsion
Telemetry
Test Facilities

Abstracts of:

Technical Reports
Technical Memorandums
Space Programs Summary
Open Literature Reporting

Jet Propulsion Laboratory/California Institute of Technology

JPL Quarterly Technical Review
Volume 1, Number 1

Jet Propulsion Laboratory
California Institute of Technology
4800 Oak Grove Drive
Pasadena, California 91103

Prepared Under Contract NAS 7-100
National Aeronautics and Space Administration

Requests for copies of JPL publications should be made in writing to the attention of: Manager, Technical Information and Documentation Division Support Section 751.

JPL Quarterly Technical Review

Volume 1 April 1971 Number 1

Contents

Bibliography of Current Reporting

Satellite Flyby Opportunities for the Multi-Outer-Planet Missions

P. A. Penzo

Mission Analysis Division

In the proposed missions to the outer planets, observations of their natural satellites will be of considerable scientific interest. In this study, the satellite encounter opportunities are generated for two multiple-flyby missions which include all five of the major planets. Many favorable encounter opportunities have been found for the large satellites of Jupiter, and some for Titan and Iapetus of Saturn. The opportunities for satellites of Uranus are least favorable. Opportunities also exist for multiple-satellite encounters on the same mission and examples are shown. Finally, for Jupiter, some arrival dates exist where very close flybys of certain satellites are possible. These opportunities, added to the multiple-planet missions, will enhance their scientific return significantly.

Introduction

During the late 1970s, the favorable configuration of the outer planets leads to unique opportunities to fly by several of these giant planets with a single spacecraft. Thus, with a bit more energy than is required to get to Jupiter, for example, it will be possible for the spacecraft to acquire a gravity-assisted energy increase at Jupiter sufficient to go on to Saturn and then to Pluto. Several combinations of such multiple-planet missions have been studied in detail (e.g., Reference 1) where Jupiter is the first planet. Two such combinations have received considerable attention recently (Reference 2) and are seriously being considered as part of NASA's program to explore the outer planets. These are the Jupiter to Saturn to Pluto (JSP) combination, which has favorable launch periods in 1976, 1977, and 1978; and the Jupiter to Uranus to Neptune (JUN) combination with favorable launch periods in 1978, 1979, and 1980. This study will concentrate on satellite encounter opportunities for two of the missions, i.e., JSP 77 and JUN 79.

Studies of these multiple-planet missions date back to 1966 (Reference 3); however, very little attention was given to the possibilities of

encountering the planets' satellites during these missions. Recently, however, scientific interest in the satellites has increased. Typical questions which may be asked concern their figures, possible atmospheres, magnetic fields, densities, and surface properties. Close encounters with the satellites may resolve some of these questions and, some scientists believe, lead to a better understanding of the origin and evolution of the solar system. This study shows that very near encounters with certain satellites are possible during multiple-planet missions and, if some sacrifice is made in approach distances, multiple-satellite encounters are also possible.

Flyby Characteristics

Due to the increased interest in the satellites, a systematic study was begun at JPL within the past year to determine possible satellite encounter opportunities during the JSP and JUN missions. Such satellite encounters require that two conditions be satisfied. The first requirement is that the

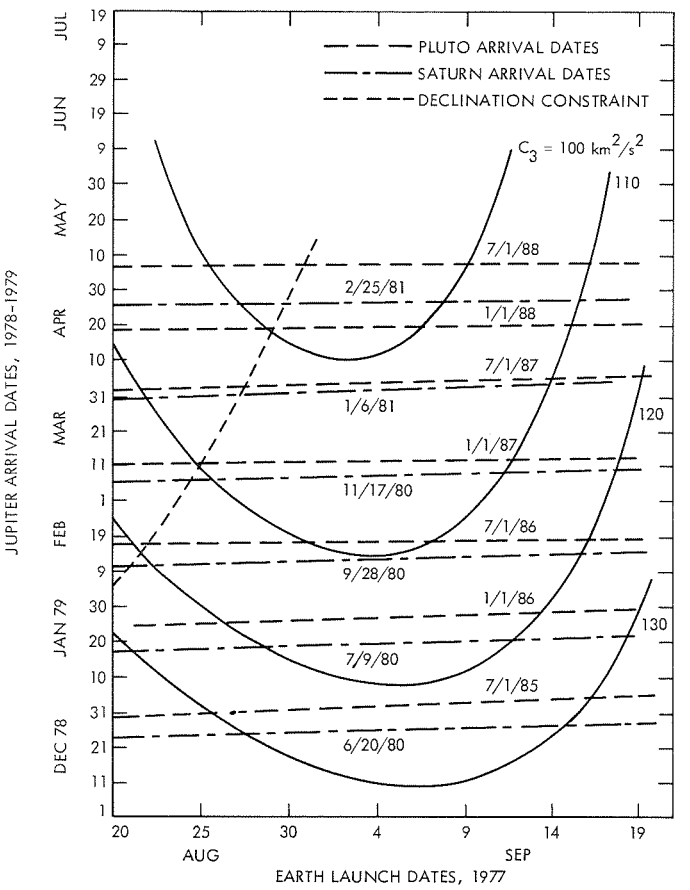

Figure 1. Launch and arrival times for the JSP 77 mission

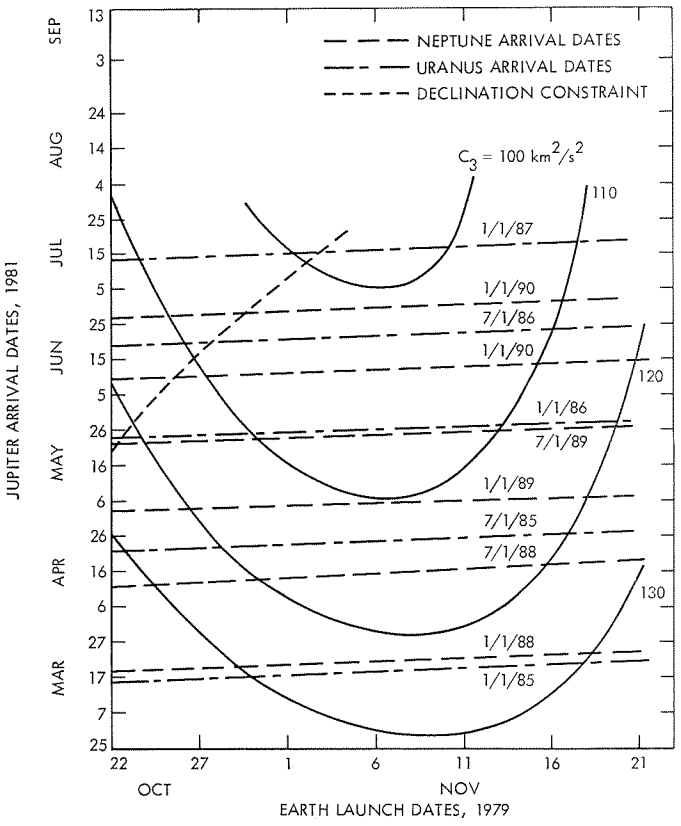

Figure 2. Launch and arrival times for the JUN 79 mission

flyby trajectory comes close to the orbit of the satellite of interest. This makes an encounter at least geometrically feasible, and will depend upon the flyby trajectory path relative to the satellite orbit. The second is that the satellite and the spacecraft be on their respective orbits at positions where the distance between the orbits is nearly minimum. Achieving this condition is primarily a matter of timing the spacecraft arrival at the planet.

The flyby characteristics,[1] in turn, are dependent on the particular planetary mission. For example, for a JSP mission, choosing an Earth launch date and Jupiter arrival date will completely specify the trajectory, except for the flyby geometry at the final planet. Elements specified include the launch energy, the intermediate planet flyby characteristics, and the arrival times at Saturn and Pluto. Figures 1 and 2, for example, present Jupiter arrival date versus Earth launch date for the JSP 77 and

[1]The data presented here has been generated with conic programs which have not considered oblateness or third body effects. The accuracy of these programs is quite sufficient for the preliminary analysis presented here.

JUN 79 missions, respectively. Plotted[2] are lines of constant Earth launch C_3, and the outer planets' arrival times. The launch asymptote declination line of ± 0.497 rad (± 28.5 deg),[3] which may limit the length of the launch window, is also shown.

Several characteristics may be noted in these figures. The first is that the flight times to the planets will increase with decreasing C_3. These flight times range from 450 to 600 days for Jupiter, 2.8 to 3.5 yr for Saturn, and 5.0 to 7.0 yr for Uranus. The flight times to the final planets, Pluto and Neptune, can vary from 7.5 to 11 yr. In addition, if the arrival date at a given planet is held fixed for a given launch period, perhaps to take advantage of a close satellite encounter which may occur on that date, the flight times to the remaining planets do not change appreciably (the actual changes may be read off these curves). The Earth launch C_3,

[2]The value of C_3 (km^2/s^2) is twice the energy per unit mass of the spacecraft after injection from Earth parking orbit. It is also equal to the square of the spacecraft hyperbolic excess velocity, V_∞.

[3]Where applicable, the International System of Units is stated first, followed by the customary units in parentheses. In each case, the value in parentheses represents the measured or calculated unit.

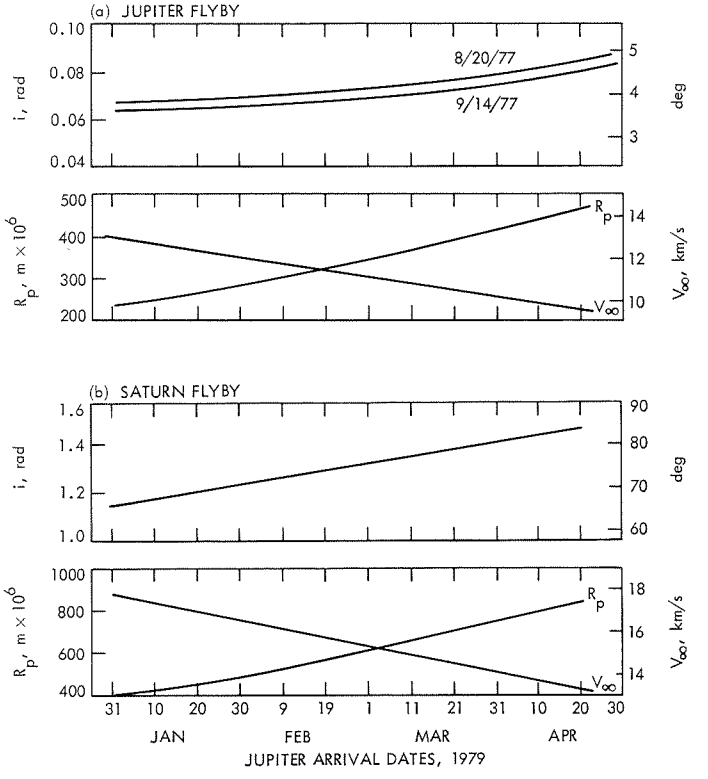

Figure 3. Hyperbolic parameters for the JSP 77 mission

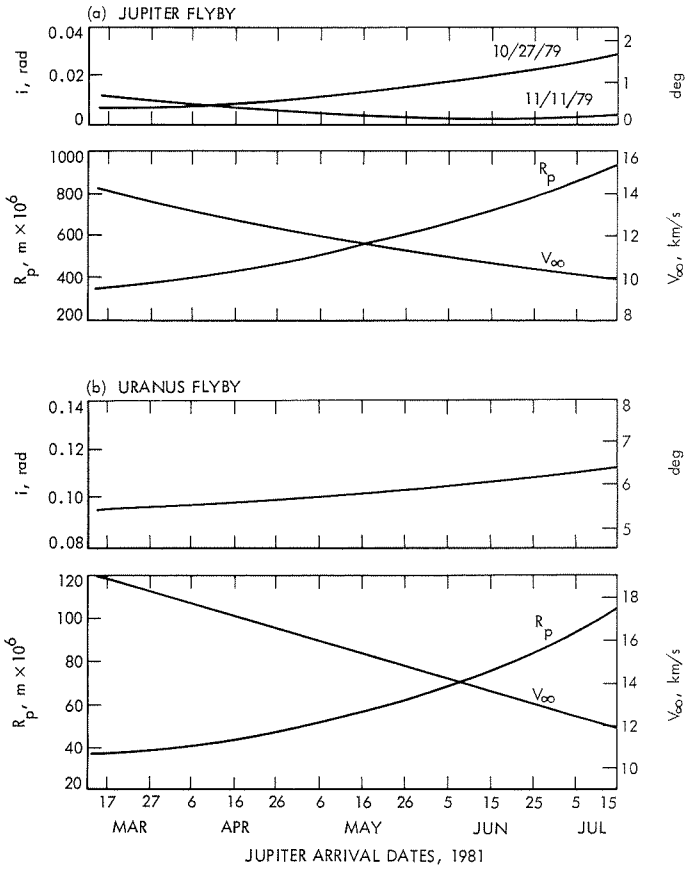

Figure 4. Hyperbolic parameters for the JUN 79 mission

however, will change, being a maximum at the beginning and end of the launch period and having a minimum near the center.

Figures 3 and 4 present some flyby parameters for the JSP 77 and JUN 79 missions, respectively, as a function of the Jupiter arrival date. These data are nearly independent of the launch date, except for slight variations in inclinations (i) at Jupiter. (All inclinations are relative to Earth ecliptic.) At Jupiter, the values and variations in the inclination are small. As discussed below, this characteristic is favorable relative to close encounters with the satellites of Jupiter. The high inclination of the Saturn flyby is due to the requirement that the spacecraft go on to Pluto, which is considerably out of the ecliptic plane at the time of Pluto arrival. Included in these figures are the radial distance of the flyby periapsis (R_p), given in kilometers, and the hyperbolic excess velocity at the planet. For flyby missions, this last parameter does not play a significant role in the planet and satellite encounters; however, for orbital missions the orbit insertion fuel requirements will have a strong dependence on this

parameter. For satellite encounters, the radial distance is important since it indicates how close to the satellite orbit the flyby trajectory may come.

Satellite Encounter Opportunities

Determining the characteristics of the flyby trajectories for the set of Jupiter arrival dates of interest, such as presented in Figures 3 and 4, is one necessary requirement for finding satellite encounter opportunities. In addition, it is necessary to know the characteristics of the satellite orbits themselves and, in fact, to know their positions as a function of time (their ephemerides). At present, for this and similar studies, JPL has implemented some long existing theories concerning the motions of the satellites of the outer planets. These ephemerides are sufficiently accurate for preliminary analyses. Anticipation of the need for greater accuracy is presently leading to increased activity at JPL and elsewhere to develop improved ephemerides for the satellites. Although the existing ephemerides were used to generate the encounter data presented in this study, it is useful to list here some of the gross characteristics of the satellite orbits.

Table 1 presents some satellite orbital data for Jupiter, Saturn, and Uranus. For Jupiter only the larger (Galilean) satellites are listed. For Saturn, two of the larger satellites are given, and these will be discussed later with regard to encounter opportunities. The five satellites of Uranus form an extremely regular system and the characteristics of all of them are presented. Considerably more information may be found in References 4 and 5.

Table 1. Satellite orbital data (The Ecliptic Coordinate System)

Satellite	Semi-major axis, km	Eccentricity	Inclination, deg	Ascending node, deg	Period, days
Jupiter					
Io	422,000	0.0	2.18	338	1.77
Europa	671,400	0.0003	2.22	350	3.55
Ganymede	1,071,000	0.0015	2.02	341	7.15
Callisto	1,884,000	0.0075	2.01	333	16.69
Saturn					
Titan	1,222,600	0.029	27.74	169	15.95
Iapetus	3,562,900	0.104	17.59	140	79.33
Uranus					
Miranda	129,800	0.0	98.0	166.4	1.41
Ariel	190,900	0.0028	98.0	166.4	2.52
Umbriel	266,000	0.0035	98.0	166.4	4.14
Titania	436,000	0.0024	98.0	166.4	8.71
Oberon	583,400	0.0007	98.0	166.4	13.46

Jupiter

Analyzing the characteristics of the flyby trajectories to the planets, and the satellite characteristics presented in Table 1, it has become evident that conditions for satellite encounter are much more favorable at Jupiter than at Saturn and Uranus. (Pluto has no known satellites, and the Satellites of Neptune may be targeted to since it is the last planet of the JUN mission.) Figure 5 presents the sets of flyby trajectories for the JSP 77 and JUN 79 missions and indicates that the flyby trajectories will lie very close to the plane of Jupiter's equator and hence to the plane of the satellite orbits. The earlier arrival date has been chosen on the basis that the total mission time is about 8 yr. The later arrival date assumes a total mission time of no more than 10 yr. The view in Figure 5 is from the ecliptic north pole. The inclinations of the flybys are all less than 0.1 rad (6 deg) to Jupiter's equator. Another favorable aspect of these trajectories is that their periapsides lie within the orbits of many of the satellites. Thus, the first condition for favorable satellite encounters is satisfied. Also, since the periods of these satellites are short (about 16 days for Callisto), compared with the range of possible arrival dates (about 3 months), there exist many Jupiter flyby times such that encounter with any given satellite is possible.

Based on the simplifying assumptions that the flyby trajectories are in the plane of the satellite orbits and that these orbits are circular (all

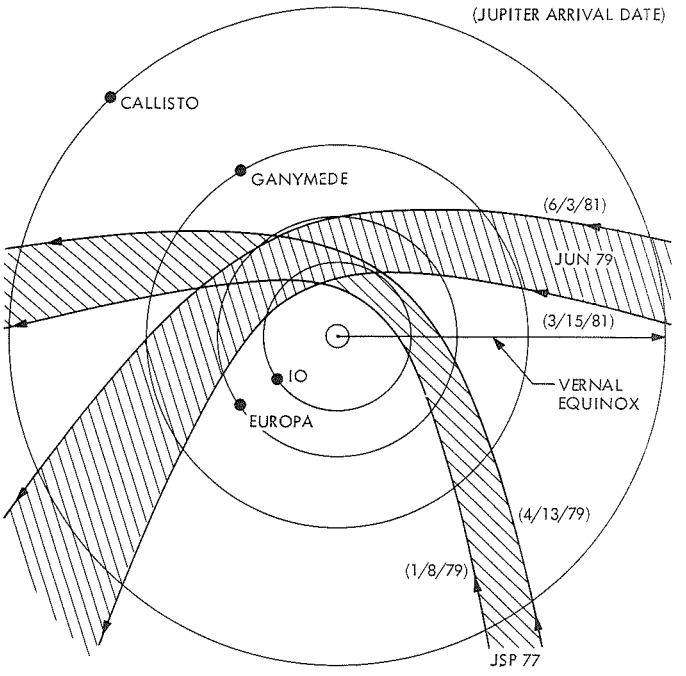

Figure 5. Sets of flyby trajectories for the JSP 77 and JUN 79 missions

eccentricities are less than 0.01), it is possible to generate satellite encounter times to an accuracy of about 0.1 day. (Actually, what is found is the Jupiter flyby time of closest approach which will produce an encounter with a given satellite.) This was done for the range of Jupiter arrival dates of interest. In determining the encounter times, the variation of the flyby altitude, energy, and orientation with the arrival date is taken into account. With these approximations as first guesses, it is a simple matter to calculate the exact encounter time and encounter characteristics with computer programs in which no simplifying assumptions are made.

Once these approximate single-satellite encounter opportunities have been generated, it is straightforward to find multiple-satellite encounters. Specifically, the data for single-satellite encounters consist of a list (for each satellite) of flyby periapsis times for which encounter with that satellite will occur. This list contains two sets, the first comprising those times for which encounter will occur prior to periapsis passage, and the second those times for which encounter will occur after periapsis passage. For multiple-satellite encounters, it is only necessary to scan the lists for all the satellites to find when the times are nearly coincident. For example, it may be found that a flyby periapsis passage on February 3.4, 1979, will result in an encounter with Europa prior to periapsis passage, whereas a periapsis passage on February 3.5, 1979, will result in an encounter with Io after periapsis passage. Thus, by compromising the

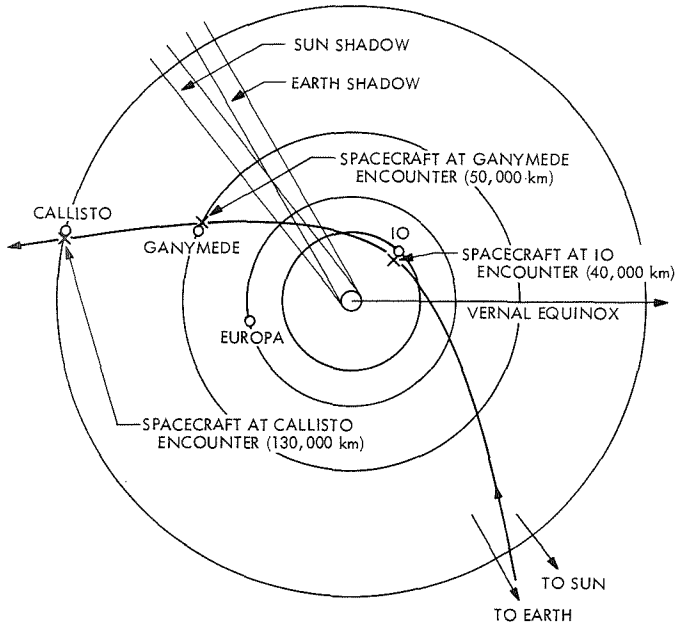

Figure 6. Possible Jupiter flyby with multiple-satellite encounters

periapsis time and targeting for a periapsis passage of February 3.45, 1979, it is possible to encounter both satellites, although some sacrifice in the closest approach distance to the two satellites will have to be made. Of course, the scan may (and does for JSP 76, as discussed in Reference 2) yield an opportunity to encounter all four of the Galilean satellites.

For the JSP 77 mission, several favorable multiple-satellite encounters exist for Io, Ganymede, and Callisto. The most favorable is shown in Figure 6, where the flyby periapsis time is March 5.3, 1979 GMT. For this case, the flyby periapsis is inside, but close to, Io's orbit, and encounter with Io (at a distance of about 40,000 km) occurs just prior to periapsis passage. Encounters with Ganymede and Callisto occur after periapsis passage with closest approach distances of about 50,000 and 130,000 km, respectively. Lighting conditions for viewing the three satellites is favorable.

Saturn

The method of analysis to generate the satellite possibilities and times that were used on Jupiter cannot be directly applied to Saturn. The reason is that the flyby trajectories are highly inclined to the ecliptic plane; about 1.3 rad (75 deg) for the JSP 77 mission as may be seen in Figure 3. On the other hand, most of Saturn's satellites are very close to the plane of the rings, which is inclined about 0.49 rad (28 deg) to the ecliptic. Thus, the flyby trajectories will be highly inclined to the satellite orbits. The first condition, then, that the flyby trajectory comes close to the satellite orbit, is less likely to be satisfied than for Jupiter, where the flyby trajectory and the satellite orbits are nearly coplanar.

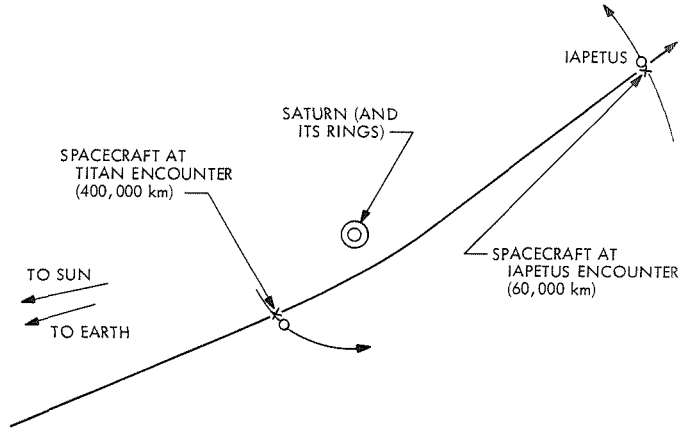

Figure 7. Possible Saturn flyby with multiple-satellite encounters

A preliminary analysis has been performed for the JSP 77 mission considering the possibilities of encountering the two larger satellites of Saturn, Titan, and Iapetus. Considering the out-of-plane condition, the possibilities are good. For Titan, the closest approach distance is about 400,000 km, and for Iapetus, about 60,000 km. Further, scanning the encounter times for Saturn arrivals ranging over a 6-mo period, a multiple encounter for Titan and Iapetus was found, where the closest approach distances are close to the values given above. The encounter opportunity is presented in Figure 7, as viewed from Saturn's north pole, where the time of periapsis passage is November 13.8, 1980 GMT. Because of the high inclination, there is no occultation of the spacecraft with Saturn as seen from Earth. This opportunity is rare because of the long period (79.3 days) for Iapetus.

Considering that Saturn has 10 known satellites, 7 of which have estimated radii, much of the analysis of encounters with these satellites lies ahead.

Uranus

For Uranus, which is considered in the JUN 79 mission, analysis of the flyby trajectory indicates that its plane is practically normal to the plane of the satellite orbits (all five of which lie in the plane of Uranus' equator and have near-zero eccentricity). In this extreme situation, a good approximation to the closest possible approach distance is simply the difference between the periapsis distance of the flyby trajectory and the semi-major axis of the satellite orbit. Referring to Figure 4, it is seen that the flyby periapsis distance is always less than the semi-major axis of Miranda (see Table 1), the innermost satellite of Uranus. Since the flyby altitude distance increases with flight time, the more favorable encounters will occur for the longer flight times (assuming that the time of periapsis is correctly chosen). A favorable aspect of the Uranus satellite encounter problem is the fact that the inner three satellites have short orbital periods (less than 5 days) allowing greater flexibility in timing the encounters, and possibly the performance of a midcourse maneuver to improve the encounter time.

Summary

The existence of favorable satellite encounter opportunities is most strongly dependent upon the geometric relationship between the flyby trajectory and the orbit of the satellite considered. For the JSP 77 and JUN 79 missions, this relationship at Jupiter is favorable. Thus, many encounter possibilities with the Jupiter satellites exist. For Saturn, the opportunities are less favorable, and for Uranus, they are quite unfavorable.

For Jupiter, with the approximate assumptions that the sets of flyby trajectories (Figure 5) are in the plane of the satellite orbits, and that

these orbits are circular, it has been possible to exhaustively determine the satellite encounter times. Essentially, these encounter times will occur twice during each revolution of the satellite, e.g., twice every 1.77 days for Io. Multiple-satellite opportunities are obtained by merely scanning the results and determining if there are several favorable encounters for the same flyby periapsis arrival time at Jupiter. Once these opportunities are found, a detailed analysis, utilizing the precise flyby trajectory and ephemerides of the satellite orbits, may be performed such as was done for the example given in Figure 6.

The encounter distance given in Figure 6 includes an out-of-plane component and, it is clear, that since the flyby trajectory characteristics change with Jupiter arrival date, this out-of-plane miss will also change. Analyzing the geometry more closely, it has become evident that this minimum distance can become quite small for certain satellites. This occurs when the flyby trajectory passes through the satellite orbit plane at the same time that it encounters the satellite. For JSP 77 this can occur for Ganymede before periapsis passage, and for Io and Europa after periapsis passage. For JUN 79, a near-zero encounter distance can occur for Io and Europa after periapsis passage. Determination of these closest approach times and the precise distance of these approaches has not been determined as yet; however, these times may offer opportunities to study a single satellite very closely, including possible occultations with Earth.

In summary, even with the trajectory restrictions which the multiple-planet missions impose, there exist possibilities to increase the scientific return and make these missions even more attractive by including close flybys with satellites.

References

1. Wallace, R. A., "Missions to the Outer Planets," in *Supporting Research and Advanced Development*, Space Programs Summary 37-54, Vol. III, pp. 35–36. Jet Propulsion Laboratory, Pasadena, Calif., Dec. 31, 1968.

2. Bourke, R. D., Friedman, L. D., Penzo, P. A., and Stavro, W., "Design of Grand Tour Missions," AIAA Paper 71-187, presented at the AIAA 9th Aerospace Sciences Meeting, New York, N. Y., Jan. 25–27, 1971.

3. Flandro, G. A., "Fast Reconnaissance Missions to the Outer Solar System Utilizing Energy Derived from the Gravitational Field of Jupiter," *Astronaut. Acta*, Vol. 12, No. 4, 1966.

References (contd)

4. Melbourne, W. G., Mulholland, J. D., Sjogren, W. L., and Sturms, F. M., Jr., *Constants and Related Information for Astrodynamic Calculations, 1968*, Technical Report 32-1306. Jet Propulsion Laboratory, Pasadena, Calif., July 15, 1968.

5. Newburn, R. L., Jr., *A Brief Survey of the Major Planets: Jupiter, Saturn, Uranus, and Neptune,* Technical Memorandum 33-424. Jet Propulsion Laboratory, Pasadena, Calif., Apr. 1, 1969.

Applications of FORMAC in the Mathematics of General Relativity

H. D. Wahlquist

Space Sciences Division

The use of FORMAC (formula manipulation by computer) to perform symbolic analysis on the computer in the field of general relativity is described. FORMAC will accept symbolic analytical expressions involving complex algebraic functions, elementary transcendental functions, user-defined functions, and unspecified functions of any number of dependent variables. In particular, FORMAC programs have now been written to implement the noncommutative calculus of exterior differential forms. Applications of this new capability to Hamiltonian cosmology and the theory of partial differential equations are discussed.

Introduction

In recent months the IBM FORMAC (formula manipulation by computer) system has become available at JPL for use with the IBM 360-75 computer. The present version of FORMAC is imbedded in the PL/1 programming language and represents a considerable improvement over the original FORTRAN version that was developed in 1965. FORMAC will accept symbolic analytical expressions involving complex algebraic functions, elementary transcendental functions, user-defined functions, and unspecified functions of any number of dependent variables. Instructions are available to manipulate these expressions algebraically, make substitutions and evaluations, take partial derivatives of any order, analyze the structure of generated expressions, print out results in an edited form (with raised exponents, for example) which is quite close to standard algebraic format, and punch intermediate expressions on cards in an appropriate form for later input.

The system performs a great deal of automatic simplification of expressions as they are generated. All transformations requiring the factoring of an expression, however, are under control of the user and *not* done automatically. As a result many elementary simplifications are missed if

not specifically programmed. In a complicated program this can lead to an explosive growth in the length of expressions, rapidly filling all available core. This is the major difficulty in using FORMAC and can be a serious drawback. However, our experience has been that it can usually be handled by careful and sometimes incremental programming.

Applications in General Relativity

The mathematics of general relativity is an excellent example of a field in which a large amount of tedious, time-consuming, and error-prone analysis must be performed. The prototypical problem is the derivation of the Christoffel symbols and Riemann tensor components from a given metric tensor. A number of FORMAC programs to accomplish this task have been written by users in the past few years; it is a straightforward and very satisfactory application of FORMAC.

The search for exact solutions of the field equations of general relativity, however, often requires less straightforward, but still very lengthy, analysis and several specialized FORMAC programs to aid in accomplishing this work have now been developed. Most recent investigations in this area involve the use of modern coordinate-independent formulations of general relativity such as exterior differential forms and the closely related tetrad formalisms, one of the latter being the dyadic formalism originated at JPL.

Differential Forms and the EXTCALC Subroutines

Actually, the language of exterior differential forms has found wide application in various fields of mathematics and theoretical physics other than general relativity. Examples are: Hamiltonian mechanics, differential geometry, and the general theory of sets of partial differential equations (see Reference 1). FORMAC is not immediately competent to deal with this language, which involves noncommutative operations. Recently, however, a set of PL/1 FORMAC subroutines (the EXTCALC package) was developed by F. Ernst of the Illinois Institute of Technology to implement this capability for calculations in general relativity. In collaboration with Professor Ernst, we have now extended the original EXTCALC package to incorporate additional operations so that it is no longer limited to a specific application, but is capable of performing virtually all the analytical operations of the exterior calculus of differential forms. Thus, quite general problems can now be formulated in this language and analyzed on the computer.

A thorough description and user's manual for the original EXTCALC package can be found in Reference 2, and only a brief summary of the

extended package is presented here. The specific operations of the exterior calculus implemented within the present EXTCALC package are:

Operation	Subroutine name
Exterior product	HAT
Vector contraction	CONTRACT
Exterior derivative	D or (@)
Lie derivative	LIE

One writes any symbolic differential form expression containing these operations (which may be nested) as a character string argument of the master subroutine #LET, in direct analogy with standard FORMAC statements. This master routine then directs the processing of the expression, calling the necessary operational subroutines, until a correct expression, interpretable by standard FORMAC, is created and returned. Several other convenient (though unessential) operations can also be performed within #LET. Thus, for example, one can order differential form expressions into a specified format, extract the coefficient of any basis form, and switch to a new set of basis forms.

Several diverse applications of this capability have been made in recent months. Within general relativity we have used the EXTCALC package to aid in developing a unified Hamiltonian theory of a class of homogeneous, anisotropic cosmological models—those with symmetry groups of Bianchi types VIII and IX. The differential geometry of such spaces is best treated in differential form language with anholonomic basis forms adapted to the appropriate symmetry group, which is an ideal application of the formalism.

Another application has been to perform some of the calculations involved in deriving symmetry groups of partial differential systems. Here again, as shown in the work reported in Reference 1, the use of differential forms permits the most elegant and concise formulation of the general theory of symmetry properties of sets of partial differential equations. In this approach the equations for the generators of the symmetry group are expressed in terms of the Lie derivatives of a set of exterior differential forms equivalent to the set of partial differential equations. To work out the content of these equations in a complex case can require a considerable amount of analysis. Using the FORMAC–EXTCALC capability for Lie differentiation of forms, it is now a simple matter to design a program (ISOVECT) to accomplish the analysis on the computer.

References

1. Harrison, B. K., and Estabrook, F. B., "Geometric Approach to Invariance Groups and Solution of Partial Differential Systems," *J. Math. Phys.*, Vol. 12, Feb. 1971 (in press).

2. Ernst, F. J., "Manipulation of Differential Forms on a Digital Computer," in *Proceedings of the Relativity Seminar*, Illinois Institute of Technology, Chicago, Ill., Sept. 1969.

A Higher Performance Electric-Arc-Driven Shock Tube

W. A. Menard

Environmental Sciences Division

The results of an experimental study made to improve the performance of electric-arc-driven shock tubes are presented. With only minor modifications to the driver, shock velocities have been increased by a factor of 3. The new driver has a conical internal design of small volume, and uses a light-weight diaphragm which disintegrates during the electrical discharge. Data obtained from a 15.2-cm-diameter driven tube, 11.3 m in length, show little shock wave attenuation in gases simulating the Jupiter and Saturn atmospheres. Shock velocities of 45 km/s with test times in excess of 4 μs have been attained. Because of the extended performance, the electric-arc-driven shock tube may now be used to study many outer-planet atmospheric entry problems.

Introduction

To study Jupiter and Saturn atmospheric entry problems in the laboratory requires a facility capable of producing shock velocities from 25 to 48 km/s. The purpose of this article is to report on the modifications made to the JPL shock tube, which have increased velocity well into the outer-planet entry range. An experiment was designed to investigate performance over a wide range of driver energies, and initial pressures from 6.66 to 6660 N/m^2 (0.05 to 50 torr).[1] Measurements of shock velocity, shock wave attenuation, and test time were made in several test gases.

Facility

The JPL electric-arc-driven shock tube was originally designed with a 3.5-cm-diameter driver, 66 cm long (Reference 1). A later design (Reference 2) provided for a variable length and increased the diameter to

[1]Where applicable, the International System of Units is stated first, followed by the customary units in parentheses. In each case, the value in parentheses represents the measured or calculated unit.

15.2 cm. Energy for the driver is supplied by a 100-capacitor (14.5 μF) storage system, rated at 290,000 J when charged to 20,000 V.

The new driver, which was designed from the driver of Reference 2 with only minor modifications, is shown in Figure 1. The cathode is a 3.2-cm-diameter cylinder made from Mallory 1000 (a sintered tungsten alloy). A hole in the cathode tip allows the trigger wire to be pulled through. The anode is a 2.5-cm-wide, 7.6-cm-diameter copper ring located 9.6 cm from the cathode. A conical Teflon insert reduces the driver volume to 350 cm^3, and provides a fairly smooth internal contour from the cathode tip to the 15.2-cm-diameter driven tube. The half angle of the cone is approximately 217 mrad (12.5 deg). The diaphragm is located on the downstream side of the anode ring. A 0.025-cm-diameter stainless steel wire is strung across the opening, and the trigger pull wire is attached to this wire. In operation, the arc is initiated by pulling the trigger wire toward the cathode.

In order to reduce diaphragm opening losses and to insure a fast opening time, Mylar diaphragms (0.035 cm thick) are used. Helium or hydrogen gas is supplied to the driver at a pressure of 1.19×10^6 N/m^2 (11.8 atm), just 4% less than the static rupture pressure of the diaphragms.

When the arc is struck, the trigger wires and the diaphragm immediately disintegrate. It was found that at high driver energies the copper anode could not hold the arc. Severe erosion on the surface of the stainless steel transition section was evidence that the arc had extended 7 cm beyond the diaphragm. Current measurements of the capacitor bank discharge show the arc burns for about 25 μs. During this time the driver

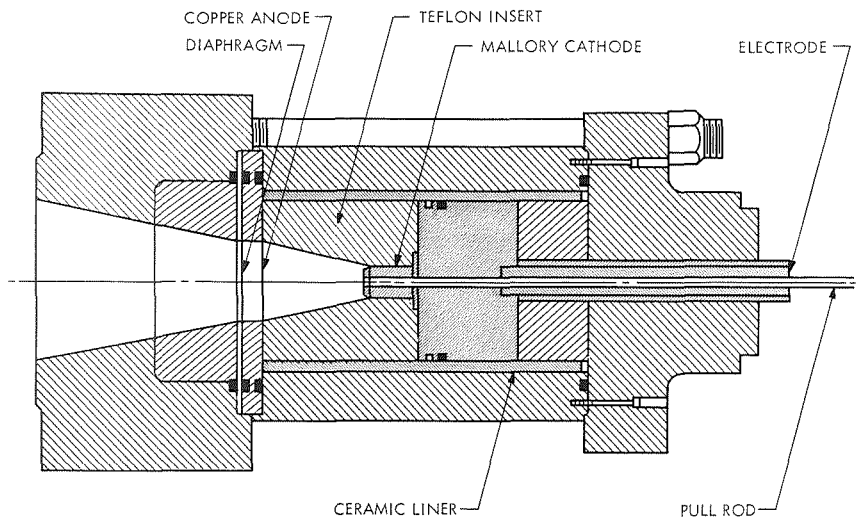

Figure 1. Schematic of driver configuration

gas can receive energy from the arc while in the driver, and as it expands down the tube.

Erosion of the cathode and copper anode was minimal. Replacing the transition section with one made of copper would reduce erosion there and improve electrode efficiency.

Shock Velocity Measurements

The most abundant elements in the atmospheres of Jupiter and Saturn are believed to be hydrogen and helium. For this reason the majority of the shock tube runs were made in a mixture of 80% He and 20% H_2 (by volume).

The driven tube was 11.3 m long and had instrument ports arranged to measure shock velocity U_s at distances L from the diaphragm of 2, 3.66, and 10.67 m. Shock speeds were measured by viewing the shock front radiation with collimated photomultipliers spaced 61 cm apart.

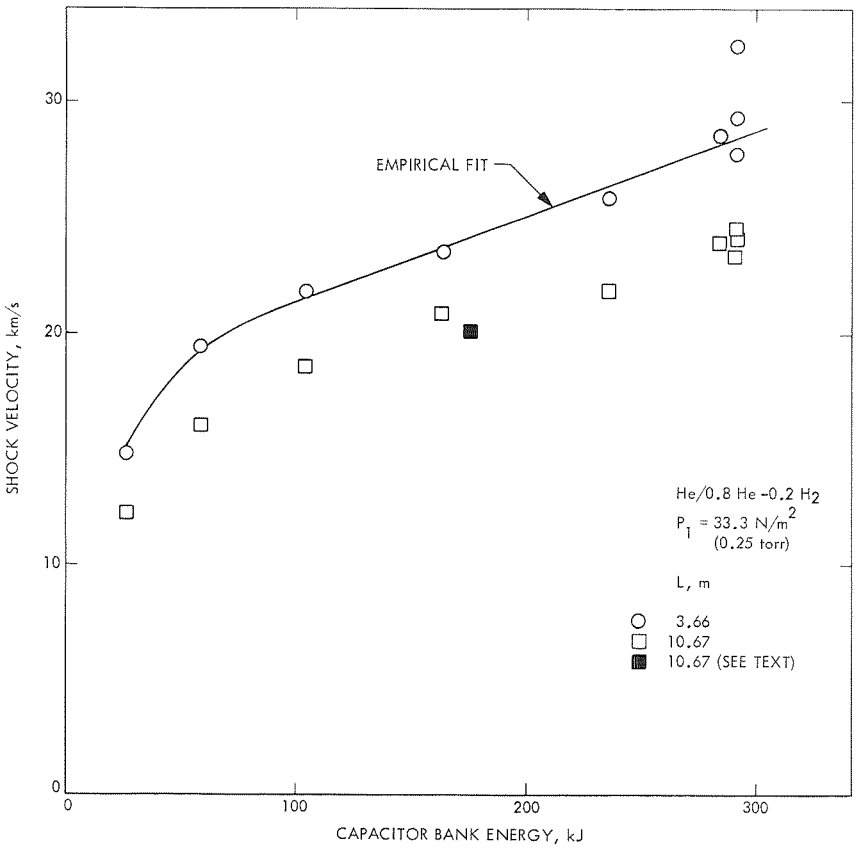

Figure 2. Variation in shock velocity with energy input

Velocities were measured to an approximate accuracy of ±3%. The tube was cleaned and pumped to 0.06 N/m² (0.5 μ) or less before each run.

Shock velocities obtained in 33.3 N/m² (0.25 torr) of the test gas, over a range of driver energies from 26,000 to 290,000 J, are presented in Figure 2. The driver gas was helium, and the data were taken at 3.66 and 10.67 m from the diaphragm. Velocities were obtained from 12 to over 32 km/s. They are seen to increase continuously as energy is increased with no indication of leveling off. If more energy were available, it would appear that even higher speeds could be reached.

The dark data point at $L = 10.67$ m was taken with one-fourth of the capacitor bank disconnected to investigate the effect of driver voltage on performance. No significant effect was observed.

The effect of initial pressure on performance is shown in Figure 3. Pressure was varied from 6.66 to 6660 N/m² (0.05 to 50 torr) while hold-

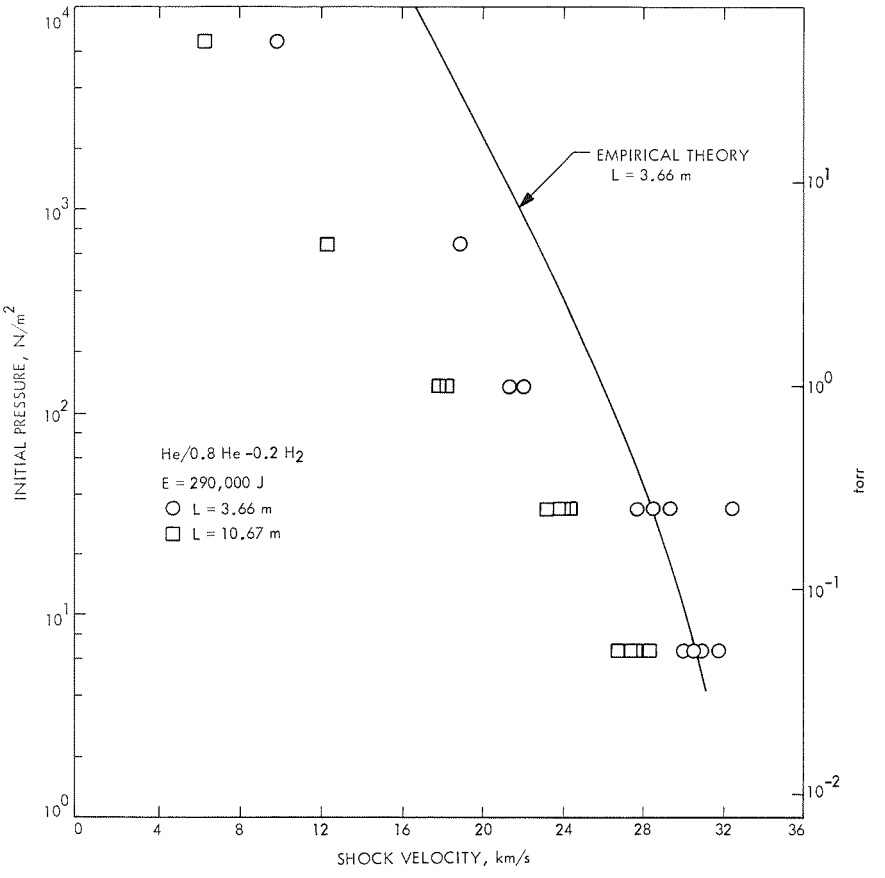

Figure 3. Shock velocity/initial pressure performance

ing energy constant. Attenuation of the shock wave is less at the lower pressures. Over a distance of 7 m, the lowest pressure data shows an attenuation of only 10%, but at pressures of 666 and 6660 N/m^2 (5 and 50 torr), the attenuation is 35%.

Other Gases

Runs were also made in pure hydrogen, helium, air, and argon, using helium and hydrogen driver gases. A summary of results is presented in Table 1. Shock velocity and test time data at two tube locations are given. The test times, in μs, are in parentheses. Where times are not shown, it is because the shock front had not completely formed.

Shock velocities, in general, decrease as molecular weight of the test gas increases. With a helium driver, shock speeds in the light gases are greater than 30 km/s, and in the heavy gases, $U_s \geq 20$ km/s. A further increase in shock velocity is obtained when hydrogen is used as the driver gas. Hydrogen-driven shock waves as fast as 45 km/s have been produced. Higher speeds were also obtained in the heavy gases, but they are accompanied by stronger attenuation.

Hydrogen is obviously more efficient in accepting electrical energy and converting it into flow energy, and damage to the driver verified its

Table 1. Shock velocity, test time, and equilibrium temperature for several driver and driven gases, measured at two distances from the diaphragm[a]

Driven gas	Helium driver gas		Hydrogen driver gas		Temperature,[b] K
	3.66 m	10.67 m	3.66 m	10.67 m	
Hydrogen	—	—	45.0* (4-7)	39.5 (6)	12,300
0.2 H_2-0.8 He	30.8 (5)	28.4 (7)	41.3* (4)	40.4 (6)	22,000
Helium	34.4* (4)	28.9 (6)	—	—	21,000
Air	27.9* (7)	23.1 (11)	32.7 —	20.3 (11)	31,000
Argon	25.7 —	20.0* (12)	31.7 —	15.8 (12)	34,700

[a]Shock velocity in km/s, test time (in parentheses) in μs; initial driven gas pressure = 6.66 N/m^2 (0.05 torr); capacitor bank energy = 2.9 x 10^5 J.

[b]For velocities with asterisk.

efficiency in absorbing energy. After several runs the Teflon insert had developed deep holes near the cathode and required replacing. The holes were apparently burned by a much hotter plasma than was generated in helium.

The final column in Table 1 shows the equilibrium temperatures calculated (Reference 3) for the asterisked data. These temperatures are extremely high for incident shock waves. In fact, comparable temperatures have not been produced in the reflected waves of other conventional shock tubes.

Test Time Measurements

Test time is the time interval between passage of the shock front and the contact surface at a point on the shock tube. Three types of measurements were made to determine test times: (1) wide-band-pass radiation measurements from the sidewall, (2) narrow-band-pass measurements from the sidewall, and (3) heat transfer measurements on a model located on the tube center line. Wide-band radiation was observed with a collimated photomultiplier having an S-11 (visible) response. The narrow-band measurements were made with a photomultiplier viewing the gas through a 5-nm (50-Å) half-width, narrow-band-pass filter. The center wavelength was selected to coincide with the intense H_α line (656.3 nm). As the test slug passed the viewing station, radiation from hydrogen would disappear upon arrival of the helium driver gas. Two calorimeter heat transfer measurements were made to verify the results from the radiation techniques. Both measurements showed a linear slope of the output which is typical of constant stagnation point heating. The temperature change at the contact surface was recorded as an abrupt voltage change in the gauge output.

Radiation Profiles

Oscillograms of strong shock waves in 6.66-N/m^2 (0.05 torr) test gases are shown in Figures 4 and 5. The top traces are narrow-band intensity profiles, I_{NB}, and the bottom traces are wide-band profiles, I_{WB}. Absolute intensity calibrations were not made but in each record the voltage outputs from I_{NB} were much less than the outputs from I_{WB}.

The oscillogram in Figure 4a is from a 30.5-km/s shock in the 0.8He–0.2H_2 mixture. Identified on the narrow-band trace are the shock front, the atomic nonequilibrium overshoot, the equilibrium level, and finally the termination of the test time by arrival of the contact surface. The equilibrium level is highly ionized, consequently there should be little H_α radiation. The radiation observed may be from the He^+ 656.0-nm

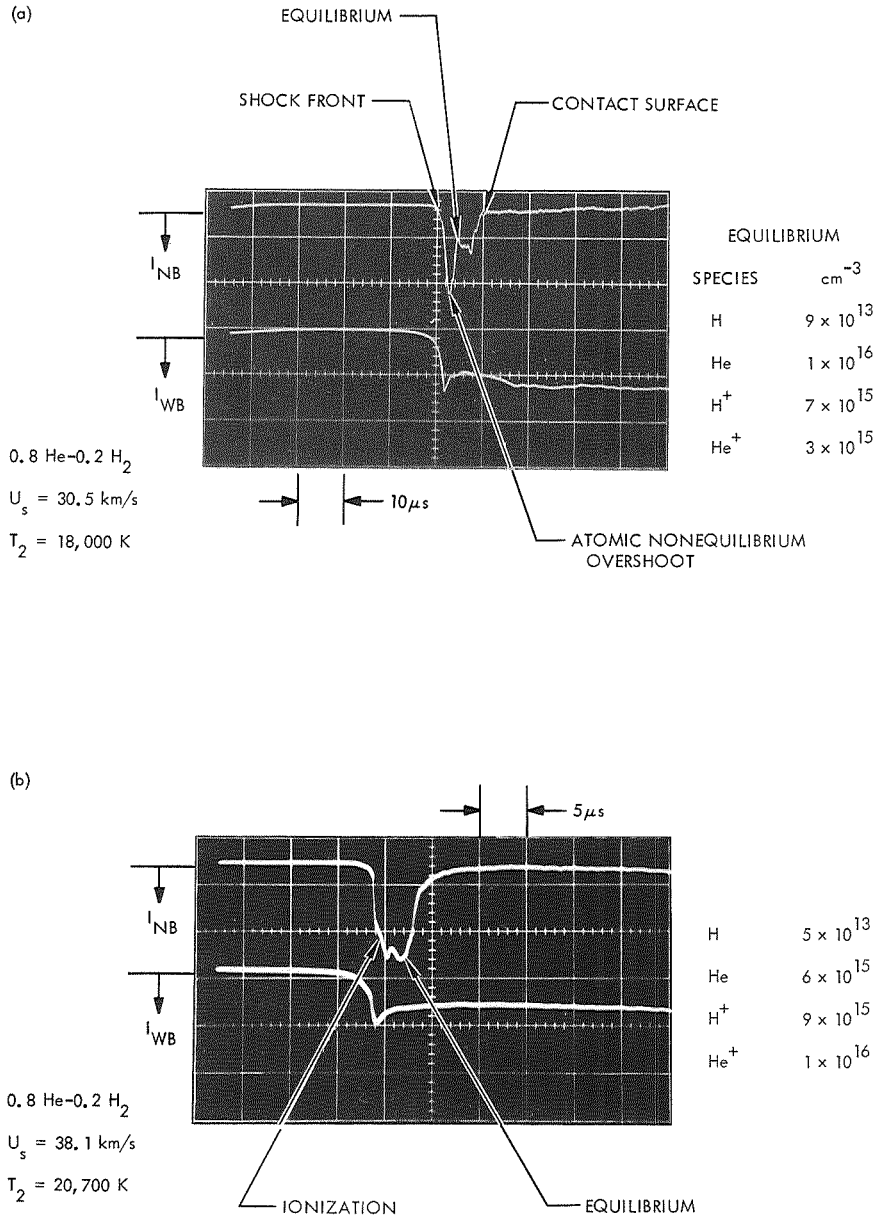

Figure 4. Narrow- and wide-band oscilloscope traces for 0.8 He–0.2 H_2 mixture

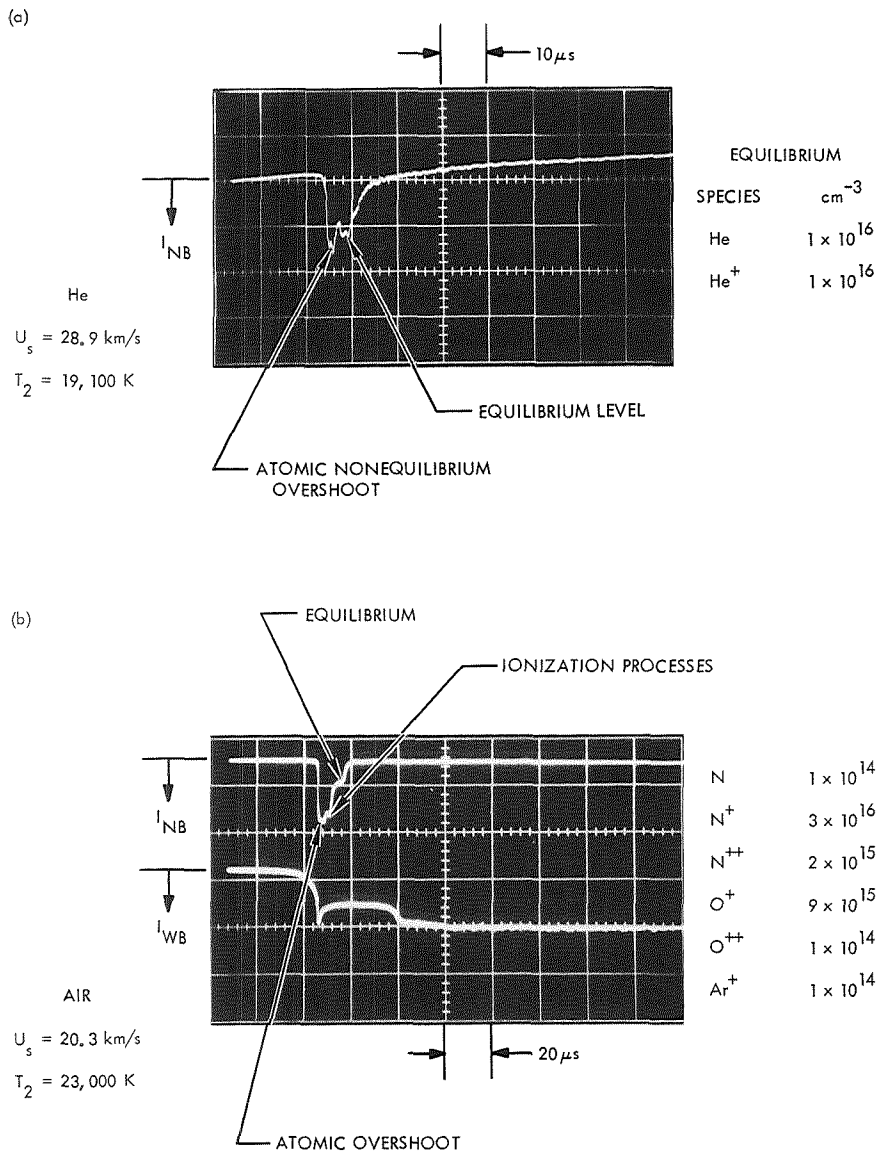

Figure 5. Narrow- and wide-band oscilloscope traces for He and air

(6560 Å) line, and the continuum. Increasing shock velocity to 38.1 km/s produces the profiles shown in Figure 4b. At this temperature the equilibrium composition is even more highly ionized. The sustained high level of equilibrium radiation may again be due to the continuum and He^+ line. Note that the helium ion number density has increased by a factor of 3 over the 30.5-km/s data. The narrow-band intensity drops sharply at the interface with the driver gas.

In Figure 5 are shown data for helium and air. Helium looks similar to the $0.8He–0.2H_2$ data. From the air trace it appears that several ionization processes are seen in the approach to equilibrium. In other runs these processes were observed to smooth out and the equilibrium level increased as temperature increased. At a temperature of 28,500 K the overshoot had disappeared and the intensity remained constant from the shock front to the interface.

The arrival of the contact surface is not obvious on most of the wide-band intensity data but is shown clearly when observed through the H_α filter. Tests made with H_2 driver gas did not alter the appearance of the test slug radiation profiles.

Correlation of Test Time Measurements

Some of the test time measurements are given in Table 1. Test times greater than 4 μs were obtained for all test conditions of the experiment, and if our interpretation of the radiation profiles is accurate, equilibrium was established in most cases.

An attempt to correlate the data with the boundary layer theories of Mirel (References 4 and 5) was unsuccessful. Laminar theory predicts "infinitesimal" test slug lengths at our Mach numbers and pressures. If one arbitrarily applies turbulent theory, lengths equal to about 25% of those measured are calculated. Similar results have been obtained by F. Livingston of this Laboratory in a pressure-driven shock tube operated at very low initial pressures. He was able to correlate his unpublished data, however, by considering two-dimensional effects.

The present measurements were correlated to the time it takes a disturbance originating at the wall to reach the center of the tube. Plotted in Figure 6 are the calculated times, $\tau_c = r/a_2$, versus the measured test times, τ_m, for all data having $U_s \geq 18$ km/s. (The radius of the tube is r and a_2 is the speed of sound.) Data for the five test gases and three initial pressures are shown. Even though there is large scatter, the general agreement is good. It would appear that more theoretical work is needed to better understand two-dimensional effects in shock tube flows.

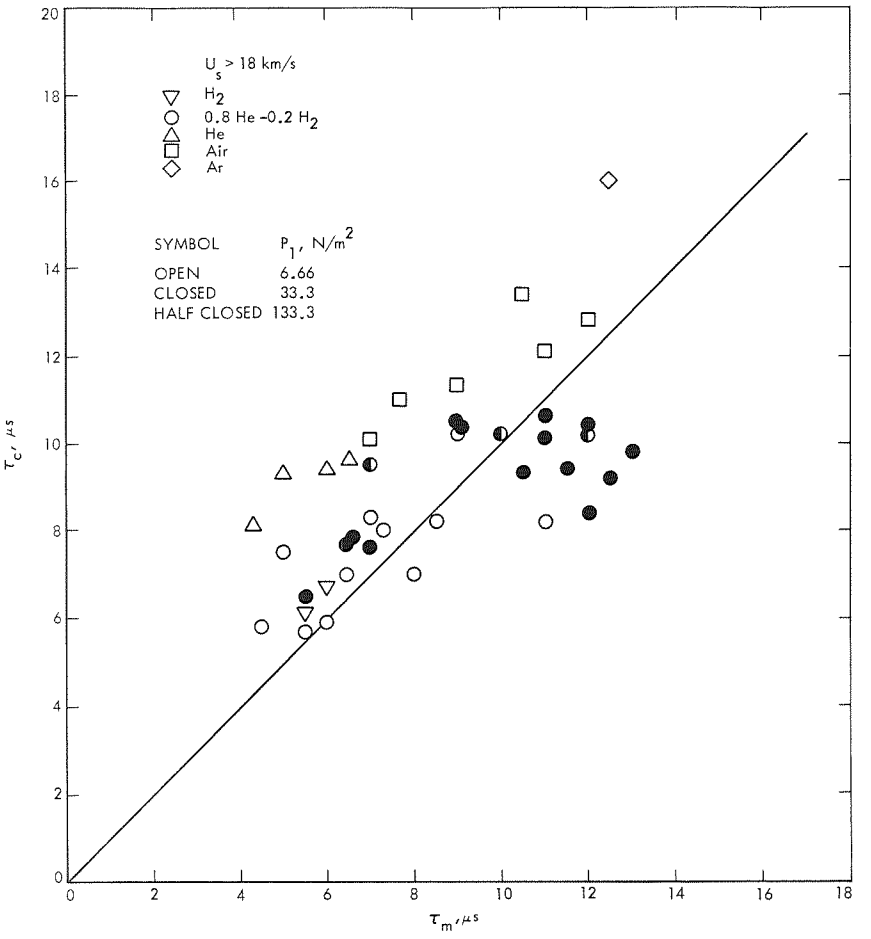

Figure 6. Correlation of test time measurements

Comparison With Other Facilities

A comparison with performance from other shock tubes is made in Figure 7. The present results are plotted for driven tube lengths from 2 to 10.67 m. The shock velocities exceed all other driving techniques except the electromagnetic driver. The modest attenuation is comparable to the combustion, piston, electrical, and two of the implosion drivers.

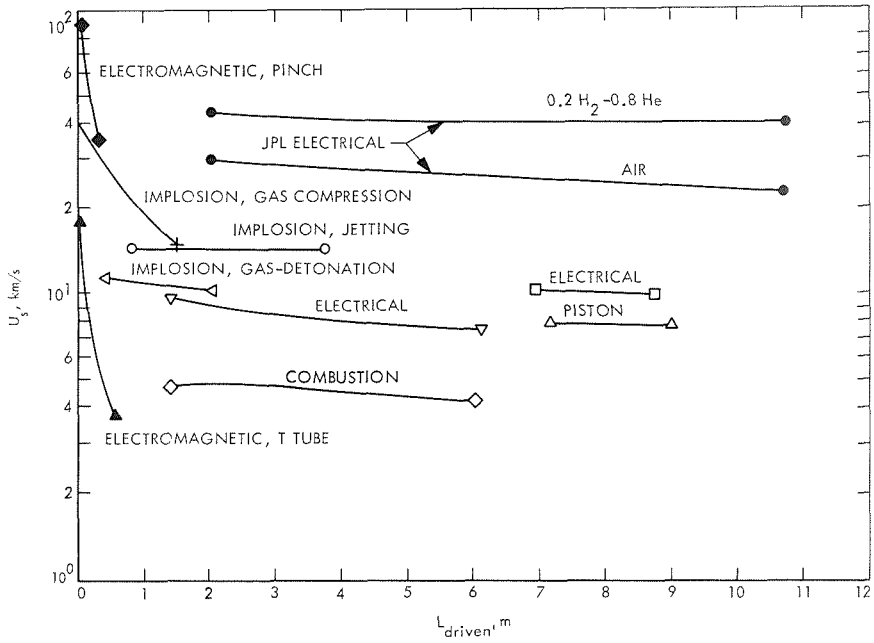

Figure 7. Comparison of present JPL performance with other driving techniques

References

1. Collins, D. J., Livingston, F. R., Babineaux, T. L., and Morgan, N. R., *Hypervelocity Shock Tube*, Technical Report 32-620. Jet Propulsion Laboratory, Pasadena, Calif., June 15, 1964.

2. Williard, J. W., "Performance of a Ceramic-Lined 6-In.-Diameter Arc Driver," Paper 68-366, AIAA 3rd Aerodynamic Testing Conference, 1968.

3. Menard, W. A., and Horton, T. E., *Shock-Tube Thermochemistry Tables for High-Temperature Gases: Vol. I. Air*, and *Vol. III. Helium, Neon, and Argon*, Technical Report 32-1408. Jet Propulsion Laboratory, Pasadena, Calif., Nov. 1, 1969 (Vol. I) and Jan. 1, 1970 (Vol. III).

References (contd)

4. Mirels, H., "Test Time in Low Pressure Shock Tubes," *Phys. Fluids*, Vol. 6, No. 9, p. 1201, 1963.

5. Mirels, H., "Shock Tube Test Time Limitation Due to Turbulent Wall Boundary Layer," *AIAA J.*, Vol. 2, No. 1, p. 84, 1964.

Solid-Propellant Burning-Rate Modification

M. F. Humphrey

Propulsion Division

Low acceleration is one of the requirements for solid-propellant orbit insertion motors for future outer-planetary missions. This article describes the research accomplished in reducing the low-pressure burning rates of modified solid propellants. Techniques developed with the saturated hydroxy-terminated polybutadiene system were successfully applied to the polyether system (JPL 540) and an unsaturated hydroxy-terminated polybutadiene propellant system. Burning-rate reductions up to 50% were obtained by the synergistic effects of increased oxidizer size, reduction of iron, and inclusion of flame retardants and endothermic combustion modifiers.

Introduction

Spacecraft design studies at JPL, for future outer-planetary missions, have shown that low acceleration is one of the requirements for solid-propellant orbit insertion motors. A prerequisite for achieving these low-acceleration, high-performance solid-propellant spacecraft motors is the development of very low burning rate propellants with specific impulses equal to or better than the JPL 540 propellant. This work was conducted to investigate applicable methods of producing the necessary low-propellant burning rates without seriously degrading the efficiency of the combustion process. The study was concerned, primarily, with tailoring existing propellant formulations and, secondarily, with developing general techniques adaptable to alternate binder compositions.

Burning-rate tailoring began by studying the effects of modifications to the following propellant formulations: saturated hydroxy-terminated polybutadiene (SHTPB), polyether–polyurethane (JPL 540), and unsaturated hydroxy-terminated polybutadiene (UHTPB). These propellant systems were developed at JPL. The modifications investigated were oxidizer particle size, cure catalysts, binder ingredient alterations, and inclusion of combustion modifiers. The modified formulations of each

propellant system were mixed in 2-kg batch sizes in a 3785.4-cm^3 (1-gal)[1] Bramley mixer. The propellant batches were cast into Crawford bomb and soda straw burning-rate strands and physical property tensile bar molds. Based on the planetary mission low-acceleration requirements, an absolute combustion pressure of 68.9 N/cm^2 (100 psi) was chosen as the comparable parameter for the development.

Saturated Hydroxy-Terminated Polybutadiene System

An existing propellant system utilizing an SHTPB binder was the first system studied as a low burning rate propellant candidate. This propellant was selected since the standard formulation already had an inherently lower burning rate than JPL 540. This SHTPB binder, called Telagen S, was produced by the General Tire and Rubber Company. The propellant was modified by combinations of increased oxidizer particle size, an organo-phosphate flame retardant, and a low concentration of a gas producer. The results of these modifications indicated that the burning rate was lowered from a standard of 0.24 to 0.13 cm/s (0.094 to 0.052 in./s) at absolute pressure 68.9 N/cm^2 (100 psi). At the same time, changes in physical properties occurred, that is, the tensile strength decreased from a standard of 198.6 to 134.5 N/cm^2 (288 to 195 psi), and the elongation increased from a standard of 35 to 44%.

Since the SHTPB propellant system cures at 377.6 K (220°F) for five days, a study was performed to lower these cure conditions. Utilizing polymerization catalysts, a more rapid low-temperature cure of 300–305 K (80–90°F) for two days was obtained with small concentrations of ferric acetoacetonate (FeAA). However, it was found that the FeAA promoted increased burning rates. Examination of other organo-metal compounds, as potential cure accelerators, indicated that vanadium acetoacetonate (VaAA) would give the desired cure without alteration of the propellant burning rate or mechanical properties.

Soluble unreactive binder additives were also evaluated. The materials studied included: tri (bromo propyl) phosphate, tri cresyl phosphate (TCP), dihydro ethoxy trimethyl quinoline (ethoxyquin), octyl diphenyl phosphate (ODDP), and isodecyl diphenyl phosphate (IDDP). Only the IDDP was found to be effective in reducing the burning rate at a low concentration of 1%.

Polyether–Polyurethane System

Since JPL 540 propellant is well understood, it was also selected as a low-acceleration candidate propellant. The burning rate for the standard

[1]Where applicable, the International System of Units is stated first, followed by the customary units in parentheses. In each case, the value in parentheses represents the measured or calculated unit.

propellant formulation is 0.356 cm/s (0.140 in./s) at absolute pressure 68.9 N/cm^2 (100 psi). Modifications were made to this propellant system which resulted in a reduction of the maximum burning rate to 0.229 cm/s (0.090 in./s) at absolute pressure 68.9 N/cm^2 (100 psi). The modifications made were as follows:

(1) The average oxidizer particle size was increased from 185 to 340 μm.

(2) One percent of an organo-phosphate flame retardant was added.

(3) Regular aluminum powder (2000 ppm iron) was replaced with an essentially iron-free aluminum (20 ppm iron).

(4) Two percent oxamide was added.

Based on the data generated from the strand burning tests, a 2.95-kg (6½-lb) batch of the 0.229-cm/s (0.090 in./s) modified propellant system was loaded into a 12.7-cm (5-in.)-diameter motor. The motor was fired at an average absolute pressure of 62.7 N/cm^2 (91 psi), resulting in an average burning rate of 0.259 cm/s (0.102 in./s). The slightly higher rate was obtained by a reduction of the oxamide concentration to 1%.

Combustion rate studies performed by Rocketdyne, a Division of North American Rockwell Corporation, indicated the burning rate of JPL 540 at absolute pressure 68.9 N/cm^2 (100 psi) could be reduced from 0.356 to 0.196 cm/s (0.14 to 0.077 in./s) by replacing 10% of the oxidizer with nitroquanidine, in addition to the other modifications. No adverse effects in processing or mechanical properties were noted in the propellant; however, in firing the 5.08-cm (2-in.)-diameter motor configurations, a reduction in predicted specific impulse resulted.

Differential scanning calorimeter studies showed a dependence of burning rate on the iron concentration of uncured propellants. Based on this information and the effect of iron on SHTPB formulations, the effort was directed toward complete removal of iron from the propellant. If a minimum burning rate could be established in an iron-free environment, then iron could be quantitatively added to provide any desired rate. The cure catalyst used in 31 experimental batches of JPL 540 was FeAA. Other organo-metallic compounds were tested as replacements for this compound, but none would effect a complete propellant cure. Two metal chelates containing lead and titanium gave excellent cures in gum stock studies, but when combined into a propellant with oxidizer, they would not produce the same degree of cure. The synergistic effects of ammonium perchlorate oxidizer and cure catalyst, trace metals, or other components in the binder are little understood. Some ammonium perchlorate solubility in polypropylene glycol with dissociation is believed to take place as evidenced by the inactivation of metallic catalysts. Bonding

agents, such as the tertiary amines, MT-4, and dihydroxy propyl cyanoethyl amine (C-1), apparently reduced this effect. Oxamide, in low concentrations, was found to reduce the required concentration of the iron cure accelerator and may be functioning in the same manner.

To obtain information on the combined effects of ammonium perchlorate on the binder polymerization process and the burning rate alterations, propellant batches were made with more chemically basic binder insoluble additives, such as calcium oxide (CaO), magnesium oxide (MgO), and disodium phosphate ($NaHPO_4$). Calcium oxide, the more basic of the additives, prevented binder cure entirely, even in the presence of the FeAA cure catalyst. Magnesium oxide produced a soft cure with increased burning rates. Disodium phosphate allowed a cure but increased the burning rate and reduced the mechanical properties. Another binder insoluble material investigated, sodium fluoborate ($NaBF_4$), produced acceptable cures with decreased burning rates but also degraded the propellant strain capabilities. Of the insoluble materials examined, oxamide was the only one that did not alter the cure capability or degrade the mechanical properties while effectively contributing to reducing the burning rate. Of the soluble unreactive binder additives, only the IDDP material was evaluated, based on previous results in the polyether–polyurethane system. Due to the very low viscosity of IDDP, a thinner mix was produced which suggests the possibility of increasing the propellant total solids content.

Another method investigated to reduce the burning rate of the polyether binder system was to change the binder polymer structure. Major changes in the binder formulation were not attempted since little change from the low-modulus, high-elongation mechanical properties of JPL 540 could be tolerated. Since the molecular weight and functionality of the polyether monomer were fixed, the only available degree of freedom to investigate was the co-reacting low molecular weight polyols containing known flame suppressant functional atoms or groups.

It was also desired to raise the melting point, or thermoplastic point, of the polymer to increase the temperature required for combustion. Among the reactive materials investigated were brominated polyols, phosphated polyols, halogenated phosphated polyols, and hydroxy-terminated amines.

Burning rates were slightly reduced with the phosphated polyols; however, an unexpected rate increase was noted with a brominated polyol. The amines showed little or no influence in the low-pressure region (absolute) of 34.47 to 172.35 N/cm^2 (50 to 250 psi). A linear aliphatic diisocyanate (DDI) was compared with the aromatic toluene diisocyanate (TDI) as a chain extender, but no improvements were detected in either the strain capability or burn-rate reduction.

Unsaturated Hydroxy-Terminated Polybutadiene System

The third propellant system investigated was an experimental propellant containing a UHTPB binder. This system is an attractive low-acceleration propellant candidate due to its inherent low burning rate characteristics. Also, it has a high solids loading capability and potentially can be cured at or near room temperatures.

An exploratory series of fifteen 3785.4-cm^3 (1-gal) batches of propellant were made with UHTPB. Although the results of the first series did not produce a high strain capability, low burning rates at absolute pressure 68.9 N/cm^2 (100 psi) were achieved. Initially, a tin cure accelerator was used but reaction rates were so rapid that polymerization occurred during the mix cycle. Complete elimination of the cure accelerator did not sufficiently reduce the reaction rate to allow casting. Inclusion of the antioxidant phenyl beta naphthyl amine (PBNA) at 1% by weight of UHTPB helped reduce the reaction rate. The addition of 2% by weight of diethanol amine stearate further reduced the reaction rate and also helped to internally plasticize the mix. However, larger quantities of the stearate tended to cause gellation, probably due to the amine reaction. A very good polymerization was obtained when DDI was substituted for TDI as the chain extender. Batches made using a plasticizer, dioctyl adipate (DOA) at 20 to 25% by weight of the binder, produced very fluid mixes which were easily processed at 86% solids loading. Burning rates for UHTPB formulations containing 82% solids were found to be 0.18 to 0.213 cm/s (0.071 to 0.084 in./s) at absolute pressure 68.9 N/cm^2 (100 psi). These rates were accomplished by using 340-μm ammonium perchlorate, a phosphated polyol, iron-free aluminum, and IDDP. One formulation containing a low molecular weight polyol, bis-hydroxy propyl aniline (Isonol C-100), gave a burning rate of 0.165 cm/s (0.065 in./s) at absolute pressure 68.9 N/cm^2 (100 psi) and a maximum stress of 186.2 N/cm^2 (270 psi) with a strain of 27% as determined from tensile specimens. Use of the ammonium perchlorate bonding agent MT-4 did not improve the strain capability of this propellant. Several hydroxy-terminated materials were co-reacted with the UHTPB in an effort to improve the strain capability but with little success. Straight UHTPB without reactive modifiers produced propellants with 5–7% strain capabilities and burning rates of 0.198 to 0.218 cm/s (0.078 to 0.086 in./s) at absolute pressure 68.9 N/cm^2 (100 psi). Use of stearates in the formulations increased the strain level to 17% without affecting the burning rate.

Conclusions

The most significant reduction in propellant burning rates was obtained by increasing the average particle size of the oxidizer. This was generally true for each binder system studied. Additional reductions in burning rates were obtained by incorporating binder soluble organo-phosphates and the binder insoluble oxamide. These modifications were made more

effective by the reduction in overall iron content of the propellant systems. Preliminary studies with the unsaturated hydroxy-terminated polybutadiene system showed promise as a low burning rate, advanced urethane-type binder.

It was demonstrated that low burning rate propellant systems could be developed without seriously degrading the standard physical property characteristics.

Low Acceleration Rate Ignition for Spacecraft

J. I. Shafer, L. D. Strand, and F. A. Robertson

Propulsion Division

A *g*-dot ignition system for solid-propellant motors has been designed to prevent damage to fragile sensors or structural members on a spacecraft by producing, from a starting transient for the spacecraft of 0.3 *g*, a controlled buildup in thrust, such as to give an acceleration rate of about 0.3 *g*/s. The system consists of a 3-s, regressive-burning, controlled-flow igniter and a highly inhibited progressive-burning charge in the main motor. The igniter must operate in a hard vacuum and sustain burning of the uninhibited portion of the propellant below its normal L^* combustion limit through mass addition and heat transfer until the propellant surface has increased sufficiently to provide a stable motor chamber pressure. A specific internal torus-shaped igniter is described along with its advantages and disadvantages as well as potential methods of initiating burning in the hard vacuum with Pyrofuze.

Introduction

Current work on low-thrust, long-burning solid-propellant motor technology is oriented primarily toward orbit insertion missions at Jupiter, Saturn, and perhaps Mercury, because of extensive scientific interest and a recent JPL study (unpublished) of outer-planet orbiter missions. Figure 1 shows an artist's rendering of a Jupiter orbiter spacecraft from that study.

Note the long, highly flexible appendages for the scientific instruments and for the radioisotope thermoelectric generator on the opposite side of the spacecraft. These dictate a maximum spacecraft acceleration tentatively set at 1 *g* until trade-off studies can be made, and imply, inherently, low thrusts and long-burning times for outer-planet orbit insertion motors. Of special concern to the effort under discussion, the flexible appendages also dictate low acceleration rates, or *g*-dots, during the starting and shut-down thrust transients if limit cycling of the guidance components is to be avoided.

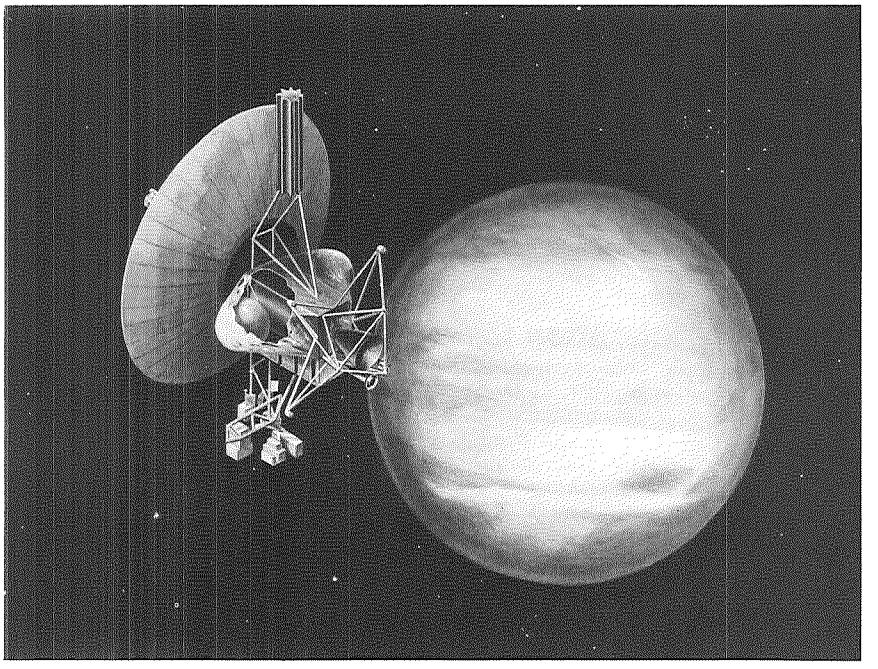

Figure 1. Jupiter orbiter spacecraft

A low spacecraft acceleration rate during thrust initiation will be achieved through the use of an unconventional *g*-dot ignition system that will gradually build up thrust at a controlled rate of about 0.2 to 0.3 *g*/s from its starting value, about one-third to one-fifth the maximum acceleration level. Reference 1 discusses some *g*-dot ignition feasibility studies and tests.

The low spacecraft deceleration rate of 0.2 to 0.3 *g*/s during thrust decay would be provided through a propellant charge geometry that automatically produces a gradual thrust tailoff, i.e., through propellant sliver formation.

Operation of the *g*-Dot Ignition System

Figure 2 shows an artist's rendering of the 363-kg (800-lb)[1] demonstration motor, designated D-2, in which the torus-shaped *g*-dot igniter will be used.

Operation of the igniter system can best be explained by reference to Figure 3, where the motor D-2 is shown in cross section with the torus-shaped *g*-dot igniter mounted on the submerged portion of the nozzle. The igniter is actually a small solid-propellant motor which burns with

[1]Where applicable, the International System of Units is stated first, followed by the customary units in parentheses. In each case, the value in parentheses represents the measured unit.

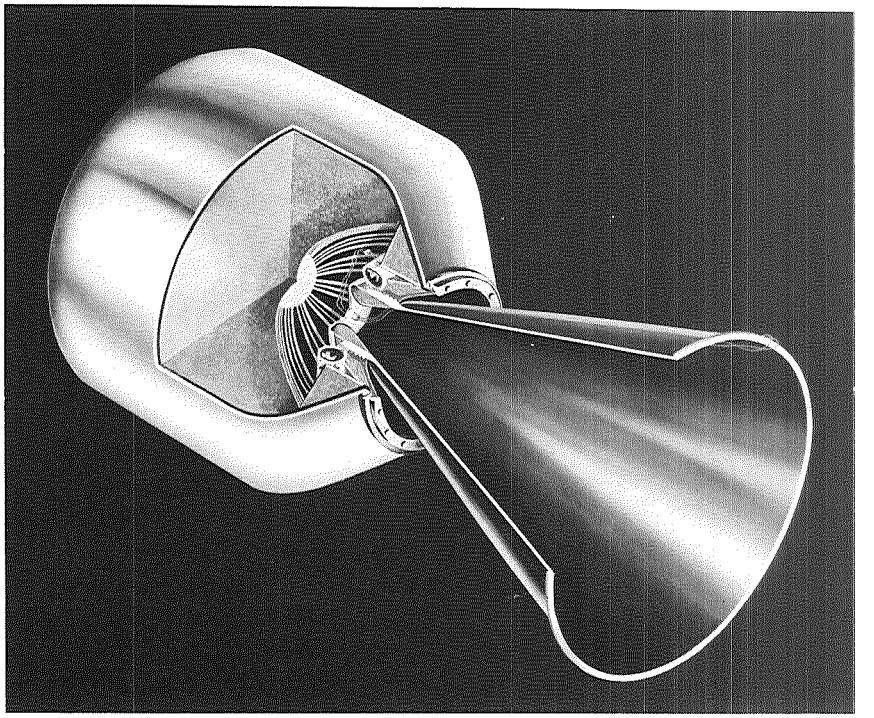

Figure 2. Demonstration motor D-2

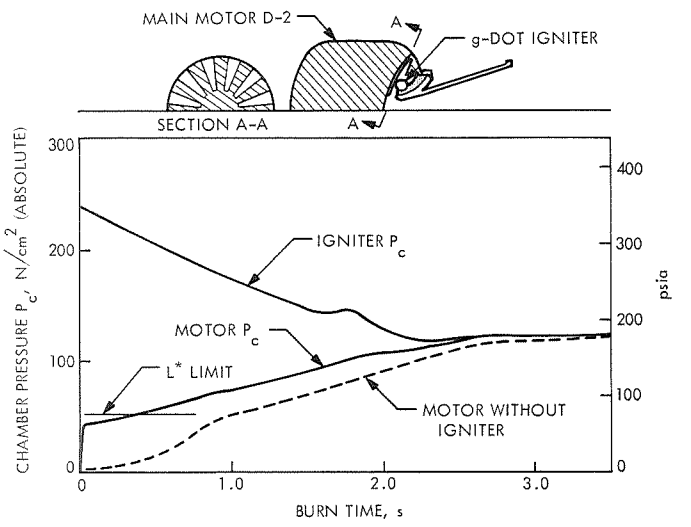

Figure 3. The *g*-dot ignition concept

supersonic exhaust for about 1½ s of its 2½-s burning time. Its combustion gases pass radially outward from numerous nozzles, impinging on the dish-shaped propellant surface. Igniter pressure (absolute) decreases from about 241 N/cm² (350 psi) to about 124 N/cm² (180 psi).

The main motor propellant surface is highly inhibited, as shown in section A-A, Figure 3, with an inhibiter pattern such as to produce a highly progressive burning surface as the propellant regresses under the inhibitor surface. Thus, if the motor propellant could burn at a very low pressure by itself, its pressure–time curve would resemble the broken line in Figure 3—with an initial pressure (absolute) of only 3.45 to 6.89 N/cm² (5 to 10 psi).

In reality, because of the L^* combustion limit of about 44.8 N/cm² (65 psi) absolute, the motor would not burn by itself below that pressure. However, when hot exhaust gases from the independent controlled-flow igniter are injected into the main motor, the mass addition raises the motor pressure (absolute) to about 34.5 to 37.9 N/cm² (50 to 55 psi) and burning of the main charge is sustained below the motor L^* limit by the heat transfer and mass addition. The resultant low pressure and thrust level permit the spacecraft to meet its 0.3-g initial acceleration requirement.

The main propellant burning surface and, consequently, chamber pressure increase with time in a controlled manner until the motor is able to sustain combustion without mass addition from the igniter. The small, thin inhibiter strips are partially, or completely, consumed before being ejected out of the nozzle.

The pressure–time relationships shown in Figure 3 represent nominal performance values. In practice, however, operation of the main motor below its normal L^* combustion limit has produced low-frequency low-amplitude oscillations characteristic of L^* combustion instability near the extinction pressure (Reference 1).

Concern about potentially unacceptable acceleration rates from these oscillations prompted a recent series of computer runs in which the effect of the oscillations on the spacecraft attitude controls was simulated using the Thermoelectric Outer-Planet Spacecraft model, modified to include the retro-propulsion for a Jupiter orbiter mission. It was concluded that, for both rigid and flexible body dynamics, the oscillations arising from the use of the *g*-dot igniter and other low-amplitude bumps and spikes which may occur in the thrust profile had no apparent effect on the attitude control system.

In the same series of computer runs, the effect of initial acceleration during igniter initiation and the acceleration rate during igniter burning on the spacecraft controls was also evaluated. The following results were obtained:

Maximum initial acceleration, *g*	Acceleration rate during igniter burning, *g*/s	Effect on spacecraft controls
0.2	0.2	Acceptable
0.4	0.4	Acceptable
0.6	0.6	Limit cycling

Because tests were not all-encompassing in their scope, conservative values of 0.3-*g* maximum acceleration and 0.3-*g*/s acceleration rate were adopted as design criteria for the ignition system and motor thrust decay. When the actual spacecraft configuration is known better, these design values should be reassessed.

Another significant deviation from the nominal performance values of Figure 3 stems from the ignition delay in initiating burning of the 71.1-cm (28-in.)-diameter main motor by the *g*-dot igniter (typically 0.2 to 0.3 s in small-motor *g*-dot firings). Figure 4 shows the igniter pressure–time curve, and the results of the calculations for main motor pressure–time curves when ignition delays were assumed to be 0, 0.3, and 0.6 s. Results were obtained from an overall mass flow balance for the motor.

The ratio of the mass flow rate of the igniter to that of the main motor, a critical parameter in sustaining burning below the L^* combustion limit, is given in Figure 4 to show that its value lies above the

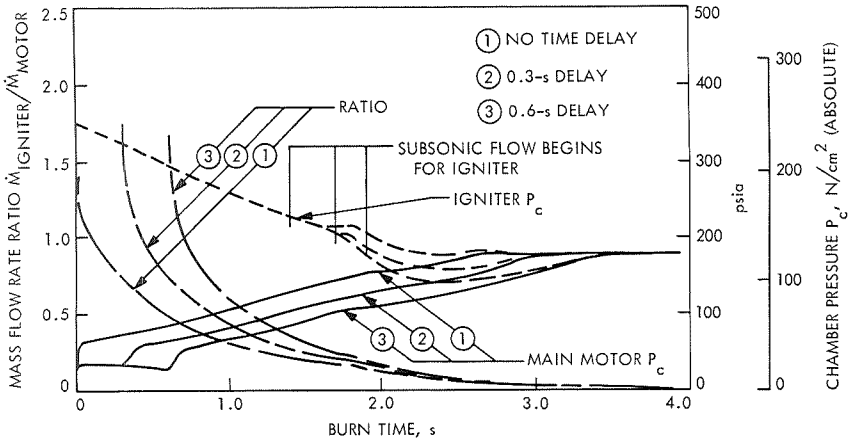

Figure 4. Mass flow rate ratio and chamber pressure vs burn time for main motor time delays of 0, 0.3, and 0.6 s

desired value of approximately one at the start of main motor burning for the given motor and igniter design conditions. Accelerations and acceleration rates fall within the 0.3 allowable values. Thus, it is believed that normal ignition delays will cause no difficulties in the firing of the demonstration motor D-2.

Internal Versus External Igniter System

There are advantages and disadvantages to an internal (torus) igniter compared to a 2- to 3-motor external igniter system, the more conventional arrangement. Figure 5 shows the two design concepts. The internal igniter was finally adopted, based on the following judgments.

The internal torus has the disadvantage that the main motor nozzle could become partially or completely plugged (disastrously) if uncontrolled breakup of the empty igniter case occurred during main motor burning. The problem appears to have been solved (1) by blocking the igniter into a cradle and cementing it to the nozzle phenolic insulation, and (2) through the use of a thermoplastic igniter case that will melt into a viscous glob around the nozzle and tend to wash away gradually into the stream of hot gases.

A second disadvantage results from the interface with the safe and arm mechanism, which, according to launch operations specifications, must be located outside the main motor. The safe and arm mechanism is relatively simple for external igniters where it could be located at the head end of the units with the initiator squibs. The use of Pyrofuze is being considered for the torus internal igniter in an effort to reduce the problem—or perhaps eliminate it.

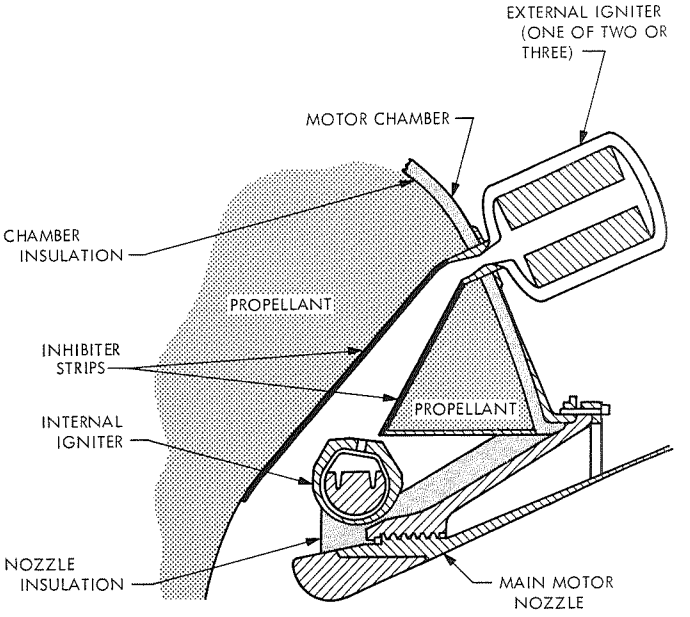

Figure 5. Internal (torus) igniter vs external igniter

Advantages of the internal igniter include (1) a required igniter hardware life of only 3 to 5 s compared to 140 s for the external igniters; (2) lower weight, fewer igniters and safe and arm mechanisms than the external system [the thickness of the insulation would be 1.02 cm (0.40 in.) in the external motor compared with 0.076 cm (0.03 in.) in the torus]; (3) flame spreading with 12 nozzles over the 71.1-cm (28-in.)-diameter charge surface should be better; and (4) the main motor case design and fabrication would be easier—no bosses on heat-treated chambers, no ports through the insulation and propellant, and fewer igniters to load with propellant.

Design of the *g*-Dot Igniter

Design features of the *g*-dot igniter are shown in Figure 6. Its outer diameter will be 28.7 cm (11.3 in.) and the small tube diameter will be about 5.33 cm (2.1 in.), with a wall thickness ranging from 0.3175 to 0.635 cm (⅛ to ¼ in.). The igniter case will be made of polycarbonate, a thermoplastic material, and will have 12 graphite nozzles equally spaced around the case and firing radially outward to promote flame spreading over the main propellant charge. Each nozzle will have a throat diameter of only 0.584 cm (0.23 in.); a propellant with only 2% aluminum has been selected in order to minimize changes in throat area and pressure from oxide deposition. The propellant weight is estimated at 1.07 kg (2.35 lb); the inert weight is the same. A layer of 0.076-cm (0.030-in.) rubber insulation on the inside, and perhaps on the outside, helps protect the plastic case for its 2½-s burning time. It has been designed with a safety factor of 2, based on limit loads.

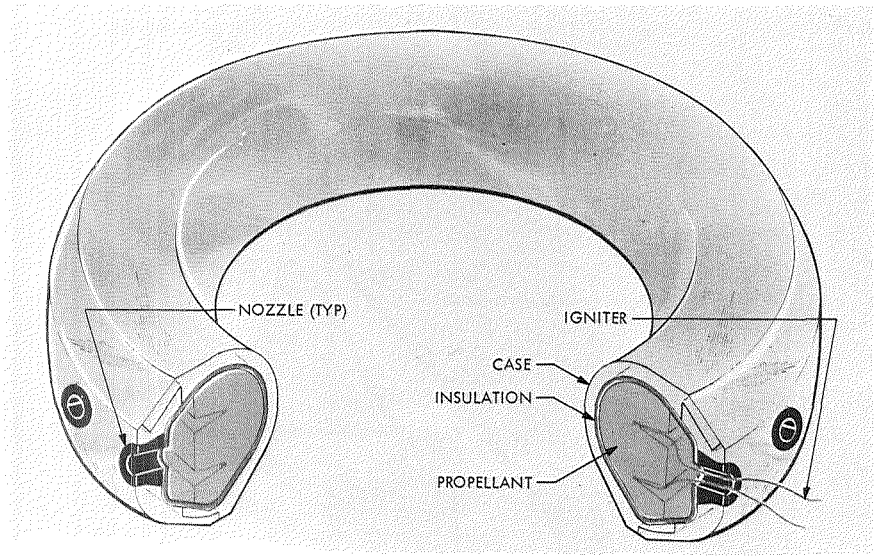

Figure 6. The g-dot igniter

Initiating Igniter Burning

The question of how best to initiate burning in the *g*-dot igniter in a hard vacuum is unanswered at this time. Vacuum ignition systems are available but an operationally simple system for a torus igniter poses something of a challenge.

Ignition, itself, involves the addition of external heat to the propellant at a rate such that its own subsequent decomposition and combustion produce sufficient heat to sustain further decomposition and burning when the external heat source is withdrawn. The process is complicated, especially in a vacuum, by (1) the propellant deflagration limit P_{dl}, that absolute pressure below which the propellant will not burn [about 2.07 to 2.76 N/cm^2 (3 to 4 psi) for the propellant under consideration]; (2) short residence times for the igniter combustion gases, i.e., low L^* motor values, so that there is insufficient time for heat transfer to the propellant to develop the required thermal gradient beneath the propellant surface, a necessary condition for sustaining burning; and (3) rapid decreases in pressure, i.e., high dp/dt, that can quench the burning—the rapid decrease may stem from the blowout of partial obstructions to gas flow or nozzle closures deliberately introduced earlier to raise the local pressure at the ignition surface above the P_{dl} value at which burning can be sustained.

The use of Pyrofuze wire is being considered for initiating burning in the igniter while in a hard vacuum. The Lockheed Propulsion Company and the Air Force Rocket Propulsion Laboratory have used Pyrofuze

successfully for igniting motors (Reference 2) but their experience appears to have been limited to firings at atmospheric pressure.

Pyrofuze itself is a coaxial wire with an aluminum core surrounded by a tube of palladium in intimate contact with the core. It has the unique property, when heated electrically or chemically to the 933 K (1220°F) melting point of aluminum, of instantly generating a large exotherm, under gas pressure or in a vacuum, due to the resultant alloying. Temperature in the wire alone can reach about 3030 K (5000°F), well above the 477 to 700 K (400 to 800°F) ignition temperature range of most solid propellants.

Figure 7 shows the cross section of the torus tube and location of the Pyrofuze, which is used here as a special type of hot wire igniter. A continuous braid of 8-strand 0.076- to 0.25-mm (3- to 10-mil) wire, or 0.025- to 0.127-mm (0.001- to 0.005-in.)-thick by 3.17-mm (0.125-in.)-wide Pyrofuze foil, would be buried just beneath the surface of the propellant slot. When current is passed through the wire, burning would be initiated throughout the charge circumference in the bottom of the slot so that hot combustion gases must pass over the walls of the propellant slot to reach the nozzle, thus promoting flame spreading and tending to raise the pressure locally near the line of ignition.

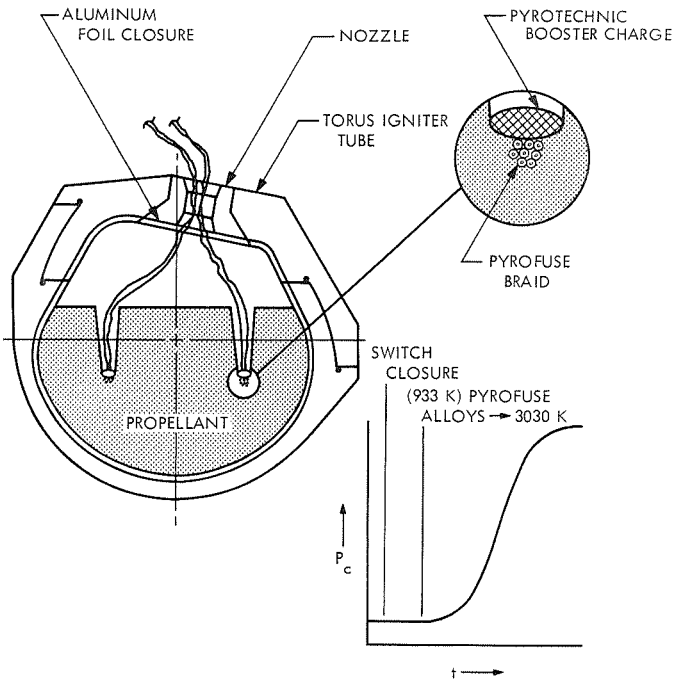

Figure 7. Initiation of g-dot igniter with Pyrofuze

Ten of the 12 nozzles in the torus will have thin aluminum foil as nozzle closures to raise the igniter L^* to 10.5 m (414 in.) for the two open nozzles and to increase the residence time of the hot gases in the igniter. To avoid abrupt drops in igniter pressure (high dp/dt) as the foil is ruptured, one nozzle will be closed with one layer of foil, three nozzles with two to three layers of foil, and six nozzles with three to five layers.

If the high igniter L^* and the nozzle closures fail to provide sustained burning from a hard vacuum start, the propellant will be (1) preheated locally by the Pyrofuze, below the propellant decomposition temperature of 450 to 477 K (350 to 400°F), by means of a low current for 5 to 30 s, then (2) ignited by triggering the Pyrofuze exotherm with a substantially higher current.

Finally, if all of the preceding approaches were to prove inadequate, a propellant that is more easily ignited than the polyether polyurethane JPL 540 Mod C will be substituted or, alternately, the use of a pyrotechnic booster charge or paste (Figure 7) will be used in the slot to provide more heat in a longer duration operation.

Processing and Igniter Testing

Although formation of the propellant charge in the torus case would appear to be difficult, practice tests have already revealed acceptable techniques. With a split mandrel of Teflon machined to form the finished propellant contour taking the place of the outer ring of the torus (Figure 7), propellant is vacuum-cast radially through the mandrel until a surplus fills the sprue. It is then cured for four days at 333 K (140°F), cooled, and the split mandrel removed. Before firing, the two sections of the torus are bonded together with an epoxy adhesive.

The future testing program should include: a proof–pressure test of the case, a qualification static firing of the igniter alone in the open, and one or more firings in an ignition test motor that duplicate the ignition phase of the D-2 motor. If practical, a simulated altitude firing of the ignition test motor should precede the firing of the demonstration motor D-2.

References

1. Strand, L. D., "Low-Acceleration Solid Propellant Rocket Ignition Study," in *Proceedings of the 26th JANNAF Meeting, Vol. I, July 14–16, 1970.* Chemical Propulsion Information Agency, Johns Hopkins University, Silver Spring, Md. (Confidential).
2. Laufman, P. N., and Dilts, H. S., *Exothermic Bimetallic Ignition System,* AIAA Paper 69-425. AIAA 5th Propulsion Joint Specialist Conference, U. S. Air Force Academy, Colo., June 9–13, 1969.

Cyanate Ion and the Uremic Syndrome

J. D. Ingham

Propulsion Division

A critical survey is made of the literature that logically provides an hypothesis that relates the symptoms of kidney failure (uremic syndrome) to the presence of cyanate ion derived from metabolic urea. If the hypothesis can be unequivocally verified, the consequences will provide a solution to the problem of defining the primary toxic factor in uremia and should lead to substantial improvements in the available treatment for patients with kidney failure.

Introduction

The potential significance of cyanate ion with respect to the uremic syndrome was noted during some recent work on alternative methods of purification of uremic blood for application to treatment of kidney failure.

Metabolites, or waste products, that are eliminated by normal kidney function include urea, uric acid, indican, phenols, guanidine bases, organic acids, magnesium, phosphate, potassium, sulfate, and excess water. Although urea is formed in the largest quantity and its concentration in uremic blood is monitored to determine the requirements and effectiveness of conventional hemodialysis, it is not considered particularly toxic to persons with normal renal function. It is generally conceded that the toxic metabolites responsible for the pathological symptoms of uremia have not yet been determined. Thus, this absence of fundamental knowledge of the chemical and physiological processes attending renal failure remains as the greatest limitation in providing adequate and more effective treatment for uremic patients (Reference 1).

Discussion

Paradoxically, there is ample evidence in the medical literature that cyanate ion formed from metabolic urea can cause symptoms characteristic of uremia. However, it has not been proven nor stated elsewhere that cyanate accumulation and consequent carbamylation of proteins or

other physiological cyanate reactions are primarily responsible for the deterioration of uremic patients. In fact, the vast majority of publications on uremia or artificial kidney research do not mention cyanate at all, and there have been no published clinical methods developed to readily measure cyanate at expected physiological concentrations.

In 1953, Merrill, et al. (Reference 2), presented results to prove that urea was not the cause of uremic symptoms. They observed that patients improved clinically following hemodialysis even if their blood urea level did not decrease. Urea is sometimes given to patients as a diuretic or to relieve intercranial or intraocular pressure. In one hospital over 1300 nonuremic patients have tolerated a daily dose of 0.001 to 0.002 kg of urea/kg body weight for short periods without any ill effects (Reference 3).

Furthermore, up to 0.008 kg of urea/kg body weight has been given daily to normal dogs intravenously for seven days without manifestation of toxicity (Reference 4). However, uremic dogs expired within a few days when a 0.5 to 3 wt % aqueous urea solution was added to their peritoneal dialysis solution, while similar dogs dialyzed without added urea survived an average of 39 days (Reference 5). Gilboe and Javid (Reference 6) treated three groups of uremic dogs with normal peritoneal dialysis solution (Group I) and with dialysis solution containing 1 wt % aqueous urea solution (Group II) or 0.015 wt % potassium cyanate (Group III). Group I survived 14 $\pm$ 0.17[1] days, whereas Groups II and III survived 7 $\pm$ 0.60 and 6 $\pm$ 0.53 days, respectively. The same uremic symptoms, i.e., weakness, refusal to eat, diarrhea, intestinal hemorrhaging, and decreasing body temperature, were observed for Groups II and III. Since the concentration of cyanate in the tissue fluid of the Group III dogs was estimated to be approximately the same as that expected to be produced from a 1% aqueous urea solution in 24 hours, it can be concluded that it is probably the cyanate formed from urea, and not urea, that is primarily responsible for uremic symptoms. Other work has shown that the pharmacological effects of large doses of cyanate on healthy rats and rabbits are caused by cyanate and not any substance into which it may conceivably be transformed in the body [urea, ammonia, cyanide, or thiocyanate (Reference 7)].

At 38°C, about seven days are required to establish the equilibrium concentration of cyanate from urea, which is about 0.5% of the initial urea concentration (U), up to (U) $\cong$ 1 molar (Reference 8).

Therefore, nonuremics would not be expected to develop uremic symptoms from relatively large doses of urea because the urea and any

[1]Standard error.

urea products would be removed by normal kidney function before toxic amounts of cyanate would form.

It has been definitively established that cyanate reacts rapidly with sulfhydryl and amino groups of proteins and inhibits ribonuclease enzymatic activity *in vitro* (References 9 and 10). In fact, cyanate carbamylation and decarbamylation of functional groups have been used as a protecting reaction in the synthesis and study of biological compounds. Thus, it appears that the physiological activity of cyanate ion probably results from carbamylation of free sulfhydryl and amino groups in proteins or amino acids.

Summary and Conclusions

(1) In aqueous solutions of urea small equilibrium concentrations of cyanate are formed:

$$NH_2-\overset{\overset{O}{\|}}{C}-NH_2 \leftrightarrows NH_4^+ + CNO^- \qquad (I)$$

(2) In uremic patients cyanate ion is probably formed by Reaction I over a period of days, from the initial metabolic urea.

(3) Urea is not toxic to normal subjects, but 1% urea or 0.15% potassium cyanate added to the peritoneal dialysate of uremic dogs greatly accelerates the onset of uremic symptoms and death.

(4) It appears likely that uremic symptoms result from reaction of cyanate ion with sulfhydryl and amino groups in body proteins and amino acids:

$$RS^- + HNCO + HOH \leftrightarrows RS-\overset{\overset{O}{\|}}{C}-NH_2 + OH^- \qquad (II)$$

No further work has been done to clarify or define the role of cyanate ion in uremia.

One suggested reason for the apparent neglect in this area is the unavailability of a direct method for cyanate analysis at expected physiological concentrations. Therefore, Dr. J. D. Arterberry[2] is actively engaged in research on a new method of analysis for cyanate in blood and urine. Preliminary results with this method indicate the presence of expected concentrations of cyanate in normal urine samples. When the reliability of the method has been unequivocally established, uremic and normal blood will be analyzed for cyanate. Further, since Reaction

[2]USC School of Medicine and Chief of Staff, Central Receiving Hospital; also collaborator and consultant to JPL on the Laboratory's Purification of Uremic Blood task.

II is readily reversed at alkaline pH, the blood proteins of uremics can be decarbamylated to form cyanate to determine the extent of reaction of physiological cyanate compared with normal blood. If it is found that uremic proteins are partially carbamylated, the implications of Statement 4, above, will have been substantively verified. Experiments will then be carried out to determine methods of inhibition of carbamylation in uremic patients. If the role of cyanate ion in uremia is as significant as suggested here, the expected consequences of a continuation of this effort may be: (1) an elucidation of the primary causes of the uremic syndrome, and (2) much more efficient and acceptable methods of treatment of uremic patients.

Although any modifications of clinical treatment would be extremely presumptive until the proposed investigations are completed, the modifications might eventually involve occasional hemodialysis to remove excessive urea and other metabolites, and frequent oral or intravenous administration of relatively small amounts of nontoxic sulfhydryl compounds or other drugs. The latter would be developed to remove cyanate as it is formed, or to promote decarbamylation by shifting the equilibrium in Reaction II to the left.

References

1. Proceedings of the Second Annual Contractor's Conference of the Artificial Kidney Program, National Institute of Arthritis and Metabolic Diseases, Bethesda, Md., Jan. 22–24, 1969.
2. Merrill, J. P., Legrain, M., and Hoigne, R., *Am. J. Med.*, Vol. 14, p. 519, 1953.
3. Javid, M. J., *Surg. Clin. N. Am.*, Vol. 38, p. 907, 1958.
4. Garvin, P. S., Jennings, R. B., and Gesler, R. M., *Pharmocologist*, Vol. 1, p. 71, 1959.
5. Grollman, E. F., and Grollman, A., *J. Clin. Invest.*, Vol. 38, p. 749, 1959.
6. Gilboe, D. D., and Javid, M. J., *Proc. Soc. Exp. Biol. Med.*, Vol. 115, p. 633, 1964.
7. Birch, K. M., and Schutz, F., *Brit. J. Pharmaco.*, Vol. 1, p. 186, 1946.
8. Dirnhuber, P., and Schutz, F., *Biochem. J.*, Vol. 42, p. 628, 1948.
9. Stark, G. R., *J. Biol. Chem.*, Vol. 239, p. 1411, 1964.
10. Stark, G. R., Stein, W. H., and Moore, S., *J. Biol. Chem.*, Vol. 235, p. 3177, 1960.

Oil-Absorbing Polymers

H. E. Marsh, Jr.

Propulsion Division

A new research program has been started to develop technology needed to make practical use of a well-known characteristic of elastomeric cross-linked polymers. Such polymers, of which class modern solid-propellant binders are members, absorb large amounts of compatible solvents, and yet remain solid. Two goals are being considered in this program. One goal is a material that can be used as a dietary additive which will selectively absorb fats and oils in the digestive tract and hold them until elimination, thus preventing their assimilation. The other goal is a material that can be used in oil-slick mop-up operations. This article presents the interim results on the formulation and testing of three polymer types. Performances amounting to oleic acid absorption of up to 20 times the dry polymer weight have been measured. Higher values are expected. Both mineral oil and a cooking oil are also absorbed, but to a smaller extent.

Introduction

The chief distinguishing structural feature of the class of polymers known as thermosetting is that the component polymeric molecules are tied together in a three-dimensional network. The average length of polymer chain between cross-linking (interconnecting) sites, together with the flexibility/stiffness character of the chain material, determines the mechanical properties of the polymer. Regardless of chain flexibility, highly cross-linked polymers are rigid. On the other hand, polymers with long chains between cross-links are rubbery, providing those chains are flexible. Another characteristic of the latter type of polymer that has been known and studied for a long time is its ability to absorb extremely large quantities of compatible solvent and yet remain solid.

A new research program has been undertaken to take practical advantage of the high absorption capacity of suitably prepared network polymers. Two goals are being considered. One goal is the development of polymers with a high affinity for the fats and oils common in foods that, being otherwise harmless, could be used as a dietary additive for the control of fat assimilation. Being inert, the polymer would pass through

the digestive tract absorbing and retaining fats and oils, including cholesterol, for elimination. The other goal is the development of similar materials that will be useful in oil-slick mop-up procedures.

Approach

The technology adopted to make high capacity absorbing cross-linked polymers is based on knowledge gained in work with solid-propellant binders (References 1 and 2). The aim is to make polymers that are cross-linked, so that they will remain solid even though swelled by large quantities of absorbed oil, but at the same time provide an average chain length between the cross-link sites as large as possible to obtain maximum capacity.

Preparation

There are two steps in the process: synthesis and extraction. The synthesis step consists of mixing together appropriate quantities of several polyfunctional ingredients, along with a polymerization catalyst, and causing them to polymerize by means of heat. Network polymer theory is used to calculate the ratios of ingredients that should yield polymers with the desired characteristics. The ideal composition is near the incipient gelation boundary (Reference 1). However, in practice, this calculation serves only as a starting point for an empirical search. The necessity for empirical experimentation is caused by the fact that polymer formulations with the best absorption capacities are so lightly cross-linked that they are almost liquids instead of solids. Factors not accounted for in the theoretical calculation, such as incomplete reaction, non-ideal functionality distribution of the components, and side reactions, all interact with the sensitivity of such formulations to cause an unpredictable shift of the real solid/liquid boundary from the theoretical one. Thus, in the empirical search for a good formulation, a series of samples are made at the same time with composition ratios varying over a range estimated to bound the problem. A satisfactory series will yield some liquid and some gelled polymers. Often, one or more additional sets must be run, either to find the correct range or to refine the desired point.

Gross distinction between liquid samples and solid ones is made by visual observation of the flow properties of the polymer. However, some samples that appear to be solid turn out later to be only high molecular-weight liquids. This is evidenced by total extraction in the next process step.

Another characteristic of the desired lightly cross-linked polymer (in practice, but not necessarily in theory) is that it consists of two separatable fractions. The desired fraction is the lightly cross-linked gel, or solid. In homogeneous solution with the gel is the sol, or liquid fraction.

The latter is a polymerized material that did not reach the size and complexity necessary for it to become part of the gel. Repetitive solvent extraction of a fresh polymer removes the sol fraction, leaving a residue of "dry" gel. Soxhlet extraction is used in the present work to carry out this operation automatically.

Screening and Evaluation

The criterion for a good polymer is its capacity to absorb a large amount of oil (of a type critical to the objectives of the program). Although the main stress in the program is in the absorption of biologically important oils and fats, a laboratory grade of mineral oil is used as one of the test materials, as a model for the oil-slick problem. In private communication, Dr. David Blankenhorn of the USC School of Medicine recommended the following compounds for testing the feasibility of the fat assimilation control concept:

(1) *Carboxylic acids:* palmitic acid, oleic acid, myristic acid, butyric acid, and a C-22 acid.

(2) *Alcohols:* cholesterol.

(3) *Esters:* triglycerides of palmitic and oleic acids, and the palmitate of cholesterol.

Since it would be very inefficient and expensive to test each new polymer with all of these materials, the oleic acid was the only one selected for the screening tests because it is the least expensive and is a liquid at room temperature. The other compounds will be used in the evaluation of polymers selected in the screening tests.

Because of experimental difficulties, the accuracy of the measurement of the absorption capacity is limited. The current procedure starts with the immersion of a weighed quantity of polymer in a volume of the test liquid. It is examined daily, and when the polymer appears to have stopped swelling, it is removed and drained (most of the surface liquid is removed by blotting with tissue). The last operation is where the uncertainty lies, because of the lack of uniformity of surface configuration from sample to sample, and also because the structural weakness of some swollen gel samples gives difficulty in carrying out the operation. Lack of accuracy in these measurements is not critical in the screening tests, however. As will appear in the results below, the differences in capacity are large in comparison to such errors in measurement.

Polymer Types Investigated

For all of the past work, and for as long as it continues to be practical, the urethane reaction is the adopted means of curing. Since this is the chief cure system used in the fabrication of JPL propellants, a wide variety of potentially useful materials are readily available.

An anticipated major factor in the absorption capacity of network polymers is the chemical nature of the chain-forming ingredient. In advance of experimentation, hydrocarbon chains were expected to have a greater affinity for the oils in question because of the long-chain hydrocarbon characteristic common to them. Several hydrocarbon prepolymers are being tested: some unsaturated (polybutadiene), and some saturated (similar to ethylene–propylene copolymers). A common polyether (polypropylene oxide) is also being tested, primarily because it is not hydrocarbon. Polyesters are under consideration; however, their stability in the digestive system may be in question.

Interim Results

Formulation Studies/Screening Tests

Three polymer systems have been investigated: unsaturated hydrocarbon, mixed saturated/unsaturated hydrocarbon, and polyether. Reasonably good absorption of oleic acid has been obtained with each system. The highest absorption capacities measured so far for the above three systems were, respectively, 1390, 1210, and 2050% oleic acid absorbed, based on the dry weight of the polymer.

In many cases, the formulation series sets did not correlate closely with theory. This was expected because no effort was made to control reaction conditions carefully for this purpose. The desired practical results were achieved, however. An example of a formulation series in search of a good absorber is given in Table 1. This set of samples was a series of unsaturated hydrocarbon formulations in which all factors except the hydroxyl-to-isocyanate ratio R were held constant. According to theory, the gel point R for this set should be 1.25. Two samples were unable to produce a gel because R was too high. The variation in sol/gel ratio and absorption capacity of the two solid products are in the expected directions. If this particular system were to be selected for further work, another series would be run in which a number of R values between 1.32 and 1.52 would be tried. A formulation having maximum absorption capacity should be found in that range.

Table 1. Effect of formulation parameters on absorption capacity

Sample number	Hydroxyl-to-isocyanate ratio	Product	Sol/gel ratio	Oleic acid absorbed, %
101	1.16	Solid	0.35	830
102	1.32	Solid	0.69	1380
103	1.52	Liquid	—	—
104	1.79	Liquid	—	—

Testing Oils and Solvent Polymerization

In most of the past work, only oleic acid was used in absorption screening tests. To broaden the screening tests, it was decided to try, as an inexpensive model for the ester-type oils, a commercial cooking oil. Cooking oils are refined natural mixtures of triglycerides from vegetable sources. Wesson oil was chosen. It was also decided to include mineral oil as a model for strictly hydrocarbon materials. It is important to mention in this regard that mineral oil was used in the first exploratory tests. An absorption capacity of over 800% was attained then, using an unsaturated hydrocarbon polymer.

First tests with the Wesson and mineral oils were made with polyether polymers. The results indicated that the polymers' capacities for these two oils were between about one-fiftieth and one-fifteenth of their previously measured capacities of oleic acid. These results are preliminary; however, if they are representative, they show that the unreacted carboxyl on the oleic acid molecule contributes largely to its solubility in polyether polymers.

The test was repeated with two unsaturated hydrocarbon polymer samples that had been in storage for many weeks. Theoretically, these oils and hydrocarbon polymer should be compatible. The results were about the same as with the polyether polymers; however, the capacity was much lower than the 800% found previously with a hydrocarbon polymer.

Two possible explanations are proposed for this undesirable result. The first is that the unsaturated hydrocarbon polymers stored for some time in air may have undergone oxidative cross-linking, similar to the process which hardens paints and varnishes.

The second explanation is that the recently tested polymers were made in bulk, whereas the earlier, more successful polymer had been made in 50% xylene. Network polymers made in solution would be more extended (would have fewer chain entanglements) and as a result might be more extensible even after drying. Two fresh sets of hydrocarbon polymers were made in solution; one polymer was unsaturated and the other was mixed saturated/unsaturated. Absorption tests have not run their full time yet, but absorption capacity for mineral oil has improved by a factor of about 2½, and even higher for Wesson oil.

Polymer Reinforcement

The mechanical weakness of some swollen gels has caused difficulty in handling during testing. Mainly for the purpose of expediting screening tests, the formation of polymers on reinforcing substrates was investigated. A secondary aim was to demonstrate that greater strength

could be provided, when needed in application. A good substrate must reinforce the polymer during absorption without restricting the absorption capacity appreciably.

The substrate materials tried were cotton fibers, pulled from cosmetic cotton batting, nylon tow, and fine-mesh nylon screen. The very high surface area of these materials proved troublesome in two respects. Formulations with as high as 3 to 5% of loose fibers appeared to be too highly loaded for useful processing. Interference with curing, probably caused by undesirable chemical activity at the surface, was also encountered. Substrate loadings in the range of 0.5% were found to be more suitable with respect to both problems.

Substrate testing is not completed. However, for testing purposes, the nylon screen with a thin film of polymer appears to be a practical arrangement. One such sample exhibited an absorption capacity of 1460%. To curtail the impairment of curing, it is planned to pretreat the screen with tolylene diisocyanate, the curing agent.

Time-Consuming Operations

Another factor, besides the lack of reproducibility in removal of surface oil in absorption tests, which has contributed to uncertainty in the data, is the length of time required for complete absorption. Although the required time has not been determined, it appears to be of the order of two weeks. The extraction operation also is slow; it takes five days.

Recent tests have shown that moderate temperature elevation increases the rate of absorption considerably. Heretofore, testing has been done at room temperature, which has been ranging from 17°C (62°F)[1] to 24°C (75°F). A study is currently being carried out at two temperatures: 38°C (100°F) and 49°C (120°F). Preliminary data indicate that absorption values obtained previously in one to two weeks at room temperature were achieved in two days at 49°C (120°F).

The preparation of thin polymer samples on nylon screen substrates is expected to increase the rates of both extraction and absorption because the reduction in, and better control of, diffusion distance.

The elevation of temperature will also be investigated in the extraction operation. This will be accomplished by the substitution of the higher boiling solvent xylene for benzene.

[1]Where applicable, the International System of Units is stated first, followed by the customary units in parentheses. In each case, the value in parentheses represents the measured unit.

Questions of Polymer Stability

Occasionally, samples which have undergone extraction, yielding a solid product, seemed to have disappeared in the absorption test. This should not occur because a solid residue from extraction is positive evidence of a cross-linked polymer. The most likely explanation is a chemical displacement of previously reacted hydroxyl in the polymer by the carboxyl group on the oleic acid. Such a reaction would simultaneously result in the introduction of an extra monofunctional component and a shift in the stoichiometric ratio, both of which would reduce the extent of cross-linking.

An experiment was started to investigate the possibility of polymer size degradation by reaction of oleic acid into the polymer. The experiment was based on the often used principle of determining the molecular weight (or size) of dissolved polymers by viscosity measurement. One of the previously made polymer samples that had remained a liquid after cure was dissolved in a plasticizer, and oleic acid was added so that the final solution had 21% polymer and 12.5% oleic acid. The solution was stored at room temperature, and the viscosity was measured once or twice a week, along with the temperature, in order to normalize viscosity and eliminate temperature as a parameter. After a period of a month, no change in the viscosity of the solution was detected. If a significant amount of the suspected reaction had occurred, the viscosity of the solution would have dropped because of the resulting decrease in molecular weight.

As far as this experiment has gone, there is no evidence that oleic acid degrades the polymer. The question of disappearing gels is still open. However, there is an indication that one factor in the intended environment will not cause degradation of urethane-cured polymers.

Conclusions

Preliminary results indicate that:

(1) All three polymer types tested (unsaturated hydrocarbon, mixed saturated/unsaturated hydrocarbon, and polyether) have good absorption capacity for oleic acid. The highest capacities measured range from 12 to 20 times the dry weight of the absorbing polymer. None of these polymers have been optimized.

(2) The absorption capacities for both mineral oil and Wesson oil by these polymers appear to be considerably less than for oleic acid.

(3) Solution polymerization produces polymers that either have higher capacities or more rapid absorption rates than bulk polymerization does.

(4) Carboxylic acids, as represented by oleic acid, do not appear to degrade the urethane-cured polymers investigated.

Future Work

Future and continuing tasks in this program are listed as follows:

(1) Formulating and processing studies of the three polymer types will be continued to produce optimum products. Technical improvements, including substrate reinforcement and solvent polymerization, will be used. Reproducibility of preferred formulations will be investigated.

(2) The absorption capacities of the selected formulations of each polymer type for oleic acid, Wesson oil, and mineral oil will be measured.

(3) Absorption of the other selected biologically important fats and oils will be studied.

(4) The general technology of producing oil-absorbing polymers will be investigated. Modifications of the types of polymers under study, as well as new types, will be tried.

(5) In consultation with medical experts, plans for future investigation will be made. Subjects to be studied must include the measurement of the stability of high absorbing polymers in simulated environments, whether or not toxic effects can be discovered, and the efficiency of absorption in the simulated environment.

References

1. Marsh, H. E., and Hutchison, J. J., "Prepolymer Functionality Determination Using a Model Polymerization System," in *Supporting Research and Advanced Development*, Space Programs Summary 37-48, Vol. III, pp. 95–99. Jet Propulsion Laboratory, Pasadena, Calif., Dec. 31, 1967.

2. Marsh, H. E., Jr., and Udlock, D., "Low-Modulus Propellant for Case-Bonded, End-Burning Motors," in *Supporting Research and Advanced Development*, Space Programs Summary 37-63, Vol. III, pp. 184–188. Jet Propulsion Laboratory, Pasadena, Calif., June 30, 1970.

Fatigue of Teflon Bladder Bag Materials

E. F. Cuddihy

Propulsion Division

A correlation between fatigue and stress–strain behavior of Teflon materials was observed during a study of the fatigue properties of liquid propellant expulsion Teflon bladder bag materials. This correlation requires only the knowledge of the ultimate breaking stress of the materials in order to obtain an estimate of the fatigue properties, and permits a rapid assessment of the expected fatigue behavior of candidate materials for bladder bags from only a comparison of their ultimate breaking stress. The general principles of this method of fatigue analysis is discussed, along with the recognition that this technique should have general application for other polymeric materials where stress–strain behavior is comparable to Teflon.

Introduction

Bladder bags prepared from a standard Teflon film laminate and employed as liquid propellant expulsion devices were failing from the formation of tears and cracks near an aluminum seal ring which forms the mouth of the bag. The failures were occurring when the bags were filled with Freon-TF and isopropyl alcohol, employed as substitute fuels, and then vibrated during a simulated launch test. From a consideration of the conditions imposed on the bags during test, four factors believed most critical in contributing to the failures were identified for study: (1) flex fatigue, (2) biaxial stresses, (3) solvent sensitivity, and (4) crystallinity. The results of that study demonstrated that the primary cause for failure of standard laminate was its sensitivity to solvent stress-cracking (References 1 and 2), and that the bladder bags failed for that reason. A new material designated co-dispersion laminate was found to be insensitive to solvent stress-cracking and has replaced the standard laminate material used in construction of JPL Teflon bladder bags.

This article describes the flex fatigue properties of both standard and co-dispersion laminate materials. The study of these properties resulted in a method of fatigue analysis which should have general application. The concepts of the method and the fatigue properties of standard and co-dispersion laminate materials in particular are presented.

Bladder Construction

The construction of the bladder bags is detailed in Figure 1. Standard laminate is constructed in two plies, one of FEP 120 and the other of TFE 30. Co-dispersion laminate is constructed in three plies; an inner ply consists of FEP 9511 while the two outer plies are formed from a co-dispersion of 80% TFE and 20% FEP 9511.

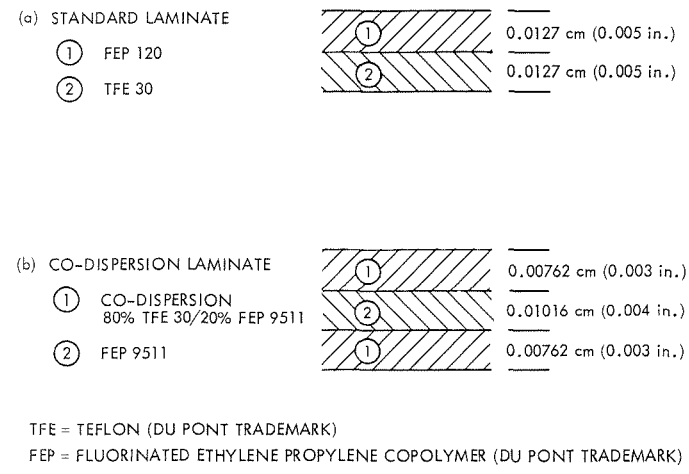

Figure 1. Bladder construction details

Fatigue Properties

Experiment

The fatigue properties of the Teflon materials were measured by cyclically stretching specimens on an Instron test machine to constant load and then correlating the number of cycles to failure with stress. For this study, dumbbell specimens of 0.0254-cm (0.010-in.)[1] thickness, 0.635-cm (0.250-in.) width, and 3.175-cm (1.25-in.) gage length were tested on the Instron operating at a crosshead speed of 0.423 cm/s (10 in./min).

Fatigue Results

The fatigue data for both standard and co-dispersion laminate materials are plotted in Figure 2 as the log of cycles to failure versus the maximum stress applied during the fatigue test. The data curve for the co-dispersion laminate is linear while curvature and a plateau are observed in the data curve for the standard laminate. This departure from linearity is believed to be caused by the tendency of standard laminate

[1]Where applicable, the International System of Units is stated first, followed by the customary units in parentheses. In each case, the value in parentheses represents the measured or calculated unit.

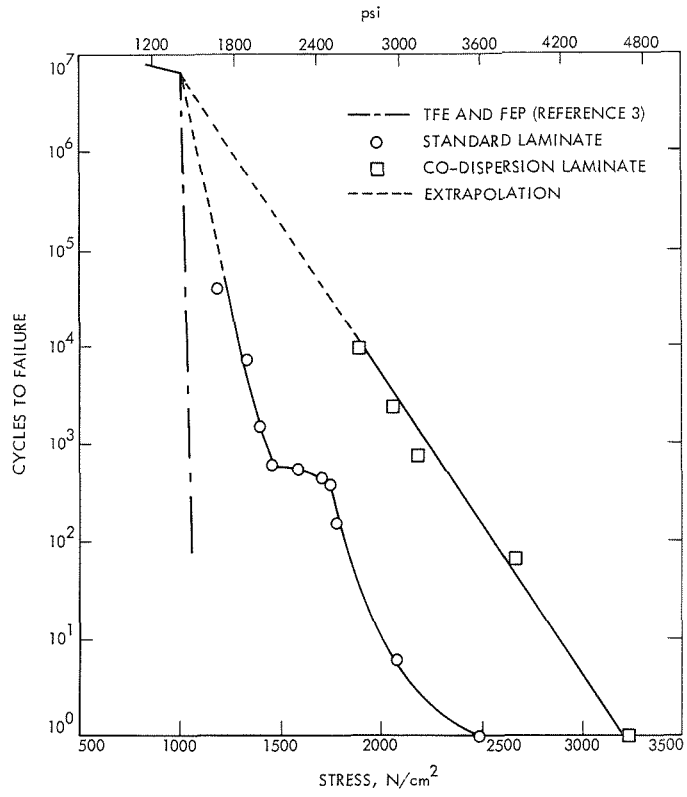

Figure 2. Fatigue properties of Teflon bladder bag materials

to delaminate during the fatigue testing. This point will be discussed later.

Both curves tend to converge to a common point near 10^7 cycles and to intercept the axis for one cycle at a stress which corresponds to their ultimate breaking stress (Figure 3). The convergence point at about 965-N/cm^2 (1400-psi) stress corresponds to the location on their stress–strain curves (Figure 3) where departure is observed from the initial linear relationship between stress and strain. This common convergence point has also been observed for fold fatigue studies (Reference 3) on FEP and TFE and has been defined as a fatigue endurance limit (this data is reproduced in both Figures 2 and 4).

These results demonstrate the existence of a correlation between fatigue properties and stress–strain behavior. For stresses within the linear portion of the stress–strain curve, fatigue failure occurs at about 10^7 cycles. But for stress exceeding those for linear behavior, i.e., in excess of the fatigue endurance limit, the number of cycles to failure decreases with increasing stress and the curves terminate at one cycle with a stress corresponding to the ultimate breaking stress. Thus, knowing the ultimate breaking stress, the fatigue properties can be predicted.

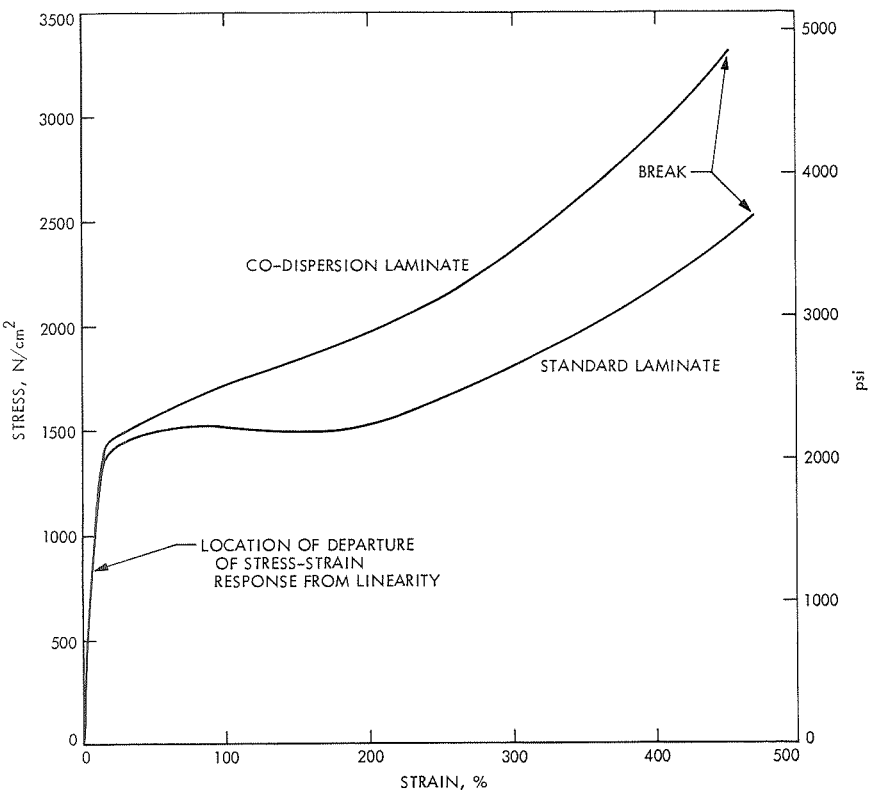

Figure 3. Stress–strain curves

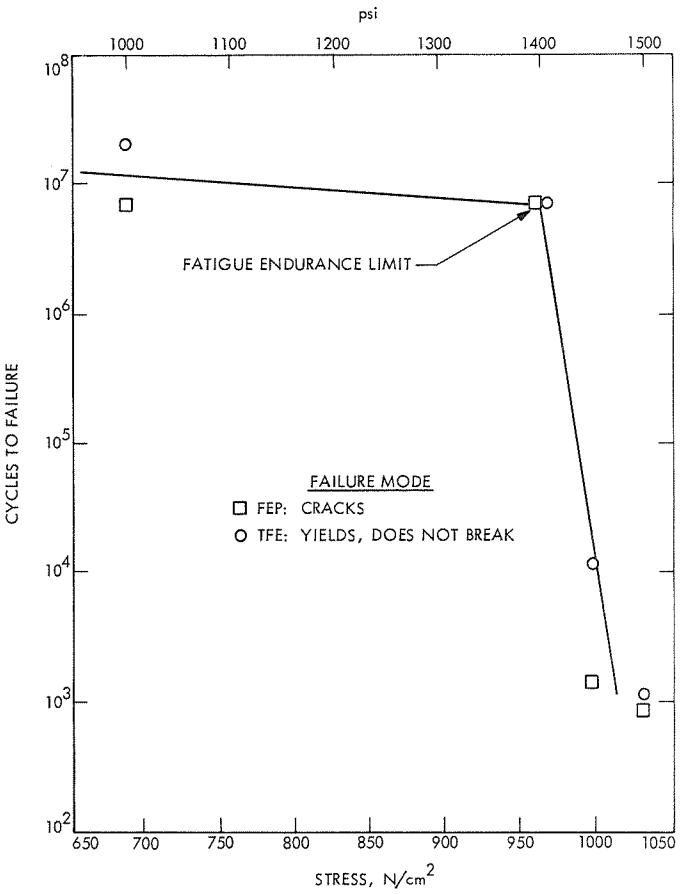

Figure 4. Fold fatigue of TFE and FEP (reproduced from data in Reference 3)

Delamination of Standard Laminate

All specimens of standard material delaminated during the fatigue testing, with the extent of delamination apparently reflected in the behavior of the data curve. For the cycle region above the plateau, substantial delamination was observed while negligible delamination was observed in the cycle region below the plateau. The plateau presumably occurs as the result of a transition from extensive delamination at high cycles to negligible and no delamination at low cycles. Delamination

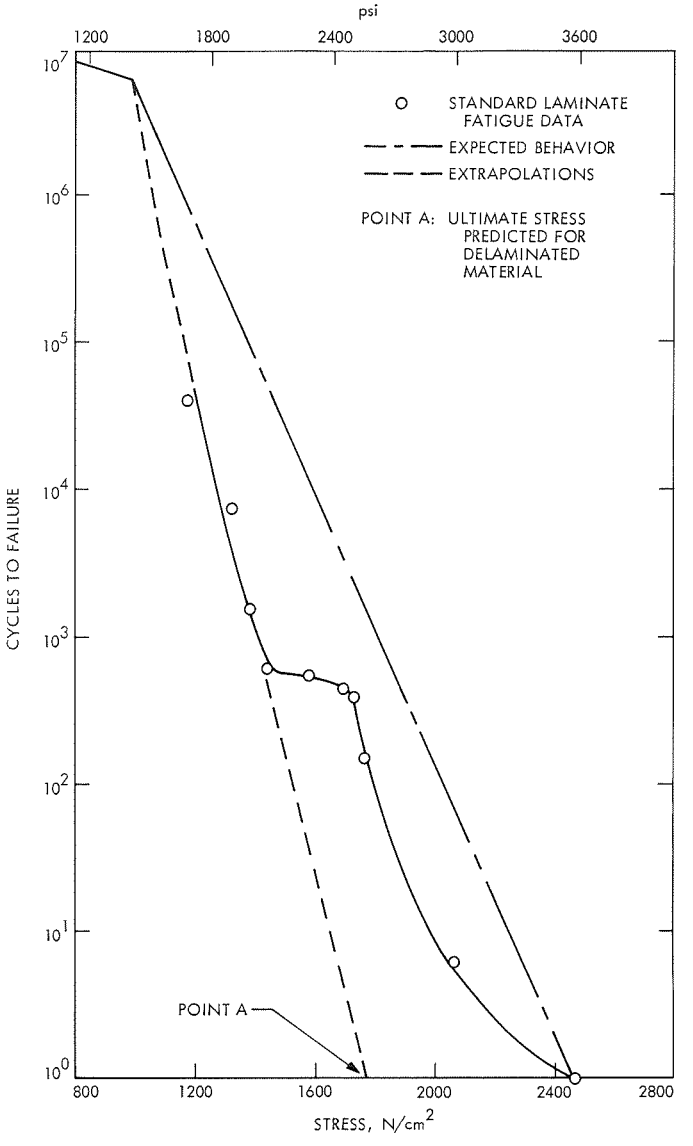

Figure 5. Comparison of actual standard laminate fatigue data with expected behavior

not only accounts for the departure of the standard laminate fatigue curve from linearity but also results in a substantial reduction in resistance to fatigue failure. This can be seen in Figure 5, where the fatigue curve is reproduced for this material along with the linear relationship expected for the absence of delamination.

One additional observation can also be made from Figure 5. The points above the plateau extrapolate to the 1-cycle line at an ultimate breaking stress of 1792 N/cm^2 (2600 psi). This value would presumably be obtained for a standard material delaminating during a uniaxial stress–strain measurement. This same value of ultimate stress was measured for standard materials which were tested while completely immersed in Freon-TF and heptane solvents (Reference 1), while exposure to isopropyl alcohol had an intermediate value near 2137 N/cm^2 (3100 psi). This suggests that part of the mechanism contributing to the solvent sensitivity of standard laminate may be a tendency to be delaminated by solvents.

Conclusion

The linear relationship between fatigue cycles and stress provides a simple method of fatigue analysis for Teflon materials. Given the ultimate breaking stress and the fatigue endurance limit, the fatigue properties can be predicted. Further, since the fatigue endurance limit is apparently common, a rapid assessment of the fatigue behavior of various Teflon materials can be made from only a comparison of the ultimate breaking stresses. Similarly the effect of environmental or other factors on fatigue properties can be inferred from their effect on the ultimate properties.

These considerations should also be applicable to materials having similar stress–strain characteristics as Teflon. These would include other crystalline polymers, such as polyethylene, and many block and graft copolymers including segmented urethanes.

References

1. "Study of the Effects of Solvent on *Mariner* Mars 1971 Liquid Propellant Expulsion Teflon Bladder Bags," in *Flight Projects*, Space Programs Summary 37-65, Vol. I, pp. 40–42. Jet Propulsion Laboratory, Pasadena, Calif., Sept. 30, 1970.
2. "Effect of Solvent on the Biaxial Properties of Liquid Propellant Expulsion Teflon Bladder Bags," in *Flight Projects*, Space Programs Summary 37-66, Vol. I, pp. 14–21. Jet Propulsion Laboratory, Pasadena, Calif., Nov. 30, 1970.
3. *Design and Engineering Data on Teflon Fluorocarbon Resins*, E. I. DuPont de Nemours and Co., Wilmington, Del. (undated).

Liquid-Metal MHD Power Conversion

D. J. Cerini

Propulsion Division

A liquid-metal magnetohydrodynamic (MHD) power converter has been successfully operated with the generation of ac electrical power. Gaseous nitrogen is used to produce the closed-cycle flow of the liquid-metal (NaK) working fluid through the MHD generator where the fluid kinetic energy is converted to electrical energy. In this article the operational characteristics of the converter are given and the results of the current series of tests are discussed.

Introduction

Liquid-metal magnetohydrodynamic (MHD) power conversion (Reference 1) is being investigated as a power source for nuclear-electric propulsion. A liquid-metal MHD system has no moving mechanical parts and operates at heat-source-temperatures between 1200 and 1400 K. Thus, the system has the potential of high reliability and long lifetime with the use of readily available containment materials such as Nb–1%Zr.

NaK–Nitrogen Converter

The NaK–nitrogen test system to evaluate the electrical and hydraulic characteristics of a liquid-metal MHD converter has been successfully operated with the generation of ac electrical power. An output of 1.0 kW at 120 V and 350 Hz has been obtained in early tests with low generator currents.

The converter is shown in Figure 1. Runs are started by feeding nitrogen at 2.5 kg/s to the 1600-orifice NaK–nitrogen mixer. NaK is then injected from a nitrogen-pressurized start-tank at 75 N/cm^2 and 40 kg/s. NaK is also supplied to the mixer through a pressure regulator at 5 kg/s from a 650-kg NaK supply under 150-N/cm^2 nitrogen pressure. The added NaK increases the circulating liquid flow rate and causes the nozzle inlet pressure to increase. When the pressure reaches the value for which the regulator is set, the regulator throttles the flow back to an

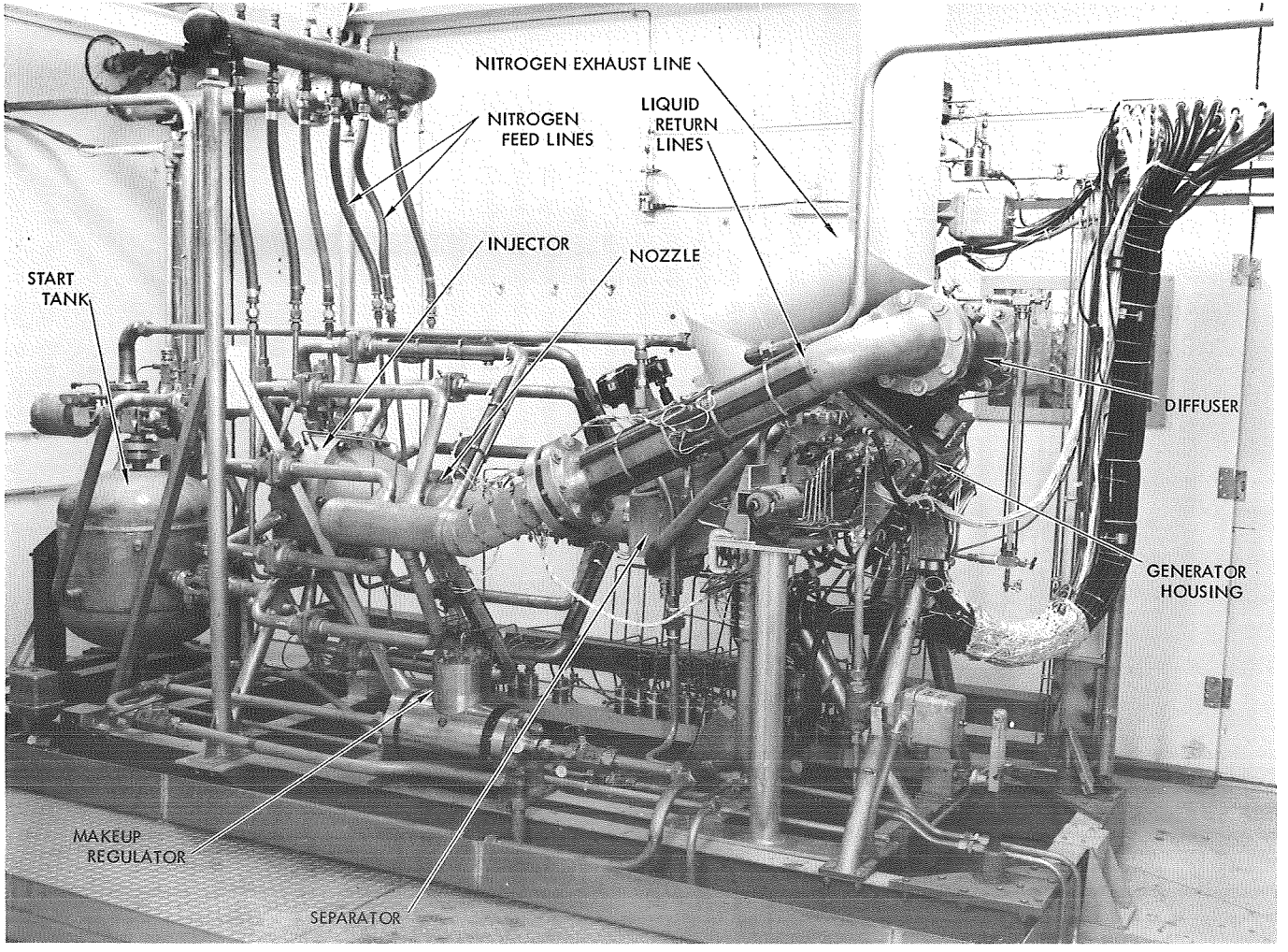

Figure 1. NaK–N_2 liquid-metal MHD system

amount equal to that lost with the nitrogen and collected in a mist separator. The main problem encountered in startup has been establishing reasonably uniform pressure of the Mach 2 to 4 NaK–nitrogen flow in the generator channel. If the nitrogen flow to the nozzle is too high, a shock forms in the generator channel upstream of the diffuser, and pressures can reach 140 N/cm^2 in the downstream part of the generator. If the nitrogen flow is too low, a shock forms at the capture slot leading to the generator, reducing the fluid power available and increasing the NaK flow to the mist separator.

After startup, which requires about 20 s, adjustments can be made in the nozzle inlet pressure and in the nitrogen flow rate to reach various flow conditions for generator operation. A nozzle inlet pressure of 103 N/cm^2 and nitrogen flow rates between 1.8 and 2.5 kg/s are currently being used. The NaK flow rates range from 47 to 62 kg/s.

The ac induction generator is then started by bringing up the alternator field. The six traveling-wave phases and the downstream compensating-pole phase are connected to capacitors and resistors of the desired values. The upstream compensating-pole phase is connected across the alternator since this phase requires power input; capacitance is still provided for the reactive power requirement. (The alternator can be replaced by transformer coupling to the other phases, but the present arrangement provides more positive control of generator current.) The currents in the seven self-excited phases rise in proportion to the current in the alternator-driven phase. When the approximate desired current levels are reached, the final trimming of current amplitudes and phase angles is done by adjusting variable transformers connecting the capacitors and resistors to the generator. After the generator currents are satisfactorily adjusted, the phase power outputs (or input, in the case of the upstream, alternator-driven phase) are recorded, together with currents, voltages, phase angles, and flow parameters.

The adjustment process has been found to be difficult and time-consuming. Changing the capacitance or resistance on one phase not only changes the amplitude and phase angle of the current in that phase, but also affects the currents in all of the other phases. A procedure is currently being developed to calculate the required capacitance and resistance changes in each of the eight phases to correct the current amplitudes and phase angles.

Current Test Series

The current test series has consisted of 14 NaK runs of 5- to 10-min duration with generator operation. The generator has operated qualitatively as expected, with power output from seven phases and input to one, but the internal power output from the NaK to the coils has been only about 65% of that predicted. When the winding loss is subtracted,

the net output is only a fraction of the predicted value. The net output was 300 W at 15-A current in the traveling-wave phases. The predicted power output was 1150 W. The most likely explanation is low fluid conductivity as a result of the flow expansion in the generator channel. The predicted power was based on the assumption that the flow in the generator channel would be at the same pressure (25–70 N/cm^2) and same gas–liquid volume ratio (0.3–0.6) as the flow leaving the upstream diffuser. In the NaK runs the generator channel pressure was only 10 N/cm^2 and if, in addition, the flow expanded to uniformly fill the channel, then the volume ratio was in the range 1.5–2.0, which would reduce the conductivity sufficiently to account for the low output power.

Empty channel tests conducted prior to the current test series indicated that the unexpectedly high stator losses in the generator are due to eddy currents in the coils caused by the field perpendicular to the flat strip coil turns.

During the NaK tests an insulation failure occurred in one of the coils as the generator voltage was being raised above the 90-V level. The failure had the effect of shorting nine turns on the upstream C-phase coil which increased the coil losses by 400 W and canceled the net output power.

The shorted turns have been removed from the coil. In order to maintain constant ampere-turns in both C-phase coils, the 31-turn coil is excited by the 40-turn coil through a current transformer.

Testing has resumed, and an output of 1.0 kW has been obtained.

Reference

1. Elliott, D. G., Hays, L. G., and Cerini, D. J., "Liquid-Metal MHD Power Conversion," in *Supporting Research and Advanced Development*, Space Programs Summary 37-51, Vol. III, pp. 120–124. Jet Propulsion Laboratory, Pasadena, Calif., June 30, 1968.

Design and Development of a 66-W/kg, 23-m² Roll-Up Solar Array

W. A. Hasbach

Guidance and Control Division

Future space missions will require greater power output, lighter weight, and decreased stowed volume for solar arrays. To meet these requirements, a program was initiated to develop the technology for a roll-up solar array by preparing a detailed design, performing the associated analyses, fabricating an engineering development model, and subjecting the engineering model to a comprehensive test program consisting of both environmental and developmental tests. The design and testing of the 66-W/kg (30-W/lb),[1] 23-m² (250 ft²) roll-up solar array developed during this program is described in this article.

Introduction

Future space missions will require greater power output, lighter weight, and decreased stowed volume for solar arrays. To meet these requirements, a program was initiated to develop the technology for a roll-up solar array by preparing a detailed design, performing the associated analyses, fabricating an engineering development model, and subjecting the engineering model to a comprehensive test program consisting of both environmental and developmental tests. The design chosen is adaptable to a variety of vehicle configurations and missions, including solar electric propulsion for unmanned planetary exploration and the manned space station for Earth orbiters.

Description

The design of the array was based upon the results of an earlier feasibility study by the General Electric Company (Reference 1). With this

[1]Where applicable, the International System of Units is stated first, followed by the customary units in parentheses. In each case, the value in parentheses represents the measured or calculated unit.

design, a 23-m^2 solar cell module area would be stored on drums until deployment of the array after launch. The array, in its fully deployed configuration, is illustrated in Figure 1. The dimensions of each panel are 1.17 m (46 in.) × 10.21 m (402 in.).

The engineering test model is representative of a flight-type design, except for a limited solar cell coverage; 4000 solar cells were bonded to the substrates, with the remaining area occupied by glass platelets to simulate the solar cell mass and interconnect bending stiffness. The locations of the various components on the engineering test model are shown in Figure 2. The weight breakdown for the model is as follows:

Component	Weight, kg
Array substrate assemblies	10.532 10.596
Solar panel actuator	5.321
Storage drum assemblies (2)	7.983
Drum-to-center-support mounting hardware	0.059
Center support	0.603
Leading edge member	0.386
Leading-edge-member support brackets (2)	0.099
Outboard end supports (2)	1.860
Total	37.439

Based on the above weights, the array power-to-weight ratio is 67 W/kg. This ratio is based on the ability of the array to generate 2500 W of power at 328 K (55°C) under "air mass zero" illumination and within ±0.1745-rad orientation with the Sun at 1.49599 × 10^8 km (1.0 AU), compared to a power-to-weight ratio of approximately 22 W/kg for typical *Mariner*-type solar panels. Cell efficiency is specified by area performance of 107.6 W/m^2 (10 W/ft^2) of gross module area. The cell selected to achieve minimum weight was 0.020 cm thick, 2 cm × 2 cm, with 3.8 cm^2 of active area per cell. The calculated array power under these conditions is 2523 W at 102 Vdc. To arrive at the maximum power available at the electrical interface on the center support, the series resistance distribution losses in the array substrate bus strip, the slip ring (including line losses within the storage drum and center support), and the solar cell interconnect were taken into account. The effect of the combined series resistance loss is to reduce the maximum power by 57 W at an operating temperature of 328 K.

The major components that form the power-producing system are described below.

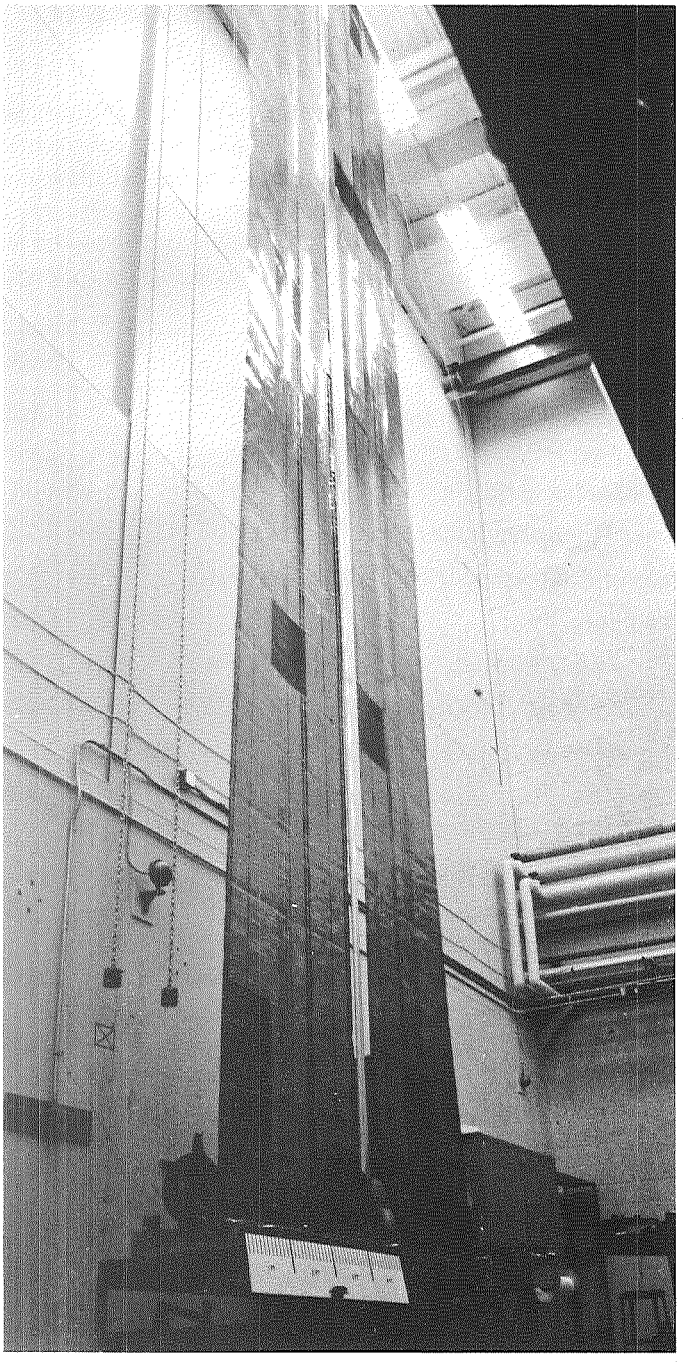

Figure 1. Fully deployed solar array

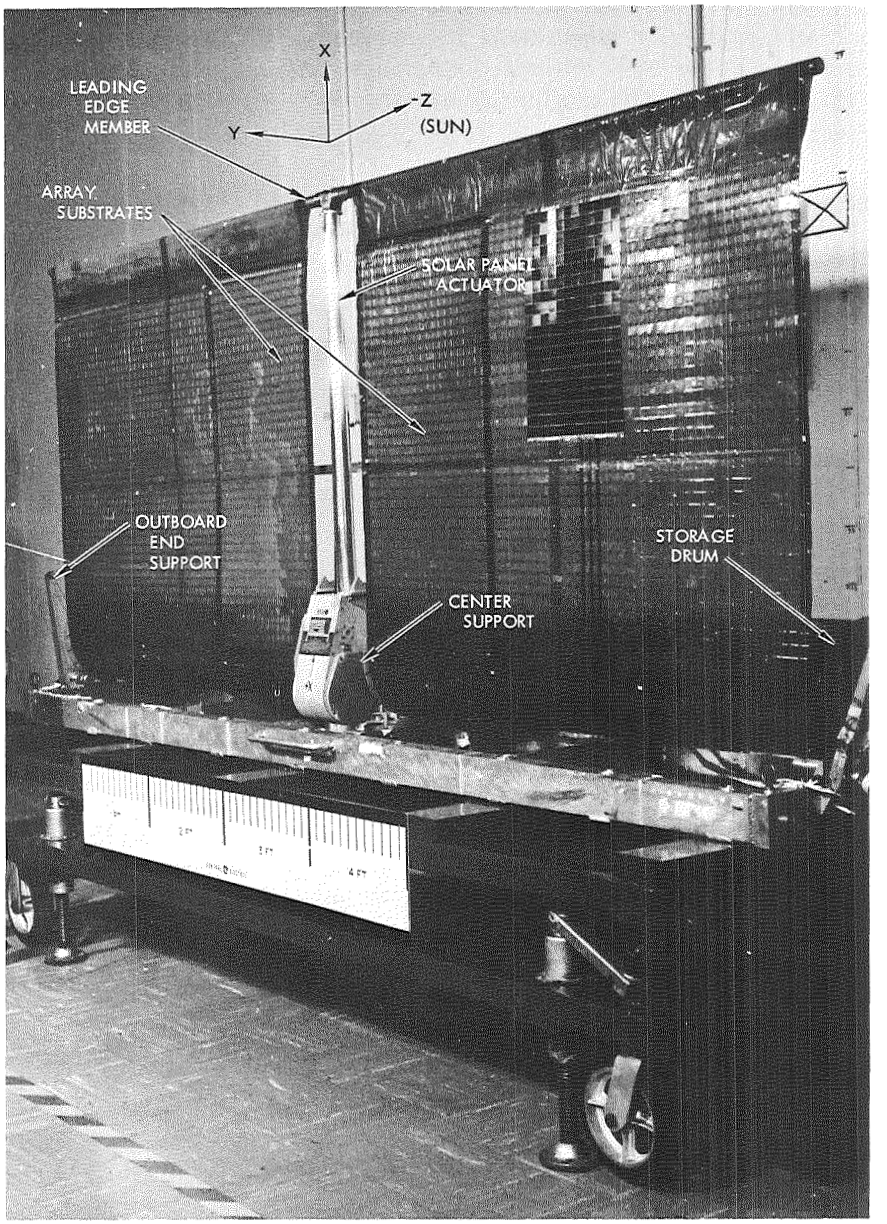

Figure 2. Solar array components

Array Substrate

The solar cells are mounted on two flexible substrates of 0.005-cm Kapton H film. Tension in these two substrates is utilized to maintain the desired single-plane geometry and to establish the natural frequency of the deployed system above the required 0.04 Hz. The flight-type design calls for each substrate to support 6 circuits, each composed of 12 series-connected modules (eleven with 20 series cells by 19 parallel cells and one with 22 series cells by 19 parallel cells).

The substrate is fabricated from copper-clad Schjel-Clad L-7510 etched to form a conductor electrical bus strip system, with each circuit feeding into the main positive and negative bus. The bus in turn connects to the feed-through section of the drum and the slip rings. All connections from the cell side of the substrate to the bus strip system are made around the edges rather than through holes in the substrate. The exposed copper bus strips on the rear side of the substrate are covered with Kapton silicone pressure-sensitive tape. Foamed RTV 560 cushioning buttons are deposited on the rear side of the substrate at the corners of each solar cell. These buttons provide the required interlayer cushioning in the stowed configuration.

Solar Panel Actuator

The solar panel actuator is a Bi-Stem deployable boom unit designed and developed by Spar Aerospace Products, Ltd. The boom element, the component which provides the actuation force for deployment and forms the primary structure in the deployed configuration, has a nominal outside diameter of 3.4 cm (1.34 in.). It is made up to two 301 stainless-steel strips, 10.2 cm (4 in.) wide and 0.018 cm (0.007 in.) thick, which are prestressed to form an overlapped tube in the deployed position. The boom is silver-plated on its outside surfaces to reduce the temperature gradients in the boom when one side is exposed to solar radiation and the other side is in shadow.

Storage Drums

The two storage drums in the system form the backbone of the stowed configuration. The drums rotate approximately 15 turns to deploy or retract the array. Each drum includes a shell, outboard end cap, inboard end cap, and edge guides. The drum shells are 1.196-m (47.10 in.)-long, 0.081-cm (0.032 in.)-thick sheet magnesium rolled into a 20.32-cm (8-in.)-diameter cylinder, which is closed with a lap-butt joint utilizing 1.9-cm (0.75 in.)-wide strip of magnesium bonded with Epon 934.

The inboard end cap assembly houses the two main bearings which allow the storage drum to rotate with respect to the support shaft. The constant torque negator spring motor, which provides the substrate preload force, is mounted on the inboard end cap with the output spool

coaxial with the main bearings. A slip ring assembly, which functions to transfer array power and signals across the rotary joint between the drums and the center support, is then mounted to the inboard end of this output spool. The outboard end cap serves as the supporting interface for the drum outer end during launch. It contains a tapered hole which mates with a tapered plug in the outboard end support. Two edge guide flanges are mounted on each storage drum to provide control forces to the substrate edge if required during retraction.

Center Support

The center support consists of a magnesium center tube, two machined magnesium end fittings, and two magnesium face sheets. The center tube is pinned to the end fittings, and the face sheets are riveted to the tube end fittings. One face sheet provides for the electrical connector installation and, together with the other face sheet, transmits shear loads. The end fittings provide the interface pads for the vehicle structure and the solar panel actuator.

Leading Edge Member

The leading edge member is the structural element on the outer-most edge of the substrate. In the deployed configuration, this member transmits the 17.8-N (4-lb) substrate preload force from the array substrates to the boom tip. In the stowed configuration, the leading edge member functions to restrain the outer substrate wrap and to cage the Bi-Stem boom element. The tips of this member are supported by the outboard end supports, and the center section is supported from the actuator housing by two saddle-type brackets. The leading edge member is made up from two 1.27-m (50.1-in.)-long cylinders fabricated from 0.05-cm (0.020 in.) beryllium sheet bonded with Epon 934. The two cylinders are inserted into a center fitting and bonded in place. This fitting also houses two instrument bearings which mate with the stainless-steel boom post. These bearings decouple the array substrate from the Bi-Stem boom for rotation about the boom axis.

Outboard End Support

This arm carries the stainless-steel tapered plugs which interface with the outboard end cap and leading edge member. Attachment of the movable arm to the vehicle-mounted bracket is through a hinge joint. A torsion spring which mounts on the hinge pin furnishes 1130 N-cm (100 in.-lb) of torque in the stowed configuration. The release of the support is accomplished by a separation nut/separation bolt/bolt catcher combination. The torsion spring forces the movable arm to rotate about the hinge pin through an angle of approximately 0.17 rad. The storage drum and the leading edge member are thus released to permit deployment of the solar panel actuator.

Testing

The engineering test model was subjected to a comprehensive test program consisting of both environmental and developmental tests. The following tests were conducted:

(1) Deployed dynamics tests to provide necessary data on the dynamic characteristics of the deployed array for use in a comparison with analytical data. Results of the comparison were used to verify the mathematical models generated in earlier phases of the program or to provide information to improve the mathematical models. During the tests, the array was deployed vertically downward in a vacuum chamber, and the system was excited with motion at the center support. Out-of-plane symmetric (Z-axis), out-of-plane antisymmetric (torsional), and in-plane (Y-axis) excitations were performed.

(2) Pyrotechnic-induced shock tests to measure acceleration levels on the array components resulting from the simultaneous firing of both separation nuts (each armed with two active squibs) on the outboard end supports.

(3) Thermal–vacuum tests to measure response of the array under deployed transient, low-temperature stowed, low-temperature deploy and retract, stowed transient and high-temperature soak, and high-temperature deploy and retract conditions.

(4) Acoustic noise test to monitor response of system exposed to 60 s of random incidence, reverberent sound with an overall sound pressure level of 150 dB.

(5) Stowed vibration tests in Y-, Z-, and X-axes. The tests consisted of: (a) several low-level sinusoidal sweeps to set initial recording gain factors and to obtain array response to a constant-level base excitation input to determine amplification factors, (b) an acceptance-level sinusoidal sweep at two-thirds of the specification level to evaluate linearity of system response and to provide a final assessment of the risks associated with the full-level qualification input, (c) a sinusoidal qualification sweep, and (d) random noise testing with the same sequence (low-level, acceptance-level, and qualification-level testing).

Test Performance

Cell/Coverglass/Glass Platelet Breakage

The percent of solar cell and coverglass breakage resulting from the environmental test program was significantly greater than that for

the dummy glass platelets. Breakage followed the relative difference in individual element thickness, i.e.,

Item	Total breakage, %
0.007-cm coverglass	3.25
0.020-cm solar cells	1.75
0.028-cm dummy glass platelets	0.47

The most severe environment for the coverglass and solar cells was the stowed vibration test. There is no breakage pattern to indicate a possible cause for the high proportion of damage in the case of the coverglass, although there are a few examples of parallel adjacent coverglass as within a module row that have cracked in a direction parallel to the axis of the storage drum. This may be an indication of insufficient cushioning between the storage drum shell and the first wrap of solar cells.

The results indicate that the cell/coverglass composite is not as resistant to damage as a corresponding glass platelet mass simulation that is 0.028 cm thick. The 0.007-cm-thick coverglass cracked independently of the cell in many cases. Since some of the damage was sustained during the acoustic noise test, it is felt that a test of this type should be retained as a system test environment for future lightweight solar array assemblies.

The thermal–vacuum tests represented the most severe environment for the dummy glass platelets. This may be explained by the fact that the areas of dummy glass were not temperature-controlled during the deploy and retract cycles and therefore were colder than the solar cell modules. Also, many localized areas of the dummy glass were affected by an overheating condition that occurred during the stowed high-temperature test. Either of these factors could account for the disproportionate percentage of glass platelet breakage during these tests.

Solar Panel Actuator Limit Switch Failures

Three microswitches are required within the solar panel actuator to maintain the fully retracted, orbital retracted (10.16 cm from fully retracted), and fully extended positions. At the conclusion of testing, none of these switches were operable. Since their function was not vital, no effort was made to fix the switches. The redesign required for corrective action is considered minimum for future applications.

Fatigue Cracking Near Leading Edge Member

A fatigue crack 0.317 cm (⅛ in.) long, near the leading edge member in the solar panel actuator rod outer element, was discovered while pre-

paring for a 35-cycle life demonstration following the stowed vibration test. No change in performance of the system or in the length of the crack was detected during or after the life demonstration.

Slip Ring Resistance Changes

At the beginning of the test program, the slip ring resistance remained constant as the storage drums turned during array deployment and retraction. Some slip ring dynamic resistance change was first recorded during the low-temperature deploy and retract cycle. Similar fluctuations, along with a slight overall increase in resistance, were recorded during the high-temperature deploy and retract cycle. The first ambient deployment following the stowed vibration test produced fluctuations in resistance which corresponded to the period of rotation of the storage drums. After 35 ambient deploy and retract cycles, the magnitude of these fluctuations in resistance had decreased. The periodic nature of the changes in resistance indicates the possibility of dirt on the power rings which was gradually removed by the brushes as the array was deployed and retracted during the 35-cycle life demonstration. There was no significant increase in the static resistance of the power rings as a result of the environmental test program.

Marginal Performance of Storage Drum Negator Spring System

The present storage drum negator spring system appeared marginal for rewrap of the array substrate during the low-temperature deploy and retract test.

Reliability Demonstration

At the conclusion of the total test program, the array was deployed to its full length and retracted 35 additional times to establish confidence in such items as cell interconnects, deployment/retraction components, and slip ring assemblies. In all, more than 100 deployment retraction cycles were performed during the term of this program. With the exception of the microswitch failures noted above, no anomalies were detected which could be attributed to rolling and unrolling the solar cell substrates on the storage drums. During the performance of the deployment/retraction tests, the deployment boom was purposely offset from its center line in the plane of the substrate to determine the array's ability to rewrap uniformly. It was demonstrated in these experiments that a boom tip deflection of up to 21 cm can be accommodated without difficulty and uniform substrate wrapping will not be compromised.

Conclusion

Since the array demonstrated its ability to survive the specified test program, the concept of this 23-m^2 roll-up solar array with a 66-W/kg power-to-weight ratio has been proven feasible.

Reference

1. *Feasibility Study 30 Watts Per Pound Roll Up Solar Array Final Report,* Report 68SD4301. General Electric Co., Philadelphia, Pa., June 21, 1968.

Large Spacecraft Antennas: New Geometric Configuration Design Concepts

R. E. Oliver

Engineering Mechanics Division

Several unconventional approaches to the configurational design of high-gain microwave antenna reflectors are presented. These approaches provide means for improving the performance of nonfurlable antennas and for improving both aperture efficiency and stowed volume efficiency of furlable antennas.

The first class of design approaches involves relatively minor modifications of conventional dual-reflector (Cassegrain and Gregorian feed) antenna concepts. These modifications eliminate the loss of transmitted energy resulting from the reflection of energy back into the feed from the subreflector as well as the loss due to interception of rays by the subreflector after reflection from the main reflector.

The second class of concepts involves the use of a conical main reflector and multiple reflections from this main reflector and from one or more subreflectors. These concepts offer the advantage of relative ease of fabrication, inspection, and furlability associated with a single curvature (conical) main reflector. In addition, they provide configurations with very small diameter subreflectors, resulting in low aperture area blockage and small furled antenna diameters.

Introduction

The objective of this activity is to develop the technology required to design, fabricate, and test large high-gain antennas for use on spacecraft. The initial phase of this program was devoted primarily to the evaluation of existing and new antenna concepts with respect to their potential application to antennas with diameters up to 30 m.

The results of this comparative evaluation indicated that the Cassegrain feed paraboloidal antenna configuration may be applicable for antennas greater than 4 m in diameter, although the folding or furling of the

doubly curved paraboloidal reflector does present problems. It was also pointed out that significant RF losses are associated with the tendency to reflect energy back into the feed horn from the subreflector in conventional Cassegrain feed designs. Although this reflection back into the feed can be avoided by modifying the subreflector surface near the antenna axis, losses are still significant, particularly in the case of dual-frequency operation. A simple configuration design modification for Cassegrain feed paraboloidal antennas, which eliminates these losses even for dual-frequency operation, is described in the following section.

The most promising concept evolved during the initial evaluation study is the conical Gregorian antenna conceived by Ludwig (Reference 1). The use of a conical main reflector offers several potential advantages in the areas of mechanical and structural design, fabrication, surface measurement, and furling. In addition, this concept exhibits excellent RF performance characteristics.

The principal disadvantage of the conical Gregorian antenna is the relatively large diameter of the subreflector (0.4 to 0.5 times the outer diameter of the main reflector). Unless the subreflector itself is furlable, it appears that this concept is limited in spacecraft application to antenna diameters below about 10 m.

Several new antenna geometrical configurations, all using conical main reflectors, are presented. These concepts retain many of the advantages of the conical Gregorian antenna concept associated with a conical main reflector. In addition, they provide a means for greatly reducing subreflector diameters (e.g., to less than one-tenth the main reflector outer diameter).

Modified Cassegrain Feed Paraboloidal Antenna

A simple approach to prevent the reflection of energy back into the feed horn of a Cassegrain feed paraboloidal antenna and at the same time to efficiently utilize all the feed-horn energy is illustrated in Figure 1.

In this modified Cassegrain feed paraboloidal antenna concept, a ray emanating from the feed F and essentially on the antenna axis is reflected by the subreflector at point C and by the main reflector at point D. This ray then grazes the subreflector at point E. Thus, all energy emitted by the feed is reflected usefully from the antenna (to the extent that the RF waves behave like optical waves).

The main reflector surface geometry is generated by rotation about the antenna axis (through F and C) of an arc D–G of a parabola. The axis of this parabola is displaced from, but is parallel to, the antenna axis. The vertex of the parabola is at A, and its focus is at B. The subreflector surface geometry is generated by rotation about the antenna axis of an

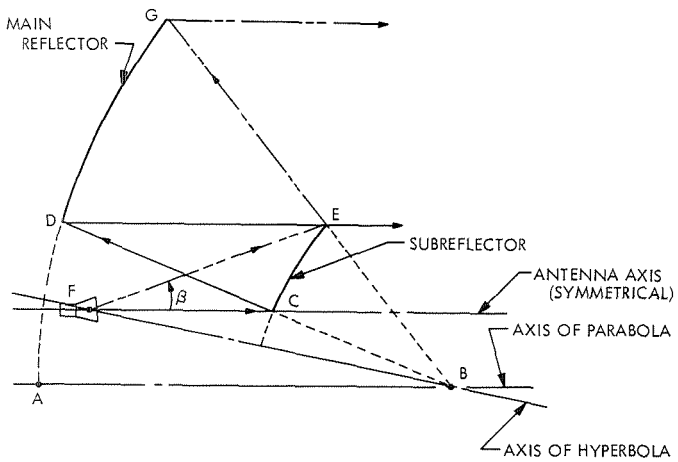

Figure 1. Modified Cassegrain feed paraboloidal antenna

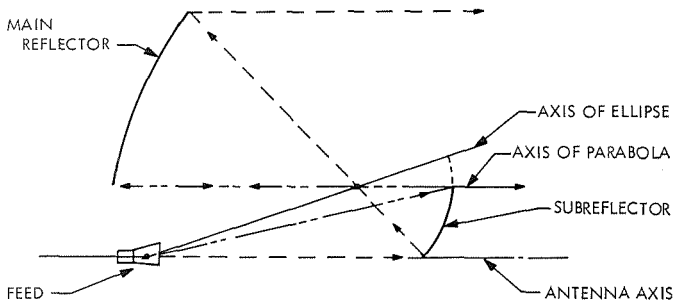

Figure 2. Modified Cassegrain with ellipse-generated subreflector

arc C–E of a hyperbola, the major axis of which passes through F and B. The subreflector thus produces an image of the point source feed F at the focus B of the parabola. The main reflector then "sees" an apparent ring source on the circle produced by rotating this focal point B about the antenna axis.

Note that this modification involves no additional elements and no increase in complexity over a conventional Cassegrain feed paraboloidal antenna design. This concept does, however, provide efficient use of the feed energy, even for dual-frequency antennas.

In concept, this modification is equally applicable to both Cassegrain and Gregorian feeds using subreflectors generated by arcs of hyperbolas or ellipses as illustrated in Figures 2 through 4.

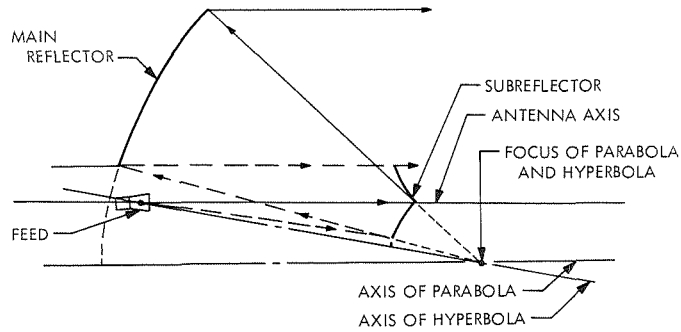

Figure 3. Modified Gregorian with hyperbola-generated subreflector

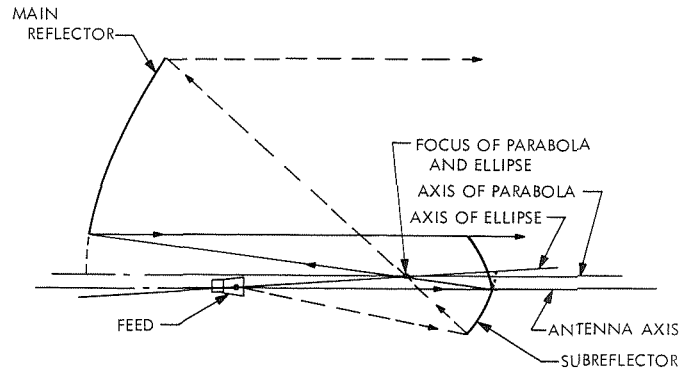

Figure 4. Modified Gregorian with ellipse-generated subreflector

Multiple-Reflection Conical Antenna

The basic principle of the multiple-reflection conical antenna concept is illustrated in Figure 5. The main reflector surface is a frustum of a cone with its apex at A and with a half cone angle θ. The subreflector surface is generated by rotation about the antenna axis (through A and F) of an arc B–C of a parabola. The vertex L and focus K of this parabola lie on the cone with half angle 2θ and with its vertex at A. The image F of this focus (as reflected in the main reflector cone) then lies on the antenna axis. The effective center of the feed is then placed at this focal point F. A ray leaving the feed center F and just grazing the subreflector at C is reflected by the main reflector at D, by the subreflector at B, and again by the main reflector near D. This ray then emerges from the antenna parallel to the antenna axis. The outermost usable ray is traced in Figure 5, traveling the path F–J–C–E and then emerging from the antenna parallel to the antenna axis. Each ray thus experiences three reflections before emerging from the antenna.

For geometrically exact and perfectly reflective surfaces, it is clear that all optical rays emanating from the feed between the cones with

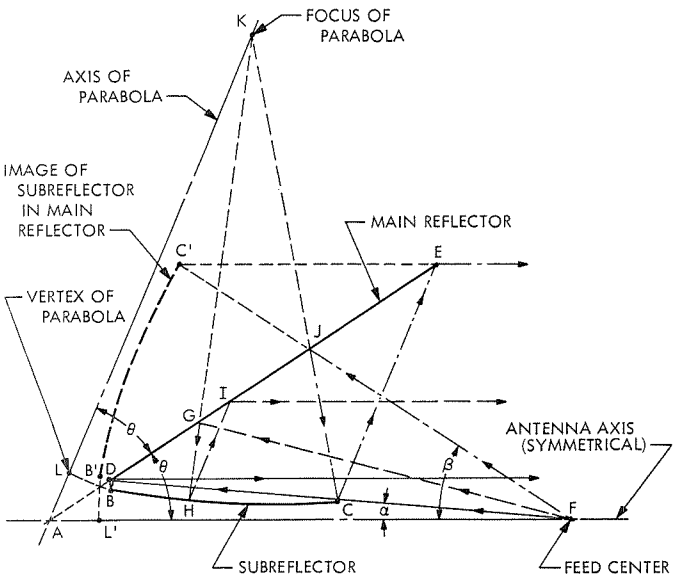

Figure 5. Multiple-reflection conical antenna

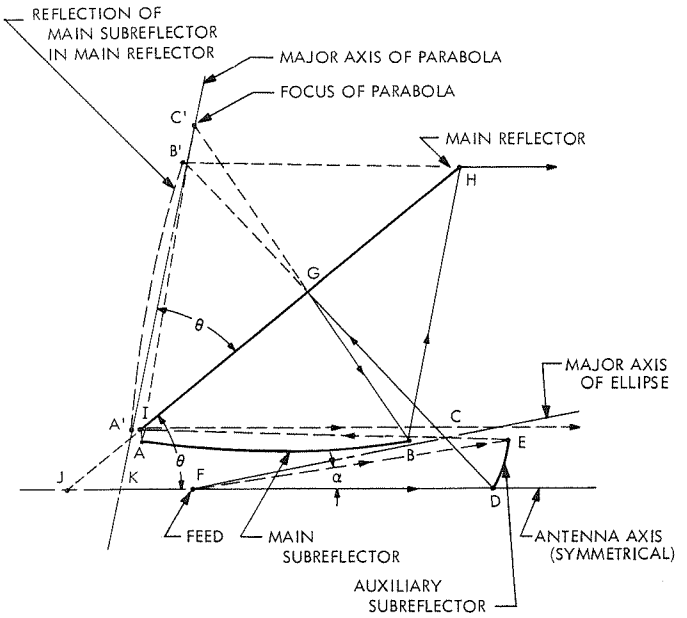

Figure 6. Multiple-reflection conical antenna with modified Cassegrain feed

half angles α and β (Figure 5) will emerge from the antenna parallel to the antenna axis. Further, it is also easily shown that all path lengths of these rays from the feed center F to any plane normal to the antenna axis and to the right of point E will be equal.

As suggested in Figure 5, the diameter of the subreflector (through point B) can be much smaller than the outer diameter of the main reflector (through point E).

It is also clear (again assuming geometrically exact and perfectly specularly reflective surfaces) that the performance of this antenna will be identical to that of a conventional focal point feed paraboloidal antenna, the generating parabola for which is shown through L′, B′, and C′ in Figure 5 and with its focus at F. Thus, this multiple-reflection conical antenna configuration represents, in a sense, an optically folded version of a conventional focal point feed paraboloidal antenna.

This similarity between this concept and a conventional focal point feed paraboloidal antenna suggests that it will exhibit some of the disadvantages of the latter. The feed horn, being relatively far forward from the vertex of the main reflector, requires long feed lines, resulting in feed line losses. Further, as suggested above, all energy associated with rays emanating from the feed within the cone with half cone angle α is lost.

Both of these disadvantages can be virtually eliminated by incorporating the modified Cassegrain feed described above. One possible version of the multiple-reflection conical antenna with a Cassegrain feed is shown in Figure 6.

In this version of the multiple-reflection conical antenna, the main subreflector surface is generated by rotation about the antenna axis of a segment A–B of a parabola, the axis of which passes through K and C′ and with its focus at C′. The reflection in the conical main reflector of this focus C′ is at C, which lies above the axis of the antenna. An auxiliary subreflector surface is generated by rotation about the antenna axis of a segment D–E of an ellipse, the major axis of which passes through the effective center F of the feed and through the point C. F and C are the foci of this generator ellipse. Thus, an effective ring source is created on the circle generated by rotating the point C about the antenna axis.

Considering the geometrical properties of ellipses, parabolas, and cones, it is clear that all (optical) rays emanating from the feed within the cone with half cone angle α will ultimately radiate from the antenna parallel to the antenna axis. All path lengths associated with these rays from the feed F to any plane normal to the antenna axis and to the right of point H (Figure 6) are equal.

For geometrically exact and perfectly specularly reflecting surfaces, the performance of this antenna would be identical to that of an antenna with a main reflector surface generated by rotation about the antenna axis of a segment A′–B′ (Figure 6) of a parabola with its focus at C, with a

point source feed at F, and using the auxiliary subreflector shown in Figure 6 as the only subreflector. Thus, this version of the multiple-reflection conical antenna represents an optically folded version of a more nearly conventional antenna configuration (i.e., that of Figure 1).

Other versions of the multiple-reflection conical antenna concept are obvious from this analogy between Figure 6 and Figure 1. For instance, conical sections can be superimposed on Figures 2, 3, and 4 to illustrate the optical folding of these configurations into multiple-reflection conical antennas.

Conclusion

The modified Cassegrain feed paraboloidal antenna concept provides a simple means for eliminating RF energy losses associated with small illumination angles in conventional Cassegrain feed antennas. The application of this concept may improve the performance characteristics of such antennas, particularly those which must operate with two RF frequencies.

The multiple-reflection conical antenna concepts described above retain many of the advantages of the conical Gregorian antenna cited by Ludwig (Reference 1). In addition, proper choices of geometric parameters (e.g., cone angle and focal length of the subreflector surface generator parabola) can provide configurations with very small diameter subreflector elements. For instance, a parametric analysis of the basic configuration shown in Figure 6 indicates that a ratio of subreflector outer diameter to main reflector outer diameter as small as 0.06 can be realized. This configuration would then produce a direct subreflector blockage of only 0.36% of the main reflector projected area (as compared with 16 to 25% blockage associated with the conical Gregorian concept).

Other important antenna design criteria may, of course, preclude the practical achievement of such low blockage ratios, particularly in smaller diameter or low radio-frequency antennas. For instance, the subreflector diameter should, in general, be many (e.g., 10 or more) wavelengths associated with the operating radio frequency. It may be necessary, also, to avoid placing a reflective surface less than several RF wavelengths from the focal ring (e.g., point C in Figure 6) of the auxiliary subreflector.

It is also recognized, of course, that the introduction of additional reflecting surfaces tends to increase performance degradation resulting from deviations of reflecting surfaces from their ideal geometries. This potential disadvantage is compensated, at least partially, by the relatively small diameters of the subreflectors. In general, the smaller the overall dimensions of a reflecting surface, the easier it is to maintain small

manufacturing tolerances and the smaller will be the thermal distortions (for a given thermal environment).

The concepts presented above have been considered only from the standpoint of basic geometric feasibility and under the assumption that the RF waves behave essentially as optical waves. Practical applications of these concepts would, of course, require more detailed comparative evaluations with respect to RF performance, ease of fabrication, structural feasibility, weight, cost, reliability, and integrability with spacecraft systems. Effort is currently being directed toward the design, fabrication, and RF testing of a small (approximately 1-m diameter) model based on the version shown in Figure 6.

Reference

1. Ludwig, A. C., and Hardy, J., "Spacecraft Antenna Research: Preliminary RF Test of Conical Gregorian Antenna," in *Supporting Research and Advanced Development*, Space Programs Summary 37-63, Vol. III, pp. 42–46. Jet Propulsion Laboratory, Pasadena, Calif., June 30, 1970.

Antenna Support Structure Aperture Blockage Loss

A. Ludwig

Telecommunications Division

Loss in antenna gain caused by support structure aperture blockage is probably the most difficult loss factor to measure or calculate. In this article the loss is determined experimentally for aluminum and fiberglass structural configurations, and empirical formulas are developed to calculate the loss for other similar configurations. Experimental and analytical data on the X-band RF transmission characteristics of thin fiberglass sheets are presented. It is concluded that fiberglass structures are far superior for minimizing gain loss.

Introduction

The feed or subreflector of an antenna must be attached to the reflector, and typically the required support structure blocks some of the RF energy, causing a loss in antenna gain. This effect is called blockage loss and has been considered by several authors (e.g., References 1, 2, and 3). The direct experimental determination of this loss is very difficult since it is necessary to (1) determine the total efficiency loss of the antenna by an absolute gain measurement, and (2) evaluate all loss factors other than the blockage loss. Both of these steps are difficult and typically introduce tolerances comparable to or larger than the effect being measured. Accurately calculating the loss for a conventional truss structure is even more difficult.

In this article, the loss is experimentally determined by comparing the gain of the antenna using a given configuration with the gain of the antenna using a configuration for which it is possible to accurately determine the loss *a priori*. The results are then used to develop empirical formulas for loss calculations, and to demonstrate that two types of fiberglass structures are far superior to aluminum structures for minimizing gain loss.

Support Configurations and Analysis

Two basic types of configurations were considered: a conventional strut-type structure as shown in Figure 1, and a single large cylindrical shell as shown in Figure 2. The structural members used in the first configuration consisted of fiberglass or aluminum tubes of different diameters; the second configuration used only one cylinder made of 0.38-mm (0.015 in.)[1]-thick fiberglass.

The analysis of the second structure, shown schematically in Figure 3, is relatively simple. For low transmission loss, multiple reflections within the cylinder may be neglected; also the radius of curvature is large compared to a wavelength, so the net loss is closely approximated by the loss of a plane wave incident on an infinite fiberglass sheet of the same thickness.

To determine the dielectric properties of the fiberglass at the 8448-MHz test frequency, several samples were tested using a method reported previously (Reference 4) in which the test sample is inserted across a section of WR 112 waveguide. As described in the above reference, at 8448 MHz this is equivalent to having a plane wave incident at 0.672 rad (38.5 deg) from the normal to the surface, with the E-field normal to the plane of incidence. The test results for three thicknesses are shown in Figure 4. Also shown are calculated results for three values of the dielectric constant ϵ, which were obtained from a computer program developed by Otoshi.[2] It is seen that for a dielectric constant of 5.0, the computed data matches the measured data reasonably well. This value of the dielectric constant is in the correct range for fiberglass (Reference 5). Using this value, the loss of a fiberglass sheet may be calculated for various angles of incidence as given in Figure 5.

To confirm this data, the transmission loss was directly measured by inserting a fiberglass sheet between two horn antennas. Compared to the waveguide measurement, this technique has the advantage of allowing measurement of either polarization for any angle of incidence, but has the disadvantage of diffraction effects which can be difficult to estimate. However, the measured data agrees very well with the computed data as shown in Figure 5, resulting in high confidence in the data.

For the support configuration shown in Figures 2 and 3, the angle of incidence γ is 0.524 rad (30 deg). For either the case of linear or circular polarization (due to the circular symmetry of the structure), the loss will

[1]Where applicable, the International System of Units is stated first, followed by the customary units in parentheses. In each case, the value in parentheses represents the measured or calculated unit.

[2]Otoshi, T. Y., private communication.

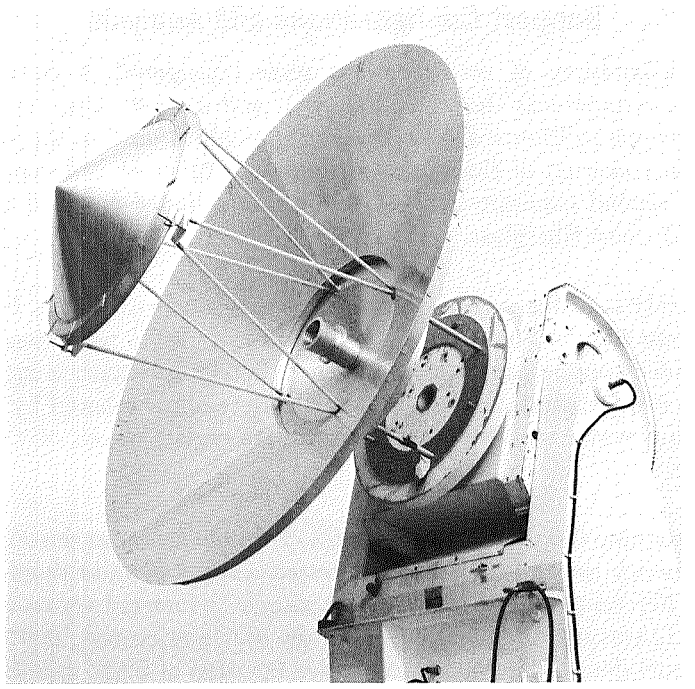

Figure 1. Strut support structure

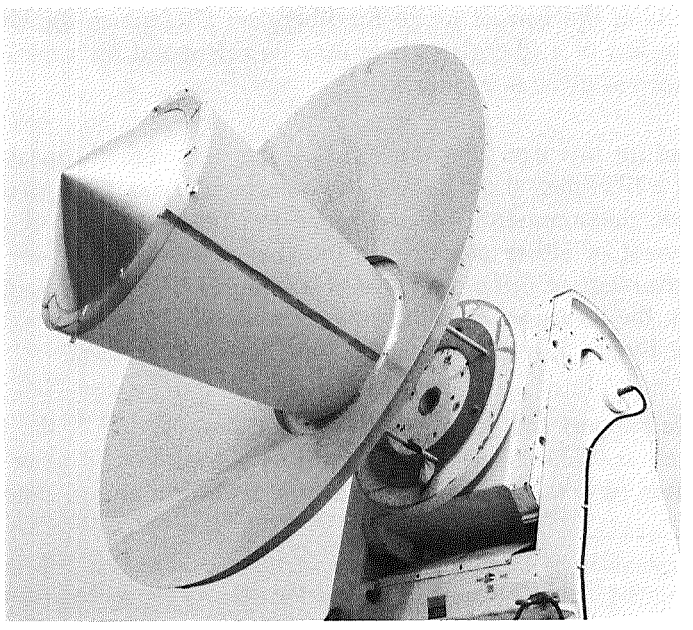

Figure 2. Cylindrical shell support structure

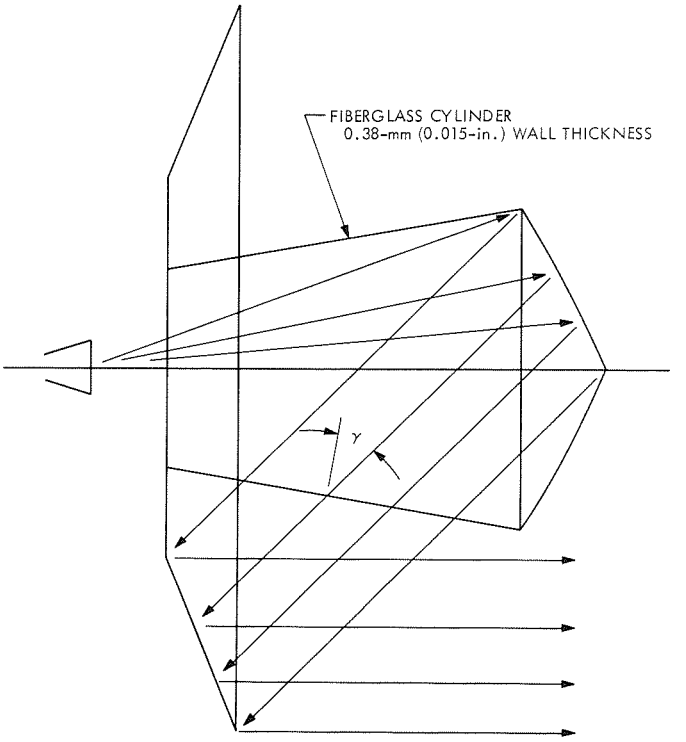

Figure 3. Cylindrical support structure for conical antenna subreflector

be the rms average of the values for E-field normal, and E-field perpendicular to the plane of incidence. Using the information in Figure 5, the loss is calculated to be 0.08 dB. There is an additional 0.05 dB of loss due to three joints where the thickness is doubled. The net loss of the structure in Figure 2 is therefore 0.13 dB. A conservative estimate of the tolerance on this value is ±0.08 dB.

The analysis of the strut structure shown in Figure 1 is not as straightforward or nearly as accurate as the cylinder analysis. In general, loss due to aperture blockage arises from two factors: (1) a fraction of the aperture is shadowed, reducing the effective aperture area of the antenna; and (2) a fraction of the radiated power is lost. To a first approximation, these two effects are equal and if the fractional area blocked is ΔA, the blockage efficiency is given approximately by

$$\eta_B = (1 - \Delta A)^2 \tag{1}$$

Somewhat more sophisticated results are given in the References 1, 2, and 3, but the whole approach is based on such uncertain assumptions that it is not clear that anything more complicated than Equation 1 is justified. (The main questionable feature is that, typically, the structural members have dimensions on the order of a wavelength, but diffraction

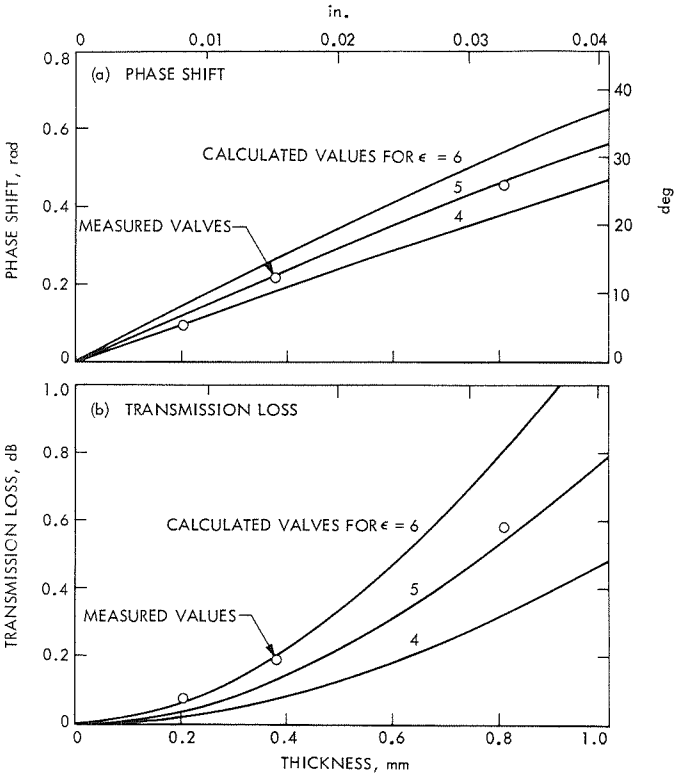

Figure 4. RF effect of fiberglass sheet in WR 112 waveguide at 8448 MHz

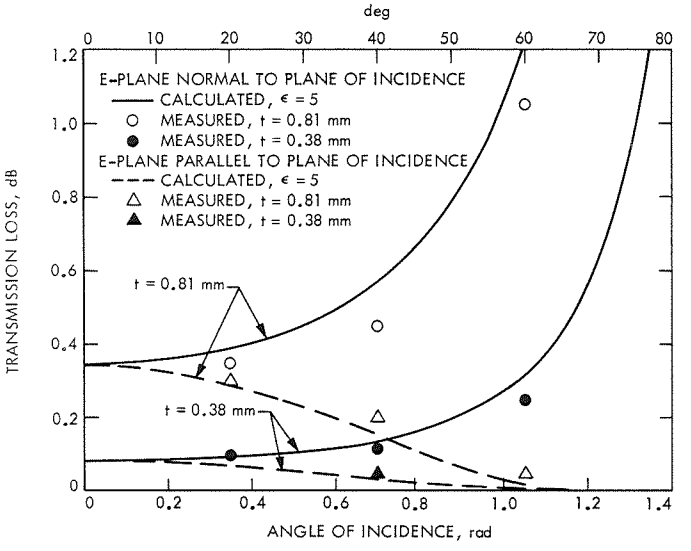

Figure 5. Transmission loss vs angle of incidence for fiberglass sheets of two thicknesses

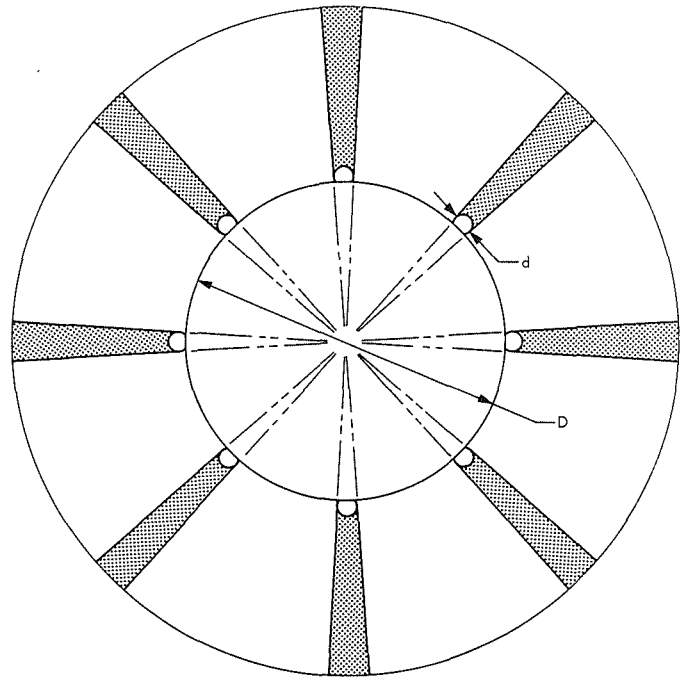

Figure 6. Area shadowed by strut structure

effects are not considered.) One modification of this application to Equation 1 has been suggested (Reference 6) which does appear to be useful; the blocking structure is assumed to be partially transparent with an opacity coefficient α, and an effective blocked area is defined by

$$\Delta A_{eff} = \alpha \Delta A \tag{2}$$

so the loss is given by

$$\eta_B = (1 - \alpha \Delta A)^2 \tag{3}$$

For a perfect conductor, neglecting diffraction effects, one would expect the opacity factor to be 1.0. For a fiberglass tube, the opacity may be estimated by averaging the transmission loss and loss due to phase shifts over various angles of incidence. Based on this very rough approach, for a 0.51-mm (0.020-in.) wall tube with a wave incident at 0.524 rad (30 deg), one would expect an opacity of about 30%, and for a 0.89-mm (0.035-in.) wall, an opacity of about 65%. However, the tolerance on these estimates is near a factor of 2.

The blocked area ΔA is defined as the projection of the optical shadow of the support members on the aperture area of the antenna. Referring to Figure 6, which is a head-on view of the antenna, if the struts of

diameter d were all parallel to the axis of the antenna, and were located on a circle of diameter D, then we would have

$$\Delta A = \frac{\pi D - 8d}{\pi D} \tag{4}$$

In the actual test antenna configuration shown in Figure 1, the struts are not parallel to the axis, but Equation 4 is still a good approximation for the area.

Experimental Results

The various structures were used to support the subreflector of the conical antenna as shown in Figures 1 and 2. The relative gain of the antenna with the various structures was then measured using a bolometer detector and HP 415 meter (1800-Hz signal modulation). Since the support structure loss is known for the case of the cylinder, this was used as the normalization to determine the absolute loss of the other structures.

Using this normalization, where the loss of the cylinder is taken to be -0.13 dB, the values shown in Table 1 are obtained. The indicated tolerance of ± 0.10 dB includes measurement errors as well as the tolerance on the calculated cylinder loss. Also shown in Table 1 are the blocked areas for the various cases. Using values for the blocked area and the loss, Equation 3 may be used to empirically determine the effective blocked area and values of α, which are also shown in Table 1. It is seen that for aluminum tubes of this size the effective area is substantially larger than the actual area, resulting in an opacity greater than the expected value of 1.0, whereas the effective area of the thin fiberglass tubes is much less than the actual area, and the opacity is less than the expected value. Of course, in both cases, the expected opacity

Table 1. Measured blockage loss and empirical values of effective opacity

Case	Aluminum struts		Fiberglass struts	
	1.27-cm diam	3.81-cm diam	1.27-cm-diam, 0.09-mm-thick wall	5.72-cm diam, 0.51-mm-thick wall
Measured blockage loss, dB	0.52 ± 0.10	2.03 ± 0.10	0.10 ± 0.10	0.29 ± 0.10
Fractional blocked area, %	3.9	11.6	3.9	17.4
Effective blocked area, %	5.8 ± 1.0	20.8 ± 0.9	1.1 ± 1.1	3.3 ± 1.1
Opacity α	1.5 ± 0.3	1.8 ± 0.1	0.3 ± 0.3	0.19 ± 0.06

Table 2. Calculated blockage loss for TOPS high-gain antenna

Case	Aluminum strut (3.81-cm diam)	Fiberglass strut (5.72-cm-diam, 0.51-mm wall)	Fiberglass cylinder (0.38-mm wall)
Fractional blocked area, %	8.7	12.0	100
Opacity α	1.8	0.19	0.016
Effective blocked area, %	15.7	2.3	1.6
Expected blockage loss, dB	1.5	0.20	0.14

values were very rough estimates. Unfortunately, the estimated tolerance swamps out the value of α for the case of the small fiberglass tube, but in the other cases the value is reasonably well determined. These empirical values of opacity may be used in Equation 3 to extrapolate the results to other antennas with similar configurations. For example, the loss of several proposed support structure configurations for the Thermoelectric Outer-Planet Spacecraft (TOPS) high-gain antenna are shown in Table 2.

To compute the loss of a cylindrical support for a conventional paraboloidal reflector is more difficult than the case of the conical reflector. For the conical antenna the angle of incidence is constant; for the TOPS paraboloidal reflector the angle of incidence varies as show in Figure 7. If we divide the antenna into several regions and take the angle of incidence as being constant within each region, approximate values of the voltage transmission coefficient t and relative phase shift $\Delta\phi$ may be obtained as given in Table 3. The relative phase shift is the difference

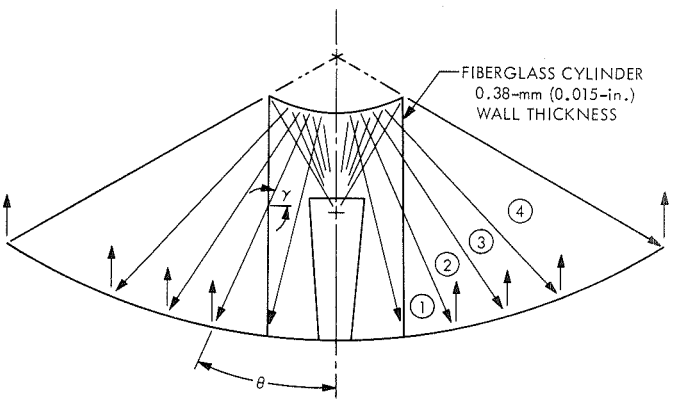

Figure 7. Cylindrical support structure for conventional paraboloidal antenna subreflector

Table 3. Transmission parameters for 0.38-mm (0.015-in.) fiberglass cylindrical support for paraboloidal antenna subreflector

Region	Range of ray angle θ, deg	Approximate angle of incidence γ, deg	E-field normal to plane of incidence			E-field parallel to plane of incidence			Fractional aperture area ΔA
			$t_\perp$	$\Delta\phi_\perp$, deg	$\tau_\perp$	$t_\parallel$	$\Delta\phi_\parallel$, deg	$\tau_\parallel$	
1	15–25	70	0.929	−11.4	0.911	0.9995	3.4	0.998	0.0944
2	25–35	60	0.964	−5.6	0.959	0.9993	3.3	0.998	0.1492
3	35–45	50	0.978	−2.9	0.976	0.9977	2.6	0.997	0.2141
4	45–60	40	0.984	−1.5	0.984	0.9957	1.7	0.995	0.5423

between the actual phase shift through the sheet for a given region and the average phase shift of all regions. The effective voltage transmission coefficient τ is then given by $\tau = t \cos \Delta\phi$. The net transmission coefficient of the cone is then given by an area weighted rms average of the transmission coefficients

$$\tau_{\text{net}} = \sum_{\substack{\text{all} \\ \text{regions}}} \frac{1}{2} \left(\tau_{\parallel}^2 + \tau_{\perp}^2 \right) \Delta A \tag{5}$$

This yields a value of $\tau_{\text{net}} = 0.9841$ for the data of Table 3, which corresponds to the loss of 0.14 dB given for this case in Table 2.

These results demonstrate the clear RF superiority of fiberglass structures over the aluminum structures (all structures are mechanically nearly equivalent) for the TOPS antenna.

Conclusion

It has been experimentally determined that aluminum tubes 1–2 wavelengths in diameter have an effective blockage area approximately 1½–2 times their physical area and that thin wall fiberglass tubes have an effective blockage area much less than their physical area. Both thin wall fiberglass tubes and large fiberglass cylinders are very good support structures for reducing gain loss. It should be noted that dielectric structures have an adverse effect on the system temperature of very low noise receiving antennas, so although the fiberglass structures are very attractive for relatively noisy spacecraft antenna systems, they are not necessarily attractive for low noise ground antennas.

References

1. Gray, C. L., "Estimating the Effect of Feed Member Blocking on Antenna Gain and Sidelobe Level," *Microwave J.*, pp. 88–91, Mar. 1964.

2. Wested, J. H., "Shadow and Diffraction Effect of Spars in a Cassegrainian System," Report P2118. Microwave Laboratory, Danish Academy of Technical Sciences, Copenhagen, Denmark, Mar. 1966.

3. Ludwig, A., "Efficient Antenna Systems: Aperture Blockage and Surface Tolerance Loss Calculations for Non-Uniform Illumination and Error Distribution," in *The Deep Space Network*, Space Programs Summary 37-41, Vol. III, pp. 89–90. Jet Propulsion Laboratory, Pasadena, Calif., Sept. 30, 1966.

References (contd)

4. Woo, K., and Otoshi, T. Y., "Spacecraft Antenna Research: An RF Study of Reflector Surface Materials for Spacecraft Antennas," in *Supporting Research and Advanced Development*, Space Programs Summary 37-61, Vol. III, pp. 99–106. Jet Propulsion Laboratory, Pasadena, Calif., Feb. 28, 1970.

5. Handbook of Chemistry and Physics, 50th Edition, p. E-66. Edited by R. C. Weast. Chemical Rubber Co., Cleveland, Ohio, 1969–1970.

6. Potter, P. D., *The Design of a Very High Power, Very Low Noise Cassegrain Feed System for a Planetary Radar*, Technical Report 32-653. Jet Propulsion Laboratory, Pasadena, Calif., Aug. 24, 1964.

Interplex Modulation

S. Butman and U. Timor

Telecommunications Division

In a conventional phase-shift-keyed/phase modulated (PSK/PM) system, the receiver tracks the frequency and phase of the carrier by means of a phase-locked loop and coherently demodulates the data. However, due to the inherent nonlinearity of the phase-modulation process, some power is transmitted as cross modulation, which reduces the useful available power. This article describes a new PSK/PM modulation scheme, called Interplex, which reduces the cross-modulation power loss. The scheme can be implemented in existing systems without significant hardware changes and appears attractive in concept for improving the performance of deep space telecommunications systems.

Introduction

In conventional multichannel frequency-multiplexed telemetry systems, several independent binary data channels are combined, using biphase-modulated subcarriers, to phase modulate a single RF carrier signal. Such systems are called phase-shift-keyed/phase-modulated (PSK/PM). The receiver tracks the frequency and phase of the carrier by means of a phase-locked loop and coherently demodulates the data. Lindsey (Reference 1) and Weber (Reference 2) analyzed the performance of such systems, which depends on the power in the data sidebands as well as on the unmodulated component of the carrier. However, due to the inherent nonlinearity of the phase-modulation process, some power is transmitted as cross modulation, which reduces the useful available power.

This article describes a new PSK/PM modulation scheme, called Interplex, which reduces the cross-modulation power loss, without affecting the basic structure of the conventional system. Thus, it can be easily incorporated into existing systems. It appears attractive in concept for improving the performance of deep space telecommunications systems.

Formulation

The general form of the phase-modulated RF signal in a multichannel PSK/PM system is

$$z(t) = \sqrt{2P} \sin [\omega_c t + \Theta(t)] \tag{1}$$

where P is the total average power, ω_c is the carrier frequency, and $\Theta(t)$ is the phase modulation. In conventional PSK/PM systems, $\Theta(t)$ is a linear combination of binary phase-shift-keyed sine-wave or square-wave subcarriers. We will temporarily assume that the system bandwidth is sufficiently large to handle square-wave subcarriers, because sine-wave subcarriers produce more cross-modulation loss and should be avoided. This of course may not be possible in very high data rate systems where bandwidth becomes a factor; however, the basic concepts are the same.

When a binary data stream $d_n(t) = \pm 1$ phase-shift-keys a unit amplitude square wave, sq $(\omega_n t) = \pm 1$, of frequency ω_n, the result is again a binary wave, $s_n(t) = \pm 1$,

$$s_n(t) = d_n(t) \text{ sq } (\omega_n t) \tag{2}$$

and the phase modulation $\Theta(t)$ in a conventional system is

$$\Theta(t) = \sum_{n=1}^{N} \theta_n s_n(t) \tag{3}$$

where N is the number of channels and the coefficients $\theta_1, \theta_2, \cdots, \theta_N$ are the modulation angles or modulation indexes whose choice determines the power allocation for each channel, the power allocated to the RF carrier, and the power that goes into cross modulation. We will analyze in detail the two-channel system. A generalization to the multichannel case will be briefly discussed in the last section.

Two-Channel Conventional PSK/PM System

When only two channels are involved, the phase-modulated RF signal is

$$\begin{aligned} z(t) = {} & [\sqrt{2P_1}\, s_1(t) + \sqrt{2P_2}\, s_2(t)] \cos (\omega_c t) \\ & + [\sqrt{2P_c} + \sqrt{2P_{cm}}\, s_1(t) s_2(t)] \sin (\omega_c t) \end{aligned} \tag{4}$$

where

$$\left.\begin{aligned} P_1 &= P \sin^2 \theta_1 \cos^2 \theta_2 = \text{power in channel 1} \\ P_2 &= P \cos^2 \theta_1 \sin^2 \theta_2 = \text{power in channel 2} \\ P_c &= P \cos^2 \theta_1 \cos^2 \theta_2 = \text{power in carrier} \\ P_{cm} &= P \sin^2 \theta_1 \sin^2 \theta_2 = \text{power in cross modulation} \end{aligned}\right\} \quad (5)$$

The cross modulation in the case of a two-channel system with square-wave subcarriers is simply the product of the two phase-shift-keyed subcarrier waveforms $s_1(t)s_2(t)$.

A block diagram of the receiver for this system is shown in Figure 1. The voltage-controlled oscillator (VCO) is in the phase-locked-loop arrangement that tracks the carrier component and produces the coherent reference signal cos $(\omega_c t + \phi)$, where ϕ is the receiver phase error. When $z(t)$ is multiplied by $\sqrt{2}$ cos $(\omega_c t + \phi)$ and the result is filtered to remove frequencies above ω_c, the result is a base-band signal of the form

$$\begin{aligned} y(t) = {} & [\sqrt{P_1}\, s_1(t) + \sqrt{P_2}\, s_2(t)] \cos \phi \\ & + [\sqrt{P_c} + \sqrt{P_{cm}}\, s_1(t)s_2(t)] \sin \phi + n_y(t) \end{aligned} \quad (6)$$

where $n_y(t)$ is the additive gaussian white noise.

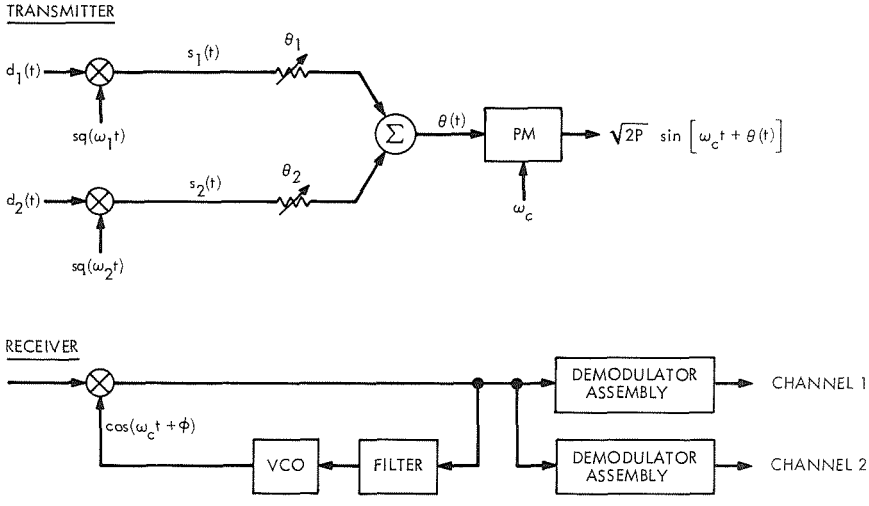

Figure 1. Conventional two-channel system

The data signals $d_1(t)$ and $d_2(t)$ are recovered from $y(t)$ by multiplying with locally generated coherent subcarriers sq $(\omega_1 t)$ and sq $(\omega_2 t)$ and filtering or bit detecting.

For a perfectly coherent system ($\phi = 0$), the efficiency of this system, measured in terms of the fraction of total power converted to data power, is

$$\eta = \frac{P_1 + P_2}{P} \tag{7}$$

From Equation 5 the total power is

$$P = P_1 + P_2 + P_c + P_{cm}$$

$$= P_1 + P_2 + P_c + \frac{P_1 P_2}{P_c} \tag{8}$$

since by Equation 5

$$P_{cm} = \frac{P_1 P_2}{P_c} \tag{9}$$

Since in the usual case, the requirement for data power in channel 1 results in $P_c < P_1$, it is clear that $P_{cm} \geq P_2$. Thus, the cross-modulation loss exceeds the power in the second (low rate) channel and indeed increases when P_c is decreased. Therefore, the total power needed is minimized when $P_{cm} = P_c = \sqrt{P_1 P_2} = P_c^*$ which corresponds to choosing $\theta_1 + \theta_2 = 90$ deg. Thus, the minimum total power is

$$P^* = P_1 + P_2 + 2\sqrt{P_1 P_2} = (\sqrt{P_1} + \sqrt{P_2})^2 \tag{10}$$

and the maximum efficiency is

$$\eta = 1 - \frac{2\sqrt{P_1 P_2}}{(\sqrt{P_1} + \sqrt{P_2})^2} \tag{11}$$

$$= 1 - \frac{2\sqrt{\alpha}}{(1 + \sqrt{\alpha})^2} \tag{12}$$

where $\alpha = P_2/P_1$ is the ratio of power in channel 2 to the power in channel 1. If both channels employ the same, or equally efficient, coding schemes, then α is also the ratio of data rates. However, in general, the lower rate channel could be more efficiently coded than the high rate link.

Referring to Equation 12 it is evident that the conventional PSK/PM two-channel system cannot be 100% efficient unless $\alpha = 0$, which corresponds to having a single channel ($P_2 = 0$). For two equal channels, i.e., $P_2 = P_1$ or $\alpha = 1$, $P_{cm} = P_c^* = P_2 = P_1$ and the efficiency is at most only

50%. It is worthwhile to observe that in this type of a system the carrier cannot be suppressed without suppressing one of the channels at the same time. Thus, power is wasted in two ways: one is in the transmission of unutilized cross-modulation power, which is larger than the low rate channel power, and the other is in the transmission of more than the required amount of unmodulated RF carrier power. These two sources of inefficiency are reduced by the Interplex modulation scheme.

Two-Channel Interplex

Let the phase-modulating signal be a linear combination of $s_1(t)$ and $s_1(t)\, s_2(t)$. The transmitted signal is

$$z(t) = \sqrt{2P} \sin [\omega_c t + \theta_1 s_1(t) + \theta_2 s_{cm}(t)] \tag{13}$$

where

$$s_{cm}(t) = s_1(t)\, s_2(t) \tag{14}$$

is the cross-modulation signal.

Again in Equation 4 the signal can be expanded trigonometrically into four terms; however, the second data channel will now be the cross-modulation term, while the new "cross modulation" will be

$$s_1(t)\, s_{cm}(t) = s_1^2(t)\, s_2(t) = s_2(t) \tag{15}$$

since $s_1^2(t) = (\pm 1)^2 = 1$.

The result is that second data channel and the cross-modulation term are interchanged, while the first data channel and the RF component remain unchanged. Therefore

$$\begin{aligned} z(t) = {} & [\sqrt{2P_1}\, s_1(t) + \sqrt{2P_{cm}}\, s_{cm}(t)] \cos(\omega_c t) \\ & + [\sqrt{2P_c} + \sqrt{2P_2}\, s_2(t)] \sin(\omega_c t) \end{aligned} \tag{16}$$

where now

$$\text{Interplex} \left\{ \begin{array}{ll} P_1 = P \sin^2 \theta_1 \cos^2 \theta_2 = P_1 \\ P_2 = P \sin^2 \theta_1 \sin^2 \theta_2 = P_{cm} \\ P_c = P \cos^2 \theta_1 \cos^2 \theta_2 = P_c \\ P_{cm} = P \cos^2 \theta_1 \sin^2 \theta_2 = P_2 \end{array} \right\} \text{Conventional} \tag{17}$$

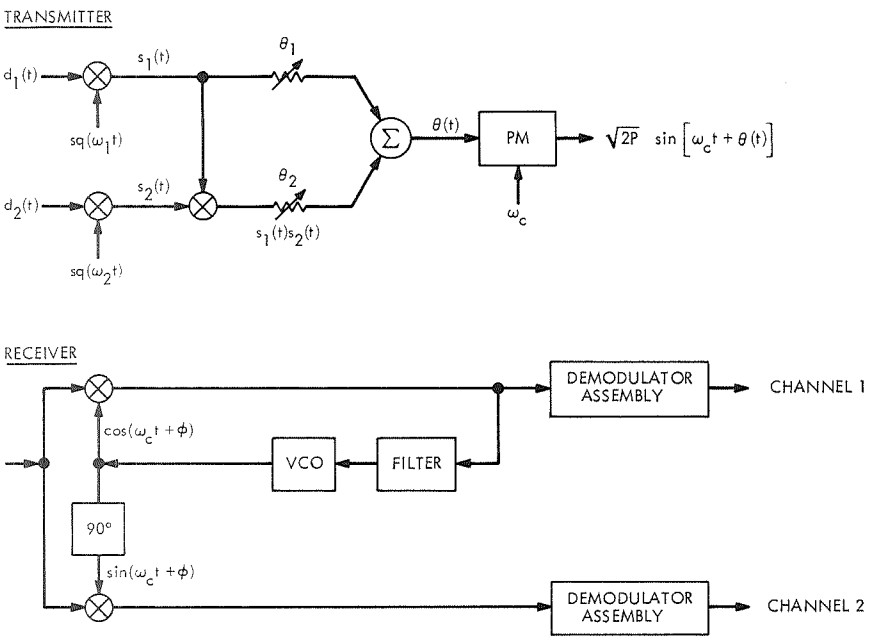

Figure 2. Interplex two-channel system

The only change relative to the conventional PSK/PM system is the use of a multiplier in the transmitter to form the product of the two binary signals $s_1(t)$ and $s_2(t)$. Since the result is also a binary signal, this requires only an *exclusive or* gate or a chopper, as shown in Figure 2. The receiver remains the same except that in addition to generating the coherent reference signal cos $(\omega_c t)$ its 90-deg phase shift sin $(\omega_c t)$ is also required. In this system $s_1(t)$ is obtained as in the conventional scheme, but $s_2(t)$ is obtained by mixing $z(t)$ with sin $(\omega_c t)$, as shown in Figure 2.

The power in the cross-modulation component

$$P_{cm} = \frac{P_c P_2}{P_1} = \alpha P_c \tag{18}$$

is now directly proportional to P_c and thus there is no advantage in transmitting more RF power than needed for tracking. Also, $P_{cm} \leq P_2$ while for the conventional scheme we had $P_{cm} \geq P_2$. In fact, of the four components, the cross modulation has the smallest power. The total power is

$$P = P_1 + P_2 + P_c + \frac{P_2}{P_1} P_c$$

$$= (1 + \alpha)(P_1 + P_c) \tag{19}$$

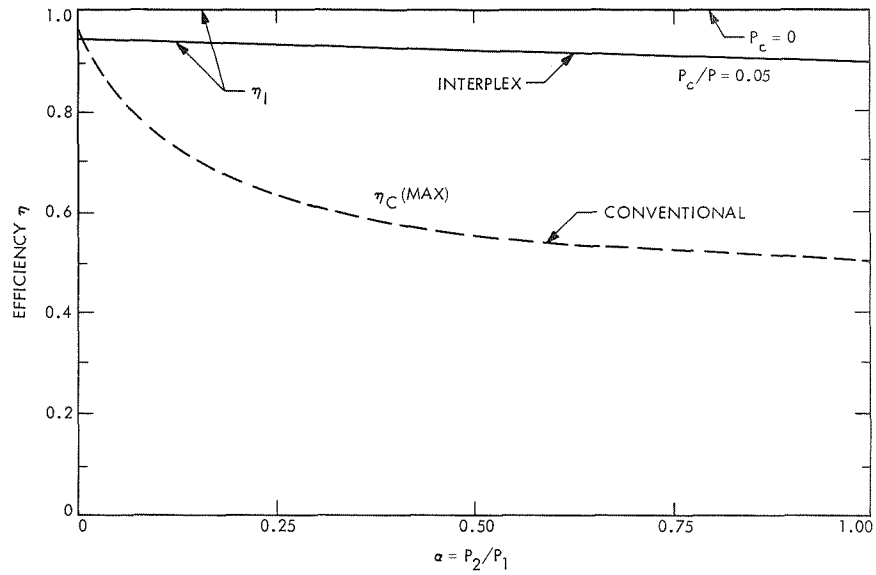

Figure 3. Data power efficiency of two-channel systems

where

$$\alpha = \frac{P_2}{P_1} = \tan^2 \theta_2 \tag{20}$$

Thus, the efficiency

$$\eta = 1 - \frac{P_c}{P_1 + P_c}$$

$$= \sin^2 \theta_1 \tag{21}$$

can be made large for all choices of α simply by taking P_c to be a small fraction of P_1, which is usually the case in practical systems. Moreover, it is now advantageous to completely suppress the carrier ($\theta_1 = 90$ deg) and achieve 100% efficiency for all ratios α. This can actually be realized because methods for tracking the phase of a suppressed carrier are theoretically feasible for the two-channel Interplex system (Reference 3).

A graph of the efficiency of the two-channel Interplex system and the conventional system as a function of α is given in Figure 3 for several values of P_c/P. Note that except for very small α the carrier power allocated by optimizing the conventional system is more than the amount required by the phase-locked receiver. The improvement gained by the Interplex scheme approaches 3 dB for the equal power case ($\alpha = 1$).

Multichannel Systems

In an N-channel PSK/PM system, the phase-modulated RF signal is still the same form as Equation 1, and the conventional modulation is given in Equation 3. However, as suggested by the two-channel Interplex system, we can let

$$\Theta(t) = \left[\theta_1 + \sum_{n=2}^{N} \theta_n \, s_n(t) \right] s_1(t) \tag{22}$$

Which of the two schemes is more efficient depends now on the power allocations required as well as on the number of channels. In general, Interplex is more efficient when N is not too large ($N \leq 4$ if the channels are equal, but larger values of N can be used when there is one high-power channel with many low-power channels). Two such cases are illustrated in Figure 4.

It is possible to show that no N-term linear combination of products of signals yields a better efficiency than either Interplex or conventional systems (Reference 4). However, if more than N terms are allowed (extended interplex) in a linear combination of signal products, then schemes are known (Reference 5) which outperform both the conventional and the simple interplex of Equation 22.

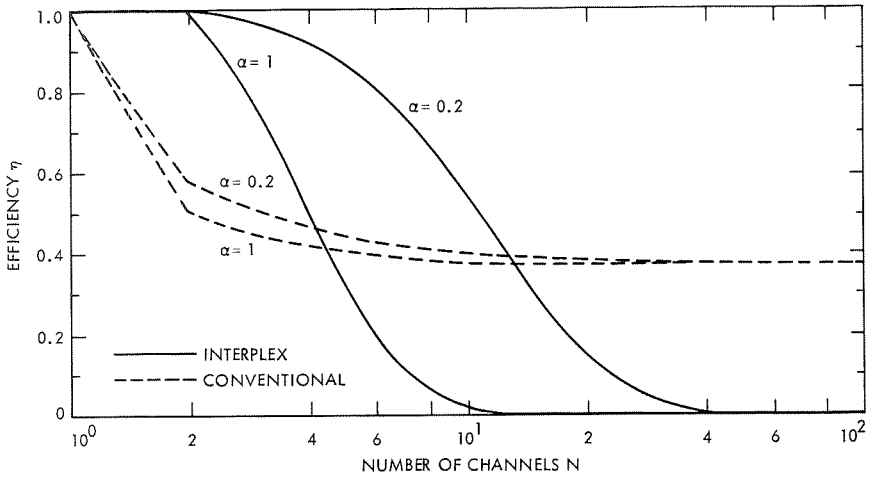

Figure 4. Efficiency for N channels with $P_k/P_1 = \alpha$, $k = 2, \cdots, N$

Conclusion

This article has presented a multichannel PSK/PM modulation scheme called Interplex which reduces cross-modulation loss and excess carrier reference power of conventional systems when the number of channels

is small. In systems with equal channels, Interplex is more efficient when the number of channels is four or less. The number of channels which can be combined efficiently via Interplex increases if there are many low-power channels and only one high-power link, as is often the case in deep space telemetry.

Although this article emphasized square-wave subcarriers, the basic ideas carry over when the subcarriers are sinusoids (Reference 6). The expressions for the various power terms will involve Bessel functions, and it is not difficult to show that Interplex offers significant improvement when N is small, as in the case of square-wave subcarriers. However, the performance with sinusoids is inferior to systems with binary waveforms.

Because of its promise of increased efficiency, further studies are being initiated to discover applicability to specific spacecraft missions. Experimental tests of the performance with simulated and actual ground and spacecraft telecommunications systems are also in progress.

References

1. Lindsey, W. C., "Design of Block-Coded Communication Systems," *IEEE Trans. Communication Technology*, Vol. COM-15, No. 4, Aug. 1967.

2. Weber, L. C., "Theory and Design of Coherent Digital Systems which Track Doppler Frequency," *Proc. IEEE*, Vol. 58, No. 6, June 1970.

3. Butman, S., and Timor, U., "Suppressed-Carrier Tracking for Two-Channel Phase Modulated Telemetry," *Proceedings of the National Electronics Conference*, Vol. 26, Dec. 1970.

4. Timor, U., "Optimum Configurations for PSK/PM Systems," in *Supporting Research and Advanced Development*, Space Programs Summary 37-66, Vol. III, pp. 33–36. Jet Propulsion Laboratory, Pasadena, Calif., Dec. 31, 1970.

5. Tausworthe, R. C., "A Boolean-Function Multiplexed Telemetry System," *IEEE Trans. Space Electronics Telemetry*, Vol. SET-9, No. 2, pp. 42–45, June 1963.

6. LaFrieda, J., "Space Station Unified Communication: Optimum Performance of Two-Channel High-Rate Interplex Systems," in *Supporting Research and Advanced Development*, Space Programs Summary 37-65, Vol. III, pp. 31–36. Jet Propulsion Laboratory, Pasadena, Calif., Oct. 31, 1970.

Calculation of Space-Charge Forces in the Analysis of Traveling-Wave Tubes

H. K. Detweiler

Telecommunications Division

A comprehensive large-signal traveling-wave tube computer program has been developed for the study and design optimization of high-efficiency space-type tubes. Studies have been made previously with a theory which employs a "deformable-disk model" (DDM) for the electron beam, but neglects RF space-charge forces in the beam. That theory was found to yield accurate predictions for tubes in which RF space-charge forces are not the predominant factor in determining device performance. However, RF space-charge effects can be very important in tubes designed for space flight applications. Thus, it is essential to include them in the computer calculations if accurate predictions of device performance are to be obtained. Expressions for the space-charge fields, appropriate to the DDM representation of the electron beam, are presented in this article and the methods used in the calculations are described.

Introduction

A comprehensive large-signal traveling-wave tube (TWT) computer program has been developed for the study and design optimization of high-efficiency space-type tubes. This program allows for a consideration of the various magnetic focusing means which are commonly employed to minimize weight and has provisions for determining the efficacy of the phase-focusing techniques used to improve efficiency.

A typical TWT configuration is schematically illustrated in Figure 1. In essence, this device consists of an electron gun, an RF circuit capable of supporting the propagation of a slow electromagnetic wave having a longitudinal electric field component, and an electron collector. Electrons are emitted from the cathode and focused into a beam in the gun region such that their motion is predominantly parallel to the axis of the slow-wave circuit. They next traverse the circuit region where an interaction takes place with the RF wave propagating on the circuit. Subsequently, the electrons enter the collector and are removed from the device. When

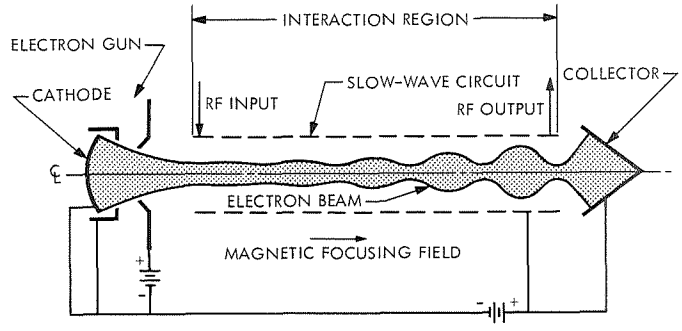

Figure 1. Schematic illustration of a traveling-wave tube

conditions are proper, the beam–wave interaction which occurs in the circuit region results in a net transfer of energy from the beam to the wave with resultant amplification of the RF signal. The increase in power carried by the circuit wave comes about as a result of a conversion of the kinetic energy of electrons in the beam. The radial circuit fields and space-charge (Coulomb) fields cause a radial perturbation of the electron trajectories during the interaction. A magnetic field is usually employed to constrain the electron beam as it passes through the circuit region; it may be a uniform axially directed field or spatially varying (e.g., periodic) field.

The performance of TWTs can be evaluated by using a nonlinear Lagrangian analysis in which the electron beam is subdivided into individual charge groups that are tracked through the interaction region. Early analyses employed a rigid-disk model for the electron beam (Reference 1). In that model, the beam is divided axially into a number of constant diameter disks of charge as illustrated in Figure 2a. The effects of radial motion of the beam electrons cannot be evaluated with such a model. Later studies (References 1 and 2) made use of a ring model in which the beam is further subdivided radially into concentric rings of charge as shown in Figure 2b. These rings were permitted to change diameter according to the radial forces acting upon them, thus accounting for the effects of radial variations. While accurate predictions of TWT performance were obtained, solutions were found to be quite costly because of the large number of charge groups required in the computer simulation. A disk model permits the use of fewer charge groups, but the modeling must be such that radial motion of the electrons and radial field variations, which have important effects in space-type TWTs, are taken into account. The "deformable-disk model" (DDM) illustrated in Figure 2c satisfies these requirements (Reference 2).

In the DDM representation of the electron beam, the disks are allowed to vary in diameter in response to the radial fields acting upon them. The radial motion of electrons contained within a disk is described

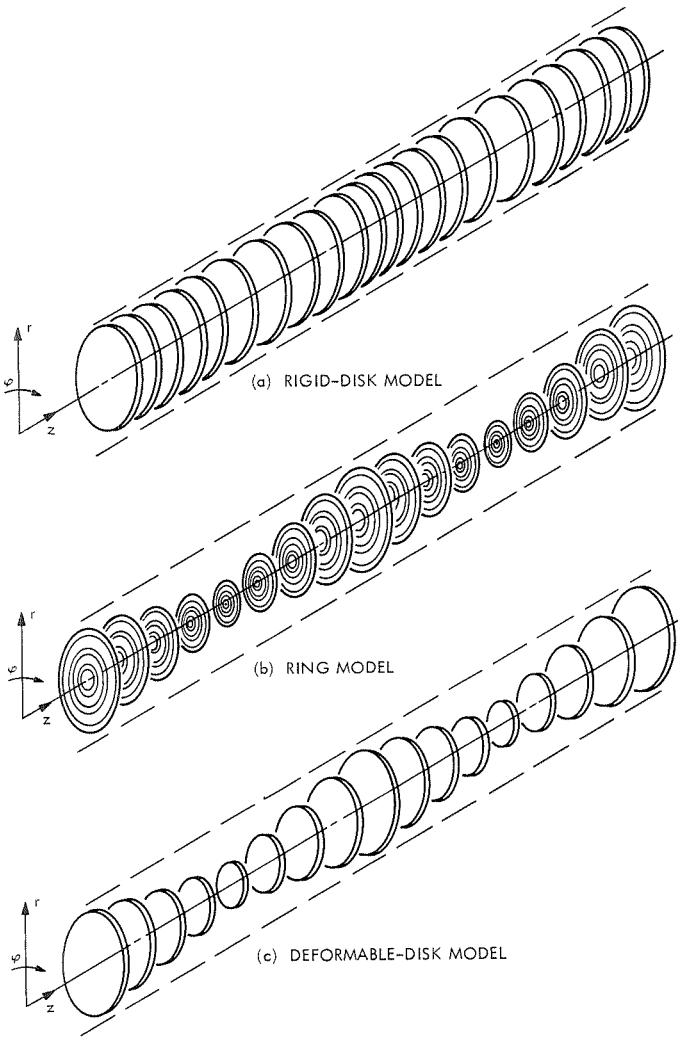

Figure 2. Electron beam models

according to laminar-flow theory. The axial motion of a disk is obtained by averaging the forces across its diameter.

Solutions to a set of nonlinear interaction equations based on the DDM representation of the electron beam, but neglecting the RF space-charge forces which result from the Coulomb interaction of the beam electrons, have been presented previously (References 2 and 3). The results show that accurate predictions are obtained for tubes in which RF space-charge forces are not the predominant factor in determining device performance. However, RF space-charge effects can be very important in the light-weight, high-efficiency traveling-wave tubes designed for space flight applications. Thus, it has been necessary to include them in the

computer calculations. Expressions for the space-charge fields, appropriate to the DDM representation of the electron beam, are presented in this article and the methods used in the calculations are described.

Expressions for the Space-Charge Fields

Explicit expressions for the space-charge fields may be obtained through the solution of Poisson's equation within the interaction region by using Green's function techniques. Rowe (Reference 1, pp. 95–97) has carried out this procedure for a ring model of the electron beam by finding the space-charge potential determined from the Green's function for a delta-function ring of charge located in a perfectly conducting drift tube. He then found expressions for the radial and axial space-charge fields by differentiating this space-charge potential function. Utilizing Rowe's results, the space-charge fields for the DDM representation of the electron beam are obtained in the following manner. The laminar-flow assumption is invoked, which permits a radial integration over all the rings of charge located at a given axial displacement plane to be performed in the ring-model space-charge-field expressions. Evaluation of the resulting equations for the radius of a disk yields the space-charge-field components at that point. The radial field component is used directly; the axial field component is averaged over the cross section of the disk.

The resulting expressions for the radial and axial space-charge-field components for the DDM representation of the electron beam are

$$E_{sc-r}(x, \Phi) = \frac{-C^2 \omega |I_0|}{u_0^2 \pi \epsilon_0 x_a^2} \int_0^{2\pi} F_{2-r}(x, x', \Phi, \Phi') \, d\Phi'_0 \tag{1}$$

and

$$E_{sc-z}(x, \Phi) = \frac{-2C^2 \omega |I_0|}{u_0^2 \pi \epsilon_0 x_a^2} \int_0^{2\pi} F_{2-z}(x, x', \Phi, \Phi') \operatorname{sgn}(\Phi - \Phi') \, d\Phi'_0 \tag{2}$$

where

$$\operatorname{sgn}(\Phi - \Phi') \triangleq \begin{cases} 1, & \text{for } \Phi > \Phi' \\ 0, & \text{for } \Phi = \Phi' \\ -1, & \text{for } \Phi < \Phi' \end{cases}$$

Table 1. Definition of symbols

a	mean radius of the circuit, m
C	gain parameter defined by $C^3 \triangleq Z_0 \lvert I_0 \rvert / 4V_0$
E_{sc-r}, E_{sc-z}	radial and axial components of the space-charge field acting on a disk of normalized radius x and phase Φ, V/m
F_{2-r}, F_{2-z}	radial- and axial-component space-charge weighting functions defined by Equations 3 and 4, respectively
I_0	dc beam current, A
$J_0(w)$	zero-order Bessel function of the first kind of argument w
$J_1(w)$	first-order Bessel function of the first kind of argument w
m	number of representative charge disks injected into the interaction region during one cycle of the RF wave
r	radial-position variable, m
u_0	average initial axial-velocity component of electrons in the beam, m/s
V_0	dc beam voltage, i.e., the dc voltage on the beam axis, V
x	normalized radius of a disk, $(C\omega/u_0)\, r$
x_a	normalized mean circuit radius, $(C\omega/u_0)\, a$
Z_0	characteristic impedance of the RF circuit (evaluated at the circuit radius) at the frequency of the wave, Ω
z	axial-distance variable, m
ϵ_0	permittivity of free space, F/m
ν_ℓ	roots of $J_0(\nu_\ell x_a) = 0$
Φ	phase position of an electron disk relative to the RF wave, rad
Φ_0	entrance phase of an electron disk, rad
ω	radian frequency of the RF wave, rad/s

The functions F_{2-r} and F_{2-z} are the space-charge weighting functions which are given by

$$F_{2-r} = \sum_{\ell=1}^{\infty} \frac{J_1(\nu_\ell x)\, J_1(\nu_\ell x')}{\nu_\ell x' \left[J_1(\nu_\ell x_a)\right]^2} \exp\left[-\nu_\ell C \left|\Phi - \Phi'\right|\right] \tag{3}$$

and

$$F_{2-z} = \sum_{\ell=1}^{\infty} \frac{J_1(\nu_\ell x)\, J_1(\nu_\ell x')}{\nu_\ell^2 x\, x' \left[J_1(\nu_\ell x_a)\right]^2} \exp\left[-\nu_\ell C \left|\Phi - \Phi'\right|\right] \tag{4}$$

where ν_ℓ is determined from the successive zeros of $J_0(\nu_\ell x_a)$, i.e., $J_0(\nu_\ell x_a) = 0$. The remaining quantities introduced in the above equations are defined in Table 1.

The space-charge weighting functions given by Equations 3 and 4 indicate the influence of a source disk of radius x' and phase Φ' on the observed disk of radius x and phase Φ. The space-charge-field components at the position of the observed disk are then evaluated by integrating over all the source disks as done in Equations 1 and 2. The radial and axial space-charge forces on the observed disk are proportional to the field components determined from these equations. This procedure can be carried out in a straightforward manner during the computer solution of the interaction equations once the radius and phase of all charge disks are known. However, the weighting functions must be evaluated many times (considering the radial and axial force on each disk due to all the disks) at each of several hundred axial displacement planes. Repeatedly evaluating them directly from Equations 3 and 4, using the actual radius and phase of each disk, would result in prohibitively long and costly computing times. Following the procedure suggested by Rowe (Reference 1) of using weighting-function tables reduces the computing time per solution appreciably and does not significantly affect the accuracy of the results.

Weighting-Function Tables

This procedure involves dividing the cross section of the interaction space into a number of annular regions (the innermost region is, of course, circular rather than annular). The weighting functions are calculated for specified values of $|\Phi - \Phi'|$ at radii corresponding to the mid-radius of each of these regions and then stored in tabular form in the computer memory. This information is used by the large-signal TWT program to evaluate the weighting functions in the manner described below, thus avoiding the need to calculate them directly so many times.

Several computer programs, separate from the DDM large-signal TWT computer program, are used to generate the weighting functions. These are used sequentially to calculate the "raw" weighting functions corresponding to the mid-radii of the space-charge regions directly from Equations 3 and 4 and then to truncate these weighting functions according to the procedure described later. The results are punched on cards which are subsequently read into the computer memory when calculations are to be made with the large-signal program. These data are in the form of tables of F_{2-r} and F_{2-z} for specified values of $|\Phi - \Phi'|$, each table corresponding to a single value of (x, x'). In the main program, the computer is instructed to scan all of the tables when particular values of x, x', Φ, and Φ' are given, select those tables (one each for F_{2-r} and F_{2-z}) corresponding to the regions within which x and x' are located, and calculate the appropriate weighting functions by interpolating (over $\Phi - \Phi'$) between the tabulated values.

It is obvious that this procedure does not yield the space-charge forces corresponding to the actual disk positions, but gives instead those forces

which would exist if each disk had a radius equal to the mid-radius of the space-charge region in which it is located. However, the resultant errors which are introduced into the calculations are not serious when a sufficient number of space-charge regions are used. This method permits a considerable reduction in computing time, which is necessary from a practical standpoint, and has given results in good agreement with experimental data. If an improvement in accuracy is desired, or required, it can be obtained by subdividing the interaction space into a larger number of space-charge regions.

Figure 3 illustrates the radial subdivision of the interaction space into seven regions, which is sufficient for most traveling-wave tubes. The values of x and x' for which the weighting functions are computed and stored are indicated in this figure, as are the radii of the space-charge-region boundaries. As mentioned previously, when looking up the weighting functions from the tables, the radius of each disk is assumed to be equal to one of these indicated values of x (or x'), regardless of its actual location within the particular region. When a disk radius crosses a region boundary, it is then assumed to be equal to the value of x (or x') for the region it has entered.

For the seven regions used in this model, there are a total of 98 weighting-function tables. Each table consists of the values of a weighting function corresponding to a single value of (x, x') at 29 distinct values of $|\Phi - \Phi'|$ which span a π range in phase. (The spacing of the $|\Phi - \Phi'|$ values was chosen as $\pi/160$ for the range 0 to $\pi/8$, $\pi/16$ for $\pi/8$ to $\pi/2$, and $\pi/4$ for $\pi/2$ to π.) Since the weighting functions are even functions of $\Phi - \Phi'$, it is only necessary to calculate and store them over a 0 to π range of $\Phi - \Phi'$ values.

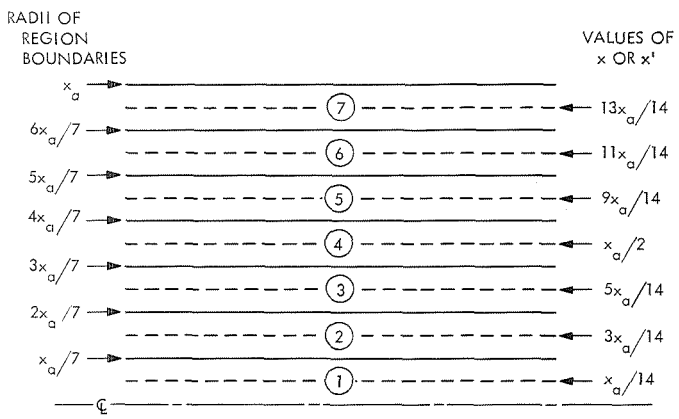

Figure 3. Division of interaction space into seven annular regions for computation of space-charge weighting functions

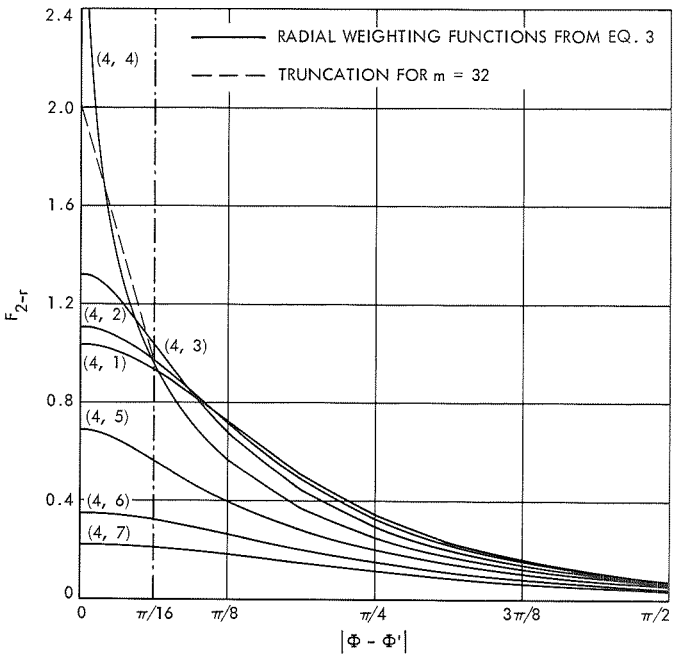

Figure 4. Radial space-charge weighting functions with $x_a/C = 1.5$, $x = x_a/2$, x' = variable

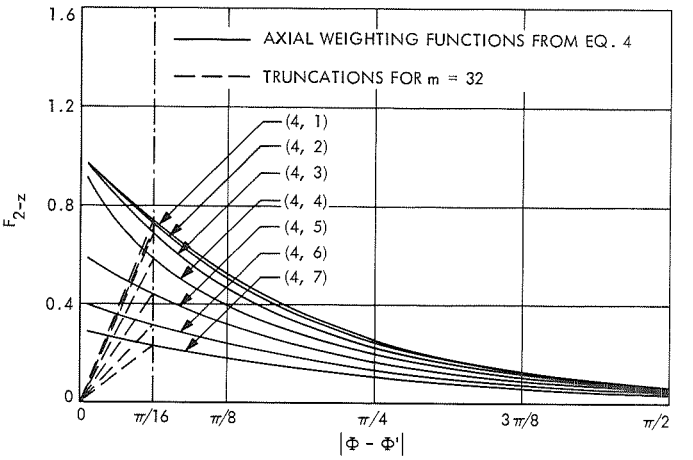

Figure 5. Axial space-charge weighting functions with $x_a/C = 1.5$, $x = x_a/2$, x' = variable

Representative radial and axial weighting functions calculated for the seven-region model using Equations 3 and 4 with $x_a/C = 1.5$ are shown by the solid curves in Figures 4 and 5. The individual weighting functions are designated by an ordered pair of numbers which correspond to the numbered space-charge regions that they represent. The first number

in a pair refers to the region in which the radius of the observed electron disk is located, while the second refers to that in which the radius of the source electron disk is located. The short-range nature of the space-charge forces is clearly indicated by these plots. As can be seen, the weighting functions are quite small at $|\Phi - \Phi'| = \pi/2$. They continue to decrease for larger phase separations and are negligibly small for $|\Phi - \Phi'| \geqq \pi$. It is this property which allows the space-charge fields to be evaluated by integrating only over a 2π phase range as done in Equations 1 and 2.

The space-charge fields calculated using the "raw" weighting functions directly are those arising from a continuous distribution of elementary charge elements, i.e., infinitesimally thin disks of charge. The discrete charge disks used in the Lagrangian analysis of the nonlinear interaction problem actually represent numerous electrons distributed over a finite volume and thus they have a finite size. The space-charge forces between these representative charge disks differ somewhat from those calculated on the basis of thin disks. However, the difference is significant only when the separation between representative charge disks becomes small enough that they, in effect, overlap. This can be taken into account approximately by truncating the weighting functions appropriately.

The method used for the axial weighting functions is to truncate them linearly to zero at $\Phi - \Phi' = 0$ from their respective values at $|\Phi - \Phi'| = 2\pi/m$, where m is the number of representative charge disks injected into the interaction region during one cycle of the RF wave. This results in a linear decrease in the axial space-charge force between two charge disks when their phase separation decreases below the initial disk spacing (which is also their effective initial phase width).

The radial weighting functions for $x = x'$ are linearly truncated from their respective values at $|\Phi - \Phi'| = 2\pi/m$ to average values at $\Phi - \Phi' = 0$ assigned according to

$$F_{2-r}(x = x')\,|_{\Phi-\Phi'=0} = \frac{m}{\pi C} \sum_{\ell=1}^{\infty} \frac{J_1(\nu_\ell x)\, J_1(\nu_\ell x')}{\nu_\ell^2 x' \,[J_1(\nu_\ell x_a)]^2} \left[1 - \exp\left(-\nu_\ell \frac{\pi C}{m}\right)\right] \tag{5}$$

This equation was derived by computing the unweighted average of F_{2-r} for $x = x'$ over the $\Phi - \Phi'$ interval from $-\pi/m$ to π/m.

The truncated weighting functions depend upon the number of charge disks per cycle of the RF wave (m) used when making the large-signal calculations. The truncations for $m = 32$ are indicated by the dashed lines in Figures 4 and 5. Although these truncation procedures certainly do not make the space-charge calculations exact, they do approximately

account for the fact that the representative charge disks are not thin disks, but instead represent a finite amount of charge distributed over a finite volume. The accuracy improves as more representative charge disks per cycle are used because they become more like the elementary charge elements for which the fields are derived and the region over which the weighting functions must be truncated is reduced. However, some sacrifice in accuracy must be accepted in order to limit the cost of the computations since the computing time increases roughly as the square of the number of charge disks employed.

Results

The accuracy of the space-charge calculations can be checked by comparing the radial forces for an unmodulated beam in Brillouin flow obtained using the weighting functions to those calculated from Gauss's law. One such calculation performed for a beam whose radius was one-half that of the circuit yielded a value of the radial space-charge force which differed from the Gauss's law value by only 1%. A computer run made with the DDM program for this case showed that the beam was perturbed by the amount expected from theoretical considerations for a 1% error in the radial space-charge force.

A number of solutions have been obtained using the DDM large-signal TWT computer program, including RF space-charge forces, for device parameters investigated previously with the TWT theory based on a ring model for the beam, a theory for which experimental verification has been obtained (Reference 2). The results were found to be in good agreement, indicating that the deformable-disk model is an adequate representation of the electron beam and that no significant errors are made in the space-charge-force calculations described here. Of particular significance is that the cost per solution using the DDM program is only about one-tenth of that required for the ring-model program.

References

1. Rowe, J. E., *Nonlinear Electron-Wave Interaction Phenomena.* Academic Press, Inc., New York, 1965.

2. Detweiler, H. K., *Characteristics of Magnetically Focused Large-Signal Traveling-Wave Amplifiers*, Technical Report 108. Electron Physics Laboratory, The University of Michigan, Ann Arbor, Oct. 1968.

3. Detweiler, H. K., and Rowe, J. E., "Electron Dynamics and Energy Conversion in O-Type Linear-Beam Devices," in *Advances in Microwaves, Vol. VI.* Academic Press, Inc., New York (to be published).

A Magnetic Tape Recorder for Long Operating Life in Space

E. Bahm

Astrionics Division

In the past, magnetic tape recorders for space applications have caused many problems. However, they are still widely used because they are the only mass memory device acceptable for spacecraft. Most of the tape recorder problems have been associated with the mechanical tape transport, while the tape recorder electronics generally achieved a satisfactory performance record. This article describes a tape recorder which uses a very simple mechanical system to transport the tape with very few possible failure modes. The simplicity of the tape transport has been achieved at the expense of added complexity of the electronic system. The resulting tape recorder is better balanced in its mechanical and electronic reliability. The test results with a feasibility model have been very encouraging.

Introduction

Outer-planet spacecraft design studies have established the need for large capacity data storage systems with a lifetime of up to 12 yr. An extensive survey of all available mass storage techniques has shown that magnetic tape recording has the highest probability of meeting the requirements of outer-planet missions until 1980. However, spacecraft and satellite tape recorders in the past have achieved a less than satisfactory performance record in spite of considerable efforts in research and development. Even though JPL has never had an inflight tape recorder failure, doubts have been expressed whether the magnetic tape recorder can ever be perfected enough to meet projected outer-planet reliability and life requirements.

A study of tape recorder failure modes in the past revealed that failures within the mechanical transport package outnumbered failures within the electronic system. However, it was not possible to identify a single part or subassembly within the transport package as being particularly failure prone. The presently used tape transports, therefore,

must be regarded as particularly suspect systems having the potential for many different failure modes.

A study of tape transports which have flown on spacecraft and satellites in the past shows that they were all complex devices with many moving parts. The reason for the complexity of the mechanical system is found in the peculiar functional and environmental requirements placed on space-borne data storage systems. One of the requirements most difficult to achieve with a tape recorder is the multiple-data rate. For certain applications in the past, data rates differed by a ratio of nearly 1:2000, which means that the highest tape speed had to be 2000 times faster than the lowest tape speed.

Several years ago JPL recognized the need for less complicated tape transports and directed a strong effort toward the development of simple, reliable tape transports. The first of these transports uses the peripheral drive principle and will be flown for the first time in 1971 on board the *Mariner* spacecraft. This machine has achieved satisfactory test results, and the confidence is high for it to set new standards for tape recorder life and reliability. However, the peripheral drive tape recorder is only one step toward the development of a truly reliable recorder, which will completely satisfy outer-planetary spacecraft requirements until 1985. Several more steps toward achieving this ultimate goal are already taking shape in the laboratory.

This article describes a data storage system utilizing a simple tape transport, of which a feasibility model has already been built. This transport uses only two rotating assemblies. None of the rotating assemblies operate at high speed. Besides the magnetic tape and the two rotating assemblies, there are no other moving parts, such as drive belts or spring tension devices. Most important, however, is the fact that this transport, due to its simplicity, is expected to have very few possible failure modes, and even those should occur with a low probability. The mechanical simplicity is achieved partly by unorthodox methods of driving and tensioning the tape and partly by elimination of the multi-speed requirement from the tape recorder while retaining it for the data storage system as a whole.

The data storage system uses a pair of solid-state buffer memories for data rate conversion. It allows the tape recorder itself to operate at a single data rate which can be selected to be compatible with the tape transport. As a consequence, the mechanical subsystem has been simplified and made more reliable at the expense of additional electronics. The advantages gained for the transport will outweigh the disadvantages caused by the introduction of additional electronics. If redundancy is used for certain circuits, such as the buffer memory, it will be possible

to further increase reliability of the data storage system. Present plans call for this tape recorder to be used for outer-planet missions.

Data Storage System Design

The data storage system will be able to store and reproduce a large amount of digital data at a variety of data rates. Figure 1 shows the data storage system in block diagram form. It uses a single-speed tape recorder and two identical serial buffer memories. The tape recorder communicates only with the buffer memories at a constant data rate, while the buffers communicate with the other subsystems at any data rate up to a certain limit R.

During recording, data is first stored in Buffer A, while Buffer B transfers its contents to the tape recorder at a sufficiently high data rate to assure the data transfer to be finished before Buffer A is filled to capacity. The tape recorder is subsequently stopped until Buffer A is full. Then the function of the two buffers is reversed, and Buffer A transfers its contents to the tape recorder while Buffer B is recording the incoming data stream. This allows the recording of a continuous data stream with a tape recorder operating in a start/stop mode. The switches indicated in Figure 1 represent logic circuits capable of properly directing the data streams and starting and stopping the tape recorder. This data storage system is described in detail in Reference 1.

The buffer memory can be a long shift register or any other semiconductor, core, or plated wire memory. The buffer capacity determines the length of a data block written on the magnetic tape. The tape recorder stops and restarts between successive data blocks during which time the tape moves at a variable speed, and no data can be recorded. This results in a gap between data blocks. The gap length is strictly a tape transport characteristic and depends upon tape speed, start time, and stop time of the transport. It is, therefore, desirable to design the tape recorder for generating short gaps. It is also desirable to use buffers with sufficient storage capacity to yield data blocks which are long compared to the gap length in order to achieve good tape utilization.

For the tape recorder described in this article, the gap length is approximately 1.27 cm (0.5 in.)[1] at a tape speed of 17.78 cm/s (7 in./s). If a linear recording density of 1575 bits/cm (4000 bits/in.) and single track recording is assumed, a pair of 8096-bit buffers would generate data blocks of 5.08 cm (2 in.). This would result in 80% of the magnetic tape being used for data recording.

[1]Where applicable, the International System of Units is stated first, followed by the customary units in parentheses. In each case, the value in parentheses represents the measured or calculated unit.

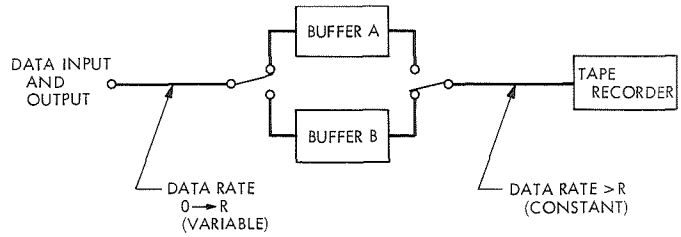

Figure 1. Data storage system

Tape Transport

The most important design requirements for the tape transport are high reliability and long life. This implies that a transport can never employ components that are basically unreliable or subject to considerable wear. Any mechanical system, however, must be satisfied with components having at least some wear and limited reliability. It is concluded, therefore, that all components and materials which are subject to wear, fatigue, or chemical instability should be known to function for 12 yr with some acceptable probability of success. Furthermore, their number should be reduced to the bare minimum.

From these rather general design rules, a number of more specific postulates can be derived:

(1) The transport mechanism shall be as simple as possible. It shall be stripped of all non-essential functions or components.

(2) Since there is no known way to construct a tape transport without bearings (which are subject to wear and fatigue), their number shall be minimized, and they shall be selected for minimum wear and fatigue. Ball bearings are generally considered most desirable for tape recorders. Their wear can be reduced to negligible values if operated at very low speed and load and assured lubrication. Material fatigue is also negligible if they are sufficiently oversized. Proper lubrication can be assured for long periods by using grease instead of oil. Again, large bearings will hold larger quantities of lubricant, and slow speed will stretch out the aging process of the lubricant.

(3) A tachometer is not an essential component and shall not be used. Playback of a prerecorded control frequency on the tape will more reliably generate a speed signal.

(4) Drive belts commonly used in tape transports can fatigue and break. There is not enough data available today to assure that belts can maintain the necessary tension over a period of 12 yr. Drive belts, therefore, shall not be used.

(5) The oxide surface of the magnetic tape should not be in sliding contact with any solid surface to minimize tape wear. If this is not possible, the total surface area sliding against the oxide and the contact pressures involved shall be minimized.

(6) Magnetic tape shall be handled as gently as possible. It, therefore, shall be guided along as few devices as possible and it shall not be wound tightly on a reel.

(7) The number of non-metallic substances shall be minimized and the chemical stability and compatibility of all materials inside the transport package shall be carefully verified.

(8) The number of connector pins feeding through the transport package shall be minimized because connector feedthroughs present a sealing hazard. This suggests incorporating part of the electronics inside the transport package, especially for multichannel recorders. All electronic components inside the transport shall be enclosed in hermetically sealed metal containers to prevent contamination of the transport by outgassing products from electronic components.

In order to satisfy Postulates 1 and 6, a coplanar reel-to-reel transport configuration is most promising. Figure 2 shows a very simple configuration. It consists of two motors with reels and tape packs on each motor shaft. It also uses two stationary tape guides, which do not touch the oxide, and a set of recording heads. All components are mounted on a precision plate.

The magnetic tape is fastened to the reel hubs. The take-up reel motor pulls the tape and winds it on its reel. The supply-reel motor

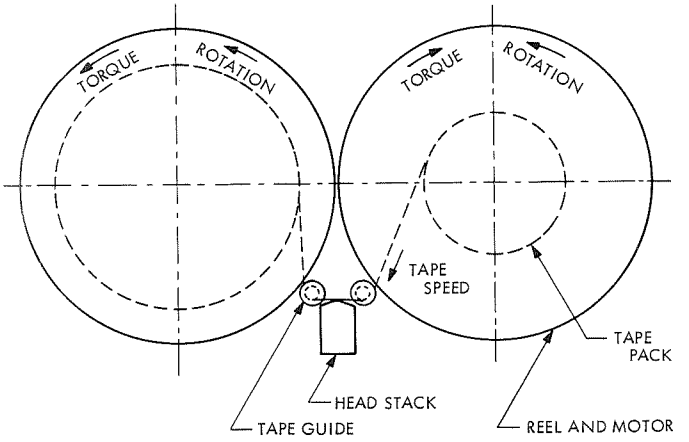

Figure 2. Two-motor tape transport

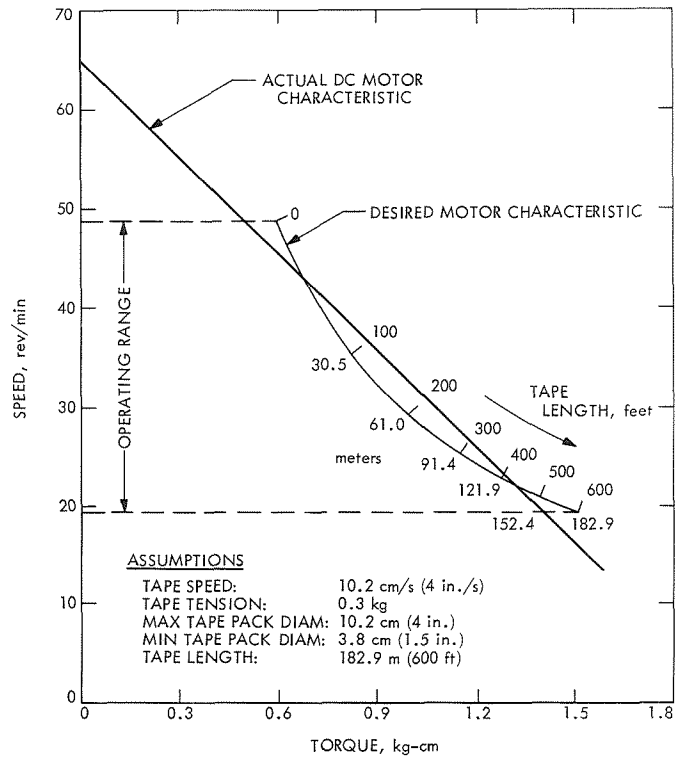

Figure 3. Take-up reel drive

develops torque in the direction opposite to the tape motion. It, therefore, pulls back on the tape, generating tape tension. While the take-up reel motor generates tape speed, the supply-reel motor provides for the necessary tape tension. The transport is symmetrical and, therefore, can drive the tape in both directions equally well. Tape speed reversal is obtained by interchanging the functions of the two motors.

During normal operation the tape speed has to be precisely constant. Since the tape pack diameter on the take-up reel changes constantly, the take-up motor speed will change throughout a tape pass. At the beginning of a tape pass, the tape pack is small and motor speed has to be high. For the same reason, motor torque is low if constant tape tension is assumed. As more tape is wound on the reel, motor speed will decrease and torque increase. Figure 3 shows the desired motor speed as a function of motor torque at constant tape tension. This hyperbolic function can be nicely approximated by the proper design of a dc motor and fine trimming with a series resistor to the motor. The take-up reel motor therefore will automatically generate approximately constant tape speed if constant tape tension is provided. Conversely, if the tape speed is held constant, tape tension will deviate from the nominal values only by a small amount.

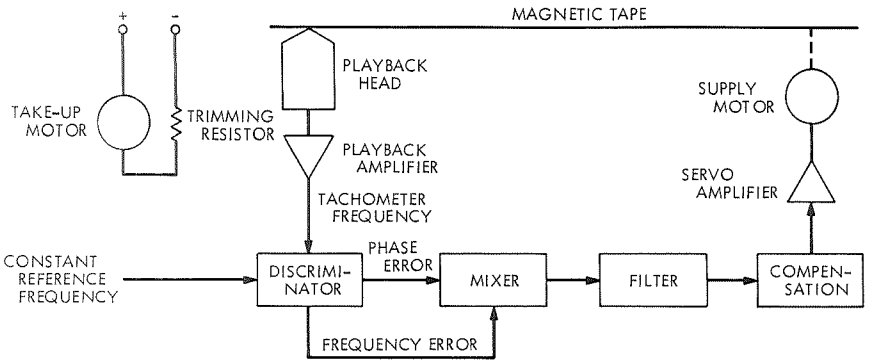

Figure 4. Drive electronics for two-motor tape transport

The supply motor generates tape tension and is being servo-controlled to regulate the tape tension in such a way that constant tape speed results. This is being done with a phase-lock servo, which compares a voltage derived from the tape with the voltage output of a stable oscillator. The tape signal is pre-recorded on a precision laboratory recorder on one track over the full length of tape. The tape recorder itself has only playback capability on this track. The frequency derived from this track is directly proportional to the tape speed.

The phase-lock servo has two feedback loops, as shown in Figure 4. One loop generates an error signal proportional to the difference of the frequencies of the two voltages. This error signal is filtered and amplified and will subsequently be used to drive the supply motor. It will regulate motor current in such a manner as to cause the tape frequency to become approximately equal to the stable reference frequency. A second feedback loop will generate an error signal proportional to the phase difference between the two voltages. Its error signal will take over the job of regulating the motor current after the first loop has brought the tape frequency within capture range of the second loop.

This double-loop servo will feed just enough electrical power into the supply motor to cause tape speed to be precisely constant at all times. The speed is determined by the external reference frequency and the density at which the tape frequency has been recorded.

A very important feature of this tape transport is the fact that the tape tension will disappear as soon as the recorder is turned off. This is very desirable because it will prevent tape-to-head stiction during prolonged periods of inoperativeness. However, the tape has to be prevented from falling off the tape guides or throwing a loop. For this purpose, the tape reels contain flanges which are more precise than for most other tape recorders. The tape is allowed to fall down on the flanges after the recorder has been turned off. Throwing a loop is prevented by using a

magnetic brake in each motor. The motors, always running at slow speed, will be stopped by the brake in a very short time.

The brake consists of a powerful permanent magnet and a weak permanent magnet which is magnetized by the powerful magnet. As one magnet rotates and the other remains stationary, the weak magnet is continually re-magnetized by the powerful magnet. This causes high hysteresis losses because the coercivity is not negligible. These losses result in a drag torque which opposes the rotation and can be made constant in the time and speed domain. Past experience indicates the required brake torque will be on the order of 0.07 to 0.36 kg-cm (1 to 5 oz-in.), depending upon the reel diameter. In a practical motor, the powerful magnet is identical with the dc motor magnet and the weak magnet takes the place of the soft iron yoke ring. Therefore, the braking action is obtained by simply selecting a proper magnetic material for the yoke ring. No geometric changes of the motor design are required.

In order to obtain good damping characteristics, the motor is designed with relatively high brake torque. This generates more tape tension than desired. The brake torque of the supply motor must therefore be reduced by driving the motor in the direction of the tape travel with very little torque. Referring again to Figure 4, the double-loop servo generates an error signal that is amplified to drive the supply motor. The servo amplifier is biased so as to drive the supply motor with low torque in the direction of tape travel if the error signal is zero. If the tachometer frequency begins to fall below the stable reference frequency, a positive error signal is generated and drives the supply motor with more torque. As the supply motor generates more torque against the brake, the pull on the tape will be relaxed somewhat, which allows the free running take-up motor to accelerate and increase the tachometer frequency. Tape speed is thus stabilized by regulating the net shaft torque of the braked supply motor.

As mentioned before, the tape transport will be operated in a start/stop mode. Because both motors run at very slow speeds and exhibit a substantial drag torque, the tape transport stops very fast. It also starts very fast because of the high starting torque of the dc motor.

The general reliability and operating life of an incrementally operated tape transport is often questioned. Increased wear of bearings, tape, and heads is claimed. This may be true to some degree. Several years ago, JPL developed an incremental tape recorder (Reference 2) which was subjected to extensive life testing at high repetition rates. This machine accumulated approximately 10^9 start/stop cycles before it was finally put in storage. No bearing, head, or tape load was ever exchanged. This test

did not preclude the possibility of accelerated wear within an incrementally operated tape transport, but showed that a properly designed machine can perform a large number of start/stop cycles.

The motors of the tape transport of Figure 2 run in the vicinity of 100 rev/min for a typical space application. If operated continuously for 1 yr at 100 rev/min, a bearing will accumulate approximately 50 million revolutions. With proper lubrication this will not wear out an originally healthy bearing. It is not clear, however, if proper lubrication is assured during a stop/start transition. Some degradation of the lubricating process must be assumed. Measurements of electrical current conductivity between inner and outer race ways of ball bearings indicate that some separation of the metallic surfaces is accomplished even when the bearing is stopped. This leads to the conclusion that at least some lubrication occurs all through the stop/start cycle.

Concluding Remarks

The tape recorder described in this article is currently being developed for future outer-planet missions. A feasibility model has been built and operated successfully for more than 1000 h without failure.

References

1. Slaughter, D. W., "A Multi-Instrument Data Conditioning, Storage and Retrieval System for Planetary Spacecraft," in *Supporting Research and Advanced Development*, Space Programs Summary 37-27, Vol. IV, pp. 101–107. Jet Propulsion Laboratory, Pasadena, Calif., June 30, 1964.
2. Bahm, E., "Tape Recorder With Incremental Playback Capabilities," in *Supporting Research and Advanced Development*, Space Programs Summary 37-40, Vol. IV, pp. 170–174. Jet Propulsion Laboratory, Pasadena, Calif., Aug. 31, 1966.

Lunar Traverse Missions

R. G. Brereton and J. D. Burke

Advanced Technical Studies Office

R. B. Coryell

Project Engineering Division

L. D. Jaffe

Space Sciences Division

The results of recent JPL studies on Lunar Traverse Missions are compared with the announced characteristics of the Soviet Lunokhod 1 rover, delivered to the Moon by the *Luna 17* spacecraft in November 1970. Except for some differences in emphasis among the scientific experiments, the Lunokhod mission is quite similar to those recommended in the JPL studies.

Introduction

It has long been recognized (References 1–3) that mobility is essential for exploring lunar and planetary surfaces. For the past several years, scientists and engineers at JPL have been working on various aspects (References 4–15) of lunar and planetary roving missions to prepare for the time when it would be possible to carry instrument payloads on mobile vehicles controlled from Earth. When the Soviet spacecraft *Luna 17* delivered an automated rover, Lunokhod 1 (Figures 1, 2, and 3), to the Moon, this prospect became a reality. In this article, we compare the results of our studies with the announced data (References 16 and 17) on the Lunokhod mission, whose main objectives appear to be almost exactly those recommended for an early mission by the JPL study teams.

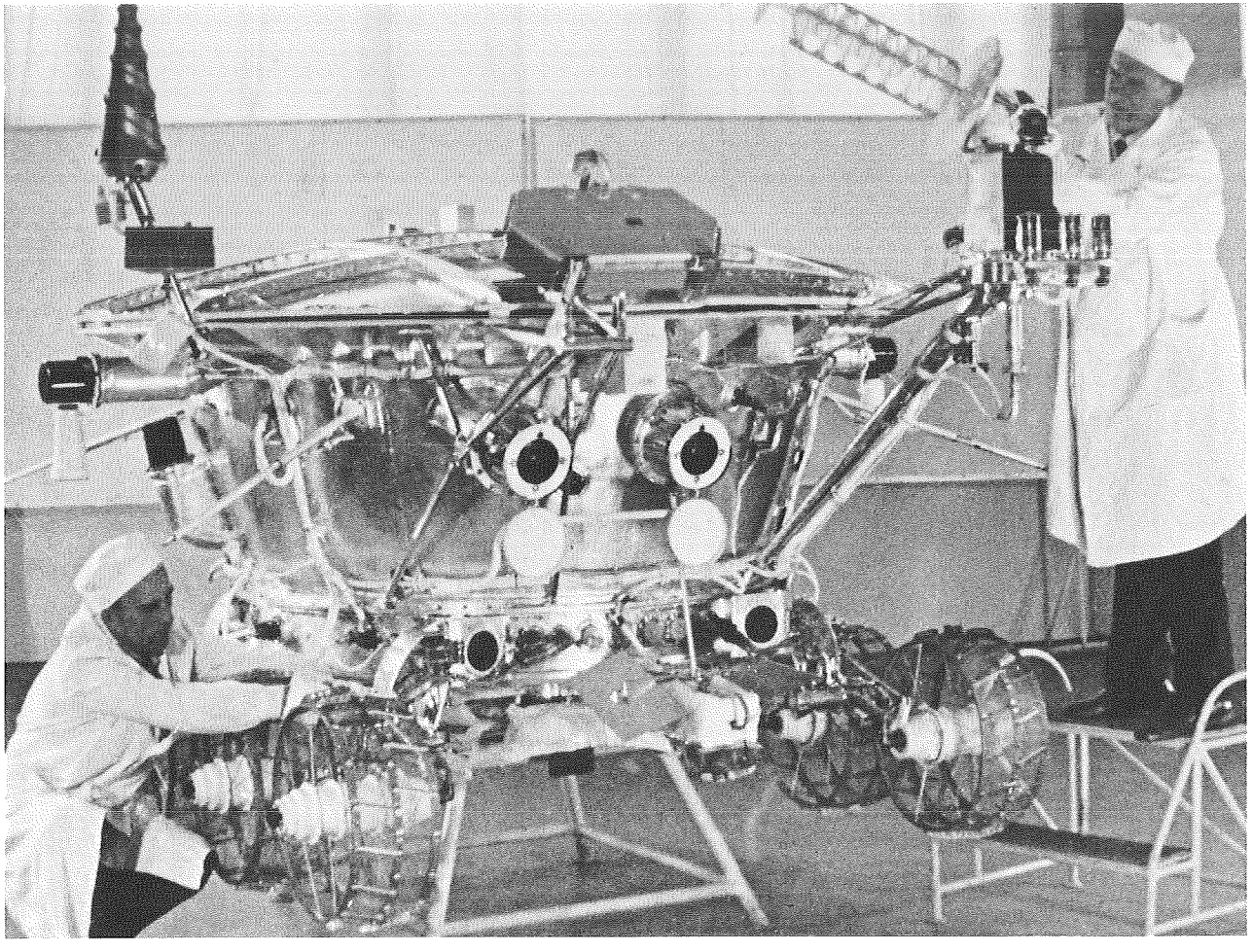

Figure 1. Soviet Moon Car Lunokhod 1 in testing-assembling building prior to flight of *Luna 17*. Two TV cameras are at front; dark cylindrical objects at sides are telephotometer (facsimile) cameras, two scanning in vertical plane and two scanning slightly below horizontal (photo credit: TASS from SOVFOTO)

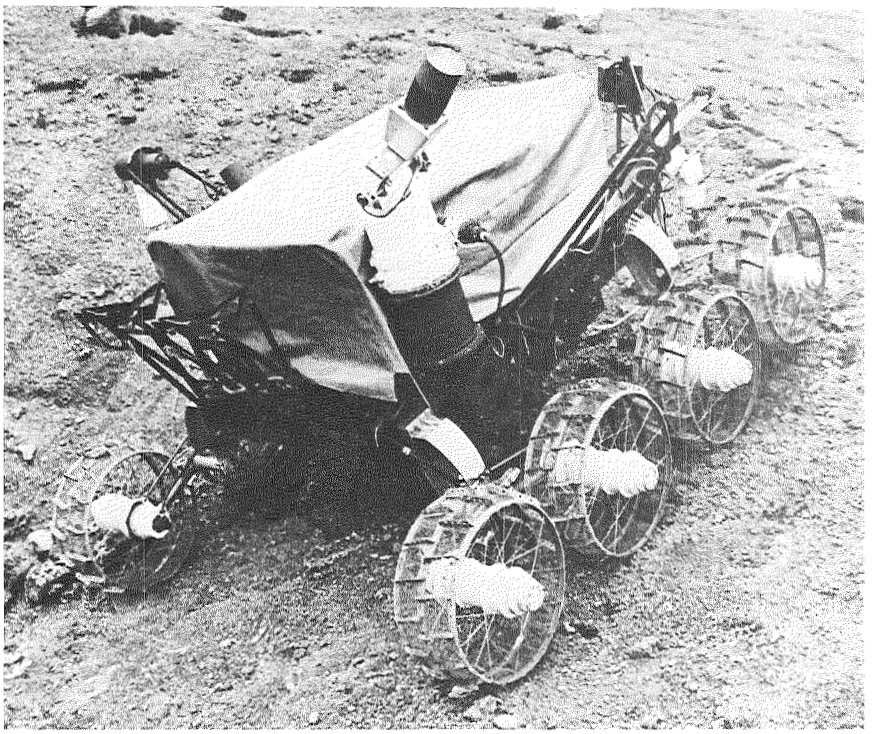

Figure 2. Working parts of Lunokhod 1 pictured during test at Lunodrome (photo credit: TASS from SOVFOTO)

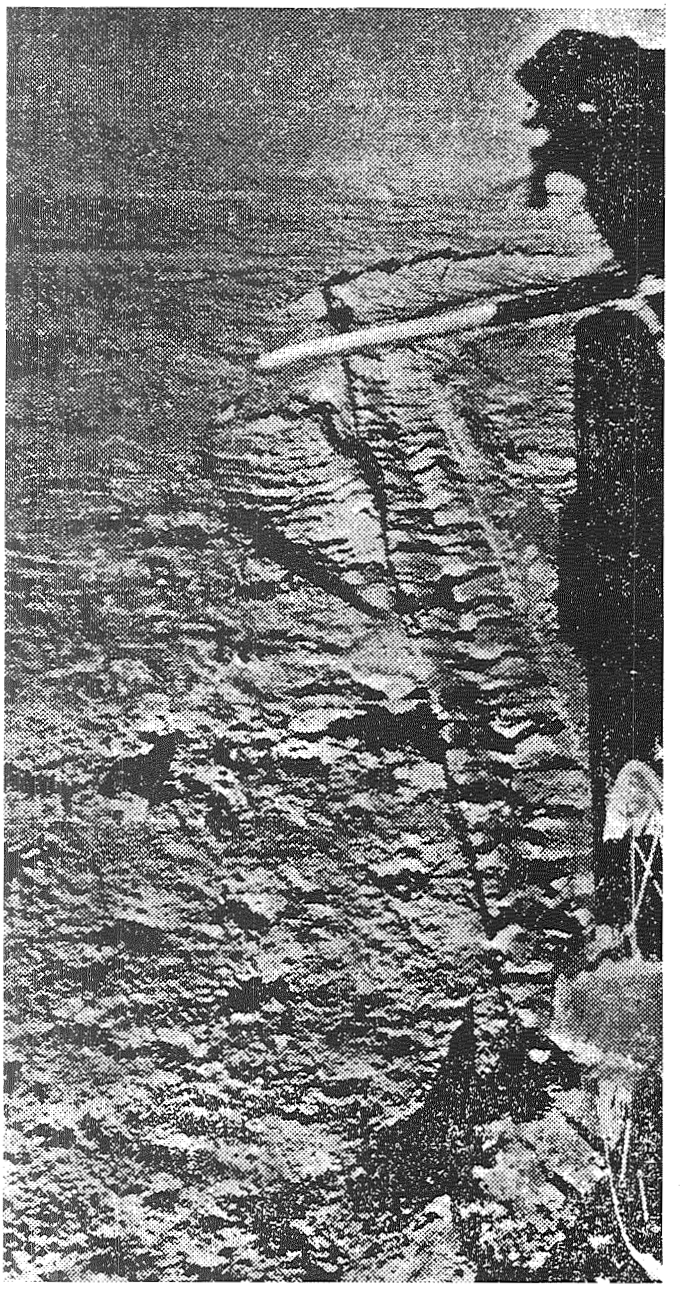

Figure 3. Image of lunar surface from Lunokhod telephotometer (facsimile) camera showing one wheel and tracks left by vehicle (photo from Pravda)

Lunar Scientific Objectives

The major goal of lunar scientific exploration remains to determine the origin and history of the Moon and its implications for the origin and history of the Earth and the solar system. In the JPL studies, the following major questions, whose answers would meet this goal, were posed:

(1) Initial source of bulk lunar material:

  (a) Where was its location in the circumsolar cloud?

  (b) What was its pre-accretion chemical evolution?

(2) Mode of accumulation of the Moon:

  (a) Did it accumulate by independent accretion or by derivation from the Earth?

  (b) What was the time of accumulation, i.e., the elapsed time since the effective cessation of nucleosynthesis?

  (c) What was the duration of accumulation?

(3) Post-accretion lunar history:

  (a) What are the major Moon-wide geological processes and their energy sources?

  (b) What is their chronology?

The following prerequisite investigations, whose results would provide a basis for answering the major questions, were suggested:

(1) The distribution of surface chemical and isotopic compositions, including trace elements.

(2) The internal structure and petrology and the physical state of the interior.

(3) The present thermal regime including internal temperature distribution, surface heat flow, and abundances and distribution of heat sources.

(4) The correlation among morphology, composition, and chronology of surface material.

At post-*Apollo* time, it is unlikely that satisfactory answers to these questions will have been obtained. Automated rovers will not provide direct answers to the major questions and prerequisite investigations, but they can provide a unique means for step-by-step accumulation of essential data.

Essential Rover Measurements

The optimum geological measurements for rovers are those that characterize surface geological units in terms of morphology and composition and those of a geophysical nature that permit determination of deeper subsurface structure. Desirable parameters for measurement are those that are likely to vary over a long traverse in a way that can be correlated with lithology or morphology as deduced from *Apollo* and *Lunar Orbiter* photographs. Undesirable parameters are those that are likely to vary randomly over the whole surface or with time.

Based on the above criteria, a few relatively simple, fundamental surface measurements are essential for a traverse over previously unexplored lunar regions. These measurements are practical and likely to be most feasible within the expected constraints of a rover program.

(1) *Imaging.* There should be:

(a) Continuous high-resolution imaging in the visible spectrum, ideally in color and with spatial resolution of at least 0.1 mm in close-up mode.

(b) Monoscopic and stereoscopic panoramic views, and magnified views of selected outcrops as well as of individual rock fragments.

(c) Search for bedrock, and delineation of field relations of rock units; e.g., distinction of intrusive and depositional contacts. It is important that the undisturbed regolith surface be viewed *in situ* and close up, since return of undisturbed surface material to Earth is difficult.

(2) *Characterization of surface material.* The bulk elemental composition of surface materials must be found using some easily measured parameters. Gamma-ray spectrometry and spectral reflectance are possible techniques.

(3) *Elemental and mineralogical characterizations.* Detailed elemental and mineralogical characterization via neutron activation and X-ray diffraction methods can be made on selected specimens at sites of special interest (Reference 18).

(4) *Geophysical measurements* should be made as follows:

(a) Gravity profiles (discrete measurements with spacing depending on observed variations).

(b) Heat flow measurements with sensitivity sufficient for detecting fluxes of 4.184×10^{-6} J-s^{-1}-cm^{-2} (10^{-6} cal-s^{-1}-cm^{-2}).[1] This is a difficult measurement and may not be feasible for an automated rover.

(c) Seismic measurements using deployed surface charges as well as natural events.

Instrumentation Techniques

Imaging

The essential instrument for guiding and navigating a rover and for observing and sampling the lunar surface to achieve the above objectives is an imaging system. The technical requirements on image quality and telecommunications bandwidth are such that two types of cameras are needed; the total number of cameras may be more than two, for redundancy or for convenience in achieving desired fields of view. The two types of cameras and their functions are listed in Table 1.

Table 1. Rover imaging systems

JPL imaging sensor requirement	Function	Lunokhod design
Television		
Near field ahead and to sides	Guidance (driving) and sampling	Two forward-looking TV cameras, one wide-angle, one narrow-angle
Close-up with magnification	Sample investigation	
Far field	Magnified views of distant features	
Photofacsimile		
Horizon panorama	Landmark navigation and geologic reconnaissance	Four telephotometers, two scanning horizon, two scanning fore and aft through vertical
Near field	Geologic observation and redundancy with TV	

On the basis of *Surveyor* and *Apollo* observations, a survey of opinions among scientists, and laboratory tests, some conclusions of the JPL imaging studies were:

(1) Stereo is desirable but not essential in the near field for driving.

[1]Where applicable, the International System of Units is stated first, followed by the customary units in parentheses. In each case, the value in parentheses represents the measured or calculated unit.

(2) Magnification and manipulation, i.e., changing illumination and viewing angles, are essential for the close-up petrologic analysis of samples, and a large depth-of-field is highly desirable.

(3) Color is not needed for the panoramic or near-field lunar views, but is highly desirable in the magnified close-ups.

The Lunokhod system apparently does not include color and is not optimized for stereo, and sample collection and manipulation are not provided. However, the system does have the main characteristic recommended; namely, it uses television for the near-field and driving functions (where speed of display is more important than picture quality) and photofacsimile for panoramic reconnaissance (where high resolution and high photometric, dimensional, and spectral fidelity are desired), with some overlap for redundancy.

Orientation and Navigation

On the basis of studies, laboratory experiments, and field tests (Reference 7) in the California desert (Figures 4 and 5), the JPL teams devised a practical scheme for landmark navigation and evaluated the requirements for rover imaging and other sensors as well as ground displays and command functions. Table 2 summarizes these results.

Table 2. Rover navigation

JPL requirement	Function	Lunokhod design
Horizon landmark identification and bearings	Position fix	Telephotometers, i.e., photofacsimile cameras
Sun, Earth azimuth and elevation	Orientation, rough position	Telephotometers and antenna servo positions
Vehicle pitch, roll and heading relative to local vertical	Orientation and hazard limit sensing	Tilt sensors in telephotometer field of view, and sun or shadow azimuth
Distance travelled	Dead reckoning	Odometer on extra towed wheel, sensors on driving wheels
Direction travelled	Dead reckoning	Unknown

It is not obvious from announcements made to date that the Lunokhod uses or needs a landmark navigation system, since it moved only a few kilometers and then returned to its landing point. It does have all the other functions listed in Table 2. The JPL studies (Reference 19) showed that landmark navigation is the only practical way to attain the accuracy needed on a traverse of hundreds of kilometers. Competing techniques such as inertial or celestial navigation require more instrumentation and

Figure 4. Lunar navigation and geological sampling field simulation test. Operators inside sealed van view terrain and samples via TV

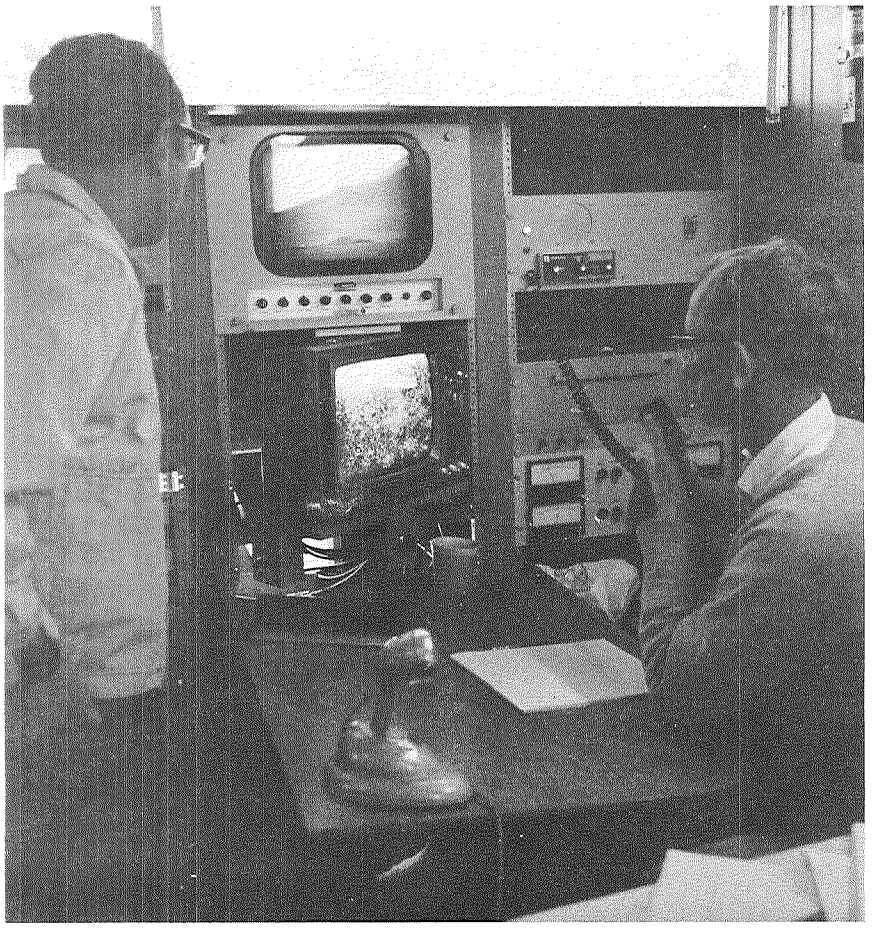

Figure 5. Interior of van (simulating Earth-based control center) showing pictorial displays: (top) panorama, (center) magnified view of part of horizon, (bottom) close-up of samples

do not offer comparable performance for the particular missions considered feasible early in a surface exploration program. Of course, the use of landmarks is limited to areas previously mapped, for example, by lunar orbiters; this is not a severe constraint for the missions studied.

Other Scientific Instruments

In addition to the television and facsimile instruments and sample manipulation device, it was concluded (as mentioned above and in References 5, 7, and 8) that early lunar rovers should carry limited instrumentation for measuring surface chemical composition, e.g., an X-ray diffractometer/spectrometer, and also, if possible, geophysical instruments such as a gravimeter and precision ranging transponder.

The Lunokhod payload includes an X-ray spectrometer that can be deployed to the lunar surface to measure soil composition, a pene-

trometer-and-vane device for measuring soil bearing and shear strength, and radiation detectors for determining the lunar radiation background environment. In addition, the rover carries an X-ray telescope aimed near the zenith with sensitivity in the 2×10^{-10} to 10×10^{-10}-m (2 to 10-Å) region and about a 52-mrad (3-deg) field of view, and a French-built laser retroreflector.

The Soviet spacecraft therefore is attempting experiments closely similar to those recommended for U.S. automated rovers for initial reconnaissance, but with relatively less emphasis on lunar mineral sampling and internal properties, and relatively more emphasis on radiation and astronomical measurements. Though the precision ranging experiment was recognized in the JPL studies as very important in the study of Earth–Moon motions, it was not recommended that the rover carry a laser reflector, since this appeared more suitable as a fixed-site experiment. The Lunokhod retroreflector, used intermittently now while the rover is stopped at night, can presumably continue in use after the machine finally stops moving.

The Lunokhod design appears adequate for every critical function, with the exception that the long traverse mission requires an order of magnitude higher average speed than Lunokhod 1 has demonstrated. The interaction among rover power supply and demand, lunar lighting, time needed for experiments, safe driving speeds, and ground-system duty cycle was worked out in the JPL studies. The resulting conclusion was that night survival, as now achieved by Lunokhod 1, would be essential because at best only a few tens of kilometers could be covered during each lunar day. The slow progress of Lunokhod 1 may be in part due to power-system limitations, but also probably reflects a proper degree of caution at the start of this new class of missions on the Moon.

References

1. *Exploration of the Moon, the Planets, and Interplanetary Space*, Report 30-1. Edited by A. R. Hibbs. Jet Propulsion Laboratory, Pasadena, Calif., Apr. 30, 1959.

2. *Lunar Exploration-Strategy for Research 1969-1975*, National Academy of Sciences, Space Science Board, Washington, D. C., Sept. 1969.

3. *1967 Summer Study of Lunar Science and Exploration, Santa Cruz, Calif.*, NASA SP-157. Edited by W. N. Hess. National Aeronautics and Space Administration, Washington, 1967.

4. Adams, J. B., et al., "Strategy for Scientific Exploration of the Terrestrial Planets," *Reviews of Geophysics*, Vol. I, pp. 623–661, Aug. 1969.

References (contd)

5. Brereton, R. G., "The Objectives for Roving Vehicles in a Lunar Exploration Program," in *Supporting Research and Advanced Development*, Space Programs Summary 37-52, Vol. III, pp. 253–255. Jet Propulsion Laboratory, Pasadena, Calif., Aug. 31, 1968.

6. Brereton, R. G., "Lunar Mission Planning," in *Supporting Research and Advanced Development*, Space Programs Summary 37-54, Vol. III, pp. 230–238. Jet Propulsion Laboratory, Pasadena, Calif., Dec. 31, 1968.

7. Brereton, R. G., and Howard, E. A., "Comments on Geological Observations From an Automated Vehicle (Field Test)," in *Supporting Research and Advanced Development*, Space Programs Summary 37-55, Vol. III, pp. 258–263. Jet Propulsion Laboratory, Pasadena, Calif., Feb. 28, 1969.

8. Brereton, R. G., "An Active Seismic Experiment for an Automated Roving Vehicle," in *Supporting Research and Advanced Development*, Space Programs Summary 37-56, Vol. III, pp. 213–216. Jet Propulsion Laboratory, Pasadena, Calif., Apr. 30, 1969.

9. Brereton, R. G., "Lunar Surface Gravity Investigations," in *Supporting Research and Advanced Development*, Space Programs Summary 37-57, Vol. III, pp. 1–6. Jet Propulsion Laboratory, Pasadena, Calif., June 30, 1969.

10. Brereton, R. G., Ulrich, G. E., and Dahlem, D. H., "Imaging and Sampling Requirements for an Automated Lunar Roving Vehicle," in *Supporting Research and Advanced Development*, Space Programs Summary 37-60, Vol. III, pp. 1–3. Jet Propulsion Laboratory, Pasadena, Calif., Dec. 31, 1969.

11. Brereton, R. G., "Geophysical Experiments for the Manned Portion of a Lunar Roving Vehicle Mission," in *Supporting Research and Advanced Development*, Space Programs Summary 37-61, Vol. III, pp. 1–4. Jet Propulsion Laboratory, Pasadena, Calif., Feb. 28, 1970.

12. Brereton, R. G., et al., "A Miniaturized Absolute Gravimeter for Terrestrial, Lunar, and Planetary Research," in *Supporting Research and Advanced Development*, Space Programs Summary 37-62, Vol. III, pp. 1–5. Jet Propulsion Laboratory, Pasadena, Calif., Apr. 30, 1970.

13. Brereton, R. G., "Automated Post-Missions for the Lunar Roving Vehicle," in *Supporting Research and Advanced Development*, Space Programs Summary 37-62, Vol. III, pp. 5–8. Jet Propulsion Laboratory, Pasadena, Calif., Apr. 30, 1970.

References (contd)

14. Strand, J. N., "Tests of Instruments Proposed for the Scientific Payload of a Lunar Rover," in *Supporting Research and Advanced Development*, Space Programs Summary 37-62, Vol. III, pp. 15–18. Jet Propulsion Laboratory, Pasadena, Calif., Apr. 30, 1970.

15. Brereton, R. G., "Mission Objectives for a Lunar Roving Vehicle," in *Supporting Research and Advanced Development*, Space Programs Summary 37-64, Vol. III, pp. 1–3. Jet Propulsion Laboratory, Pasadena, Calif., Aug. 31, 1970.

16. *Soviet-Bloc Research in Geophysics, Astronomy, and Space*, JPRS 51991, No. 242. Joint Publications Research Service, Dec. 15, 1970.

17. *Soviet-Bloc Research in Geophysics, Astronomy, and Space*, JPRS 52087, No. 243. Joint Publications Research Service, Dec. 30, 1970.

18. Nash, D. B., *Sampling of Planetary Surface Solids for Unmanned In Situ Geological and Biological Analysis: Strategy, Principles, and Instrument Requirements*, Technical Report 32-1225. Jet Propulsion Laboratory, Pasadena, Calif., Nov. 15, 1967.

19. Lewis, R. A., "A Computerized Landmark Navigator: Development and Test Plan," in *Supporting Research and Advanced Development*, Space Programs Summary 37-65, Vol. III, pp. 1–2. Jet Propulsion Laboratory, Pasadena, Calif., Oct. 31, 1970.

Author Index With Abstracts

Supporting Research and Advanced Development, Space Programs Summary 37-66, Vol. III, pp. 187–189, December 31, 1970

For abstract, see Moacanin, J.

AKYUZ, F. A.

A04 VISCEL—A General-Purpose Computer Program for Analysis of Linear Viscoelastic Structures: User's Manual

F. A. Akyuz and E. Heer

Technical Memorandum 33-466, Vol. I, February 15, 1971

A general-purpose computer program (VISCEL) for the solution of linear viscoelastic structures is described. VISCEL is an extension of the program ELAS, which has been developed for the in-core solution of linear equilibrium problems of structural mechanics of limited size (approximately 500–600 unknowns) and with a minimum of computer time (3–4 min in the IBM 7094, Model I). The standard features and capabilities of ELAS have been preserved. The solution is obtained by means of the displacement method and the finite element technique, together with the use of incremental time steps and a synchronized material property concept. The solution is obtained at the end of each time step as incremental and accumulative displacements and stresses. The recursive equations expressing the property of the material with memory have been incorporated in the computations. Also, a scheme which employs constant time steps in the logarithmic scale can be used to minimize the number of computations resulting from the accumulative effects of the material memory.

Almost any structure with linear elastic material properties and continuous structures with linear viscoelastic material properties can be handled by VISCEL. The program is written in FORTRAN IV language for use in 32K IBM 7094 machines with a standard hardware configuration having a minimum of 15 system units. The source deck consists of about 8600 cards; the object deck contains about 1500 cards. The physical program VISCEL is available from the Computer Software Management and Information Center (COSMIC), the NASA agency for the distribution of computer programs.

ALLEY, C. O.

A05 *Surveyor* Final Report—Principal Scientific Results From the *Surveyor* Program

L. D. Jaffe, C. O. Alley (University of Maryland),

S. A. Batterson (Langley Research Center), E. M. Christensen, S. E. Dwornik (NASA Headquarters), D. E. Gault (Ames Research Center), J. W. Lucas, D. O. Muhleman (California Institute of Technology), R. H. Norton, R. F. Scott (California Institute of Technology), E. M. Shoemaker (U.S. Geological Survey), R. H. Steinbacher, G. H. Sutton (University of Hawaii), and A. L. Turkevich (University of Chicago)

Icarus: Int. J. Sol. Sys., Vol. 12, No. 2, pp. 156–160, March 1970

For abstract, see Jaffe, L. D.

ANDERSON, T. O.

A06 Integrated-Circuit Packaging System

T. O. Anderson and D. Bodkin

The Deep Space Network, Space Programs Summary 37-66, Vol. II, pp. 29–31, November 30, 1970

This article describes a model of an integrated-circuit packaging system for use as the Deep Space Network standard. The basic technique used was first developed in the construction of a video data compressor reported earlier. The advanced model of this packaging scheme has been adopted, with minor modifications, for the prototype of the telemetry data decoder assembly for *Pioneer F* to be used throughout the Deep Space Instrumentation Facility.

ARNETT, J. C.

A07 Evaluation of 26- to 32-AWG Wire for Outer Planet Mission Applications

J. C. Arnett

Supporting Research and Advanced Development, Space Programs Summary 37-65, Vol. III, pp. 142–147, October 31, 1970

Tests were performed establishing dimensional, physical, electrical, and handling characteristics of small-gage wire for outer planet mission applications. Environmental tests in vacuum and low temperature were made to evaluate exposure-related degradation effects. The most promising candidates for volume- and weight-limited electronic packaging applications on future spacecraft were selected.

ASHLOCK, J. C.

A08 Applying Nonadaptive Transversal Filters to Playback of Digital Tape Recorder Signals

J. C. Ashlock

Supporting Research and Advanced Development, Space Programs Summary 37-65, Vol. III, pp. 148–152, October 31, 1970

Previous work leading to an attractive detector for use in bit detection of digital tape recorder signals is reviewed. It is shown that the design of the matched and transversal filters in this detection scheme can be approached from more than one point of view; two of these approaches are examined in detail and experimentally compared for the case of 10,000 bits/in./track. Detector waveforms and bit error rate data are given.

BACK, L. H.

B01 Changes in Heat Transfer From Turbulent Boundary Layers Interacting With Shock Waves and Expansion Waves

L. H. Back and R. F. Cuffel

AIAA J., Vol. 8, No. 10, pp. 1871–1873, October 1970

This article discusses heat transfer from turbulent boundary layers in supersonic flows where changes in surface curvature can produce shock waves and expansion waves (e.g., corner flows) or where shock waves generated elsewhere in the flow impinge on the boundary layer. Heat-transfer measurements are presented in these interaction regions, and a rather simple method involving the integral form of the energy equation is used to estimate the change in heat transfer that is observed. The prediction is then compared to other experimental data obtained at shock impingement locations.

B02 Relationship Between Temperature and Velocity Profiles in a Turbulent Boundary Layer Along a Supersonic Nozzle With Heat Transfer

L. H. Back and R. F. Cuffel

AIAA J., Vol. 8, No. 11, pp. 2066–2069, November 1970

The relationship between measured temperature and velocity profiles is presented for an accelerating, turbulent boundary-layer flow of air through a cooled, convergent divergent nozzle. Boundary-layer measurements were made upstream, along the

convergent section, and near the end of the divergent section where the flow is supersonic. These measurements span a relatively large flow speed range, the inlet and exit Mach numbers being 0.06 and 3.7, respectively. The operating conditions were such that the boundary layer remained essentially turbulent; i.e., laminarization did not occur in the accelerating flow. The wall was cooled externally, the ratio of wall-to-stagnation temperature being 0.43–0.56.

The measurements are also related to current interest in the structure of very-high-speed turbulent boundary layers. For example, measurements are often made near the exit of supersonic nozzles with wall cooling. The present measurements provide information on the upstream history of the accelerating flow and on the relationship of upstream profiles to the profile near the nozzle exit.

BALL, J. E.

B03 The *Mariner VI* and *VII* Flight Paths and Their Determination From Tracking Data

H. J. Gordon, D. W. Curkendall, D. A. O'Handley, N. A. Mottinger, P. M. Muller, C. C. Chao, B. D. Mulhall, V. J. Ondrasik, S. K. Wong, S. J. Reinbold, J. W. Zielenback, J. K. Campbell, R. T. Mitchell, J. E. Ball, W. G. Breckenridge, T. C. Duxbury, and R. E. Koch

Technical Memorandum 33-469, December 1, 1970

For abstract, see Gordon, H. J.

BAMFORD, R. M.

B04 Equivalent Spring-Mass System for Normal Modes

R. M. Bamford, B. K. Wada, and W. H. Gayman

Technical Memorandum 33-380, February 15, 1971

Since the lower resonant frequencies are of interest in most structural problems, a significant reduction of independent variables is possible by the use of the normal modes of structural subsystems as independent variables. This memorandum describes a technique that can be used to generate equivalent spring-mass models for the normal modes of a structural subsystem when the generalized mass matrix and resonant frequencies are available. Where modal truncation is employed, the residual mass matrix is used to preserve the correctness of the rigid-body mass properties. Applications of the modeling technique and the residual mass matrix are discussed.

BANES, R.

B05 Heat-Sterilizable Battery Development [August–September 1970]

R. Banes

Supporting Research and Advanced Development, Space Programs Summary 37-65, Vol. III, pp. 80–81, October 31, 1970

In the program to develop heat-sterilizable silver–zinc cells, production model cells of the 70-A-h primary design have been characterization-tested and are being evaluated under space flight conditions. The goals for the 25-A-h cells capable of ninety 60% cycles have been attained and this development has been discontinued. The development of the four hundred 60% cycle cell has been modified to provide for more experimental work before testing to simulate flight profiles.

BARENGOLTZ, J. B.

B06 Jupiter's Electron Dose Calculations on Metal Oxide Semiconductor Structures

S. P. Li and J. B. Barengoltz

Supporting Research and Advanced Development, Space Programs Summary 37-66, Vol. III, pp. 166–170, December 31, 1970

For abstract, see Li, S. P.

BATELAAN, P. D.

B07 Improved RF Calibration Techniques: PDS Cone Waveguide/ Polarimeter Calibrations

P. D. Batelaan, B. Seidel, and R. B. Lyon

The Deep Space Network, Space Programs Summary 37-66, Vol. II, pp. 61–63, November 30, 1970

The waveguide losses and reflection coefficient measurements are presented for the polarization diversity S-band (PDS) cone. Tests were also conducted to verify the polarimeter capabilities of the PDS cone. Results indicated excellent agreement with theory.

BATTERSON, S. A.

B08 *Surveyor* Final Report—Principal Scientific Results From the *Surveyor* Program

L. D. Jaffe, C. O. Alley (University of Maryland),

S. A. Batterson (Langley Research Center), E. M. Christensen, S. E. Dwornik (NASA Headquarters), D. E. Gault (Ames Research Center), J. W. Lucas, D. O. Muhleman (California Institute of Technology), R. H. Norton, R. F. Scott (California Institute of Technology), E. M. Shoemaker (U.S. Geological Survey), R. H. Steinbacher, G. H. Sutton (University of Hawaii), and A. L. Turkevich (University of Chicago)

Icarus: Int. J. Sol. Sys., Vol. 12, No. 2, pp. 156–160, March 1970

For abstract, see Jaffe, L. D.

BAUMAN, A. J.

B09 Isolation and Characterization of Coal in Antarctic Dry-Valley Soils

A. J. Bauman, E. M. Bollin, G. P. Shulman, and R. E. Cameron

Antarc. J. U.S., Vol. V, No. 5, pp. 161–162, September–October 1970

The Allison wet combustion method applied to soils from two Antarctic dry-valley sites showed that they contained 0.1–0.7% "organic carbon." However, solvent extraction and combined pyrolysis/gas chromatography/mass spectrometry unexpectedly showed no indication of the free or kerogen-bound carbon compounds usually present in these soils. Heavy-liquid density flotation and oxidative differential thermal analysis were then applied to the samples, both before and after digestion with HF, in an effort to elucidate the nature of the anomalous "Allison carbon." Sub-surface samples were collected at the junction of McKelvey and Victoria Valleys, 1.5 km west of Lake Vida, and in Wheeler Valley above Miller Glacier, opposite Killer Ridge. The results of the investigation are presented.

BAUMERT, L. D.

B10 Evolution and Coding: Inverting the Genetic Code

L. D. Baumert and D. Cantor (University of California, Los Angeles)

Supporting Research and Advanced Development, Space Programs Summary 37-65, Vol. III, pp. 41–44, October 31, 1970

The amino acid sequences of proteins together with a presumed evolutionary model have been used to specify the genetic nucleo-

tide sequences of these proteins. Sample results are presented. The number of possible nucleotide sequences for human cytochrome c has now been reduced by a factor of 1.4×10^8.

BERMAN, P. A.

B11 Effects of Lithium Doping on the Behavior of Silicon and Silicon Solar Cells

P. A. Berman

Technical Report 32-1514, February 1, 1971

The Jet Propulsion Laboratory is sponsoring investigations into the applicability of lithium doping for improvement of silicon solar cell radiation resistance. This report discusses the author's interpretation of the results of the industry programs, in particular the efforts to improve cell processing techniques and the experiments conducted to improve the theoretical understanding of the action of lithium in irradiated silicon and silicon solar cells. The major conclusions reached as a result of the investigations are presented, and suggestions for future work are made. It appears that lithium-doped solar cells can be fabricated which exhibit (recovered) efficiencies significantly in excess of efficiencies associated with state-of-the-art N/P solar cells after exposure to high fluences of 1-MeV electrons and neutrons.

B12 Effects of High-Temperature, High-Humidity Environment on Silicon Solar Cell Contacts

R. K. Yasui and P. A. Berman

Technical Report 32-1520, February 15, 1971

For abstract, see Yasui, R. K.

B13 Activation Energy of Annealing in Lithium-Doped Silicon

P. A. Berman

Supporting Research and Advanced Development,
Space Programs Summary 37-65, Vol. III, pp. 68–69,
October 31, 1970

A very strong point of agreement among investigators is that the activation energy associated with neutralization of radiation-induced defects in lithium-doped silicon (whether the defects be caused by 1-MeV electrons, 30-MeV electrons, or neutrons) is very close to the activation energy associated with diffusion of lithium in silicon and gives strong support to the theory that neutralization of radiation-induced defects is a result of lithium

diffusion to the defect sites. The experimental results and analysis performed by the various investigators leading to this conclusion are summarized.

BERWIN, R.

B14 RF Techniques: Superconducting Magnet for X-Band Maser

R. Berwin and P. Dachel

Supporting Research and Advanced Development, Space Programs Summary 37-65, Vol. III, pp. 45–47, October 31, 1970

The current experimental development of an X-band superconducting magnet is reported. The advantages of using the superconducting magnet as an integral part of the traveling wave maser in the cloud-cycle refrigerator are examined in relation to the presently used external permanent magnets.

BODKIN, D.

B15 Integrated-Circuit Packaging System

T. O. Anderson and D. Bodkin

The Deep Space Network, Space Programs Summary 37-66, Vol. II, pp. 29–31, November 30, 1970

For abstract, see Anderson, T. O.

BOLLIN, E. M.

B16 Isolation and Characterization of Coal in Antarctic Dry-Valley Soils

A. J. Bauman, E. M. Bollin, G. P. Shulman, and R. E. Cameron

Antarc. J. U.S., Vol. V, No. 5, pp. 161–162, September–October 1970

For abstract, see Bauman, A. J.

BOUNDY, R. A.

B17 Fabrication Development of Lightweight Honeycomb-Sandwich Structures for Extraterrestrial Planetary Probe Missions

R. G. Nagler and R. A. Boundy

Technical Report 32-1473, January 15, 1971

For abstract, see Nagler, R. G.

BOWERS, M. T.

B18 On the Relative Proton Affinity of Argon and Deuterium

M. T. Bowers (University of California, Santa Barbara) and
D. D. Elleman

J. Am. Chem. Soc., Vol. 92, No. 25, pp. 7258–7262,
December 16, 1970

In mixtures of Ar and D_2 at high pressures, the following ion–molecule reaction scheme is observed:

$$D_2^+ + D_2 \rightarrow (D_3^+)^* + D \quad (1)$$

$$(D_3^+)^* + (D_2)^2 \rightarrow (D_3^+)\dagger + D_2 \quad (2)$$

$$(D_3^+)^* + Ar \rightarrow ArD^+ + D_2 \quad (3)$$

$$(D_3^+)\dagger + Ar \not\rightarrow ArD^+ + D_2 \quad (4)$$

$$ArD^+ + D_2 \rightarrow D_3^+ + Ar \quad (5)$$

$(D_3^+)^*$ has of the order of 2 eV of energy according to the experiments of Leventhal and Friedman. $(D_3^+)\dagger$ is the lowest vibrational state obtainable by collision of $(D_3^+)^*$ with D_2. The results given here suggest that $(D_3^+)\dagger$ is *not* the ground state but has at least 1 and possibly 2 quanta of vibrational energy (i.e., 10–20 kcal/mol). From pressure dependence studies, it is shown that a maximum of three collisions is needed to moderate all $(D_3^+)^*$ to $(D_3^+)\dagger$. From reaction 5, $PA(D_2) > PA(Ar)$. From threshold-double-resonance experiments on reaction 4, $PA(D_2)^+ \cong PA(Ar) + 7$ kcal/mol, with an uncertainty of ± 5 kcal/mol. $PA(D_2)\dagger$ is the energy required to remove D^+ from $(D_3^+)\dagger$. The intrinsic proton (or deuteron) affinity of D_2, $PA(D_2)$, is felt to be 10–20 kcal/mol larger than that of $PA(D_2)\dagger$.

BRANDT, R. D.

B19 Computer Refreshed Display

R. D. Brandt

Supporting Research and Advanced Development,
Space Programs Summary 37-65, Vol. III, pp. 16–18,
October 31, 1970

This article describes the design philosophy and hardware implementation of a computer refreshed display which has a repetition rate of approximately 28 fields per second. The display is used to view video information that has been processed by a digital computer. The display greatly reduces the time necessary to yield the end process because it allows the operator to view the intermediate processes while the "job" is being run on the computer.

BRATENAHL, A.

B20 Experimental Study of Magnetic Flux Transfer at the Hyperbolic Neutral Point

A. Bratenahl and C. M. Yeates

Phys. Fluids, Vol. 13, No. 11, pp. 2696–2709, November 1970

Reported here is a laboratory study of a plasma flow process sometimes referred to as the severing and reconnecting of magnetic field lines at a hyperbolic or X-type neutral point. It is found that a hyperbolic pinch develops at the neutral point, resulting in plasma compression. The ohmic electric field of the pinch current enables field line reconnection to take place through resistive diffusion. The reconnection rate is substantially increased by a reduction in the size of the pinch region effected by flow adjustment through pairs of stationary slow-mode shocks in a manner similar to that deduced and described by Petschek. Strong evidence is presented for this wave-dominated configuration. However, it is found that the pinch current becomes progressively concentrated at the neutral point and along the shock loci until eventually a critical current density is reached, marked by a sudden and large anomalous increase in resistivity as predicted by Friedman and Hamberger. At this point the wave-assisted diffusion mode is terminated and there is observed: (1) a cutoff in pinch current, (2) a large increase in the electric field, (3) a corresponding increase in reconnection rate, and (4) the generation of a system of large-amplitude fast-mode waves. The waves, bearing evidence of the onset of plasma turbulence, effect a rapid and gross redistribution of flux among the cells defined by the separatrix and blow the slow-mode shocks off downstream. The increased electric field raises the possibility of rapid magnetic energy dissipation through acceleration of particles to high energy.

BRECKENRIDGE, W. G.

B21 The *Mariner VI* and *VII* Flight Paths and Their Determination From Tracking Data

H. J. Gordon, D. W. Curkendall, D. A. O'Handley, N. A. Mottinger, P. M. Muller, C. C. Chao, B. D. Mulhall, V. J. Ondrasik, S. K. Wong, S. J. Reinbold, J. W. Zielenback, J. K. Campbell, R. T. Mitchell, J. E. Ball, W. G. Breckenridge, T. C. Duxbury, and R. E. Koch

Technical Memorandum 33-469, December 1, 1970

For abstract, see Gordon, H. J.

BRERETON, R. G.

B22 Lunar Elevation Correction for Gravity Measurements

R. G. Brereton

Supporting Research and Advanced Development, Space Programs Summary 37-66, Vol. III, pp. 1–3, December 31, 1970

This article reviews some of the corrections that will be required for lunar surface gravity observations. Because the lunar Bouguer correction is smaller than its terrestrial counterpart, elevation control for lunar gravity surveys can be reduced by a factor of 2 for most field operations.

BUFFINGTON, J. P.

B23 Post-Detection Recorder Evaluation

J. P. Buffington

The Deep Space Network, Space Programs Summary 37-66, Vol. II, pp. 136–137, November 30, 1970

The difficulties in reproducing baseband telemetry recordings have been attributed to time displacement error. This article discusses a method of comparing tape transports with good accuracy. The results of pragmatic tests are presented on a particular tape transport having very low time displacement error on which phase-modulated telemetry data are recorded and subsequently demodulated, using a phase-locked loop subcarrier demodulator assembly.

BURNS, T. L.

B24 DSS Upgrades for *Mariner* Mars 1971

T. L. Burns

The Deep Space Network, Space Programs Summary 37-66, Vol. II, pp. 114–115, November 30, 1970

During the period July through December 1970, the deep space stations (DSSs) committed to the *Mariner* Mars 1971 Project have undergone or are scheduled to undergo reconfiguration in preparation for the mission. The reconfiguration consists of block upgrades of subsystems, rearrangement of the control and communications rooms to provide space for new equipment, and major maintenance on older equipment. The work performed on each subsystem is described in this article.

CALLAHAN, P. S.

C01 DSN Progress Report for November–December 1970: Probing the Solar Plasma With *Mariner* Radio Metric Data, Preliminary Results

P. F. MacDoran, P. S. Callahan, and A. I. Zygielbaum

Technical Report 32-1526, Vol. I, pp. 14–21, February 15, 1971

For abstract, see MacDoran, P. F.

CAMERON, R. E.

C02 Soil Microbial and Ecological Investigations in the Antarctic Interior

R. E. Cameron, R. B. Hanson, G. H. Lacy, and F. A. Morelli

Antarc. J. U.S., Vol. V, No. 4, pp. 87–88, July–August 1970

In November–December 1969, 10 soil samples were collected aseptically from the surface to the depth of permafrost at five sites on a traverse west of Coalsack Bluff (approximately 84° 15′S, 162°E). Another 14 samples were collected from five sites on a traverse north of the Bluff. During the latter traverse, a camp site was established for 1 wk just below the west end of "Coalsack Bluff West," and environmental measurements were made continually or every 3 h for soil and/or microclimatic characteristics. Air sampling for microflora was also undertaken on four sides of the camp site. The results of the investigations are briefly discussed.

C03 Microbiological Analyses of Snow and Air From the Antarctic Interior

G. H. Lacy, R. E. Cameron, R. B. Hanson, and F. A. Morelli

Antarc. J. U.S., Vol. V, No. 4, pp. 88–89, July–August 1970

For abstract, see Lacy, G. H.

C04 Isolation and Characterization of Coal in Antarctic Dry-Valley Soils

A. J. Bauman, E. M. Bollin, G. P. Shulman, and R. E. Cameron

Antarc. J. U.S., Vol. V, No. 5, pp. 161–162, September–October 1970

For abstract, see Bauman, A. J.

CAMPBELL, J. K.

C05 **The *Mariner VI* and *VII* Flight Paths and Their Determination From Tracking Data**

H. J. Gordon, D. W. Curkendall, D. A. O'Handley, N. A. Mottinger, P. M. Muller, C. C. Chao, B. D. Mulhall, V. J. Ondrasik, S. K. Wong, S. J. Reinbold, J. W. Zielenback, J. K. Campbell, R. T. Mitchell, J. E. Ball, W. G. Breckenridge, T. C. Duxbury, and R. E. Koch

Technical Memorandum 33-469, December 1, 1970

For abstract, see Gordon, H. J.

CANTOR, D.

C06 **Evolution and Coding: Inverting the Genetic Code**

L. D. Baumert and D. Cantor (University of California, Los Angeles)

Supporting Research and Advanced Development, Space Programs Summary 37-65, Vol. III, pp. 41–44, October 31, 1970

For abstract, see Baumert, L. D.

CAPEN, C. F.

C07 **Observational Patrol of Mars in Support of *Mariners VI* and *VII***

C. F. Capen

Technical Report 32-1492, June 15, 1970

A summary of the physical appearance of Mars during the 1969 apparition is presented for use in planetary research and in support of the *Mariner VI* and *VII* missions. An account is given of the seasonal meteorological activity and surface conditions before and during the *Mariner* encounters. Diameter measurements of the regressing south polar cap are tabulated. For comparison with *Mariner* pictures, a current Regional Mars Map 1969 of longitudes 240 to 100 deg (inclusive) was prepared from high-resolution observations (0.1 to 0.2 arc sec) acquired during late Martian summer. Selected photographs and drawings are reproduced for reference with the text.

CAPUTO, R. S.

C08 **Review of Radioisotope Thermoelectric Generators for Outer Planet Missions**

R. S. Caputo

Supporting Research and Advanced Development, Space Programs Summary 37-66, Vol. III, pp. 70–75, December 31, 1970

The nominal performance of current radioisotope thermoelectric generator (RTG) programs is reviewed and performance predictions are made for long-term operations based on the most recent module data. The RTG programs that are considered for service of up to 5 or 7 yr are *Transit* (Isotec), *Pioneer* (SNAP 19-TAGS), and SNAP 27 Integral, which all use a lead telluride thermoelectric material; the multi-hundred watt (MHW) silicon germanium generator is considered for missions as long as 12 yr. The MHW system, using the advanced technology fuel capsule for near-term missions or the less-developed Helipak heat source for later missions, holds the greatest potential for future RTG applications.

CARTER, K. R.

C09 DSN Progress Report for November–December 1970: SFOF Configuration Control

K. R. Carter

Technical Report 32-1526, Vol. I, pp. 122–123, February 15, 1971

This article describes the need for and design of a Space Flight Operations Facility (SFOF) configuration control system based on the highly dynamic nature of the facility and the unique, critical requirements levied upon it by multiple and simultaneous flight projects supported by various JPL functional organizations. Only hardware changes are discussed.

CASPERSON, R.

C10 DSS 61/63 Facility Modifications and Construction

R. Casperson, G. Kroll, and L. Kushner

The Deep Space Network, Space Programs Summary 37-66, Vol. II, pp. 154–158, November 30, 1970

DSS 61/63 (Robledo Deep Space Station) is being reconfigured to an 85-ft-diam/210-ft-diam antenna complex. This article describes the facility modifications and construction necessary to accomplish this reconfiguration.

CHADWICK, H. D.

C11 Signal Design for Single-Sideband Phase Modulation

H. D. Chadwick

Supporting Research and Advanced Development,
Space Programs Summary 37-66, Vol. III, pp. 54–58,
December 31, 1970

A single-sideband phase-modulated (SSB-PM) signal is a function of both a time function and its Hilbert transform. In this article a set of time functions is derived whose Hilbert transform contains minimum energy outside of a specified time interval. These functions are useful for reducing the intersymbol interference problem that arises when SSB-PM signals are detected with a correlation detector.

CHAHINE, M. T.

C12 Inverse Problems in Radiative Transfer: Determination of Atmospheric Parameters

M. T. Chahine

Technical Report 32-1351, Pt. II (Reprinted from *J. Atmos. Sci.*, Vol. 27, No. 6, pp. 960–967, September 1970)

It is shown that the relaxation method for inverse solution of the full radiative transfer equation leads to unique temperature profiles. Apart from its attractive simplicity, the algorithm is also capable of discriminating between noise and valid information without any need for data smoothing. A set of new inverse problems is formulated for the determination of the concentration of absorbing gases in an atmosphere, the extent and height of clouds, and surface elevations. The proposed methods are illustrated by examples in the earth's atmosphere for the region of the 4.3-μ CO_2 band.

CHAO, B. T.

C13 Thermal Modeling of Spacecrafts With Imperfect Models

B. T. Chao (University of Illinois)

Supporting Research and Advanced Development,
Space Programs Summary 37-65, Vol. III, pp. 136–137,
October 31, 1970

Theoretical requirements for thermal scale modeling of unmanned spacecrafts are well understood at the present time. Difficulties arise in practice mainly because of their structural complexity. This study explored a concept of model testing, utilizing models that do not completely satisfy the similitude criteria. The concept is based upon representing the error states in a multi-dimensional euclidean space, separating the errors

into positive and negative groups, and extrapolating the error states to the zero error condition.

CHAO, C. C.

C14 Tracking System Analytic Calibration Activities for the *Mariner* Mars 1969 Mission

B. D. Mulhall, C. C. Chao, N. A. Mottinger, P. M. Muller, V. J. Ondrasik, W. L. Sjogren, K. L. Thuleen, and D. W. Trask

Technical Report 32-1499, November 15, 1970

For abstract, see Mulhall, B. D.

C15 DSN Progress Report for November–December 1970: A Cursory Examination of the Sensitivity of the Tropospheric Range and Doppler Effects to the Shape of the Refractivity Profile

L. F. Miller, V. J. Ondrasik, and C. C. Chao

Technical Report 32-1526, Vol. I, pp. 22–30, February 15, 1971

For abstract, see Miller, L. F.

C16 The *Mariner VI* and *VII* Flight Paths and Their Determination From Tracking Data

H. J. Gordon, D. W. Curkendall, D. A. O'Handley, N. A. Mottinger, P. M. Muller, C. C. Chao, B. D. Mulhall, V. J. Ondrasik, S. K. Wong, S. J. Reinbold, J. W. Zielenback, J. K. Campbell, R. T. Mitchell, J. E. Ball, W. G. Breckenridge, T. C. Duxbury, and R. E. Koch

Technical Memorandum 33-469, December 1, 1970

For abstract, see Gordon, H. J.

C17 Polar Motion: Doppler Determinations Using Satellites Compared to Optical Results

C. C. Chao and H. F. Fliegel

The Deep Space Network, Space Programs Summary 37-66, Vol. II, pp. 23–26, November 30, 1970

Determinations of polar motion from doppler observation of navigation satellites made by the U.S. Naval Weapons Laboratory over a 2-yr span (1968.0–1969.9) are compared to those of the three primary optical agencies for polar motion. Formulas

are given for estimating the true variance of each data source. The order of precision, measured by inverse standard deviation, of the various sources of polar motion is as follows: International Polar Motion Service, Bureau International de L'Heure, International Latitude Service, and U.S. Naval Weapons Laboratory. The doppler data are considered to be useful and important because they are presumably independent of the systematic errors affecting optical sources.

CHEN, C. J.

C18 Transition Probabilities for Xe I

C. J. Chen and R. H. Garstang (University of Colorado)

J. Quant. Spectrosc. Radiat. Transfer, Vol. 10, No. 12, pp. 1347–1348, December 1970

Renewed interest in the spectra of the rare gases in connection with shock tubes, high temperature arcs, and lasers has led to fresh demands for transition-probability data. The rare gases show large departures from *LS*-coupling, and *jl*-coupling is also inadequate for many of the lower multiplets. Intermediate coupling calculations are therefore required. Calculations of this type have been performed for many transitions in Ne I, Ar I, and Kr I, but the authors were unable to find any studies of Xe I in the literature. Intermediate coupling line strengths for the $5p^5 6s–5p^5 6p$ and $5p^5 6s–5p^5 7p$ transition arrays in Xe I have now been calculated. The final transition probabilities are tabulated in this article.

CHEN, J. C.

C19 Structural Analysis of a Solid Propellant Motor Under Axisymmetric Thermal and Pressure Loading

J. C. Chen

Supporting Research and Advanced Development, Space Programs Summary 37-65, Vol. III, pp. 176–178, October 31, 1970

The stresses in a circular solid propellant grain section have been solved for axisymmetric transient thermal and pressure loading. The propellant is assumed to be linear, rheologically simple, viscoelastic material. The material property is represented by an exponential series in time which leads to a recurrence relation, eliminating the problem of recalculating the history of material response at each time step.

CHRISTENSEN, E. M.

C20 *Surveyor* Final Report—Principal Scientific Results From the *Surveyor* Program

L. D. Jaffe, C. O. Alley (University of Maryland), S. A. Batterson (Langley Research Center), E. M. Christensen, S. E. Dwornik (NASA Headquarters), D. E. Gault (Ames Research Center), J. W. Lucas, D. O. Muhleman (California Institute of Technology), R. H. Norton, R. F. Scott (California Institute of Technology), E. M. Shoemaker (U.S. Geological Survey), R. H. Steinbacher, G. H. Sutton (University of Hawaii), and A. L. Turkevich (University of Chicago)

Icarus: Int. J. Sol. Sys., Vol. 12, No. 2, pp. 156–160, March 1970

For abstract, see Jaffe, L. D.

CLAUSS, R. C.

C21 Low Noise Receivers: Microwave Maser Development [September–October 1970]

R. C. Clauss

The Deep Space Network, Space Programs Summary 37-66, Vol. II, pp. 49–51, November 30, 1970

Isolators used with comb-type traveling wave masers (TWMs) have been described previously in several Space Programs Summaries. Efforts to improve the isolator performance have been one of the objectives of maser development for several years. This work has improved TWM performance by reducing losses in the comb structure. A cryogenic switching circulator for use at X-band has been developed for JPL by E and M Laboratories. A versatile liquid nitrogen-cooled dewar system has been used for hard vacuum testing of the circulator.

CLAYTON, R. M.

C22 Experimental Observations Relating the Inception of Liquid Rocket Engine Popping and Resonant Combustion to the Stagnation Dynamics of Injection Impingement

R. M. Clayton

Technical Report 32-1479, December 15, 1970

Ordinary liquid rocket combustion processes are never truly steady processes. They are usually observed as low-intensity,

random combustion-chamber pressure variations. However, a clearly distinguishable, aperiodic form of nonsteadiness is also frequently observed. This form of nonsteadiness is characterized by discrete, large-amplitude waves propagated throughout the combustion volume and is classified as popping. Popping and resonant combustion, as exhibited by annular and cylindrical versions of an 18-in.-diam engine, are found to occur for a particular range of propellant temperature and mixture ratio conditions used in a boundary (near-wall) injection system.

The correlation of these conditions of temperature and mixture ratio is based on the argument that the impingement of two streams of equal dynamic pressure is inherently unsteady, and that small variations to either side of unity dynamic-pressure ratio can produce relatively large changes in the mixture and direction of the efflux from the impingement region. Pops are extremely effective in precipitating sustained combustion resonance, unless the combustor is stabilized by control devices such as baffles. Reactive streams (hypergolic systems) and nonreactive streams (like-on-like systems) are discussed, as well as a proposed mechanism for producing initial combustion disturbances.

C23 Injector Hydrodynamics Effects on Baffled-Engine Stability—A Correlation of Required Baffle Geometry With Injected Mass Flux

R. M. Clayton

Supporting Research and Advanced Development,
Space Programs Summary 37-66, Vol. III, pp. 222–232,
December 31, 1970

Baffle stabilizing performance for the last of a series of three high-impedance research injectors is presented and the results for all three injectors are compared. It is shown that high dynamic-stability margins can be provided by baffles without extensive trial and error injector design changes when well-decoupled, reproducible injection schemes are used initially. The stable configurations required (1) a large enough baffle length L to reduce the ratio of local mass flux (evaluated for individual injection elements at L) to the average mass flux over the chamber cross section, $\mathcal{G}_{rel}$, to approximately 3 (out of a typical range for these experiments of $0.05 < \mathcal{G}_{rel} < 1000$), and (2) simultaneously a sufficient number of baffle blades to reduce the ratio of average peripheral width of the baffle cavities to the first tangential wave length to <0.57.

COFFIN, R. C.

C24 Development of Techniques for Mark III Implementation

R. C. Coffin

The Deep Space Network, Space Programs Summary 37-66, Vol. II, pp. 124–127, November 30, 1970

The implementation of the Deep Space Development Plan is resulting in significant changes in the Deep Space Network. This article describes the changes that are evident in packaging, circuitry, and computer concepts. The new packaging technique, characterized by the Mark III module, is designed to reflect the emphasis on integrated circuitry and printed circuit techniques. In the area of circuitry, developments are being made to allow for the increased application of automatic control and checkout. In addition to these "concrete" examples of new developments, there are also changes occurring in the very concepts by which the equipment is designed. All new designs are being evaluated in light of increased use of computer control.

COLLINS, R. J.

C25 *Surveyor* Final Report—Lunar Theory and Processes: Discussion of Chemical Analysis

R. A. Phinney (Princeton University), D. E. Gault (Ames Research Center), J. A. O'Keefe (Goddard Space Flight Center), J. B. Adams, G. P. Kuiper (University of Arizona), H. Masursky (U.S. Geological Survey), E. M. Shoemaker (U.S. Geological Survey), and R. J. Collins (University of Minnesota)

Icarus: Int. J. Sol. Sys., Vol. 12, No. 2, pp. 213–223, March 1970

For abstract, see Phinney, R. A.

C26 *Surveyor* Final Report—Lunar Theory and Processes: Post-Sunset Horizon "Afterglow"

D. E. Gault (Ames Research Center), J. B. Adams, R. J. Collins (University of Minnesota), G. P. Kuiper (University of Arizona), J. A. O'Keefe (Goddard Space Flight Center), R. A. Phinney (Princeton University), and E. M. Shoemaker (U.S. Geological Survey)

Icarus: Int. J. Sol. Sys., Vol. 12, No. 2, pp. 230–232, March 1970

For abstract, see Gault, D. E.

COSTOGUE, E. N.

C27 **Electric Propulsion Power Conditioning [August–September 1970]**

E. N. Costogue

Supporting Research and Advanced Development, Space Programs Summary 37-65, Vol. III, pp. 84–88, October 31, 1970

The primary function of the electric propulsion power conditioning system is to control the flow of power from the solar panel source to the ion thrusters to obtain high propellant utilization. To verify the power requirements of the hollow cathode ion thruster and to determine the control loop characteristics of the power conditioner, a task was initiated to modify an available breadboard power conditioner for an oxide cathode thruster configuration to operate with the hollow cathode thruster power requirements. The characteristics of the new supplies are presented with a brief description of the circuit techniques employed.

CRAWFORD, W. E.

C28 **Stepper Motor Drive Electronics for the Solar Electric Thrust Vector Control Subsystem**

W. E. Crawford

Supporting Research and Advanced Development, Space Programs Summary 37-66, Vol. III, pp. 108–110, December 31, 1970

This article describes the design of a stepper motor drive electronics. This work was done in conjunction with the design and construction of the solar electric thrust vector control system. Unique features of this stepper motor drive are discussed and a comparison with commercially available stepper motor drivers is made.

CUDDIHY, E. F.

C29 **Superposition of Dynamic Mechanical Properties in the Glassy State**

E. F. Cuddihy and J. Moacanin

Technical Report 32-1509 (Reprinted from *J. Polym. Sci., Pt. A-2: Polym. Phys.*, Vol. 8, No. 9, pp. 1627–1634, September 1970)

Superposition of the loss tangent curves could be achieved for the β-transition of a series of homologous epoxy resins. It was found that both a vertical and horizontal shift were necessary to achieve superposition when the curves were plotted as the logarithm of the loss tangent versus reciprocal absolute temperature. Resins from the diglycidyl ether of bisphenol A (DGEBA) were prepared with five different curing agents and their loss tangent curves measured on a free-oscillation torsion pendulum (ca. 1 cps). The β transition is caused by DGEBA, which was found via molecular models to contain a mobile group. The intensity of the loss for three of the resins was found to be proportional to the concentration of DGEBA, molecular models revealing that no additional mobile groups were introduced by these curatives. The remaining two curing agents introduced mobile groups into their systems, and, for these two, no separate transitions were identified but the intensity of the DGEBA β transition was increased. This may be caused by a coupling of the DGEBA mobile groups through the flexibility of the curative-introduced mobile groups.

C30 On the Presence of Crystallinity in Hydrogenated Polybutadienes

J. Moacanin, A. Eisenberg (McGill University, Canada), E. F. Cuddihy, D. D. Lawson, B. G. Moser (Moser Dental Manufacturing Company), and R. F. Landel

Technical Report 32-1512 (Reprinted from *J. Appl. Polym. Sci.*, Vol. 14, No. 9, pp. 2416–2420, September 1970)

For abstract, see Moacanin, J.

C31 Investigation of Sterilizable Battery Separators [August–September 1970]

E. F. Cuddihy, D. E. Walmsley, J. Moacanin, and H. Y. Tom

Supporting Research and Advanced Development, Space Programs Summary 37-65, Vol. III, pp. 171–176, October 31, 1970

Graft copolymer membranes prepared by grafting poly(potassium acrylate) onto a thin film of crosslinked polyethylene are employed as separator membranes in sterilizable silver–zinc batteries. Changes that occur in the morphological state of the graft copolymer membrane resulting from exposure to the battery environment were investigated using electron microscopy, electron microprobe analysis, and scanning electron microscopy. The observed results were then discussed and correlated with chemical changes that are known to occur in the membrane.

CUFFEL, R. F.

C32 **Changes in Heat Transfer From Turbulent Boundary Layers Interacting With Shock Waves and Expansion Waves**

L. H. Back and R. F. Cuffel

AIAA J., Vol. 8, No. 10, pp. 1871–1873, October 1970

For abstract, see Back, L. H.

C33 **Relationship Between Temperature and Velocity Profiles in a Turbulent Boundary Layer Along a Supersonic Nozzle With Heat Transfer**

L. H. Back and R. F. Cuffel

AIAA J., Vol. 8, No. 11, pp. 2066–2069, November 1970

For abstract, see Back, L. H.

CURKENDALL, D. W.

C34 **The *Mariner VI* and *VII* Flight Paths and Their Determination From Tracking Data**

H. J. Gordon, D. W. Curkendall, D. A. O'Handley, N. A. Mottinger, P. M. Muller, C. C. Chao, B. D. Mulhall, V. J. Ondrasik, S. K. Wong, S. J. Reinbold, J. W. Zielenback, J. K. Campbell, R. T. Mitchell, J. E. Ball, W. G. Breckenridge, T. C. Duxbury, and R. E. Koch

Technical Memorandum 33-469, December 1, 1970

For abstract, see Gordon, H. J.

DACHEL, P.

D01 **RF Techniques: Superconducting Magnet for X-Band Maser**

R. Berwin and P. Dachel

Supporting Research and Advanced Development, Space Programs Summary 37-65, Vol. III, pp. 45–47, October 31, 1970

For abstract, see Berwin, R.

DAMLAMAYAN, D.

D02 **Spacecraft Antenna Research: Antenna Tolerances**

D. Damlamayan

Supporting Research and Advanced Development, Space Programs Summary 37-66, Vol. III, pp. 43–49, December 31, 1970

The effect of systematic and random errors on the gain of antennas representable by a field distribution over an aperture are discussed, with particular reference to reflectors and lenses. It is shown quantitatively that the manufacturing tolerances for lenses can be far less stringent than for reflectors. Indeed the easier tolerances of lenses constitute their main advantage over reflectors.

DeGENNARO, L.

D03 High-Speed Data/Wide-Band Data Input/Output Assembly

R. Wengert, L. DeGennaro, and J. McInnis

The Deep Space Network, Space Programs Summary 37-66, Vol. II, pp. 133–136, November 30, 1970

For abstract, see Wengert, R.

DEO, N.

D04 Extraction of Complete Subgraphs: Command Prefix Code for TOPS

N. Deo

Supporting Research and Advanced Development, Space Programs Summary 37-66, Vol. III, pp. 164–166, December 31, 1970

Sandwiched between the idle sequence and the actual command words, a prefix word can be transmitted for synchronizing the command decoder aboard the spacecraft. Since the Thermoelectric Outer-Planet Spacecraft (TOPS) will have several command decoders, it is important to obtain the largest set of mutually compatible prefix words of a specified length and specified error-correcting capability. Linear graph theory is used to solve this problem. The solution requires extraction of maximal complete subgraphs out of a given graph. An algorithm for such extraction is sketched. Algorithms for connectedness of a graph and for identification of articulation points, as well as maximally connected nonseparable blocks, serve as subalgorithms.

DIEM, W.

D05 Video Image Display Assembly

W. Diem

The Deep Space Network, Space Programs Summary 37-66, Vol. II, pp. 94–96, November 30, 1970

The advent of imaging devices on most spacecraft has led to the development of a Video Image Display Assembly by the Deep Space Network. This assembly will provide high quality tonal image displays and operational prints for real-time validation and preliminary analysis of spacecraft pictures. A functional description of the assembly is presented.

DONNELLY, H.

D06 Block IV Receiver–Exciter Development

H. Donnelly, A. C. Shallbetter, and R. E. Weller

The Deep Space Network, Space Programs Summary 37-66, Vol. II, pp. 115–124, November 30, 1970

The Block IV receiver–exciter is an automated subsystem designed to meet the future requirements of the Deep Space Network. This article gives a summary of the development of the engineering model of the Block IV, describing basic design goals and listing pertinent subsystem specifications. Photographs showing packaging techniques and the physical layout of the system are also included.

DORE, M. A.

D07 Neutron Yield From (α, n) Reaction With O^{18} Isotope

M. Taherzadeh and M. A. Dore

Supporting Research and Advanced Development, Space Programs Summary 37-65, Vol. III, pp. 58–64, October 31, 1970

For abstract, see Taherzadeh, M.

DOWNS, G. S.

D08 Observations of Interstellar Scintillations of Pulsar Signals at 2388 MHz

G. S. Downs and P. E. Reichley

Astrophys. J., Vol. 163, No. 1, Pt. 2, pp. L11–L16, January 1, 1971

The scintillation index and fading time have been measured at 2388 MHz. These measurements, together with low-frequency measurements, are interpreted in terms of the extended-medium

theory of Uscinski. Typically we find a scale size of electron irregularities of 4×10^{10} cm and an rms value of the electron density fluctuations of 2×10^{-5} cm^{-3}. Failure to observe long-term variations suggests a second component of density fluctuations.

DUXBURY, T. C.

D09 The *Mariner VI* and *VII* Flight Paths and Their Determination From Tracking Data

H. J. Gordon, D. W. Curkendall, D. A. O'Handley, N. A. Mottinger, P. M. Muller, C. C. Chao, B. D. Mulhall, V. J. Ondrasik, S. K. Wong, S. J. Reinbold, J. W. Zielenback, J. K. Campbell, R. T. Mitchell, J. E. Ball, W. G. Breckenridge, T. C. Duxbury, and R. E. Koch

Technical Memorandum 33-469, December 1, 1970

For abstract, see Gordon, H. J.

D10 Navigation Data From *Mariner* Mars 1969 TV Pictures

T. C. Duxbury

Navigation, Vol. 17, No. 3, pp. 219–225, Fall 1970

As described in this article, a navigation experiment on the 1969 *Mariner* mission to Mars used TV pictures of Mars in estimating the spacecraft trajectory. The lit limb of Mars was measured to determine the direction to the center of Mars in TV coordinates. The location of the center of Mars was determined to $\sim$50 km (1σ) from the TV data. Additional processing of the TV data is expected to yield the center location to $\sim$30 km (1σ).

DWORNIK, S. E.

D11 *Surveyor* Final Report—Principal Scientific Results From the *Surveyor* Program

L. D. Jaffe, C. O. Alley (University of Maryland), S. A. Batterson (Langley Research Center), E. M. Christensen, S. E. Dwornik (NASA Headquarters), D. E. Gault (Ames Research Center), J. W. Lucas, D. O. Muhleman (California Institute of Technology), R. H. Norton, R. F. Scott (California Institute of Technology), E. M. Shoemaker (U.S. Geological Survey), R. H. Steinbacher, G. H. Sutton (University of Hawaii), and A. L. Turkevich (University of Chicago)

Icarus: Int. J. Sol. Sys., Vol. 12, No. 2, pp. 156–160, March 1970

For abstract, see Jaffe, L. D.

EISENBERG, A.

E01 **On the Presence of Crystallinity in Hydrogenated Polybutadienes**

J. Moacanin, A. Eisenberg (McGill University, Canada), E. F. Cuddihy, D. D. Lawson, B. G. Moser (Moser Dental Manufacturing Company), and R. F. Landel

Technical Report 32-1512 (Reprinted from *J. Appl. Polym. Sci.*, Vol. 14, No. 9, pp. 2416–2420, September 1970)

For abstract, see Moacanin, J.

EISENBERGER, I.

E02 **Estimating the Parameter of an Exponential Distribution Using Quantiles**

I. Eisenberger

The Deep Space Network, Space Programs Summary 37-66, Vol. II, pp. 31–36, November 30, 1970

This article presents the results of an investigation into the effects of a finite sample size on the bias and efficiency of quantile estimators of the parameter of an exponential distribution, arising in Deep Space Instrumentation Facility wearout detection. These estimators were derived on the basis of the asymptotic normal distribution of the quantiles used. The exact moments of the quantiles and estimators are derived and computed for sample size $n = 50$, 100, and 200. Unbiased optimum or near-optimum estimators are also constructed using up to seven quantiles for these sample sizes. The results show that, even for moderate values of n, the bias of the asymptotic estimators are not excessive.

ELLEMAN, D. D.

E03 **On the Relative Proton Affinity of Argon and Deuterium**

M. T. Bowers (University of California, Santa Barbara) and D. D. Elleman

J. Am. Chem. Soc., Vol. 92, No. 25, pp. 7258–7262, December 16, 1970

For abstract, see Bowers, M. T.

ERICKSON, D.

E04 DSN Progress Report for November–December 1970: Concatenation of Short Constraint Length Convolutional Codes

D. Erickson

Technical Report 32-1526, Vol. I, pp. 46–51, February 15, 1971

Several methods of decoding a concatenated pair of $K = 6$, $V = 2$ convolutional codes are investigated. It was found that none of the methods provides performance which is suitable for space channel application.

ESTABROOK, F. B.

E05 Solution of Partial Differential Systems

F. B. Estabrook, B. K. Harrison (Brigham Young University), and H. D. Wahlquist

Supporting Research and Advanced Development, Space Programs Summary 37-66, Vol. III, p. 17, December 31, 1970

This article summarizes a new method that has been found for obtaining various kinds of special solutions of sets of nonlinear partial differential equations. It has been applied to representative sets of equations in fluid physics, plasma physics, and general relativity.

EVANS, R. H.

E06 High-Speed Data Block Demultiplexer

R. H. Evans

The Deep Space Network, Space Programs Summary 37-66, Vol. II, pp. 105–106, November 30, 1970

This article presents a functional description of the block demultiplexer (BDXR). The BDXR will be used in the Deep Space Network Ground Communications Facility (GCF) Deep Space Station Communications Equipment Subsystem to provide a new interface between the receiving circuit of one high-speed-data channel and a maximum of six on-station computers (OSCs). The BDXR will examine the OSC destination codes of each data block and transfer only those blocks properly addressed to any combination up to six OSCs. The BDXR application will minimize the OSC machine loading for the receive data function, and the GCF High-Speed-Data System function of transferring data blocks from source to sink is precisely performed.

FERRERA, J. D.

F01 TOPS Attitude-Control Single-Axis Simulator

J. D. Ferrera and G. S. Perkins

Supporting Research and Advanced Development,
Space Programs Summary 37-65, Vol. III, pp. 118–119,
October 31, 1970

This article describes the configuration of the single-axis simulator which will be used to provide a breadboard hardware verification of the present Thermoelectric Outer-Planet Spacecraft (TOPS) baseline attitude-control system. The gas bearing and table are detailed with preliminary information on the systems which will be mounted on the table.

FINNIE, C.

F02 DSN Progress Report for November–December 1970: Frequency Generation and Control: Atomic Hydrogen Maser Frequency Standard

C. Finnie

Technical Report 32-1526, Vol. I, pp. 73–75,
February 15, 1971

System considerations are described for a prototype hydrogen maser cavity tuner for use with the atomic hydrogen maser frequency standard developed at the Jet Propulsion Laboratory. The tuner system and the tuner operation sequence are illustrated.

FISHER, J. G.

F03 Mesh Materials for Deployable Antennas

J. G. Fisher

Supporting Research and Advanced Development,
Space Programs Summary 37-65, Vol. III, pp. 122–125,
October 31, 1970

Evaluation of mesh materials for deployable antennas continues. The results of RF testing of Paliney 7, a precious metal alloy, as a substitute for Chromel R are given, with a preliminary value for its solar-absorptance-to-emittance ratio. A description is included of equipment developed to evaluate the elastic characteristics of mesh materials at various temperatures, along with representative curves derived from its use.

F04 Development of a Conical–Gregorian High-Gain Antenna

J. G. Fisher

Supporting Research and Advanced Development, Space Programs Summary 37-66, Vol. III, pp. 118–119, December 31, 1970

Continued development of the conical–Gregorian antenna concept is described. A furlable 6-ft-diameter model utilizing a 0.020-in.-thick 2024-T3 aluminum alloy sheet as the reflective surface was constructed. Problems associated with the design, fabrication, and testing of this model are discussed, as well as plans for continued development in the direction of compliant reflective surfaces supported by stiff but furlable members. Results of preliminary tests to evaluate materials and design details for this concept are included.

FLIEGEL, H. F.

F05 Polar Motion: Doppler Determinations Using Satellites Compared to Optical Results

C. C. Chao and H. F. Fliegel

The Deep Space Network, Space Programs Summary 37-66, Vol. II, pp. 23–26, November 30, 1970

For abstract, see Chao, C. C.

FREILEY, A. J.

F06 DSN Progress Report for November–December 1970: Tracking and Data Acquisition Elements Research: Polarization Diverse S-Band Feed Cone

D. E. Neff and A. J. Freiley

Technical Report 32-1526, Vol. I, pp. 66–72, February 15, 1971

For abstract, see Neff, D. E.

GALE, G.

G01 Hydrostatic Bearing Runner Level Reference

G. Gale and H. Phillips

The Deep Space Network, Space Programs Summary 37-66, Vol. II, pp. 80–83, November 30, 1970

This article describes a method used to survey a 70-ft-diameter circle, which is used as an elevation reference for surveying the

210-ft-diameter antenna hydrostatic bearing runner at DSS 14 (Mars Deep Space Station). The surface surveyed, and then used as an intermediate height reference, is the top of the azimuth drive bull gear, which is set on the antenna concrete pedestal. The center of the circle is shielded from the reference circle so that conventional optical methods are not applicable. The method described gives a probable error in elevation of less than 0.001 in.

GARSIA, A. M.

G02 A Real Variable Lemma and the Continuity of Paths of Some Gaussian Processes

A. M. Garsia, E. Rodemich, and H. Rumsey, Jr.

Ind. Univ. Math. J., Vol. 20, No. 6, pp. 565–578, December 1970

The now standard method of constructing a separable and measurable model for a mean continuous stochastic process, starting from a given consistent system of joint distributions, although somewhat arbitrary, is perhaps unavoidable in the general case. However, a more direct approach that is frequently used by communications engineers in the gaussian case is to expand the paths in terms of the eigenfunctions of the covariance kernel. The resulting expression, which is usually referred to as the Karhunen–Loève expansion and was apparently introduced quite early by M. Kač, is a very natural tool to use.

The purpose of this article is to show that, at least in the cases when the paths are known to be almost surely continuous, this procedure can indeed be used to produce the desired models. In fact, it is shown that the best possible estimates for the modulus of continuity of the sample paths can be directly obtained from a study of the partial sums of this expansion.

The main tool here is a real variable lemma whose significance will, perhaps, transcend the applications that have led to its discovery. This is a lemma which, roughly speaking, states that the finiteness of a certain integral involving a given function has a bearing on the modulus of continuity of such a function. Results of similar nature have appeared in Fourier analysis and partial differential equations, but, as far as the authors know, no result of the generality of this lemma has appeared in the literature before. The power of the lemma lies in the fact that it provides a step which enables the user to pass from global estimates, often readily available in a probabilistic setting, to local estimates, which usually appear to be of a more elusive nature.

GARSTANG, R. H.

G03 Transition Probabilities for Xe I

C. J. Chen and R. H. Garstang (University of Colorado)

J. Quant. Spectrosc. Radiat. Transfer, Vol. 10, No. 12, pp. 1347–1348, December 1970

For abstract, see Chen, C. J.

GARTHWAITE, K.

G04 A Preliminary Special Perturbation Theory for the Lunar Motion

K. Garthwaite, D. B. Holdridge, and J. D. Mulholland

Technical Report 32-1517 (Reprinted from *Astron. J.*, Vol. 75, No. 10, pp. 1133–1139, December 1970)

A combination of literal and numerical integration techniques has been used to produce a lunar ephemeris more adequate for high-precision applications than has heretofore been available. The numerical integration was differentially fitted to source positions computed from a reduced theory at half-day intervals over a 20-yr span, a process intended to eliminate the gravitational defect in the literal theory. Spectral analysis of the residuals confirms the earlier conjecture that this defect is a truncation effect in the planetary perturbation terms of the theory. Comparison of the final ephemeris with transit circle observations shows a small systematic effect in right ascension and the previously known bias in declination, but the standard deviation is less than 0.8 arc sec for each coordinate. Comparison with a few preliminary laser range observations shows residuals of the order of 100 m.

GAULT, D. E.

G05 *Surveyor* Final Report—Principal Scientific Results From the *Surveyor* Program

L. D. Jaffe, C. O. Alley (University of Maryland), S. A. Batterson (Langley Research Center), E. M. Christensen, S. E. Dwornik (NASA Headquarters), D. E. Gault (Ames Research Center), J. W. Lucas, D. O. Muhleman (California Institute of Technology), R. H. Norton, R. F. Scott (California Institute of Technology), E. M. Shoemaker (U.S. Geological Survey), R. H. Steinbacher, G. H. Sutton (University of Hawaii), and A. L. Turkevich (University of Chicago)

Icarus: Int. J. Sol. Sys., Vol. 12, No. 2, pp. 156–160, March 1970

For abstract, see Jaffe, L. D.

G06 ***Surveyor* Final Report— Lunar Theory and Processes: Discussion of Chemical Analysis**

R. A. Phinney (Princeton University), D. E. Gault (Ames Research Center), J. A. O'Keefe (Goddard Space Flight Center), J. B. Adams, G. P. Kuiper (University of Arizona), H. Masursky (U.S. Geological Survey), E. M. Shoemaker (U.S. Geological Survey), and R. J. Collins (University of Minnesota)

Icarus: Int. J. Sol. Sys., Vol. 12, No. 2, pp. 213–223, March 1970

For abstract, see Phinney, R. A.

G07 ***Surveyor* Final Report—Lunar Theory and Processes: Post-Sunset Horizon "Afterglow"**

D. E. Gault (Ames Research Center), J. B. Adams, R. J. Collins (University of Minnesota), G. P. Kuiper (University of Arizona), J. A. O'Keefe (Goddard Space Flight Center), R. A. Phinney (Princeton University), and E. M. Shoemaker (U.S. Geological Survey)

Icarus: Int. J. Sol. Sys., Vol. 12, No. 2, pp. 230–232, March 1970

Observations of the western horizon shortly after sunset during the *Surveyor VII* mission revealed, along the crest of the horizon, a bright line of light similar to that previously reported for the *Surveyor V* and *VI* missions. Though not sufficiently well-defined to be recognized at the time, the phenomenon also occurred during the *Surveyor I* mission. Although no sunset observations were made on *Surveyor III*, it appears that this postsunset phenomenon along the western horizon (and probably the eastern horizon at sunrise) is not an unusual event, but occurs regularly as the natural consequence of some aspect of the lunar environment. A discussion of the phenomenon is presented here.

GAYMAN, W. H.

G08 **Equivalent Spring-Mass System for Normal Modes**

R. M. Bamford, B. K. Wada, and W. H. Gayman

Technical Memorandum 33-380, February 15, 1971

For abstract, see Bamford, R. M.

GOLD, T.

G09 *Surveyor* Final Report—Lunar Theory and Processes: Chemical Observations by *Surveyor V*

T. Gold (Cornell University)

Icarus: Int. J. Sol. Sys., Vol. 12, No. 2, pp. 224–225, March 1970

The important observation that the lunar soil at the *Surveyor V* landing site is basaltic in composition is taken by many to substantiate the viewpoint, previously widespread, that volcanism formed most of the lunar surface, supplying a differentiated type of rock. The case for this is, however, by no means so simple or so clearcut. The arguments previously voiced against a widespread differentiation on the moon are now just as strong, or in some cases even strengthened, by recent observations. This controversy is briefly discussed in this article.

G10 *Surveyor* Final Report—Lunar Theory and Processes: The Physical Condition of the Lunar Surface

T. Gold (Cornell University)

Icarus: Int. J. Sol. Sys., Vol. 12, No. 2, pp. 226–229, March 1970

The five successful *Surveyor* soft landings demonstrated that the lunar surface is composed, in general, or very fine, slightly cohesive rock powder. The depth of this material, the particle size, and the ubiquity of this type of surface can still be debated; but very significant constraints can be placed on each. This article describes the *Surveyor* results pertinent to the physical condition of the lunar surface, particularly the observed spray phenomena. A discussion is included on the importance of the results for future lunar technology.

GORDON, H. J.

G11 The *Mariner VI* and *VII* Flight Paths and Their Determination From Tracking Data

H. J. Gordon, D. W. Curkendall, D. A. O'Handley, N. A. Mottinger, P. M. Muller, C. C. Chao, B. D. Mulhall, V. J. Ondrasik, S. K. Wong, S. J. Reinbold, J. W. Zielenback, J. K. Campbell, R. T. Mitchell, J. E. Ball, W. G. Breckenridge, T. C. Duxbury, and R. E. Koch

Technical Memorandum 33-469, December 1, 1970

This report describes the current best estimate of the *Mariner VI* and *VII* flight paths and the way in which they were determined using Deep Space Instrumentation Facility tracking data. The flight paths are separated into three phases: (1) launch to maneuver or pre-maneuver phase, (2) cruise or post-maneuver phase, and (3) encounter phase. Discussions of the Precision Navigation Project, flight operations, maneuver analyses, and optical observables are included.

GOSS, W. C.

G12 TOPS Attitude-Control Single-Axis Simulator True Position Encoder

W. C. Goss and L. S. Smith

Supporting Research and Advanced Development, Space Programs Summary 37-65, Vol. III, pp. 119–121, October 31, 1970

The Thermoelectric Outer-Planet Spacecraft (TOPS) single-axis simulator is being built upon a gas-bearing table as a test bed for future attitude-control systems. To evaluate the attitude-control system performance, a frictionless technique of monitoring the positional activity of the test bed was developed. This article describes the true position encoder developed and its functional characteristics. Performance tests demonstrating the achievement of 0.01-deg angular accuracy over a full 360-deg rotation are presented.

HABBAL, N.

H01 SFOF IBM 360/75 User Device Switching Assemblies

N. Habbal

The Deep Space Network, Space Programs Summary 37-66, Vol. II, pp. 75–77, November 30, 1970

Two IBM 360/75 computers are installed in the Space Flight Operations Facility (SFOF). Either computer may be used for real-time mission support while the other is used for off-line processing or as backup to the real-time computer. To gain maximum flexibility and economy, a switching system has been developed to provide switching of user input/output devices such as cathode-ray tube displays, card readers, and line printers. These switching assemblies, which form part of the real-time input/output interface subsystem, are described in this article.

HADEK, V.

H02 Energy Transfer in Bipyridilium (Paraquat) Salts

A. Rembaum, V. Hadek, and S. P. S. Yen

Supporting Research and Advanced Development,
Space Programs Summary 37-66, Vol. III, pp. 189–191,
December 31, 1970

For abstract, see Rembaum, A.

H03 Electrical Properties of TCNQ Salts of Ionene Polymers and Their Model Compounds

V. Hadek, H. Noguchi, and A. Rembaum

Supporting Research and Advanced Development,
Space Programs Summary 37-66, Vol. III, pp. 192–198,
December 31, 1970

Electrically conducting polysalts were prepared by the reaction of ionene polymers with LiTCNQ in presence or in absence of neutral TCNQ. The specific resistivity, the activation energy for conductivity, and the Seebeck coefficient were determined as a function of the number of CH_2 group between positively charged nitrogens. The wide variations of electrical properties could not be correlated with the length of the polymethylene chain in the polymer. X-ray analysis of single crystals of model compounds revealed that the electrical properties depend mainly on crystal geometry.

HAMILTON, T. W.

H04 DSN Progress Report for November–December 1970: DSN Inherent Accuracy Project

T. W. Hamilton and D. W. Trask

Technical Report 32-1526, Vol. I, pp. 11–13,
February 15, 1971

The Deep Space Network (DSN) Inherent Accuracy Project was formally established in July 1965 to: (1) determine (and verify) the inherent accuracy of the DSN as a radio navigation instrument for lunar and planetary missions, and (2) formulate designs and plans for refining this accuracy to its practical limits. The organization of the project and the current technical work performed are summarized in this article.

HAND, P. J.

H05 Digital Gyro System (Phase I)

P. J. Hand

Supporting Research and Advanced Development, Space Programs Summary 37-66, Vol. III, pp. 105–107, December 31, 1970

A complete, self-contained, single-axis, digital gyro system has been developed and built for use with the Thermoelectric Outer-Planet Spacecraft single-axis attitude-control system simulator. The gyro system has been under test for more than one month and has accumulated over 900 h of operational time. Measured performance is shown by two charts of long- and short-term drift rate and of pulse scale factor calibration stability.

HANSELMAN, R.

H06 Wideband Digital Data System Terminal Configuration

R. Hanselman

The Deep Space Network, Space Programs Summary 37-66, Vol. II, pp. 107–110, November 30, 1970

This article covers the specific configuration of each of the terminals involved in the data portion of the Deep Space Network Ground Communications Facility 1971–1972 Wideband System. A description of each of the major equipments used in the system is also covered. This article is an amplification of a previous article on this subject earlier in this SPS series.

HANSON, R. B.

H07 Soil Microbial and Ecological Investigations in the Antarctic Interior

R. E. Cameron, R. B. Hanson, G. H. Lacy, and F. A. Morelli

Antarc. J. U.S., Vol. V, No. 4, pp. 87–88, July–August 1970

For abstract, see Cameron, R. E.

H08 Microbiological Analyses of Snow and Air From the Antarctic Interior

G. H. Lacy, R. E. Cameron, R. B. Hanson, and F. A. Morelli

Antarc. J. U.S., Vol. V, No. 4, pp. 88–89, July–August 1970

For abstract, see Lacy, G. H.

HANSON, R. J.

H09 Automatic Error Bounds for Real Roots of Polynomials Having Interval Coefficients

R. J. Hanson

Technical Report 32-1497 (Reprinted from *Comput. J.*, Vol. 13, No. 3, pp. 284–288, August 1970)

A generalized Newton–Raphson method for use with interval arithmetic is described. This algorithm can, for example, be used with great effectiveness to obtain precise bounds for the real roots of real polynomials whose coefficients are not exactly known. Two eigenvalue problems for real matrices are given as examples.

H10 Unitary Similarity Transformation of a Hermitian Matrix to a Real Symmetric Tridiagonal Matrix

R. J. Hanson

Supporting Research and Advanced Development, Space Programs Summary 37-66, Vol. III, pp. 10–12, December 31, 1970

The details necessary for transforming a general complex hermitian matrix to real tridiagonal form are given. To accomplish this, Householder unitary transformations are used primarily. Some computational points are also presented which can be used to decrease the amount of computer storage and time.

HARPER, L.

H11 DSIF Integrated-Circuit Layout and Isoperimetric Problems

L. Harper

The Deep Space Network, Space Programs Summary 37-66, Vol. II, pp. 37–42, November 30, 1970

This article shows how to lay out 16 integrated circuits for the maximum-likelihood convolutional decoder on a linear card so that the total length of connecting wires is mimimized. The methods used can be applied to any circuit diagram of reasonable size, since all calculations were done by hand using special properties of the graph of the circuit. In general, growth of the calculations is exponential with the number of circuits, but the particular graphs that arise in the Deep Space Instrumentation Facility (DSIF) subsystems usually have properties such as symmetries or regularity which allow great simplification by ad hoc

means. The methods are extended to rectangular cards, and can be extended to higher dimensions in an obvious way. The problem of minimizing the maximal length of a connecting wire is also considered, and areas for further research are suggested.

HARRISON, B. K.

H12 Solution of Partial Differential Systems

F. B. Estabrook, B. K. Harrison (Brigham Young University), and H. D. Wahlquist

Supporting Research and Advanced Development, Space Programs Summary 37-66, Vol. III, p. 17, December 31, 1970

For abstract, see Estabrook, F. B.

HASBACH, W. A.

H13 Lightweight Solar Panel Development [August–September 1970]

W. A. Hasbach

Supporting Research and Advanced Development, Space Programs Summary 37-65, Vol. III, pp. 73–80, October 31, 1970

The design, analysis, fabrication, and testing of a lightweight solar panel made of built-up beryllium structure with an active solar cell area of 29 ft^2 are described. Testing included modal survey, reverberant acoustic, random vibration, sinusoidal vibration, static load, thermal-vacuum-shock, substrate frequency check, and power output tests. The design goal of 20-W/lb specific power output was achieved.

HAUDENSCHILD, C.

H14 Multi-Phase Ammonia Water System (Rev. 1)

C. Haudenschild

Supporting Research and Advanced Development, Space Programs Summary 37-66, Vol. III, pp. 4–9, December 31, 1970

Equations are fitted to tabular laboratory data available for ammonia water systems. The equations relate temperature, concentration, and partial pressures over solution, solid hydrate, solid

water, and solid ammonia. The freezing curve, in the form of an equation for temperature as a function of concentration, is given for the phase boundary of each region. Finally, a phase diagram displaying all equations is produced. This article is a revision of that appearing in Space Programs Summary 37-64, Vol. III, and includes changes in tabular data.

HEER, E.

H15 VISCEL—A General-Purpose Computer Program for Analysis of Linear Viscoelastic Structures: User's Manual

F. A. Akyuz and E. Heer

Technical Memorandum 33-466, Vol. I, February 15, 1971

For abstract, see Akyuz, F. A.

H16 Optimum Pressure Vessel Design Based on Fracture Mechanics and Reliability Criteria

E. Heer and J.-N. Yang

Technical Memorandum 33-470, February 1, 1970

Spacecraft structural systems and subsystems are subjected to a number of qualification tests in which the proof loads are chosen at some level above the simulated loads expected during the space mission. Assuming fracture to be the prime failure mechanism, and allowing for time effects due to cyclic and sustained loadings, this memorandum treats an optimization method in which the statistical variability of loads and material properties are taken into account, and in which the proof load level is used as an additional design variable. In the optimization process, the structural weight is the objective function, while the total expected cost due to coupon testing for material characterization, failure during proof testing, and mission degradation is a constraint. Numerical results indicate that, for a given expected cost constraint, substantial weight savings and improvements in reliability can be realized by proof testing.

H17 Optimization of Space Antenna Structures

E. Heer and J.-N. Yang

Technical Memorandum 33-472, March 15, 1971

This memorandum develops an optimization scheme that can readily be applied to the optimum design of space antennas, as

well as to the evaluation and comparison of antenna concepts, antenna structural types, and antenna structural materials. The objective function is either cost or weight; the design variables are diameter, weight per unit area, manufacturing precision measure, and sizes of structural elements. With system requirements such as antenna gains, communication frequencies, etc., as constraints, the objective function is minimized with respect to the design variables. Through this optimization process, it can be demonstrated whether the effort of improving a particular technology, such as manufacturing, has advantages under certain operational requirements.

H18 Reliability of Randomly Excited Structures

J.-N. Yang and E. Heer

Supporting Research and Advanced Development,
Space Programs Summary 37-66, Vol. III, pp. 128–136,
December 31, 1970

For abstract, see Yang, J.-N.

HOFFMAN, J. K.

H19 Evaluation of Spacecraft Magnetic Recording Tapes and Magnetic Heads [August–September 1970]

S. H. Kalfayan, R. H. Silver, and J. K. Hoffman

Supporting Research and Advanced Development,
Space Programs Summary 37-65, Vol. III, pp. 168–171,
October 31, 1970

For abstract, see Kalfayan, S. H.

H20 Evaluation of Recording Tape and Heads for Spacecraft Magnetic Tape Recorder Applications [October–November 1970]

J. K. Hoffman, S. H. Kalfayan, and R. H. Silver

Supporting Research and Advanced Development,
Space Programs Summary 37-66, Vol. III, p. 160,
December 31, 1970

Phase III of a study of the characteristics of magnetic recording tapes and the tape-to-head interface in the spacecraft environment was completed. This article briefly describes the work, but gives no results.

H21 **Evaluation of Magnetic Recording Tapes: A Method for the Quantitative Determination of Stick-Slip**

R. H. Silver, S. H. Kalfayan, and J. K. Hoffman

Supporting Research and Advanced Development, Space Programs Summary 37-66, Vol. III, pp. 198–200, December 31, 1970

For abstract, see Silver, R. H.

HOLDRIDGE, D. B.

H22 **A Preliminary Special Perturbation Theory for the Lunar Motion**

K. Garthwaite, D. B. Holdridge, and J. D. Mulholland

Technical Report 32-1517 (Reprinted from *Astron. J.*, Vol. 75, No. 10, pp. 1133–1139, December 1970)

For abstract, see Garthwaite, K.

HOLMES, J.

H23 **Decoding and Synchronization Research: A Note on the Optimality of the All-Digital Command System Timing Loop**

J. Holmes

Supporting Research and Advanced Development, Space Programs Summary 37-65, Vol. III, pp. 19–21, October 31, 1970

A more general sampling geometry is investigated for the timing update portion of the all-digital, single-channel, command system that has been developed as part of the Thermoelectric Outer-Planet Spacecraft Project. With the existing threshold of 2.2 dB, it is shown that the optimum sampling geometry, constrained to 16 equally spaced samples per cycle, is the existing single-sample procedure.

HOPPER, E. T.

H24 **Ion Thruster Connectors**

E. T. Hopper

Supporting Research and Advanced Development, Space Programs Summary 37-66, Vol. III, pp. 211–212, December 31, 1970

A commercially available connector has been modified for use in an ion thruster system. Modifications permit use in vacuum of a single connector for leads with voltage differentials up to 3000 V without arc-over or detectable leakage. This connector appears suitable for flight application.

HORTON, T. E.

H25 **Shock-Tube Thermochemistry Tables for High-Temperature Gases: Nitrogen**

W. A. Menard and T. E. Horton

Technical Report 32-1408, Vol. IV, December 1, 1970

For abstract, see Menard, W. A.

HULTBERG, J. A.

H26 **Thermal Analysis System I: User's Manual**

J. A. Hultberg and P. F. O'Brien

Technical Report 32-1416, March 1, 1971

A computer program (Thermal Analysis System I) was written to calculate steady-state temperatures for a radiation-conduction-coupled constant-property thermal model. A two-region spectral analysis is provided for the radiation portion of the computation. The "script $\mathcal{F}$" technique is used for infrared heat transfer, and the radiosity technique is used for solar heat input. The program is designed for maximum ease of use from the user's standpoint. The rules for order and placement of user input data to the program are almost free-form. The output is formatted for ease of user understanding and diagnosis of errors. Some user control of output is provided.

HURD, W. J.

H27 **Digital Clean-Up Loop Transponder for Sequential Ranging System**

W. J. Hurd

Supporting Research and Advanced Development,
Space Programs Summary 37-66, Vol. III, pp. 18–27,
December 31, 1970

The theory, implementation, and experimental performance of an improved ranging transponder for sequential component ranging systems are presented. The new transponder system, called a clean-up loop, regenerates the ranging signal from the signal plus noise at the spacecraft receiver so that only signal and not receiver noise is transmitted on the downlink. The improvement in downlink signal-to-noise ratio afforded by this system is up to 46 dB in the present model, with further improvement possible. This will enable accurate ranging at distances of 31 AU using a low-gain spacecraft antenna, and could solve the uplink noise problem for ranging a solar electric multi-mission spacecraft at closer distances.

H28 Performance of a Phase-Locked Loop During Loss of Signal

W. J. Hurd

Supporting Research and Advanced Development, Space Programs Summary 37-66, Vol. III, pp. 28–32, December 31, 1970

When a phase-locked loop (PLL) is tracking the phase of a signal in noise, and the signal is suddenly removed, the phase error variance increases with time after loss of signal. This article derives the statistics of the N state variables for an Nth order PLL as a function of time after loss of signal. A specific result is that for first-order loops with no frequency offset and for perfect integrator second-order loops, the rms phase error doubles in about $0.4/b_L$ seconds after loss of signal, where b_L is the one-sided loop bandwidth in hertz.

JACKSON, E. B.

J01 DSS 13 Operations

E. B. Jackson

The Deep Space Network, Space Programs Summary 37-66, Vol. II, p. 89, November 30, 1970

Operations at DSS 13 (Venus Deep Space Station) are reported for the period August 16 through October 15, 1970. During this period, the station maintained a reduced schedule of clock synchronization transmissions, continued its support of the program of pulsar observations, participated in cooperative planetary radar experiments with DSS 14 (Mars DSS), and continued development of the Ephemeris Offset Tracking Program. Major maintenance performed on the 1.2-MW, 400-Hz motor–generator set and progress on the FIRE-X program are also reported.

JAFFE, L. D.

J02 *Surveyor* Final Reports—Introduction

L. D. Jaffe and R. H. Steinbacher

Icarus: Int. J. Sol. Sys., Vol. 12, No. 2, pp. 145–155, March 1970

This article introduces a series of articles in this issue that review and summarize preliminary *Surveyor* findings, compare the results from each mission, and, in some cases, give results of analyses made after the publication of the preliminary mission reports issued just subsequent to the end of each mission. Those spacecraft characteristics most necessary to an understanding of the scientific data obtained and the corresponding characteristics of spacecraft operations are discussed here.

J03 *Surveyor* Final Report—Principal Scientific Results From the *Surveyor* Program

L. D. Jaffe, C. O. Alley (University of Maryland), S. A. Batterson (Langley Research Center), E. M. Christensen, S. E. Dwornik (NASA Headquarters), D. E. Gault (Ames Research Center), J. W. Lucas, D. O. Muhleman (California Institute of Technology), R. H. Norton, R. F. Scott (California Institute of Technology), E. M. Shoemaker (U.S. Geological Survey), R. H. Steinbacher, G. H. Sutton (University of Hawaii), and A. L. Turkevich (University of Chicago)

Icarus: Int. J. Sol. Sys., Vol. 12, No. 2, pp. 156–160, March 1970

The successful soft landings made by five *Surveyor* spacecraft permitted detailed examinations of the lunar surface at four mare sites along an equatorial belt and at one highland site in the southern hemisphere. The aiming areas, selected before launch, were chosen after examination of telescopic and *Lunar Orbiter* photographs (except for the *Surveyor I* mission, which preceded the *Lunar Orbiter* flights). All five spacecraft landed within these selected areas. The landing sites were:

Surveyor I. Flat surface inside a 100-km crater in Oceanus Procellarum, 1 radius from the edge of a rimless 200-m crater.

Surveyor III. Interior of a subdued 200-m crater, probably of impact origin, in Oceanus Procellarum.

Surveyor V. Steep, inner slope of a 9- by 12-m crater, which may be a subsidence feature, in Mare Tranquillitatis.

Surveyor VI. Flat surface near a mare ridge in Sinus Medii.

Surveyor VII. Ejecta or flow blanket north of, and less than 1 radius from, the rim of the crater Tycho in the highlands.

The small craters; resolvable rock fragments; particle size; structure and mechanical behavior of the fine material; optical, thermal, and radar characteristics; and chemical composition for these landing sites are described here. Observations of the earth and of the solar corona are also discussed.

J04 Lunar Surface: Changes in 31 Months and Micrometeoroid Flux

L. D. Jaffe

Science, Vol. 170, No. 3962, pp. 1092–1094, December 4, 1970

Comparison of pictures of the lunar surface taken 31 mo apart by *Surveyor III* and *Apollo 12* show only one change in the areas disturbed by *Surveyor*: a 2-mm particle, in a footpad imprint, that may have fallen in from the rim or been kicked in by an approaching astronaut. Vertical walls 6 cm high did not collapse, and dark ejecta remained dark. No meteorite craters as large as 1.5 mm in diameter were seen on a smooth soil surface 20 cm in diameter; this indicates a micrometeoroid flux lower than 4×10^{-7} micrometeoroids/m^2-s at an energy equivalent to about 3×10^{-8} g at 20 km/s. This flux is near the lower limit of previous determinations.

JAWORSKI, W.

J05 *Mariner* Venus–Mercury 1973 Solar Array Components: 500-h Irradiation Test Results

W. Jaworski

Supporting Research and Advanced Development, Space Programs Summary 37-65, Vol. III, pp. 125–131, October 31, 1970

Test results of the 500-h irradiation of *Mariner* Venus–Mercury 1973 solar array components are briefly described. Three identical groups of samples (6 samples in each) have been subjected to testing in the vacuum chamber at 5×10^{-7} torr. A different type of irradiation was applied to each group: ultraviolet, proton, and simultaneous ultraviolet and proton. The fluxes and energy were those likely to be present in the vicinity of Mercury; sample temperature was 140°C (maximum allowable).

The optical measurements of solar reflectance, transmittance, and absorptance do not indicate significant changes caused by the

irradiation applied; however, some components sustained mechanical damage due to possible thermal incompatibility.

J06 Cracking of Filter Layers in a High Performance Solar Cell Filter

W. Jaworski

Supporting Research and Advanced Development,
Space Programs Summary 37-66, Vol. III, pp. 115–117,
December 31, 1970

The incident of cracking of the filter layers in a high performance filter cover for solar cells (modified 4026 filter) has been investigated, and the results are evaluated and discussed. It appears that a probable cause of cracking was a combined effect of induced manufacturing stresses and elevated temperature during the test. There is some evidence to believe that if these manufacturing stresses were absent, this type of filter could perform satisfactorily, and would be suitable for solar arrays designed for the near-sun missions at about 0.5 AU.

JET PROPULSION LABORATORY

J07 *Mariner* Mars 1969 Project Report: Performance

Jet Propulsion Laboratory

Technical Report 32-1460, Vol. II, March 1, 1971

This second of three volumes of the *Mariner* Mars 1969 Project Report describes the performance of the mission by flight and Earth-based elements during the launch and space flight phases. The first volume describes the pre-operational activities, including planning, development and design, manufacture, and testing; the third volume deals with the scientific program, including experiment results.

The dual-spacecraft (*Mariners VI* and *VII*) Mars flyby mission was successfully conducted according to plan. A number of flight anomalies were observed, including a major incident involving the *Mariner VII* spacecraft shortly before its Mars encounter, but these difficulties were overcome. The performance of all elements was generally excellent, and copious scientific data were returned to the Earth, including television pictures, ultraviolet and infrared spectral data, surface-temperature measurements, and other information.

The flight performance of each element is analyzed, problems are discussed, and recommendations based on the experience are presented.

JET PROPULSION LABORATORY: ASTRIONICS DIVISION

J08 *Mariner* Mars 1971: Astrionics [September–October 1970]

Jet Propulsion Laboratory: Astrionics Division

Flight Projects, Space Programs Summary 37-66, Vol. I, pp. 9–12, November 30, 1970

Although the concept of a peripheral belt drive had been proven feasible prior to its selection for the *Mariner* Mars 1971 tape transporter, it had not been adequately mathematically modeled to achieve a thorough understanding of the mechanism. When stick-slip (random incremental tape velocity) occurred at the tape-to-head interface early in the developmental stages of the project, a thorough understanding of the tape tension, tension variation, and mechanism for developing tape tension became inperative. A rigorous analytical model of the transport drive was developed. The quasistatic analysis was used to develop an expression for take-up tension as a function of: (1) pay-out tape tension, (2) deck reel and idler geometry, (3) static force and moment equilibrium, (4) belt and tape elasticity, (5) magnetic head drag, (6) tape length, and (7) the relationships between belt thickness and tape thickness. The analytical model and the conclusions reached are described in this article.

J09 *Viking*, Orbiter System: Astrionics [September–October 1970]

Jet Propulsion Laboratory: Astrionics Division

Flight Projects, Space Programs Summary 37-66, Vol. I, pp. 53–56, November 30, 1970

The *Mariner* engineering data formats were fixed in both length and content. A flight data subsystem using a reprogrammable data format would enable more efficient usage of the data link during the *Viking* missions, since the option would be available to program various subsets of the total telemetry measurement list into the format when they are needed and to program them out of the format at other times. Such a system is described in this article.

JET PROPULSION LABORATORY: DATA SYSTEMS DIVISION

J10 *Mariner* Mars 1971: Data Systems [September–October 1970]

Jet Propulsion Laboratory: Data Systems Division

Flight Projects, Space Programs Summary 37-66, Vol. I, pp. 3–4, November 30, 1970

The mission and test computer system completed the real-time support of the *Mariner* Mars 1971 proof-test-model system tests using a data system based on a single Univac 1219 computer. A second data input subsystem, telemetry assemblers, and remote and local serial interface equipment for intercommunication with display equipment were added to the hardware in order to provide for the simultaneous testing of two flight spacecraft, which began in late-September. A Univac 1219 computer was assigned to each spacecraft for this test phase. By mid-October, sufficient programming development was completed to begin using the Univac 1230 computer and the two Univac 1219 computers in an integrated three-computer system configuration. Activities related to the test phases and the initial use of the new configuration are described in this article.

JET PROPULSION LABORATORY: ENGINEERING MECHANICS DIVISION

J11 *Mariner* Mars 1971: Engineering Mechanics [September–October 1970]

Jet Propulsion Laboratory: Engineering Mechanics Division

Flight Projects, Space Programs Summary 37-66, Vol. I, pp. 21–30, November 30, 1970

Some or all of a spacecraft's mass properties must be known in order to perform launch vehicle performance calculations, spacecraft ΔV capability calculations, autopilot stability and performance analyses, attitude-control gas consumption estimates, and spacecraft/launch-vehicle separation analyses. The analytical and measurement activities to determine the mass properties for the *Mariner* Mars 1971 spacecraft are described, and the measured and calculated values are tabulated.

The second discussion involves an evaluation of the capability of the peak select acceleration control system. This evaluation was necessitated by dynamic test implementation problems encountered during forced vibration testing of the propulsion module. The particular phase of the evaluation that is described was performed with the aid of an analog computer that simulated the dynamic characteristics of the propulsion module and vibration exciter and the vibration exciter and amplifier electrical characteristics. The uniqueness of the evaluation was the combination of the real-time analog simulation of the test structure and shaker system with the actual test control system.

An evaluation was also made of the codispersion propellant expulsion bladder. This bladder is a flexible TFE–FEP Teflon laminate membrane that fits inside a 30-in.-diameter titanium

propellant tank and is pressurized by nitrogen to expel propellants contained therein under 0-*g* conditions. This article summarizes some significant test results on the codispersion material derived prior to production of flight bladders of this type.

The final discussion involves an evaluation of the spacer rod material for the spring-loaded spacer system employed by the narrow-angle television camera to maintain dimensional requirements between critical optical elements. The tests were made on random samples to verify material requirements and to obtain property data.

J12 *Viking*, Orbiter System: Engineering Mechanics [September–October 1970]

Jet Propulsion Laboratory: Engineering Mechanics Division

Flight Projects, Space Programs Summary 37-66, Vol. I, pp. 51–52, November 30, 1970

This article discusses the *Viking*-spacecraft/*Centaur* adapter and the orbiter/lander adapter separation interfaces. Each separation interface consists of four dual-squib release-nut mechanisms that provide the structural load path across the four interface hardpoints and four caged stoke spring assemblies that provide the separation force.

JET PROPULSION LABORATORY: GUIDANCE AND CONTROL DIVISION

J13 *Mariner* Mars 1971: Guidance and Control [September–October 1970]

Jet Propulsion Laboratory: Guidance and Control Division

Flight Projects, Space Programs Summary 37-66, Vol. I, pp. 4–8, November 30, 1970

Calibration of the reference and telemetry/monitor potentiometers that was performed on the scan electronics proof test model is described in this article. The calibration procedure was developed for use on the *Mariner* Mars 1971 Project. The reference potentiometers store the scan platform reference angles in such a way that each stored angle is proportional to the voltage on the reference potentiometer wiper. The telemetry/monitor potentiometer is mechanically coupled to the reference potentiometer and is used to monitor the position of the reference potentiometer and, hence, the stored reference angle. The stored angle may be varied in increments by stepping the reference potentiometer shaft by a drive mechanism. Calibration was

achieved by recording the potentiometer wiper positions as functions of a number of position increments.

An important activity in building an attitude-control gas system is the proper sizing of the gas nozzles to meet spacecraft control torque requirements. A nozzle-sizing computer analysis program and a thrust measurement stand are utilized. With two exceptions that necessitated additional test work, the procedure is similar to that developed for the *Mariner* Mars 1969 Project. The two exceptions, the test program, and the resulting conclusions are discussed.

J14 *Viking*, Orbiter System: Guidance and Control [September–October 1970]

Jet Propulsion Laboratory: Guidance and Control Division

Flight Projects, Space Programs Summary 37-66, Vol. I, pp. 47–51, November 30, 1970

During the orbit of Mars by the *Viking* orbiter system, the Sun will periodically be occulted. The design of the circuit for automatic sensing of occultation and the associated logic is presented in this article.

An articulation control subsystem has been proposed for the *Viking* spacecraft. Similar subsystems whose prime function is the articulation of bodies on spacecraft would be combined into a single subsystem. This article describes the design of a stepper motor control system that offers an excellent opportunity for a substantial hardware savings by multiplexing or time-sharing a major portion of the circuitry among the various functions in the subsystems. This is possible without any degradation in accuracy or performance. The only difference between the two designs being evaluated is the error-correction technique. One employs an error-actuated constant-rate mechanization, while the other corrects continuously, using a rate proportional to the error amplitude. A description of the systems functional elements and the results of an error analysis are included.

JET PROPULSION LABORATORY: *MARINER* MARS 1971 PROJECT

J15 *Mariner* Mars 1971: Project Description [September–October 1970]

Jet Propulsion Laboratory: *Mariner* Mars 1971 Project

Flight Projects, Space Programs Summary 37-66, Vol. I, pp. 1–2, November 30, 1970

The primary objective of the *Mariner* Mars 1971 Project is to place two spacecraft in orbit around Mars that will be used to perform scientific experiments directed toward achieving a better understanding of the physical characteristics of that planet. Principal among these experiments are measurements of atmospheric and surface parameters at various times and locations to determine the dynamic characteristics of the planet. An engineering objective is to demonstrate the ability of the spacecraft to perform orbital operations in an adaptive mode wherein information from one orbital pass is used to develop the operations plan for subsequent orbital passes. Specific mission objectives, the spacecraft, its scientific experiments, and management and support responsibilities for the project are briefly described.

JET PROPULSION LABORATORY: *MARINER* VENUS–MERCURY 1973 PROJECT

J16 *Mariner* Venus–Mercury 1973: Project Description [September–October 1970]

Jet Propulsion Laboratory: *Mariner* Venus–Mercury 1973 Project

Flight Projects, Space Programs Summary 37-66, Vol. I, p. 31, November 30, 1970

The primary objective of the *Mariner* Venus–Mercury 1973 Project is to launch one spacecraft in October 1973 to obtain environmental and atmospheric data for the planet Venus in February 1974 and to conduct exploratory investigations of the planet Mercury's environment, atmosphere, surface, and body characteristics some 7 wk later, with first priority assigned to the Mercury investigations. The secondary objectives are to perform interplanetary experiments enroute to Mercury and to obtain experience with the gravity-assist mission mode. The spacecraft, its scientific experiments, and preliminary project planning are described.

JET PROPULSION LABORATORY: PROPULSION DIVISION

J17 *Mariner* Mars 1971: Propulsion [September–October 1970]

Jet Propulsion Laboratory: Propulsion Division

Flight Projects, Space Programs Summary 37-66, Vol. I, pp. 12–21, November 30, 1970

The *Mariner* Mars 1971 spacecraft incorporates an on-board modularized propulsion subsystem to furnish impulse to the

spacecraft for trans-Mars trajectory correction, orbit insertion, and orbit trims. The propulsion subsystem operates on the liquid propellants nitrogen tetroxide and monomethylhydrazine. The effects of propellant saturation with gaseous nitrogen on the hydraulic resistance are discussed.

Standard laminate Teflon bladder bags employed as liquid-propellant expulsion devices have failed due to the formation of tears and cracks near an aluminum seal ring that forms the mouth of the bag. These failures occurred during flight-acceptance tests in which various solvents were used as referee fuels. From a consideration of the conditions imposed on the bags during the tests, it was recognized that the neck regions of the bags are biaxially stressed while, at the same time, being bathed by the test solvent. This article presents the results of a study on the effects of solvents on the biaxial properties of standard laminate materials. Also included are test results obtained on a new candidate material designated codispersion laminate, as well as the results of a study on the effects of solvents on the Teflon components used in the construction of the laminate materials.

JET PROPULSION LABORATORY: SPACE SCIENCES DIVISION

J18 *Mariner* Venus–Mercury 1973: Space Sciences [September–October 1970]

Jet Propulsion Laboratory: Space Sciences Division

Flight Projects, Space Programs Summary 37-66, Vol. I, pp. 32–37, November 30, 1970

The objectives of the *Mariner* Venus–Mercury 1973 imaging experiment are to: (1) map and identify the major physiographic province of Mercury on the basis of topographic forms and optical properties of surface materials; (2) determine the similarities and differences between the major surface features of Mercury and those on the earth, the moon, and Mars, with special emphasis on the recognition of endogenic structures; (3) determine the distribution of surface features with reference to the dynamic axes of Mercury and investigate the boundaries with surrounding terrain; and (4) establish correlations with earth-based observations. For the planet Venus, close-up photography will produce additional spectral, radio emission, and radio occultation observations. This article discusses the scientific information about the planets that will be obtained with the experiment, the interplanetary measurements that will be performed,

the in-flight calibration and test observations, and the preliminary mission sequence. A description of the television subsystem is included.

JET PROPULSION LABORATORY: TELECOMMUNICATIONS DIVISION

J19 *Mariner* Venus–Mercury 1973: Telecommunications [September–October 1970]

Jet Propulsion Laboratory: Telecommunications Division

Flight Projects, Space Programs Summary 37-66, Vol. I, pp. 37–41, November 30, 1970

It is planned that the *Mariner* Venus–Mercury 1973, as well as the *Mariner* Mars 1971 and *Viking*, spacecraft communications systems will use science data words whose lengths are different from the 6-bit block-coded words that will be transmitted over the spacecraft-to-earth communications links and received with the multi-mission telemetry system of the Deep Space Network. In the analysis presented in this article, science words of length M bits are assumed to be serially time-multiplexed onto the 6-bit words. These 6-bit words are mapped onto (32,6) biorthogonal coded words and transmitted from the spacecraft to earth. The 6-bit coded words are received and block decoded, and then the science words are decommutated from the received serial bit stream. The analysis shows the error rate for the data words of various word lengths when the error rate for 6-bit coded words is known.

J20 *Viking*: Telecommunications [September–October 1970]

Jet Propulsion Laboratory: Telecommunications Division

Flight Projects, Space Programs Summary 37-66, Vol. I, pp. 43–47, November 30, 1970

The *Viking* relay link will operate at various times during the mission to provide the capability for lander-to-orbiter (uplink) and orbiter-to-lander (downlink) communications via a UHF channel. The uplink will be supported by a telemetry transmitter in the lander and a telemetry receiver/detector in the orbiter. The downlink will be supported by an amplitude-modulated transmitter in the orbiter and a receiver/tone detector in the lander. Previous flight projects have not used relay links, and the design of this link represents a first effort in many areas.

Accordingly, little experience is available on which to base predictions of performance. To ensure integrity of design and to evaluate link parameters, a simulation program was undertaken to duplicate link signals at various mission phases and to measure actual equipment responses. The background, objectives, and test configuration for this simulation program are described in this article.

JET PROPULSION LABORATORY: *VIKING* PROJECT

J21 *Viking*: Project Description and Status [September–October 1970]

Jet Propulsion Laboratory: *Viking* Project

Flight Projects, Space Programs Summary 37-66, Vol. I, pp. 42–43, November 30, 1970

The primary objective of the *Viking* Project is to significantly advance current knowledge of the planet Mars by direct measurements in the atmosphere and on the surface and by observations of the planet during approach and from orbit. Particular emphasis will be placed on obtaining information concerning biological, chemical, and environmental factors relevant to the existence of life on the planet at this time or some time in the past or the potential for the development of life in the future. Two spacecraft, each consisting of an orbiter system and a lander system, are planned for launch during the 1975 opportunity. The orbiter system is being developed by JPL; Langley Research Center is responsible for the lander system, being developed under contract by the Martin-Marietta Corporation. Langley Research Center also has overall management responsibility for the project. The specific objectives for the orbiter system and the lander system are described. Status information includes reviews, breadboard testing, and engineering model design.

JUVINALL, G. L.

J22 Studies of the Reaction Geometry of the Alkaline Silver Electrode

G. L. Juvinall

Supporting Research and Advanced Development, Space Programs Summary 37-65, Vol. III, pp. 82–84, October 31, 1970

The results of studies of the phenomena occurring at the surface of the alkaline silver electrode during electrochemical oxidation are reported. The scanning electron microscope was used for observing the reaction sites. The unique capabilities of this instrument permit definite conclusions to be drawn concerning the nature of the reactions taking place on the electrode surface. Photographs with magnification in the range of 10,000 to 13,000 are included.

KALFAYAN, S. H.

K01 Evaluation of Spacecraft Magnetic Recording Tapes and Magnetic Heads [August–September 1970]

S. H. Kalfayan, R. H. Silver, and J. K. Hoffman

Supporting Research and Advanced Development,
Space Programs Summary 37-65, Vol. III, pp. 168–171,
October 31, 1970

Monel-metal-bracketed magnetic heads were compared to brass-bracketed heads in their behavior toward 3M 20250 magnetic recording tape. The two kinds of heads showed about the same degree of frictional resistance and stickiness, under various environmental conditions, to new, outgassed, and "vacoted" 3M 20250 tape specimens.

K02 Evaluation of Recording Tape and Heads for Spacecraft Magnetic Tape Recorder Applications [October–November 1970]

J. K. Hoffman, S. H. Kalfayan, and R. H. Silver

Supporting Research and Advanced Development,
Space Programs Summary 37-66, Vol. III, p. 160,
December 31, 1970

For abstract, see Hoffman, J. K.

K03 Evaluation of Magnetic Recording Tapes: A Method for the Quantitative Determination of Stick-Slip

R. H. Silver, S. H. Kalfayan, and J. K. Hoffman

Supporting Research and Advanced Development,
Space Programs Summary 37-66, Vol. III, pp. 198–200,
December 31, 1970

For abstract, see Silver, R. H.

KATOW, M. S.

K04 DSN Progress Report for November–December 1970: Antenna Structures: Evaluation of Reflector Surface Distortions

M. S. Katow

Technical Report 32-1526, Vol. I, pp. 76–80,
February 15, 1971

The reflector surface distortions of the 210-ft-diam antenna, as evaluated by the linearized formulation of the rms paraboloid best-fitting computer program, has provided sufficient significant digits in its answers for meaningful results. This article presents a clearer documentation as well as the error bounds of the formulation. Since basically the solution is a non-linear problem, improved formulation would be desirable. However, the program should be useful for evaluating larger than 210-ft-diam antennas with about the same degree of distortion.

KELLER, O. F.

K05 Material Compatibility [August–September 1970]

O. F. Keller and L. R. Toth

Supporting Research and Advanced Development,
Space Programs Summary 37-65, Vol. III, pp. 180–181,
October 31, 1970

A material compatibility program is in progress to evaluate the effects of long-term storage of earth-storable propellants with selected materials of construction for spacecraft propulsion systems. All aspects of the total system are considered and include propellant, material, test fixture, test container, instrumentation, test environment, and facility. The present status of specimen/capsule testing at the Edwards Test Station is reported. Fuel specimen/capsules, under test at 110°F, are described and preliminary results of post-test evaluations are discussed.

KINNEY, T. P.

K06 A System of Computer Programs for Interactive Trajectory Design

T. P. Kinney

Supporting Research and Advanced Development,
Space Programs Summary 37-65, Vol. III, pp. 12–15,
October 31, 1970

Mission trajectory design has been accomplished at JPL with the aid of various computer programs that are run sequentially. The procedure is vulnerable to delays caused by normal processing of the individual computer runs. The Flight Path Design (system of) Program(s), FPDP, allows the analyst to perform a major portion of necessary design work from a remote computer terminal. Intermediate graphical output is displayed on a cathode-ray tube. The analyst interacts with FPDP, modifying parameters and cueing programs, thus obtaining in a single computer run results which previously required several passes. Significant decreases in both man and machine time can be achieved.

KNOELL, A. C.

K07 Basic Concepts in Composite Beam Testing

J. V. Mullin (General Electric Company) and A. C. Knoell

Mater. Res. Stan., Vol. 10, No. 12, pp. 16–33, December 1970

For abstract, see Mullin, J. V.

KOCH, R. E.

K08 The *Mariner VI* and *VII* Flight Paths and Their Determination From Tracking Data

H. J. Gordon, D. W. Curkendall, D. A. O'Handley, N. A. Mottinger, P. M. Muller, C. C. Chao, B. D. Mulhall, V. J. Ondrasik, S. K. Wong, S. J. Reinbold, J. W. Zielenback, J. K. Campbell, R. T. Mitchell, J. E. Ball, W. G. Breckenridge, T. C. Duxbury, and R. E. Koch

Technical Memorandum 33-469, December 1, 1970

For abstract, see Gordon, H. J.

KOLBLY, R. B.

K09 Switched-Carrier Experiments

R. B. Kolbly

The Deep Space Network, Space Programs Summary 37-66, Vol. II, pp. 84–88, November 30, 1970

This article describes experiments to investigate the feasibility of time sharing a klystron amplifier between two uplink channels in order to simultaneously track two spacecraft. Two frequency experiments are described.

KROLL, G.

K10 **DSS 61/63 Facility Modifications and Construction**

R. Casperson, G. Kroll, and L. Kushner

The Deep Space Network, Space Programs Summary 37-66, Vol. II, pp. 154–158, November 30, 1970

For abstract, see Casperson, R.

KUIPER, G. P.

K11 ***Surveyor* Final Report—Lunar Theory and Processes: Discussion of Chemical Analysis**

R. A. Phinney (Princeton University), D. E. Gault (Ames Research Center), J. A. O'Keefe (Goddard Space Flight Center), J. B. Adams, G. P. Kuiper (University of Arizona), H. Masursky (U.S. Geological Survey), E. M. Shoemaker (U.S. Geological Survey), and R. J. Collins (University of Minnesota)

Icarus: Int. J. Sol. Sys., Vol. 12, No. 2, pp. 213–223, March 1970

For abstract, see Phinney, R. A.

K12 ***Surveyor* Final Report—Lunar Theory and Processes: Post-Sunset Horizon "Afterglow"**

D. E. Gault (Ames Research Center), J. B. Adams, R. J. Collins (University of Minnesota), G. P. Kuiper (University of Arizona), J. A. O'Keefe (Goddard Space Flight Center), R. A. Phinney (Princeton University), and E. M. Shoemaker (U.S. Geological Survey)

Icarus: Int. J. Sol. Sys., Vol. 12, No. 2, pp. 230–232, March 1970

For abstract, see Gault, D. E.

KURIGER, W. L.

K13 **A Proposed Laser Obstacle Detection Sensor for a Mars Rover**

W. L. Kuriger (University of Oklahoma)

Supporting Research and Advanced Development, Space Programs Summary 37-66, Vol. III, pp. 80–89, December 31, 1970

A mechanization is proposed for a laser obstacle detector that has characteristics appropriate for a Mars rover. This application will require the utmost possible in simplicity, small size, and

minimum power needs. A pulsed gallium–arsenide laser is suggested, scanned in a vertical plane, together with an avalanche photodiode detector for ranging between 5 and 30 m. A discussion of a simple signal-processing technique is included, and the expected signal-to-noise ratio is calculated.

KUSHNER, L. H.

K14 DSS 61/63 Facility Modifications and Construction

R. Casperson, G. Kroll, and L. Kushner

The Deep Space Network, Space Programs Summary 37-66, Vol. II, pp. 154–158, November 30, 1970

For abstract, see Casperson, R.

K15 85-ft-diam Antenna Tracking Station Power Plant Reconfiguration

L. H. Kushner

The Deep Space Network, Space Programs Summary 37-66, Vol. II, pp. 159–160, November 30, 1970

The existing power plants of the seven Deep Space Instrumentation Facility 85-ft tracking stations are planned for reconfiguration. This article summarizes the reconfiguration plans, which include modification/rearrangement of existing power plant equipment and installation of new equipment. The final configuration is directed toward a standardization of power generating units consisting of one size diesel engine (Caterpillar D-398) driving 350- and 50-kW generators. This standardization provides for required operational power growth of stations with minimum number of different size/ratings of engine–generator units.

LACY, G. H.

L01 Soil Microbial and Ecological Investigations in the Antarctic Interior

R. E. Cameron, R. B. Hanson, G. H. Lacy, and F. A. Morelli

Antarc. J. U.S., Vol. V, No. 4, pp. 87–88, July–August 1970

For abstract, see Cameron, R. E.

L02 Microbiological Analyses of Snow and Air From the Antarctic Interior

G. H. Lacy, R. E. Cameron, R. B. Hanson, and F. A. Morelli

Antarc. J. U.S., Vol. V, No. 4, pp. 88–89, July–August 1970

Snow and air were collected by aseptic techniques and examined for the presence of microorganisms at the Beardmore camp (approximately 84°17′S, 162°22′E; 2100-m elevation) on the Walcott Névé, Queen Alexandra Range, during the austral summer 1969–1970. The results of the analyses performed are briefly discussed in this article.

LAESER, R. P.

L03 DSN Progress Report for November–December 1970: *Mariner* Mars 1971 Mission Support

R. P. Laeser

Technical Report 32-1526, Vol. I, pp. 4–6, February 15, 1971

The Deep Space Network (DSN) support plans for the *Mariner* Mars 1971 mission have been modified by a move of the analog playback function from the Space Flight Operations Facility media conversion center to the Deep Space Instrumentation Facility Compatibility Test Area and by the DSN assumption of the responsibility for sequence of event generation computer software. Both of these new plans are discussed.

LA FRIEDA, J.

L04 Space Station Unified Communication: Optimum Performance of Two-Channel High-Rate Interplex Systems

J. La Frieda

Supporting Research and Advanced Development, Space Programs Summary 37-65, Vol. III, pp. 31–36, October 31, 1970

The optimum data efficiency and bit-error performance of two-channel digital coherent systems are determined, where the data signals phase-modulate an RF carrier with biphase-modulated sine-wave subcarriers. Two types of phase modulation are considered: linear binary phase-shift keying (BPSK) and interplex BPSK. It is shown that interplex BPSK outperforms linear BPSK and that the improvement in performance increases as the ratio of channel data rates (power) approaches unity. The sine-wave subcarriers considered are necessary in the Manned Space Station, where the data rates are so high that square-wave subcarriers can not be considered.

LANDEL, R. F.

L05 On the Presence of Crystallinity in Hydrogenated Polybutadienes

J. Moacanin, A. Eisenberg (McGill University, Canada), E. F. Cuddihy, D. D. Lawson, B. G. Moser (Moser Dental Manufacturing Company), and R. F. Landel

Technical Report 32-1512 (Reprinted from *J. Appl. Polym. Sci.*, Vol. 14, No. 9, pp. 2416–2420, September 1970)

For abstract, see Moacanin, J.

LAUE, E.

L06 Multichannel Radiometer Narrow-Band Solar Spectral Irradiance at 75 km

E. Laue

Supporting Research and Advanced Development, Space Programs Summary 37-65, Vol. III, pp. 158–162, October 31, 1970

Spectral filter radiometric measurements of the solar irradiance obtained during an X-15 flight approximately 80 km above the earth's surface are compared with four normalized solar spectral curves. A solar spectral irradiance curve is developed using portions of those curves whose integrated pass-band values most nearly approach the X-15 measurements.

LAWSON, D. D.

L07 On the Presence of Crystallinity in Hydrogenated Polybutadienes

J. Moacanin, A. Eisenberg (McGill University, Canada), E. F. Cuddihy, D. D. Lawson, B. G. Moser (Moser Dental Manufacturing Company), and R. F. Landel

Technical Report 32-1512 (Reprinted from *J. Appl. Polym. Sci.*, Vol. 14, No. 9, pp. 2416–2420, September 1970)

For abstract, see Moacanin, J.

LAYLAND, J. W.

L08 An Optimum Squaring Loop Prefilter

J. W. Layland

IEEE Trans. Commun. Technol., Vol. COM-18, No. 5, pp. 695–697, October 1970

Squaring loops are often discussed as a means of establishing a coherent carrier reference for bi-phase PSK (phase-shift-keyed) modulation. The optimal presquaring filter is derived under the assumptions that the modulating spectrum is narrow with respect to the carrier frequency and that the phase-locked loop bandwidth is much narrower than the modulating spectrum.

LEAHEY, C. F.

L09 **DSN Progress Report for November–December 1970: Mark IIIA Simulation Center EMR 6050–Univac 1108 Computer Interface**

C. F. Leahey

Technical Report 32-1526, Vol. I, pp. 88–92, February 15, 1971

The Mark IIIA simulation center is capable of simultaneously simulating two spacecraft and three deep space stations using the Univac 1108 and EMR 6050 computers. The EMR 6050 and the Univac 1108 were interfaced using Bell System 303C modems and a JPL-designed interface adapter. The design of the interface was constrained by two factors: (1) the final location of the Univac 1108 was undetermined at the time of finalization of the interface assembly design, and (2) the EMR 6050 and the Univac 1108 have different word lengths. The hardware and software approaches used to satisfactorily mate the two computers are explained.

LEAVITT, R. K.

L10 **DSN Progress Report for November–December 1970: Refractivity Influence on DSS Doppler Data**

F. B. Winn and R. K. Leavitt

Technical Report 32-1526, Vol. I, pp. 31–41, February 15, 1971

For abstract, see Winn, F. B.

LEONARD, W. D.

L11 **Thermoelectric Generator Performance Correlation**

W. D. Leonard (Resalab, Inc.)

Supporting Research and Advanced Development, Space Programs Summary 37-65, Vol. III, pp. 89–95, October 31, 1970

The experimental test results of a thermoelectric generator were compared to the analytically predicted performance. The generator under consideration was a thermoelectric generator designed and built by RCA and referred to as the RCA reference design converter. The method used to calculate the performance of the generator is detailed to illustrate the flexibility of a computer code to predict the performance of a variety of thermoelectric generator designs. Included in the analysis is the method used to account for extraneous resistance and shunt heat losses.

LEVY, G. S.

L12 The Quasi-Stationary Coronal Magnetic Field and Electron Density as Determined From a Faraday Rotation Experiment

C. T. Stelzried, G. S. Levy, T. Sato, W. V. T. Rusch (University of Southern California), J. E. Ohlson, (University of Southern California), K. H. Schatten (Goddard Space Flight Center), and J. M. Wilcox (University of California, Berkeley)

Sol. Phys., Vol. 14, No. 2, pp. 440–456, October 1970

For abstract, see Stelzried, C. T.

LEVY, R.

L13 DSN Progress Report for November–December 1970: Antenna Rigging Angle Optimization Within Structural Member Size Design Optimization

R. Levy

Technical Report 32-1526, Vol. I, pp. 81–87, February 15, 1971

It is shown in this article that the horizon rms deviation of the antenna from the best-fitting paraboloid is a representative measure of the cosine-weighted average rms for the complete elevation attitude range. Therefore, the horizon rms can be used as a substitute merit function in a structural redesign program that generates improved member size distributions to reduce the weighted-average rms. Validity of the substitution follows because: (1) the optimal rigging angle is a slowly changing function of changes in member size distributions; (2) the weighted average rms is not sensitive to small rigging angle changes; (3) at rigging angles near the optimal, ranking according to the minimum horizon rms is equivalent to ranking according to the

minimum cosine-weighted average for alternative designs with different member size distributions.

LEWIS, J. C.

L14 Crack Propagation Threshold for Isopropanol and Ti–6Al–4V Titanium Alloy

J. C. Lewis

Supporting Research and Advanced Development,
Space Programs Summary 37-65, Vol. III, pp. 131–135,
October 31, 1970

Stress corrosion crack propagation data for isopropanol and Ti-6Al-4V titanium alloy are reported. The fracture mechanics approach was used to determine the stress intensity at which crack growth began in isopropanol at 70–80°F and 300 ±20 psig for 96 h. A threshold of approximately 38 ksi-in.$^{1/2}$ was observed for isopropanol as compared to approximately 40 ksi-in.$^{1/2}$ for inhibited nitrogen tetroxide on the same material under the same conditions.

LEWIS, R. A.

L15 A Computerized Landmark Navigator: Development and Test Plan

R. A. Lewis

Supporting Research and Advanced Development,
Space Programs Summary 37-65, Vol. III, pp. 1–2,
October 31, 1970

A computer program that determines the position and heading of a roving vehicle on the lunar surface has been developed. The assumptions, hardware, and inputs required by the algorithm are minimal in the sense that the requirements of the program are met by the general lunar terrain and baseline roving vehicle. This article describes the algorithm, the use of the computer program, and a planned series of tests to evaluate the capabilities of the program.

L16 Roving Vehicle Navigation Subsystem Feasibility Study: Inertial and Gyrocompass/Odometer Navigators

R. A. Lewis

Supporting Research and Advanced Development,
Space Programs Summary 37-65, Vol. III, pp. 105–107,
October 31, 1970

A roving vehicle motion control computer simulation has been applied to determine the feasibility of two automated roving vehicle navigation subsystems. An inertial navigator using a triad of mutually orthogonal accelerometers mounted on a platform stabilized by three single-degree-of-freedom gyros was simulated and the configuration was found to be infeasible when the characteristics of state-of-the-art hardware were assumed. A navigation configuration using gyrocompass and odometer was found to be feasible under the assumptions of the study.

LI, S. P.

L17 A Survey of Hardening Techniques for a Complementary-Symmetry MOSFET Memory

S. P. Li

Supporting Research and Advanced Development,
Space Programs Summary 37-65, Vol. III, pp. 152–155,
October 31, 1970

Current techniques in hardening metal-oxide semiconductor devices against radiation damage are surveyed and reported, with the possibility of a complementary-symmetry metal-oxide semiconductor field-effect transistor (MOSFET) memory on long missions considered. The silicon oxynitride film, in place of silicon dioxide in the regular MOSFET, appears most promising. Sufficiently hard laboratory samples are already available, while large scale integration techniques are yet to be developed.

L18 Jupiter's Electron Dose Calculations on Metal Oxide Semiconductor Structures

S. P. Li and J. B. Barengoltz

Supporting Research and Advanced Development,
Space Programs Summary 37-66, Vol. III, pp. 166–170,
December 31, 1970

Estimates of the effects on metal oxide semiconductor devices onboard an outer-planet spacecraft due to the trapped electrons at Jupiter have been made. The system was modeled by an aluminum–silicon sandwich, lying behind a magnesium shield. The aluminum layer was taken to be 6000 angstrom, the silicon layer 2000 angstrom, and the magnesium shield between 50 and 500 mils thick. The ionization dose absorbed by the silicon due to a suitable spectral model of Jovian electrons was calculated, including bremsstrahlung. Results of the calculations show an expected dose due to electrons of 2×10^4 rad, to which the bremsstrahlung contribution was less than 3%.

LIKINS, P. W.

L19 **Finite Element Modeling for Appendage Interaction With Spacecraft Control**

P. W. Likins (University of California, Los Angeles) and E. L. Marsh

Supporting Research and Advanced Development, Space Programs Summary 37-66, Vol. III, pp. 100–105, December 31, 1970

A hybrid coordinate formulation has been previously developed and applied to the analysis of the effect of flexible appendages on spacecraft flight control systems. This article presents a synopsis of an improved flexible appendage model which utilizes finite element analysis. This model has been incorporated into the hybrid coordinate formulation. The finite element analysis provides for more accurate prediction of spacecraft flight control performance.

LINDSEY, W. C.

L20 **The Effect of Loop Stress on the Performance of Phase-Coherent Communication Systems**

W. C. Lindsey (University of Southern California) and M. K. Simon

IEEE Trans. Commun. Technol., Vol. COM-18, No. 5, pp. 569–588, October 1970

In phase-coherent communication systems which use phase-locked loops to provide synchronization of the data detector, the communications engineer is frequently faced with the problem of determining the effects of noisy timing upon detection efficiency. This paper is concerned with determining these effects when second-order phase-locked loops, operating in the presence of frequency detuning, are used as a means of providing phase synchronization. The results are also applicable to the problem of establishing noisy reference losses in a broad class of coherent pulse-code-modulated telemetry systems (e.g., pulse-code-modulated/phase-shift-keyed/phase-modulated). Also presented are results which can be used to determine steady-state statistical dynamics of second-order loops.

LIVANOS, A. C. R.

L21 **Diffraction of a High-Order Gaussian Beam by an Aperture**

A. C. R. Livanos

Supporting Research and Advanced Development, Space Programs Summary 37-66, Vol. III, pp. 181–186, December 31, 1970

In this article the diffraction of a high-order gaussian beam by an aperture is examined. The beam considered corresponds to the transfer electromagnetic mode of a laser, which, after leaving the resonator, is focused by a lens and then diffracted by an aperture located at the focal point. The intensity distribution of the diffracted beam is calculated using Huygen's principle, and employing approximations that are weaker than those of Fresnel and Fraunhofer.

LUCAS, J. W.

L22 *Surveyor* Final Report—Principal Scientific Results From the *Surveyor* Program

L. D. Jaffe, C. O. Alley (University of Maryland), S. A. Batterson (Langley Research Center), E. M. Christensen, S. E. Dwornik (NASA Headquarters), D. E. Gault (Ames Research Center), J. W. Lucas, D. O. Muhleman (California Institute of Technology), R. H. Norton, R. F. Scott (California Institute of Technology), E. M. Shoemaker (U.S. Geological Survey), R. H. Steinbacher, G. H. Sutton (University of Hawaii), and A. L. Turkevich (University of Chicago)

Icarus: Int. J. Sol. Sys., Vol. 12, No. 2, pp. 156–160, March 1970

For abstract, see Jaffe, L. D.

L23 Revised Lunar Surface Thermal Characteristics Obtained From the *Surveyor V* Spacecraft

L. D. Stimpson and J. W. Lucas

J. Spacecraft Rockets, Vol. 7, No. 11, pp. 1317–1322, November 1970

For abstract, see Stimpson, L. D.

LUNDY, C. C.

L24 Thrust Collar Survey (DSS 14)

C. C. Lundy

The Deep Space Network, Space Programs Summary 37-66, Vol. II, pp. 77–80, November 30, 1970

In the 210-ft-diameter antennas, radial loads of a few hundred tons exist between the rotating alidade and the fixed thrust collar. The thrust collar resists these loads and also defines the axis of rotation in azimuth. This article describes the installation of 24 monuments in the radial bearing thrust collar at DSS 14 (Mars Deep Space Station). The monuments form a net of surveyed points from which the circularity of the radial bearing runner can be measured.

LUTWACK, R.

L25 Permeability of Membranes

R. Lutwack

Supporting Research and Advanced Development, Space Programs Summary 37-65, Vol. III, p. 81, October 31, 1970

The diffusive transport of K^+, H_2O, and Zn species has been measured for a system containing the SWRI-GX separator material and concentrated KOH solutions. The value of the mass transfer coefficient for Zn makes untenable the assumption that only the $Zn(OH)_4^=$ species is present in the KOH solutions.

LYON, R. B.

L26 Improved RF Calibration Techniques: A Study of the RF Properties of the 210-ft-diam Antenna Mesh Material

T. Y. Otoshi and R. B. Lyon

The Deep Space Network, Space Programs Summary 37-66, Vol. II, pp. 52–57, November 30, 1970

For abstract, see Otoshi, T. Y.

L27 Improved RF Calibration Techniques: PDS Cone Waveguide/Polarimeter Calibrations

P. D. Batelaan, B. Seidel, and R. B. Lyon

The Deep Space Network, Space Programs Summary 37-66, Vol. II, pp. 61–63, November 30, 1970

For abstract, see Batelaan, P. D.

MacDORAN, P. F.

M01 DSN Progress Report for November–December 1970: Probing the Solar Plasma With *Mariner* Radio Metric Data, Preliminary Results

P. F. MacDoran, P. S. Callahan, and A. I. Zygielbaum

Technical Report 32-1526, Vol. I, pp. 14–21, February 15, 1971

A radio technique exploiting the opposite changes of group and phase velocity in a dynamic plasma was used to probe the solar corona during the superior conjunctions of the *Mariner VI* and *VII* spacecraft. From an analysis of range and doppler radio metric data generated by the Deep Space Network (DSN) in tracking the spacecraft, it was possible to establish a correspondence between plasma fluctuations in the radio raypath and McMath sunspot regions on the solar surface. Estimates of 3000 electrons/cm^3 and scale sizes of 6×10^4 and 2×10^6 km were made for plasma clouds transisting the radio path when tracking within a few degrees of the sun.

MacGLASHAN, W. F.

M02 Component Storage With Propellants

W. F. MacGlashan and L. R. Toth

Supporting Research and Advanced Development, Space Programs Summary 37-65, Vol. III, p. 179, October 31, 1970

Fill valves and service connections were tested for 3 mo with pressurized (400 psig) OF_2 and B_2H_6 at $-230°F$. A separate environmental testing chamber was used for each of the two propellants. Each chamber contained an aluminum, stainless steel, and titanium fill valve and two service connections. Post-test evaluations for internal leakage are being performed and the work will be concluded with a metallurgical analysis of all components.

MACK, L. M.

M03 Response of Supersonic Laminar Boundary Layer to a Moving External Pressure Field

L. M. Mack

Supporting Research and Advanced Development, Space Programs Summary 37-66, Vol. III, pp. 13–16, December 31, 1970

The response of a laminar boundary layer to the external pressure field created by a wavy wall moving supersonically with respect to the free stream is computed numerically using modifications of the inviscid and viscous computer programs originally developed for linear stability theory. Specific results are given at a free-stream Mach number of 4.5 for an insulated-wall boundary layer. It is found that an effective amplification occurs at low Reynolds number which increases the peak mass-flow fluctuation in the boundary layer by 10–20 times over the free-stream value of the external pressure field. The Reynolds number at which this amplification ceases increases with decreasing frequency and is well within the laminar instability region for a wide range of frequencies.

MARKO, W. J.

M04 Near-Field Supersonic Boom Pressure Tests in the JPL 20-in. Supersonic Wind Tunnel

W. J. Marko

Supporting Research and Advanced Development, Space Programs Summary 37-65, Vol. III, pp. 156–157, October 31, 1970

Near-field supersonic boom pressure measurements have been recorded for ten combinations of two wing and five nose configurations in the JPL 20-in. supersonic wind tunnel at Mach numbers of 1.68 and 2.7. Data demonstrating the effects of lift and configuration changes on the near-field overpressure were obtained.

MARSH, E. L.

M05 The Attitude Control of a Flexible Solar Electric Spacecraft

E. L. Marsh

Supporting Research and Advanced Development, Space Programs Summary 37-66, Vol. III, pp. 92–99, December 31, 1970

The problem of the attitude control of a solar electric spacecraft is studied. A linear analysis of the system of differential equations of attitude motion was performed. Root locus and eigenvalue procedures were utilized for determining stable configurations. Parametric studies, where the varying parameters were the gains of the sensor units associated with the control system, were made.

M06 Finite Element Modeling for Appendage Interaction With Spacecraft Control

P. W. Likins (University of California, Los Angeles) and E. L. Marsh

Supporting Research and Advanced Development, Space Programs Summary 37-66, Vol. III, pp. 100–105, December 31, 1970

For abstract, see Likins, P. W.

MARTIN, K. E.

M07 Radiation Effects on Electronic Parts: Literature Search and Data Evaluation

K. E. Martin

Supporting Research and Advanced Development, Space Programs Summary 37-66, Vol. III, pp. 145–147, December 31, 1970

A survey has been made of the radiation effects literature pertinent to the influence of low-level steady-state neutron, gamma, and proton environments on electronic components. The accumulated data are reviewed and an analysis is made of the radiation effects on electronic components estimated to comprise a deep space mission spacecraft exposed to planetary radiation belts and to on-board radioisotope thermoelectric generator environments. Emphasis was placed on permanent parameter degradation, temporary parameter drifts, parameter degradation factors, hardening techniques, and screening techniques.

MASEK, T. D.

M08 Thrust Subsystem Design for Nuclear Electric Spacecraft

T. D. Masek

Supporting Research and Advanced Development, Space Programs Summary 37-66, Vol. III, pp. 207–210, December 31, 1970

A method for sizing a nuclear electric thrust subsystem is presented. The results are applied to a 300-kW spacecraft design. The resulting thrust subsystem mass is estimated to be about 970 kg.

MASURSKY, H.

M09 *Surveyor* Final Report—Lunar Theory and Processes: Discussion of Chemical Analysis

R. A. Phinney (Princeton University), D. E. Gault (Ames Research Center), J. A. O'Keefe (Goddard Space Flight Center), J. B. Adams, G. P. Kuiper (University of Arizona), H. Masursky (U.S. Geological Survey), E. M. Shoemaker (U.S. Geological Survey), and R. J. Collins (University of Minnesota)

Icarus: Int. J. Sol. Sys., Vol. 12, No. 2, pp. 213–223, March 1970

For abstract, see Phinney, R. A.

McCLURE, J. P.

M10 Ground Communications Facility Functional Design for 1971–1972

J. P. McClure

The Deep Space Network, Space Programs Summary 37-66, Vol. II, pp. 99–102, November 30, 1970

The Ground Communications Facility (GCF) consists of four systems: voice, high-speed data, teletype, and wideband data. These systems are undergoing evolutionary change to accommodate higher data rates and increased volumes of traffic for future space missions. This article discusses the general design of the GCF for the 1971–1972 era. The Voice System is changing only in regard to total number of circuits required. The High-Speed Data System is being upgraded to provide outbound, in addition to inbound transmission capability, data rate increase to 4800 bits/s, and increased block size from 600 to 1200 bits. The Teletype System remains essentially unchanged. The Wideband System will provide 50-kbit/s data transmission capability.

McCREA, F. E.

M11 High-Power Feed Component Development

F. E. McCrea, H. F. Reilly, Jr., and D. E. Neff

The Deep Space Network, Space Programs Summary 37-66, Vol. II, pp. 64–68, November 30, 1970

Since the introduction of high-powered S-band transmitters (500 kW, CW) at the Venus (DSS 13) and Mars (DSS 14) Deep Space Stations, three feed systems, in various developmental

states, have been used. The components used in these systems are discussed, including rotary joints, waveguide transitions, quarter-wave plates, and an orthomode transducer. It is concluded that complex polarization diverse low-noise/high-power feeds are possible.

M12 S-Band Polar Ultra Cone Improvement

H. F. Reilly, Jr., and F. E. McCrea

The Deep Space Network, Space Programs Summary 37-66, Vol. II, p. 69, November 30, 1970

For abstract, see Reilly, H. F., Jr.

McELIECE, R.

M13 Decoding and Synchronization Research: Euler Products, Cyclotomy, and Coding

R. McEliece and H. Rumsey, Jr.

Supporting Research and Advanced Development, Space Programs Summary 37-65, Vol. III, pp. 22–27, October 31, 1970

A theorem of Davenport and Hasse is used to calculate the weight distributions of a large and important class of binary and nonbinary codes, the irreducible cyclic codes. A discussion on the cyclotomy of finite fields and some remarks about the recently investigated hyper-Kloosterman sums are included.

McINNIS, J.

M14 High-Speed Data/Wide-Band Data Input/Output Assembly

R. Wengert, L. DeGennaro, and J. McInnis

The Deep Space Network, Space Programs Summary 37-66, Vol. II, pp. 133–136, November 30, 1970

For abstract, see Wengert, R.

MENARD, W. A.

M15 Shock-Tube Thermochemistry Tables for High-Temperature Gases: Nitrogen

W. A. Menard and T. E. Horton

Technical Report 32-1408, Vol. IV, December 1, 1970

Thermodynamic properties and species concentrations of equilibrium nitrogen are tabulated for moving, standing, and reflected shock waves. Initial pressures range from 0.05 to 50.0 torr, and temperatures from 2000 to over 75,000°K.

MENICHELLI, V. J.

M16 Terminated Capacitor Discharge Firing of Electroexplosive Devices

L. A. Rosenthal (Rutgers University) and V. J. Menichelli

Technical Report 32-1521, February 15, 1971

For abstract, see Rosenthal, L. A.

M17 Nondestructive Testing of 1-W, 1-A Electro-Explosive Devices [October–November 1970]

V. J. Menichelli

Supporting Research and Advanced Development,
Space Programs Summary 37-66, Vol. III, pp. 175–178,
December 31, 1970

The results of dissecting a squib which gave abnormal responses to two nondestructive tests are presented. The heating curves indicated poor bridgewire welds and poor contact between bridgewires and explosive. The predictions were confirmed through the dissection.

MILLER, C. G.

M18 Holographic Study of Operating Compact-Arc Lamp

C. G. Miller and C. L. Youngberg

Supporting Research and Advanced Development,
Space Programs Summary 37-66, Vol. III, pp. 171–174,
December 13, 1970

Flash holograms have been made of a xenon compact-arc discharge while in operation. No evidence of gas density variation in the vicinity of the center core of the arc was found. With the anodes used, the holograms showed laminar flow at the interface of the arc stream–anode surface. Improvement in operation could be expected if turbulent flow could be induced. Electron

densities in the arc stream were shown to be too low to introduce significant refraction in looking through the arc.

MILLER, L. F.

M19 DSN Progress Report for November–December 1970: A Cursory Examination of the Sensitivity of the Tropospheric Range and Doppler Effects to the Shape of the Refractivity Profile

L. F. Miller, V. J. Ondrasik, and C. C. Chao

Technical Report 32-1526, Vol. I, pp. 22–30, February 15, 1971

The different shapes that refractivity profiles may assume during a year are grossly represented by 21 simple analytical expressions. As shown in this article, by comparing the results obtained by using ray tracing techniques on these various profiles, it is possible to obtain an approximate bound on the error induced by mapping a tropospheric zenith range effect down to lower elevation angles with the wrong profile. For an elevation angle of 10 deg, these approximate error bounds are 1.3 and 2.6% in the range and doppler effect, respectively.

MILLER, L. W.

M20 DSN Status Code

R. B. Rung and L. W. Miller

The Deep Space Network, Space Programs Summary 37-66, Vol. II, pp. 141–143, November 30, 1970

For abstract, see Rung, R. B.

MITCHELL, R. T.

M21 The *Mariner VI* and *VII* Flight Paths and Their Determination From Tracking Data

H. J. Gordon, D. W. Curkendall, D. A. O'Handley, N. A. Mottinger, P. M. Muller, C. C. Chao, B. D. Mulhall, V. J. Ondrasik, S. K. Wong, S. J. Reinbold, J. W. Zielenback, J. K. Campbell, R. T. Mitchell, J. E. Ball, W. G. Breckenridge, T. C. Duxbury, and R. E. Koch

Technical Memorandum 33-469, December 1, 1970

For abstract, see Gordon, H. J.

MO, T. C.

M22 Electromagnetic Wave Propagation in a Uniformly Accelerated Simple Medium

T. C. Mo (California Institute of Technology)

Supporting Research and Advanced Development, Space Programs Summary 37-65, Vol. III, pp. 182–190, October 31, 1970

Electromagnetic wave propagation in a uniformly accelerated simple medium is generalized to the case of arbitrary direction. The wave splits into two natural modes relative to the acceleration–propagation plane. The case of high frequency and weak acceleration is solved in detail, demonstrating an apparent gravity-dragging effect to medium comoving observers and an acceleration-dragging effect to inertial observers. A preferred asymptotic cone of propagation, with cone angle determined by the parameter $(\mu\epsilon - 1)^{1/2}$, where μ is the permeability and ϵ is the dielectric constant of the medium, is found in the accelerated frame. Various dragging effects are physically interpreted.

MOACANIN, J.

M23 Superposition of Dynamic Mechanical Properties in the Glassy State

E. F. Cuddihy and J. Moacanin

Technical Report 32-1509 (Reprinted from *J. Polym. Sci., Pt. A-2: Polym. Phys.*, Vol. 8, No. 9, pp. 1627–1634, September 1970)

For abstract, see Cuddihy, E. F.

M24 On the Presence of Crystallinity in Hydrogenated Polybutadienes

J. Moacanin, A. Eisenberg (McGill University, Canada), E. F. Cuddihy, D. D. Lawson, B. G. Moser (Moser Dental Manufacturing Company), and R. F. Landel

Technical Report 32-1512 (Reprinted from *J. Appl. Polym. Sci.*, Vol. 14, No. 9, pp. 2416–2420, September 1970)

A low level of crystallinity in hydrogenated hydroxy-terminated polybutadiene and in elastomers prepared from this prepolymer was surmised. However, no crystallinity could be detected by direct measurements such as X-rays or volume changes. This

article discusses recent results of optical and rheological measurements that provide evidence for the presence of very small crystallites.

M25 Investigation of Sterilizable Battery Separators [August–September 1970]

E. F. Cuddihy, D. E. Walmsley, J. Moacanin, and H. Y. Tom

Supporting Research and Advanced Development,
Space Programs Summary 37-65, Vol. III, pp. 171–176,
October 31, 1970

For abstract, see Cuddihy, E. F.

M26 Viscoelastic Behavior of Elastomers Undergoing Crosslinking Reactions

J. Moacanin and J. J. Aklonis (University of Southern California)

Supporting Research and Advanced Development,
Space Programs Summary 37-66, Vol. III, pp. 187–189,
December 31, 1970

Previously a method was developed for predicting the viscoelastic response of elastomers undergoing scission reactions. These results are now extended to include crosslinking reactions. As for scission, at any given time, the character of the network chains is determined by the instantaneous crosslink density. For scission all chains were assumed to carry the same stress, whereas for crosslinking, stress is distributed between the "new" and "old" chains. Equations for calculating the relative stresses are derived.

MOLINDER, J. I.

M27 Space Station Unified Communication: Standard Run-Length Coding for Multi-Level Sources

J. I. Molinder

Supporting Research and Advanced Development,
Space Programs Summary 37-65, Vol. III, pp. 39–40,
October 31, 1970

The optimum single-standard run lengths for a binary first-order Markov source are extended to multi-level first-order Markov sources. The optimal single-standard run length for each symbol is shown to satisfy an implicit equation of the same form as for the binary case. An expression for the resulting overall com-

pression ratio cannot be given in closed form, however. The optimum run lengths are determined by maximizing a quantity called the run-length compression ratio. This ratio is defined as the average compression ratio when runs of only one particular output symbol are considered.

MORELLI, F. A.

M28 Soil Microbial and Ecological Investigations in the Antarctic Interior

R. E. Cameron, R. B. Hanson, G. H. Lacy, and F. A. Morelli

Antarc. J. U.S., Vol. V, No. 4, pp. 88–89, July–August 1970

For abstract, see Cameron, R. E.

M29 Microbiological Analyses of Snow and Air From the Antarctic Interior

G. H. Lacy, R. E. Cameron, R. B. Hanson, and F. A. Morelli

Antarc. J. U.S., Vol. V, No. 4, pp. 88–89, July–August 1970

For abstract, see Lacy, G. H.

MORRIS, E. C.

M30 *Surveyor* Final Report—Geology: Regional Setting

E. C. Morris (U.S. Geological Survey)

Icarus: Int. J. Sol. Sys., Vol. 12, No. 2, pp. 161–166, 211–212, March 1970

The landing sites for the five *Surveyor* spacecraft that successfully soft-landed on the moon are as follows:

Surveyor I. Flat surface inside a 100-km crater in Oceanus Procellarum, 1 radius from the edge of a rimless 200-m crater.

Surveyor III. Interior of a subdued 200-m crater, probably of impact origin, in Oceanus Procellarum.

Surveyor V. Steep, inner slope of a 9- by 12-m crater, which may be a subsidence feature, in Mare Tranquillitatis.

Surveyor VI. Flat surface near a mare ridge in Sinus Medii.

Surveyor VII. Ejecta or flow blanket north of, and less than 1 radius from, the rim of the crater Tycho in the highlands.

The general terrain in the area of these landing sites is described and illustrated in this article.

M31 *Surveyor* Final Report—Geology: Craters

E. C. Morris (U.S. Geological Survey) and
E. M. Shoemaker (U.S. Geological Survey)

Icarus: Int. J. Sol. Sys., Vol. 12, No. 2, pp. 167–172, 211–212, March 1970

Small craters are the most abundant of the topographic features observed on the lunar surface and account for the irregularities of largest relief on the surface at the *Surveyor* landing sites in the maria. Several types of small craters can be recognized: (1) shallow, cup-shaped craters with subdued rims; (2) cup-shaped craters with sharp, raised rims; (3) rimless craters; and (4) irregular or asymmetric craters. The characteristics of the craters at the *Surveyor I, III, V, VI,* and *VII* landing sites are described in this article.

M32 *Surveyor* Final Report—Geology: Fragmental Debris

E. C. Morris (U.S. Geological Survey) and
E. M. Shoemaker (U.S. Geological Survey)

Icarus: Int. J. Sol. Sys., Vol. 12, No. 2, pp. 173–187, 211–212, March 1970

The surface on which the five successful *Surveyor* spacecraft landed consists of a fragmental debris layer, or regolith, composed of poorly sorted or well-graded fragments that range in size from large blocks to fine particles too small to be resolved by the *Surveyor* camera (<0.5 mm). The number of resolvable particles per unit area varies from site to site; 3 to 18% of the surface was found to be occupied by fragments larger than 1 mm. The fragmental debris at the *Surveyor I, III, V, VI,* and *VII* landing sites is described and illustrated in this article.

M33 *Surveyor* Final Report—Geology: Physics of Fragmental Debris

E. M. Shoemaker (U.S. Geological Survey) and
E. C. Morris (U.S. Geological Survey)

Icarus: Int. J. Sol. Sys., Vol. 12, No. 2, pp. 188–212, March 1970

For abstract, see Shoemaker, E. M.

MOSER, B. G.

M34 **On the Presence of Crystallinity in Hydrogenated Polybutadienes**

J. Moacanin, A. Eisenberg (McGill University, Canada), E. F. Cuddihy, D. D. Lawson, B. G. Moser (Moser Dental Manufacturing Company), and R. F. Landel

Technical Report 32-1512 (Reprinted from *J. Appl. Polym. Sci.*, Vol. 14, No. 9, pp. 2416–2420, September 1970)

For abstract, see Moacanin, J.

MOTTINGER, N. A.

M35 **Tracking System Analytic Calibration Activities for the *Mariner* Mars 1969 Mission**

B. D. Mulhall, C. C. Chao, N. A. Mottinger, P. M. Muller, V. J. Ondrasik, W. L. Sjogren, K. L. Thuleen, and D. W. Trask

Technical Report 32-1499, November 15, 1970

For abstract, see Mulhall, B. D.

M36 **The *Mariner VI* and *VII* Flight Paths and Their Determination From Tracking Data**

H. J. Gordon, D. W. Curkendall, D. A. O'Handley, N. A. Mottinger, P. M. Muller, C. C. Chao, B. D. Mulhall, V. J. Ondrasik, S. K. Wong, S. J. Reinbold, J. W. Zielenback, J. K. Campbell, R. T. Mitchell, J. E. Ball, W. G. Breckenridge, T. C. Duxbury, and R. E. Koch

Technical Memorandum 33-469, December 1, 1970

For abstract, see Gordon, H. J.

MUDGWAY, D. J.

M37 **DSN Progress Report for November–December 1970: *Viking* Mission Support**

D. J. Mudgway

Technical Report 32-1526, Vol. I, pp. 7–10, February 15, 1971

The support provided to the *Viking* Project by the Tracking and Data System is discussed in the following areas: trajectory design factors, launch/arrival times, look angle between spacecraft, communication range and signal level, solar conjunction, and near-earth phase trajectories.

MUHLEMAN, D. O.

M38 *Surveyor* Final Report—Principal Scientific Results From the *Surveyor* Program

L. D. Jaffe, C. O. Alley (University of Maryland), S. A. Batterson (Langley Research Center), E. M. Christensen, S. E. Dwornik (NASA Headquarters), D. E. Gault (Ames Research Center), J. W. Lucas, D. O. Muhleman (California Institute of Technology), R. H. Norton, R. F. Scott (California Institute of Technology), E. M. Shoemaker (U.S. Geological Survey), R. H. Steinbacher, G. H. Sutton (University of Hawaii), and A. L. Turkevich (University of Chicago)

Icarus: Int. J. Sol. Sys., Vol. 12, No. 2, pp. 156–160, March 1970

For abstract, see Jaffe, L. D.

MULHALL, B. D.

M39 Tracking System Analytic Calibration Activities for the *Mariner* Mars 1969 Mission

B. D. Mulhall, C. C. Chao, N. A. Mottinger, P. M. Muller, V. J. Ondrasik, W. L. Sjogren, K. L. Thuleen, and D. W. Trask

Technical Report 32-1499, November 15, 1970

This report describes the tracking system analytic calibration activities of the Deep Space Network in support of an entire mission, in particular, the Mars encounter phase of the *Mariner* Mars 1969 mission. The support functions encompass calibration of tracking data by estimating physical parameters whose uncertainties represent limitations to navigational accuracy; validation of the calibration data and utilization of these data during a mission; and detailed postflight analysis of tracking data to uncover and resolve any anomalies. Separate articles treat tracking system improvements presently under consideration and error source reductions that may be realizable for future missions; solutions for deep space station locations; timing errors and polar motion; methods of correcting the tracking data for charged-particle effects (ionospheric corrections); and a model of tropospheric refraction.

M40 The *Mariner VI* and *VII* Flight Paths and Their Determination From Tracking Data

H. J. Gordon, D. W. Curkendall, D. A. O'Handley, N. A. Mottinger, P. M. Muller, C. C. Chao, B. D. Mulhall, V. J. Ondrasik, S. K. Wong, S. J. Reinbold, J. W. Zielenback,

J. K. Campbell, R. T. Mitchell, J. E. Ball, W. G. Breckenridge, T. C. Duxbury, and R. E. Koch

Technical Memorandum 33-469, December 1, 1970

For abstract, see Gordon, H. J.

MULHOLLAND, J. D.

M41 A Preliminary Special Perturbation Theory for the Lunar Motion

K. Garthwaite, D. B. Holdridge, and J. D. Mulholland

Technical Report 32-1517 (Reprinted from *Astron. J.*, Vol. 75, No. 10, pp. 1133–1139, December 1970)

For abstract, see Garthwaite, K.

MULLER, P. M.

M42 Tracking System Analytic Calibration Activities for the *Mariner* Mars 1969 Mission

B. D. Mulhall, C. C. Chao, N. A. Mottinger, P. M. Muller, V. J. Ondrasik, W. L. Sjogren, K. L. Thuleen, and D. W. Trask

Technical Report 32-1499, November 15, 1970

For abstract, see Mulhall, B. D.

M43 The *Mariner VI* and *VII* Flight Paths and Their Determination From Tracking Data

H. J. Gordon, D. W. Curkendall, D. A. O'Handley, N. A. Mottinger, P. M. Muller, C. C. Chao, B. D. Mulhall, V. J. Ondrasik, S. K. Wong, S. J. Reinbold, J. W. Zielenback, J. K. Campbell, R. T. Mitchell, J. E. Ball, W. G. Breckenridge, T. C. Duxbury, and R. E. Koch

Technical Memorandum 33-469, December 1, 1970

For abstract, see Gordon, H. J.

MULLIN, J. V.

M44 Basic Concepts in Composite Beam Testing

J. V. Mullin (General Electric Company) and A. C. Knoell

Mater. Res. Stan., Vol. 10, No. 12, pp. 16–33, December 1970

This article presents basic concepts relating to composite beam testing and the interpretation of test results. Both the short-beam and honeycomb-beam configurations are investigated under three-

and four-point loading. Interaction strength relations delineating the transition between flexural and shear failure are developed, and the effect of material property variations on these relations is shown. Associated beam displacement fields are analyzed to show the effect that shear deformation can have on materials characterization data and specimen design. Application is then made of the short-beam interaction relation to graphite epoxy test results.

NAGLER, R. G.

N01 Fabrication Development of Lightweight Honeycomb-Sandwich Structures for Extraterrestrial Planetary Probe Missions

R. G. Nagler and R. A. Boundy

Technical Report 32-1473, January 15, 1971

Extraterrestrial planetary entry probes require new concepts in lightweight entry-vehicle design if the scientific payloads of missions are to be maximized. For a number of missions, communications and sensing requirements imply the need for an RF transparent aeroshell structure. Such an aeroshell would increase the view angle of the transmitters and receivers while providing equivalent protection from the entry environment.

Presented are the results of an extensive study of lightweight resin-fiberglass honeycomb-sandwich structures that was performed to define the fabricability and economics of RF transparent structures and to provide design data for detail analysis. As part of this study, a comparison was made with lightweight adhesive-bonded aluminum honeycomb-sandwich structures so that any penalties for RF transparency could be established. The results showed that there was little difference in strength to weight in lightweight configurations for resin-fiberglass and aluminum honeycomb-sandwich structures. Aluminum showed some advantage in stiffness to weight, but resin fiberglass was easier and less expensive to fabricate and was adaptable to a wider range of aeroshell configurations.

NEFF, D. E.

N02 DSN Progress Report for November–December 1970: Tracking and Data Acquisition Elements Research: Polarization Diverse S-Band Feed Cone

D. E. Neff and A. J. Freiley

Technical Report 32-1526, Vol. I, pp. 66–72, February 15, 1971

Development of the polarization diverse S-band (PDS) feed cone that is used on the Mars Deep Space Station (DSS 14) 210-ft-diam antenna tricone is described. The PDS system integrates the knowledge gained in two previous feed system developments and provides a highly flexible microwave front end. Right-handed circular polarization, left-handed circular polarization, and orthogonal linear polarizations are available on low-noise listen-only or diplexed channels. Additionally, a research and development radar capability for 500-kW continuous-wave power is provided. The system further provides manual or automatic servo tracking of the position angle of received linear polarization, which will be used for radio science purposes.

N03 High-Power Feed Component Development

F. E. McCrea, H. F. Reilly, Jr., and D. E. Neff

The Deep Space Network, Space Programs Summary 37-66, Vol. II, pp. 64–68, November 30, 1970

For abstract, see McCrea, F. E.

NIGHTINGALE, D.

N04 [GCF] High-Speed System Design Mark IIIA

D. Nightingale

The Deep Space Network, Space Programs Summary 37-66, Vol. II, pp. 103–105, November 30, 1970

The Deep Space Network systems selected high speed as the prime data transmission medium to fulfill the requirements of the multiple-mission support concept. This increase in traffic load, both into and out of the Space Flight Operations Facility, required substantial design changes to be made to the existing operational High-Speed System. This article describes the requirements, trade-offs, and plans that were used to develop the Mark IIIA design, including a bit-rate increase, expanded and improved interfaces, and demultiplexing techniques without deterioration in performance. All objectives of the design were met and the necessary equipment was installed and checked out in time to support *Mariner* Mars 1971 operations.

NISHIKAWA, K.

N05 Interaction Between an Electron Wave and an Ion Wave Due to Scattering by Electrons

K. Nishikawa

J. Phys. Soc. Japan, Vol. 29, No. 2, pp. 449–458, August 1970

Some basic properties of the coupling between an electron wave and an ion wave due to scattering by thermal electrons are compared with those of the coupling due to three-wave interactions. Using the kinetic wave equation which describes the relevant wave-particle interaction, the following three special problems are discussed in detail:

(1) Effect of an enhancement of short-wavelength ion-wave fluctuations on the long-wavelength electron waves.

(2) Effect of an enhancement of long-wavelength electron waves on the short-wavelength ion waves.

(3) Effect of the beam-excited short-wavelength electron waves on the long-wavelength ion waves.

NISHIMURA, T.

N06 Spectral Factorization in Discrete Systems

T. Nishimura

Supporting Research and Advanced Development,
Space Programs Summary 37-66, Vol. III, pp. 233–235,
December 31, 1970

The spectral factorization in discrete systems is studied in this article. Three theorems describing the solution and its characteristics are presented. A computer program incorporating this technique is applied to the orbit determination problem using the ranging system.

NOGUCHI, H.

N07 Electrical Properties of TCNQ Salts of Ionene Polymers and Their Model Compounds

V. Hadek, H. Noguchi, and A. Rembaum

Supporting Research and Advanced Development,
Space Programs Summary 37-66, Vol. III, pp. 192–198,
December 31, 1970

For abstract, see Hadek, V.

NORTON, D. J.

N08 Microwave Measurement of Solid Propellant Burning Rates

D. J. Norton and A. L. Schultz

Supporting Research and Advanced Development,

Space Programs Summary 37-65, Vol. III, pp. 163–167, October 31, 1970

An experimental technique employing an X-band microwave system for continuous measurement of solid propellant burning rates is used to determine burning rates under conditions of rapid depressurization. The technique uses a microwave network analyzer to measure the phase shift of a microwave signal reflected from the regressing propellant surface.

NORTON, R. H.

N09 *Surveyor* Final Report—Principal Scientific Results From the *Surveyor* Program

L. D. Jaffe, C. O. Alley (University of Maryland), S. A. Batterson (Langley Research Center), E. M. Christensen, S. E. Dwornik (NASA Headquarters), D. E. Gault (Ames Research Center), J. W. Lucas, D. O. Muhleman (California Institute of Technology), R. H. Norton, R. F. Scott (California Institute of Technology), E. M. Shoemaker (U.S. Geological Survey), R. H. Steinbacher, G. H. Sutton (University of Hawaii), and A. L. Turkevich (University of Chicago)

Icarus: Int. J. Sol. Sys., Vol. 12, No. 2, pp. 156–160, March 1970

For abstract, see Jaffe, L. D.

O'BRIEN, P. F.

001 Thermal Analysis System I: User's Manual

J. A. Hultberg and P. F. O'Brien

Technical Report 32-1416, March 1, 1971

For abstract, see Hultberg, J. A.

O'HANDLEY, D. A.

002 The *Mariner VI* and *VII* Flight Paths and Their Determination From Tracking Data

H. J. Gordon, D. W. Curkendall, D. A. O'Handley, N. A. Mottinger, P. M. Muller, C. C. Chao, B. D. Mulhall, V. J. Ondrasik, S. K. Wong, S. J. Reinbold, J. W. Zielenback, J. K. Campbell, R. T. Mitchell, J. E. Ball, W. G. Breckenridge, T. C. Duxbury, and R. E. Koch

Technical Memorandum 33-469, December 1, 1970

For abstract, see Gordon, H. J.

OHLSON, J. E.

003 The Quasi-Stationary Coronal Magnetic Field and Electron Density as Determined From a Faraday Rotation Experiment

C. T. Stelzried, G. S. Levy, T. Sato, W. V. T. Rusch (University of Southern California), J. E. Ohlson, (University of Southern California), K. H. Schatten (Goddard Space Flight Center), and J. M. Wilcox (University of California, Berkeley)

Sol. Phys., Vol. 14, No. 2, pp. 440–456, October 1970

For abstract, see Stelzried, C. T.

OHTAKAY, H.

004 In-Flight Calibration of a TV Instrument for Optical Spacecraft Navigation

H. Ohtakay

Supporting Research and Advanced Development, Space Programs Summary 37-65, Vol. III, pp. 97–100, October 31, 1970

The results of an analytical investigation of the geometrical calibration of a navigation instrument during interplanetary flight are presented. The instrument, similar to a television camera, would view selected natural satellites and reference stars simultaneously for navigating to the outer planets. An 11×11 reseau grid, etched onto the target raster of a vidicon tube, would be used to remove electromagnetic distortion from the satellite and reference star data to less than 1.2 arc sec ($1\ \sigma$). Fifty star images would be used to remove optical distortion to less than 4.3 arc sec ($1\ \sigma$). Therefore, the use of the reseau grid and star images could enable the navigation measurements to be geometrically calibrated to an accuracy of 5 arc sec ($1\ \sigma$).

O'KEEFE, J. A.

005 *Surveyor* Final Report—Lunar Theory and Processes: Discussion of Chemical Analysis

R. A. Phinney (Princeton University), D. E. Gault (Ames Research Center), J. A. O'Keefe (Goddard Space Flight Center), J. B. Adams, G. P. Kuiper (University of Arizona), H. Masursky (U.S. Geological Survey), E. M. Shoemaker (U.S. Geological Survey), and R. J. Collins (University of Minnesota)

Icarus: Int. J. Sol. Sys., Vol. 12, No. 2, pp. 213–223, March 1970

For abstract, see Phinney, R. A.

006 ***Surveyor* Final Report—Lunar Theory and Processes: Post-Sunset Horizon "Afterglow"**

D. E. Gault (Ames Research Center), J. B. Adams, R. J. Collins (University of Minnesota), G. P. Kuiper (University of Arizona), J. A. O'Keefe (Goddard Space Flight Center), R. A. Phinney (Princeton University), and E. M. Shoemaker (U.S. Geological Survey)

Icarus: Int. J. Sol. Sys., Vol. 12, No. 2, pp. 230–232, March 1970

For abstract, see Gault, D. E.

ONDRASIK, V. J.

007 **Tracking System Analytic Calibration Activities for the *Mariner* Mars 1969 Mission**

B. D. Mulhall, C. C. Chao, N. A. Mottinger, P. M. Muller, V. J. Ondrasik, W. L. Sjogren, K. L. Thuleen, and D. W. Trask

Technical Report 32-1499, November 15, 1970

For abstract, see Mulhall, B. D.

008 **DSN Progress Report for November–December 1970: A Cursory Examination of the Sensitivity of the Tropospheric Range and Doppler Effects to the Shape of the Refractivity Profile**

L. F. Miller, V. J. Ondrasik, and C. C. Chao

Technical Report 32-1526, Vol. I, pp. 22–30, February 15, 1971

For abstract, see Miller, L. F.

009 **The *Mariner VI* and *VII* Flight Paths and Their Determination From Tracking Data**

H. J. Gordon, D. W. Curkendall, D. A. O'Handley, N. A. Mottinger, P. M. Muller, C. C. Chao, B. D. Mulhall, V. J. Ondrasik, S. K. Wong, S. J. Reinbold, J. W. Zielenback, J. K. Campbell, R. T. Mitchell, J. E. Ball, W. G. Breckenridge, T. C. Duxbury, and R. E. Koch

Technical Memorandum 33-469, December 1, 1970

For abstract, see Gordon, H. J.

OTOSHI, T. Y.

O10 Spacecraft Antenna Research: Further RF Study of Reflector Surface Materials for Spacecraft Antennas

K. Woo and T. Y. Otoshi

Supporting Research and Advanced Development, Space Programs Summary 37-65, Vol. III, pp. 47–52, October 31, 1970

For abstract, see Woo, K.

O11 Improved RF Calibration Techniques: A Study of the RF Properties of the 210-ft-diam Antenna Mesh Material

T. Y. Otoshi and R. B. Lyon

The Deep Space Network, Space Programs Summary 37-66, Vol. II, pp. 52–57, November 30, 1970

This article describes a procedure for improving the accuracy of reflectivity loss measurements on highly reflective mesh materials. Through the use of the waveguide method and procedure described, the reflectivity losses of the 210-ft-diam antenna mesh material were measured to be 0.001 and 0.008 dB at 2295 and 8448 MHz, respectively. The transmission losses were measured to be 43.1 dB at 2295 MHz and 30.5 dB at 8448 MHz. These results, however, are restricted to the equivalent free-space case where a linearly polarized plane wave is (1) obliquely incident on a very large sample of the 210-ft antenna mesh material, and (2) the E-field is normal to the plane of incidence.

PACE, G.

P01 UBV: Subroutine to Compute Photometric Magnitudes of the Planets and Their Satellites

G. Pace

Technical Report 32-1523, February 15, 1971

This computer subroutine computes the visual, blue, and ultraviolet photometric magnitudes of the planets, their natural satellites, and the sun at varying observation distances and phase angles. Currently available observational magnitude and phase function data are stored in the program and used in the computation.

P02 Subroutine To Compute Planet and Satellite Photometric Magnitudes

G. Pace

Supporting Research and Advanced Development, Space Programs Summary 37-65, Vol. III, p. 96, October 31, 1970

A computer subroutine has been developed to compute the visual, blue, and ultraviolet magnitudes of the planets, their satellites, and the sun at varying observation distances and phase angles. Currently available observational magnitude and phase function data are stored in the program and used in the computation.

PASSELL, D. W.

P03 DSN Progress Report for November–December 1970: Communications Control Group Assembly: Teletype Line Switching Equipment

D. W. Passell

Technical Report 32-1526, Vol. I, pp. 113–116, February 15, 1971

This article describes the teletype portion of the communications control group assembly installed in the Ground Communications Facility's deep space station communications equipment subsystem. The functions, developmental status, and operational features of the teletype switching equipment are discussed, and the necessity for interfacing with a variety of communications common carriers is explained.

P04 Communications Control Group Assembly Voice Data Switching Equipment

D. W. Passell

The Deep Space Network, Space Programs Summary 37-66, Vol. II, pp. 111–113, November 30, 1970

The transmission, monitoring, control, and distribution of voice and/or data audio frequencies are accomplished within the Deep Space Network through several interconnected Ground Communications Facility (GCF) subsystems and assemblies. This article describes the purpose, interfaces, development and status, and configuration of the voice data portion of the Communications Control Group Assembly equipment installed at the GCF Deep Space Station Communications Equipment Subsystem.

PATTERSON, R. E.

P05 Development of a Long-Life High-Cycle-Life 30 A-h Sealed AgO–Zn Battery

R. E. Patterson

Supporting Research and Advanced Development,
Space Programs Summary 37-65, Vol. III, pp. 69–72,
October 31, 1970

A two-phase program is under way to develop sealed AgO–Zn cells capable of performing 6-mo wet-charged stand during interplanetary travel plus an orbiting life of 100 or more 24-h cycles at 50% depth of discharge. Following 4 mo of charged stand (open-circuit voltage between 1.85 and 1.86 V), Phase I design 1 (utilizing wedge-shaped negative electrodes) and design 2 (41% KOH group) completed 226 and 213 cycles, respectively, before the first cell failures occurred. The Phase I design 1 cells containing 45% KOH completed 245 cycles without any failures. Phase II cells completed 9 mo of charged stand and are currently being cycle tested.

PAWLIK, E. V.

P06 Performance of a 20-cm-Diameter Electron-Bombardment Hollow-Cathode Ion Thruster

E. V. Pawlik

Technical Memorandum 33-468, February 15, 1971

Experimental system studies on solar-electric primary propulsion for deep space probes are presently under way at the Jet Propulsion Laboratory. These studies are performed with a 20-cm-diameter electron-bombardment ion thruster. The electron emitter used to create the thruster plasma has been changed from an oxide to a hollow cathode type in order to improve thruster efficiency and lifetime. The performance of this modified thruster is detailed over a wide range of variations in thruster parameters. Thruster output power can be varied from 1000 to 2600 W.

P07 Ion Thruster Electron Baffle Sizing

E. V. Pawlik

Supporting Research and Advanced Development,
Space Programs Summary 37-66, Vol. III, pp. 201–203,
December 31, 1970

This article presents the results of an experimental investigation that was undertaken to examine the effects of changing the diameter of the electron baffle on ion thruster performance. This baffle is located within the thruster near the hollow cathode and serves to distribute electrons emitted into the arc chamber. Four baffle sizes were investigated. A minimum diameter was found below which poor thruster throttling properties and noisy arc chamber operation would result.

P08 **An Ion Thruster Utilizing a Combination Keeper Electrode and Electron Baffle**

E. V. Pawlik

Supporting Research and Advanced Development,
Space Programs Summary 37-66, Vol. III, pp. 204–206,
December 31, 1970

This article presents the results of an experimental investigation that was undertaken to examine the effects on ion thruster performance of operating with a combination keeper electrode and electron baffle. These items are usually present in thrusters employing hollow cathodes and serve to maintain the cathode discharge and distribute electrons into the arc chamber. No improvement in the level of arc chamber losses was noted. A reduction in arc current oscillations under certain thruster operating conditions was observed.

PEAVLER, P. F.

P09 **DSN Progress Report for November–December 1970: Inbound High-Speed and Wideband Data Synchronizers**

P. F. Peavler

Technical Report 32-1526, Vol. I, pp. 93–94, February 15, 1971

The Space Flight Operations Facility (SFOF) high-speed and wideband data synchronizers accept serial, blocked, digital data from the Ground Communications Facility. These synchronizers establish synchronization, detect and delete filler blocks, perform serial-to-parallel conversion, and output these data to two IBM 360/75 computers. Their functional characteristics, input, synchronization, conversion, and output are described in this article.

PERKINS, G. S.

P10 **TOPS Attitude-Control Single-Axis Simulator**

J. D. Ferrera and G. S. Perkins

Supporting Research and Advanced Development,
Space Programs Summary 37-65, Vol. III, pp. 118–119,
October 31, 1970

For abstract, see Ferrera, J. D.

PERLMAN, M.

P11 The Decomposition of the States of a Linear Feedback Shift Register Into Cycles of Equal Length

M. Perlman

Technical Report 32-1511 (Reprinted from *IEEE Trans. Computers*, Vol. C-19, No. 11, pp. 1029–1035, November 1970)

This article presents a derivation of a linear feedback function for an r-stage feedback shift register that results in branchless cycles of equal length. The linear recurrence relationship and generating function, which characterize the r-stage feedback shift register's behavior, are used to prove that both of the 2^r states lie in cycles of equal length.

P12 The Implementation of m-ary Linear Feedback Shift Registers With Binary Devices

M. Perlman

Supporting Research and Advanced Development, Space Programs Summary 37-66, Vol. III, pp. 161–163, December 31, 1970

An m-ary linear feedback shift register (LFSR) is first decomposed into p-ary parallel LFSRs where each p is a distinct prime factor of the integer m. The states of each p-ary LFSR, where $p > 2$, are coded in binary and unspecified states are treated optionally. For a given p, a total of n binary shift registers with *interdependent* binary feedback functions, where $2^{n-1} < p < 2^n$, are used in the implementation of the p-ary LFSR.

PHILLIPS, H.

P13 Hydrostatic Bearing Runner Level Reference

G. Gale and H. Phillips

The Deep Space Network, Space Programs Summary 37-66, Vol. II, pp. 80–83, November 30, 1970

For abstract, see Gale, G.

PHINNEY, R. A.

P14 *Surveyor* Final Report—Lunar Theory and Processes: Discussion of Chemical Analysis

R. A. Phinney (Princeton University), D. E. Gault (Ames Research Center), J. A. O'Keefe (Goddard Space Flight Center), J. B. Adams, G. P. Kuiper (University of Arizona),

H. Masursky (U.S. Geological Survey), E. M. Shoemaker (U.S. Geological Survey), and R. J. Collins (University of Minnesota)

Icarus: Int. J. Sol. Sys., Vol. 12, No. 2, pp. 213–223, March 1970

The central scientific questions about the moon that might be answered by chemical compositional data are:

(1) What is the bulk composition of the moon? How does this compare with the composition of the earth and the meteorites?

(2) What are the composition and mode of origin of the lunar crust? Is it derived in ways similar to the terrestrial crust?

(3) What is responsible for the known differences between highlands and maria, e.g., the differences in albedo, elevation, and crater numbers?

Preliminary results from the alpha-scattering experiment on *Surveyors V, VI,* and *VII* are described in this article. Among the subject discussed are contrasts in albedo, estimated density of lunar surface rocks, bulk composition of the moon, the thermal regime in the moon, chondritic meteorites and the moon, tektites, and solar system implications.

P15 *Surveyor* Final Report—Lunar Theory and Processes: Post-Sunset Horizon "Afterglow"

D. E. Gault (Ames Research Center), J. B. Adams, R. J. Collins (University of Minnesota), G. P. Kuiper (University of Arizona), J. A. O'Keefe (Goddard Space Flight Center), R. A. Phinney (Princeton University), and E. M. Shoemaker (U.S. Geological Survey)

Icarus: Int. J. Sol. Sys., Vol. 12, No. 2, pp. 230–232, March 1970

For abstract, see Gault, D. E.

PRICE, T. W.

P16 High-Thrust Throttleable Monopropellant Hydrazine Reactors

T. W. Price

Supporting Research and Advanced Development, Space Programs Summary 37-66, Vol. III, pp. 213–221, December 31, 1970

Two series of subscale throttling tests, using surplus *Mariner* Mars 1969 catalytic reactors, were conducted. Rapid dynamic throttling of a monopropellant hydrazine/Shell-405 catalytic decomposition chamber was demonstrated, and the performance

of the reactor was measured. Heat sterilization of a catalytic reactor was also shown to have no significant deleterious effects, although measurable differences in the reactor start transient characteristics were noted.

RAHEB, M. E.

R01 Effect of Elastic End Rings on the Eigenfrequencies of Finite Length Thin Cylindrical Shells

M. E. Raheb

Technical Report 32-1489, March 1, 1971

The effect of elastic end rings on the eigenfrequencies of thin cylindrical shells was studied by using an exact solution of the linear eigenvalue problem. The in-plane boundary conditions which proved to be very influential in the neighborhood of the minimum frequency were exactly satisfied. The out-of-plane and torsional rigidities of the ring were found to govern the overall shell stiffness. Considerable mode interaction was noticed at low circumferential wave numbers for low values of the ring stiffness.

Rings with closed section were found to be more efficient than those with open section for the same values of weight ratio. No appreciable difference was noticed between rings fixed from the inside or the outside of the shell mid-surface.

REICHLEY, P. E.

R02 Observations of Interstellar Scintillations of Pulsar Signals at 2388 MHz

G. S. Downs and P. E. Reichley

Astrophys. J., Vol. 163, No. 1, Pt. 2, pp. L11–L16, January 1, 1971

For abstract, see Downs, G. S.

REID, M. S.

R03 Improved RF Calibration Techniques: System Operating Noise Temperature Calibrations of Low Noise Cones [September–October 1970]

M. S. Reid

The Deep Space Network, Space Programs Summary 37-66, Vol. II, pp. 57–61, November 30, 1970

The system operating noise temperature performance of the low noise cones in the Goldstone Deep Space Communications Complex is reported for the period June 1 through September 30, 1970. The operating noise temperature calibrations were performed using the ambient termination technique. Averaged operating noise temperature calibrations for the S-band polarization ultra cone, S-band research operational cone, and S-band Cassegrain ultra cone are presented. Preliminary noise temperature data of the polarization diversity S-band cone are also included.

REILLY, H. F., JR.

R04 High-Power Feed Component Development

F. E. McCrea, H. F. Reilly, Jr., and D. E. Neff

The Deep Space Network, Space Programs Summary 37-66, Vol. II, pp. 64–68, November 30, 1970

For abstract, see McCrea, F.E.

R05 S-Band Polar Ultra Cone Improvement

H. F. Reilly, Jr., and F. E. McCrea

The Deep Space Network, Space Programs Summary 37-66, Vol. II, p. 69, November 30, 1970

This article presents the results of recent work performed on standard Deep Space Instrumentation Facility 2-position S-band switches to improve insertion loss, isolation, and the voltage standing-wave ratio. Improved choke design using standard stators and rework rotors to improve performance was successful in lowering system noise temperature and increasing needed isolation in a new feed cone design.

REINBOLD, S. J.

R06 The *Mariner VI* and *VII* Flight Paths and Their Determination From Tracking Data

H. J. Gordon, D. W. Curkendall, D. A. O'Handley, N. A. Mottinger, P. M. Muller, C. C. Chao, B. D. Mulhall, V. J. Ondrasik, S. K. Wong, S. J. Reinbold, J. W. Zielenback, J. K. Campbell, R. T. Mitchell, J. E. Ball, W. G. Breckenridge, T. C. Duxbury, and R. E. Koch

Technical Memorandum 33-469, December 1, 1970

For abstract, see Gordon, H. J.

REMBAUM, A.

R07 Energy Transfer in Bipyridilium (Paraquat) Salts

A. Rembaum, V. Hadek, and S. P. S. Yen

Supporting Research and Advanced Development, Space Programs Summary 37-66, Vol. III, pp. 189–191, December 31, 1970

Bipyridils quaternized by means of mineral acids and reacted with LiTCNQ exhibit an anomalously high electronic conductivity. This phenomenon is not observed when the quaternization is carried out by means of alkyl halides. Examination of electrical and optical properties of several bipyridilium TCNQ Salts revealed an electron transfer from the radical ion to the paraquat. The postulated mechanism of electron transfer involves the formation of a hydrogen atom and a neutral TCNQ molecule.

R08 Electrical Properties of TCNQ Salts of Ionene Polymers and Their Model Compounds

V. Hadek, H. Noguchi, and A. Rembaum

Supporting Research and Advanced Development, Space Programs Summary 37-66, Vol. III, pp. 192–198, December 31, 1970

For abstract, see Hadek, V.

RENZETTI, N. A.

R09 DSN Progress Report for November–December 1970: DSN Functions and Facilities

N. A. Renzetti

Technical Report 32-1526, Vol. I, pp. 1–3, February 15, 1971

The objectives, functions, and organization of the Deep Space Network (DSN) are summarized. The Deep Space Instrumentation Facility, the Ground Communications Facility, and the Space Flight Operations Facility are described.

R10 Tracking and Data System Support for the *Pioneer* Project: *Pioneer VI*. Extended Mission: July 1, 1966–July 1, 1969

N. A. Renzetti

Technical Memorandum 33-426, Vol. V, February 1, 1971

The *Pioneer VI* mission (inward trajectory, heliocentric orbit) employed six scientific instruments to accumulate information

relative to interplanetary high-energy particles, solar phenomena, and plasma. The tracking of the spacecraft also made possible the support of a celestial mechanics experiment based on the radio metric data generated by the Deep Space Network. The network provided support for all of the science and engineering telemetry data return and transmission of commands to the spacecraft.

RINDERLE, E. A.

R11 DSN Progress Report for November–December 1970: Choice of Integrators for Use With a Variation-of-Parameters Formulation

T. D. Talbot and E. A. Rinderle

Technical Report 32-1526, Vol. I, pp. 117–121, February 15, 1971

For abstract, see Talbot, T. D.

RODEMICH, E.

R12 A Real Variable Lemma and the Continuity of Paths of Some Gaussian Processes

A. M. Garsia, E. Rodemich, and H. Rumsey, Jr.

Ind. Univ. Math. J., Vol. 20, No. 6, pp. 565–578, December 1970

For abstract, see Garsia, A. M.

ROPER, W. D.

R13 Spacecraft Adhesives for Long Life and Extreme Environment

W. D. Roper

Supporting Research and Advanced Development, Space Programs Summary 37-66, Vol. III, pp. 111–114, December 31, 1970

A laboratory evaluation was performed on several high performance adhesive materials in order to establish their suitability for future spacecraft application. The adhesive materials tested included the polyimide, polybenzimidazole, and polyquinoxaline polymers. In this evaluation, the thermal shock resistance of each adhesive was determined by thermal cycling through the temperature range of +400 to −100°F. The mode of cycling was typical of what might be required of adhesives in future planetary missions. The order of decreasing preference of the adhe-

sives for future spacecraft application was found to be: polyimide, polyquinoxaline, and polybenzimidazole. Additional long-term elevated-temperature aging tests are underway to further characterize the materials as spacecraft adhesives.

ROSCHKE, E. J.

R14 Heat Transfer From Partially Ionized Argon Flowing in a Conducting Channel With an Applied, Transverse Magnetic Field

E. J. Roschke

Technical Report 32-1510, December 15, 1970

Wall heat transfer measurements were obtained for laminar flow of partially ionized argon flowing in a square channel with and without an applied, transverse magnetic field. Tests were conducted for subsonic flows and for flows that were supersonic before a magnetic field was applied. Principal results are presented in terms of the Stanton number. The Stanton number increased by a factor of as much as six at the highest magnetic field strengths available (nearly 10 kG) over results observed at zero field. Heat transfer and flow data were used to estimate the effective values of the Joule heating parameter, the Hall coefficient, the Hartmann number, and the current density; these values appeared to be physically realistic. It is believed that the large increases in heat transfer observed with an applied magnetic field were due to (1) a small but sufficient amount of Joule heating, which caused significant changes in the temperature distribution, augmented or accompanied by (2) magnetically induced nonequilibrium ionization. These results represent the only known experimental measurements obtained thus far for heat transfer from a partially ionized gas in steady internal flow with an applied, transverse magnetic field.

ROSENTHAL, L. A.

R15 Terminated Capacitor Discharge Firing of Electroexplosive Devices

L. A. Rosenthal (Rutgers University) and V. J. Menichelli

Technical Report 32-1521, February 15, 1971

By terminating the discharge of energy into an insensitive electroexplosive device, firing energy parameters can be determined. A simple capacitor discharge system providing exponential pulses terminated at an adjustable width is described. Development technique and application to testing are discussed.

ROUKLOVE, P.

R16 Thermoelectric Generators for Deep Space Application

P. Rouklove and V. Truscello

Technical Report 32-1495, January 15, 1971

To provide a source of electrical energy independent of the sun for use in unmanned spacecraft investigation of the outer planets, JPL is evaluating radioisotope thermoelectric generators. Criteria for the selection of the thermoelectric materials, the design of the generator, and its integration with the spacecraft are discussed. Results of the tests of 10 generators that have been, or are presently, under test at JPL are also presented.

RUBINSTEIN, R.

R17 The DSN User Requirements Forecast

R. Rubinstein

The Deep Space Network, Space Programs Summary 37-66, Vol. II, pp. 144–145, November 30, 1970

The *DSN User Requirements Forecast* has been adopted as the single source for project information by all Deep Space Network (DSN) planning and systems engineering personnel. This article describes the development and composition of the *Requirements Forecast* and illustrates how the compiled data can be used to plan for future requirements imposed on the DSN.

RUMSEY, H., JR.

R18 Decoding and Synchronization Research: Euler Products, Cyclotomy, and Coding

R. McEliece and H. Rumsey, Jr.

Supporting Research and Advanced Development, Space Programs Summary 37-65, Vol. III, pp. 22–27, October 31, 1970

For abstract, see McEliece, R.

R19 A Real Variable Lemma and the Continuity of Paths of Some Gaussian Processes

A. M. Garsia, E. Rodemich, and H. Rumsey, Jr.

Ind. Univ. Math. J., Vol. 20, No. 6, pp. 565–578, December 1970

For abstract, see Garsia, A. M.

RUNG, R. B.

R20 DSN Status Code

R. B. Rung and L. W. Miller

The Deep Space Network, Space Programs Summary 37-66, Vol. II, pp. 141–143, November 30, 1970

The Deep Space Network (DSN) Status Code provides an automated display of the current status of DSN support organized by both deep space station and spacecraft. Information is derived from the DSN Monitor System on the configuration and quality of the data flow for each DSN system. A display will be driven which indicates on a 0–9 scale the support status of each DSN system or facility, with a 9 being proper system performance, lesser numbers indicating partial failures, and a 0 indicating that the system is not scheduled.

RUSCH, W. V. T.

R21 The Quasi-Stationary Coronal Magnetic Field and Electron Density as Determined From a Faraday Rotation Experiment

C. T. Stelzried, G. S. Levy, T. Sato, W. V. T. Rusch (University of Southern California), J. E. Ohlson, (University of Southern California), K. H. Schatten (Goddard Space Flight Center), and J. M. Wilcox (University of California, Berkeley)

Sol. Phys., Vol. 14, No. 2, pp. 440–456, October 1970

For abstract, see Stelzried, C. T.

RUSSELL, R. K.

R22 The Use of Sequential Estimation With Process Noise for Processing DSN Tracking Data During Planetary Orbiter Missions

R. K. Russell

The Deep Space Network, Space Programs Summary 37-66, Vol. II, pp. 14–22, November 30, 1970

Much experience with orbiter state estimation and prediction based on the "batch" least-squares method has been accumulated. During the *Lunar Orbiter* missions, severe problems were experienced with the batch filter operating in a real-time operations mode. Since these problems arose due to gravitational perturbations, there is the distinct possibility similar problems will exist for the *Mariner* Mars 1971 orbiter phase. To circumvent some of the problems associated with the batch filter operating in the

presence of gravitational perturbations, the sequential data filter, incorporating process noise, is considered. The inclusion of an appropriately chosen process noise may obviate the need to solve for harmonics in real-time while providing a more accurate state estimate than that of the batch filter. In addition, this filter seems to eliminate the problem of "optimum data spans" as additional data does not degrade the state estimate.

SABELMAN, E. E.

S01 TOPS Mechanical Devices

E. E. Sabelman

Supporting Research and Advanced Development, Space Programs Summary 37-66, Vol. III, pp. 148–156, December 31, 1970

This article summarizes the development of three mechanical devices for the Thermoelectric Outer-Planet Spacecraft (TOPS). These devices include the radioisotope thermoelectric generator and science boom actuator–damper, the magnetometer boom, and the regenerative pump for the TOPS fluid loop. The design and functional characteristics of each device are given and test procedures and results of test models are included.

SATO, T.

S02 Radio Science Support [by DSN, September–October 1970]

T. Sato, L. Skjerre, and D. Spitzmesser

The Deep Space Network, Space Programs Summary 37-66, Vol. II, pp. 151–153, November 30, 1970

This article presents a summary of radio science operations at Deep Space Network facilities during the period September 1 to October 31, 1970. Activities of the Radio Astronomy Experiment Selection Panel are also included.

S03 The Quasi-Stationary Coronal Magnetic Field and Electron Density as Determined From a Faraday Rotation Experiment

C. T. Stelzried, G. S. Levy, T. Sato, W. V. T. Rusch (University of Southern California), J. E. Ohlson, (University of Southern California), K. H. Schatten (Goddard Space Flight Center), and J. M. Wilcox (University of California, Berkeley)

Sol. Phys., Vol. 14, No. 2, pp. 440–456, October 1970

For abstract, see Stelzried, C. T.

SCHATTEN, K. H.

S04 The Quasi-Stationary Coronal Magnetic Field and Electron Density as Determined From a Faraday Rotation Experiment

C. T. Stelzried, G. S. Levy, T. Sato, W. V. T. Rusch (University of Southern California), J. E. Ohlson, (University of Southern California), K. H. Schatten (Goddard Space Flight Center), and J. M. Wilcox (University of California, Berkeley)

Sol. Phys., Vol. 14, No. 2, pp. 440–456, October 1970

For abstract, see Stelzried, C. T.

SCHLOSS, A.

S05 Capacitance of Solar Cells and Panels Under Various Load Conditions

A. Schloss

Technical Memorandum 33-464, February 1, 1971

Associated with a solar cell is a diffusion capacitance that is directly proportional to the short circuit current capability of the cell. If one attempts to measure the maximum power capability of a cell or panel by a sweep-loading technique, the current provided by the diffusion capacitance will affect the measurement. In order to reduce the error thus introduced to acceptable levels, the magnitude of the diffusion capacitance must be known. This report presents values one can expect as well as a measurement technique to determine capacitance of cells of various manufacture.

SCHORN, R. A. J.

S06 High-Dispersion Spectroscopic Observations of Venus: IX. The Carbon Dioxide Bands at 12,030 and 12,177 Å

L. D. G. Young, R. A. J. Schorn, and H. J. Smith (University of Texas)

Icarus: Int. J. Sol. Sys., Vol. 13, No. 1, pp. 74–81, July 1970

For abstract, see Young, L. D. G.

S07 Improved Constants for the 7820 Å and 7883 Å Bands of CO_2

L. D. G. Young, A. T. Young, and R. A. Schorn

J. Quant. Spectrosc. Radiat. Transfer, Vol. 10, No. 12, pp. 1291–1300, December 1970

For abstract, see Young, L. D. G.

S08 **Improved Solar Wavelengths Between 7780 and 7925 Å**

A. T. Young and R. A. Schorn

Sol. Phys., Vol. 15, No. 1, pp. 97–101, November 1970

For abstract, see Young, A. T.

SCHULTZ, A. L.

S09 **Microwave Measurement of Solid Propellant Burning Rates**

D. J. Norton and A. L. Schultz

Supporting Research and Advanced Development, Space Programs Summary 37-65, Vol. III, pp. 163–167, October 31, 1970

For abstract, see Norton, D. J.

SCOTT, R. F.

S10 ***Surveyor* Final Report—Principal Scientific Results From the *Surveyor* Program**

L. D. Jaffe, C. O. Alley (University of Maryland), S. A. Batterson (Langley Research Center), E. M. Christensen, S. E. Dwornik (NASA Headquarters), D. E. Gault (Ames Research Center), J. W. Lucas, D. O. Muhleman (California Institute of Technology), R. H. Norton, R. F. Scott (California Institute of Technology), E. M. Shoemaker (U.S. Geological Survey), R. H. Steinbacher, G. H. Sutton (University of Hawaii), and A. L. Turkevich (University of Chicago)

Icarus: Int. J. Sol. Sys., Vol. 12, No. 2, pp. 156–160, March 1970

For abstract, see Jaffe, L. D.

SCULL, J. R.

S11 ***Mariner* Mars 1969 Navigation, Guidance and Control**

J. R. Scull

Automatica, Vol. 6, No. 5, pp. 755–766, November 1970

Design, mechanization, and flight test results of the *Mariner* Mars 1969 navigation, guidance, and control systems are discussed. A trajectory design section describes the near-earth launch trajectory and planetary targeting and constraints, as well as the tradeoffs made on the trajectory selection. Among the factors considered are reliability, direct ascent vs. parking orbit, and higher spacecraft weight vs. extended launch window. Guid-

ance and orbit determination factors are discussed, including earth-based radio and spacecraft optical navigation and the accuracy of orbit determination and maneuver execution.

The control systems section identifies differences in the attitude control, midcourse maneuver, and science instrument scan pointing systems from those used in previous *Mariner* spacecraft. A description is given of the new central computer and sequencer system, used for the first time on this mission, which allows extremely flexible spacecraft operation using in-flight reprogramming of the computer memory by radio command.

Finally, reliability summaries and performance evaluations permit conclusions as to the effectiveness of the *Mariner* Mars 1969 navigation, guidance, and control systems to conduct near-term and more advanced planetary missions.

SEIDEL, B.

S12 Improved RF Calibration Techniques: PDS Cone Waveguide/ Polarimeter Calibrations

P. D. Batelaan, B. Seidel, and R. B. Lyon

The Deep Space Network, Space Programs Summary 37-66, Vol. II, pp. 61–63, November 30, 1970

For abstract, see Batelaan, P. D.

SHALLBETTER, A. C.

S13 Block IV Receiver–Exciter Development

H. Donnelly, A. C. Shallbetter, and R. E. Weller

The Deep Space Network, Space Programs Summary 37-66, Vol. II, pp. 115–124, November 30, 1970

For abstract, see Donnelly, H.

SHAW, D. T.

S14 Theoretical Considerations of the Prebreakdown Characteristics in a Cesium Thermionic Discharge

D. T. Shaw

Supporting Research and Advanced Development, Space Programs Summary 37-65, Vol. III, pp. 101–104, October 31, 1970

The transition from the electron-rich, unignited mode to the ignited mode of cesium thermionic diodes is considered analyti-

cally. Although a number of experimental results on cesium ignition have been reported, the theoretical understanding of the potential distribution in the collector sheath, that was found to be correlated with the ignition, has been limited.

This article attempts to analyze this potential in the sheath having a finite thickness. Most analyses have been made on the assumption of infinitesimal thickness. The new analysis is formulated on the assumption that, in the prebreakdown region, the Debye length is of the same order of magnitude as the electron mean-free-path. Thus, the collector sheath region, within which most of the potential drop takes place in the pre-ignition condition of the diode, cannot be treated as collisionless. Based upon the collision-dominated model, the voltage drop and the electric field in the collector sheath was calculated. Since the field intensity in the sheath was determined as a function of voltage applied to the cesium diode, a rate of cesium ionization that accounts for the diode ignition is now calculable.

SHIMADA, K.

S15 Optimization and Reliability Calculations for Multi-Thermionic-Converter Systems

R. Szejn and K. Shimada

Supporting Research and Advanced Development,
Space Programs Summary 37-66, Vol. III, pp. 76–80,
December 31, 1970

For abstract, see Szejn, R.

SHOEMAKER, E. M.

S16 *Surveyor* Final Report—Principal Scientific Results From the *Surveyor* Program

L. D. Jaffe, C. O. Alley (University of Maryland), S. A. Batterson (Langley Research Center), E. M. Christensen, S. E. Dwornik (NASA Headquarters), D. E. Gault (Ames Research Center), J. W. Lucas, D. O. Muhleman (California Institute of Technology), R. H. Norton, R. F. Scott (California Institute of Technology), E. M. Shoemaker (U.S. Geological Survey), R. H. Steinbacher, G. H. Sutton (University of Hawaii), and A. L. Turkevich (University of Chicago)

Icarus: Int. J. Sol. Sys., Vol. 12, No. 2, pp. 156–160,
March 1970

For abstract, see Jaffe, L. D.

S17 *Surveyor* Final Report—Geology: Craters

E. C. Morris (U.S. Geological Survey) and
E. M. Shoemaker (U.S. Geological Survey)

Icarus: Int. J. Sol. Sys., Vol. 12, No. 2, pp. 167–172, 211–212, March 1970

For abstract, see Morris, E. C.

S18 *Surveyor* Final Report—Geology: Fragmental Debris

E. C. Morris (U.S. Geological Survey) and
E. M. Shoemaker (U.S. Geological Survey)

Icarus: Int. J. Sol. Sys., Vol. 12, No. 2, pp. 173–187, 211–212, March 1970

For abstract, see Morris, E. C.

S19 *Surveyor* Final Report—Geology: Physics of Fragmental Debris

E. M. Shoemaker (U.S. Geological Survey) and
E. C. Morris (U.S. Geological Survey)

Icarus: Int. J. Sol. Sys., Vol. 12, No. 2, pp. 188–212, March 1970

The size–frequency distribution of the resolvable fragments on the lunar surface was studied at each of the five *Surveyor* landing sites by choosing sample areas near the spacecraft so that the resolution and area covered would provide particle counts spanning different, but overlapping, parts of the particle size range. Studies were made of the parts of the surface undisturbed by the spacecraft at each site. Sample areas were selected that appeared to be representative of the areas surrounding the spacecraft; areas that appeared to have anomalously high or anomalously low particle abundances were avoided. The fragmental material disturbed by the footpads of the spacecraft during landing also was studied at some sites, and special studies were made at the *Surveyor III* landing site of the size distribution of the fragmental debris in the strewn fields of blocks surrounding craters with raised rims. The results of these studies and conclusions that may be drawn concerning the physics of fragmental debris are reported in this article.

S20 *Surveyor* Final Report—Lunar Theory and Processes: Discussion of Chemical Analysis

R. A. Phinney (Princeton University), D. E. Gault (Ames Research Center), J. A. O'Keefe (Goddard Space Flight Center), J. B. Adams, G. P. Kuiper (University of Arizona),

H. Masursky (U.S. Geological Survey), E. M. Shoemaker (U.S. Geological Survey), and R. J. Collins (University of Minnesota)

Icarus: Int. J. Sol. Sys., Vol. 12, No. 2, pp. 213–223, March 1970

For abstract, see Phinney, R. A.

S21 ***Surveyor* Final Report—Lunar Theory and Processes: Post-Sunset Horizon "Afterglow"**

D. E. Gault (Ames Research Center), J. B. Adams, R. J. Collins (University of Minnesota), G. P. Kuiper (University of Arizona), J. A. O'Keefe (Goddard Space Flight Center), R. A. Phinney (Princeton University), and E. M. Shoemaker (U.S. Geological Survey)

Icarus: Int. J. Sol. Sys., Vol. 12, No. 2, pp. 230–232, March 1970

For abstract, see Gault, D. E.

SHULMAN, G. P.

S22 **Isolation and Characterization of Coal in Antarctic Dry-Valley Soils**

A. J. Bauman, E. M. Bollin, G. P. Shulman, and R. E. Cameron

Antarc. J. U.S., Vol. V, No. 5, pp. 161–162, September–October 1970

For abstract, see Bauman, A. J.

SIEGMETH, A. J.

S23 ***Pioneer* Mission Support [by DSN, September–October 1970]**

A. J. Siegmeth

The Deep Space Network, Space Programs Summary 37-66, Vol. II, pp. 4–11, November 30, 1970

The continuation of the tracking and data acquisition support of the still active *Pioneer VI, VII, VIII,* and *IX* missions is presented. The quantitative and qualitative assessment of the Deep Space Network support is given. The data return was enhanced by the near-optimum-type utilization of the 85-ft antenna stations. A summary of the *Pioneer F* and *G* mission support planning activities is given with emphasis on the telecommunications link design and its interfaces. These missions, to be launched in 1972 and 1974, will provide the first closeup reconnaissance of Jupiter.

SILVER, R. H.

S24 Evaluation of Spacecraft Magnetic Recording Tapes and Magnetic Heads [August–September 1970]

S. H. Kalfayan, R. H. Silver, and J. K. Hoffman

Supporting Research and Advanced Development,
Space Programs Summary 37-65, Vol. III, pp. 168–171,
October 31, 1970

For abstract, see Kalfayan, S. H.

S25 Evaluation of Recording Tape and Heads for Spacecraft Magnetic Tape Recorder Applications [October–November 1970]

J. K. Hoffman, S. H. Kalfayan, and R. H. Silver

Supporting Research and Advanced Development,
Space Programs Summary 37-66, Vol. III, p. 160,
December 31, 1970

For abstract, see Hoffman, J. K.

S26 Evaluation of Magnetic Recording Tapes: A Method for the Quantitative Determination of Stick-Slip

R. H. Silver, S. H. Kalfayan, and J. K. Hoffman

Supporting Research and Advanced Development,
Space Programs Summary 37-66, Vol. III, pp. 198–200,
December 31, 1970

A method is described to measure "stock–slip" that is manifested in magnetic recording tapes. It consists of determining the apparent period of a prerecorded signal on the *test* tape. As the speed of the tape varies with stick–slip, the cycle period of the signal will also vary. The extent of the variation of the period from its initial value will, therefore, be a measure of stick–slip.

SIMON, H. S.

S27 DSN Progress Report for November–December 1970: SFOF Mark IIIA Central Processing System Model Development

H. S. Simon

Technical Report 32-1526, Vol. I, pp. 95–102,
February 15, 1971

Simulation models are currently being used for Space Flight Operations Facility (SFOF) development at the Jet Propulsion Laboratory. The results of two modeling studies are described

that were performed during the early stages of the SFOF Mark IIIA central processing system development.

S28 **Functional Design of the Space Flight Operations Facility for the 1970–1972 Era**

H. S. Simon

The Deep Space Network, Space Programs Summary 37-66, Vol. II, pp. 90–94, November 30, 1970

The overall design of the Mark IIIA Space Flight Operations Facility is described in general terms. Systems and subsystems are identified, and new capabilities are listed. Also identified are interfaces with the Ground Communications Facility and the Scientific Computing Facility.

SIMON, M. K.

S29 **On the Stability of Second-Order Tracking Loops With Arbitrary Time Delay**

M. K. Simon

Supporting Research and Advanced Development, Space Programs Summary 37-66, Vol. III, pp. 50–53, December 31, 1970

The introduction of data-aided loops has increased problems in loop stability due to the presence of a delay element in the open-loop transfer function. This delay, which is ideally equal to the reciprocal of the data rate, will cause instability problems at sufficiently low data rates. This article approaches the general question of second-order tracking loop stability in the presence of arbitrary time delay. A specific application of the results yields an approximate answer to the question of how low in data rate one can go before the data-aided loop becomes unstable. The principal tool used in the linear stability analysis is the Nyquist diagram as applied to the open-loop, noise-free, transfer function of a generalized second-order tracking loop. For nonlinear stability performance, a method based on an approximation to the phase-plane behavior is used.

S30 **The Steady-State Performance of a Data-Transition Type of First-Order Digital Phase-Locked Loop**

M. K. Simon

Supporting Research and Advanced Development, Space Programs Summary 37-66, Vol. III, pp. 59–68, December 31, 1970

A fully suppressed carrier data-aided carrier tracking loop and attendant data detector have been implemented recently and proposed for possible application to future planetary spacecraft programs, communication satellites, and the Manned Space Station. One of the significant advantages of the proposed data-aided receiver is its ability to give satisfactory tracking (phase-noise) and bit error probability performance in the presence of a coarse estimate of bit sync timing. In this article, the development of a mathematical model is given which describes the coarse bit synchronizer used in the data-aided receiver, and its steady-state performance is analyzed. The behavior and performance of the bit synchronizer itself is also included.

S31 Optimum Modulation Index for a Data-Aided, Phase-Coherent Communication System

M. K. Simon

Supporting Research and Advanced Development, Space Programs Summary 37-66, Vol. III, p. 69, December 31, 1970

Results were presented in Space Programs Summary 37-63, Vol. III, for optimally choosing a modulation factor for a data-aided, phase-coherent communication system. This article is an addendum to that previous article, giving updated information and an erratum to an incorrect equation.

S32 The Effect of Loop Stress on the Performance of Phase-Coherent Communication Systems

W. C. Lindsey (University of Southern California) and M. K. Simon

IEEE Trans. Commun. Technol., Vol. COM-18, No. 5, pp. 569–588, October 1970

For abstract, see Lindsey, W. C.

S33 Nonlinear Analysis of an Absolute Value Type of an Early–Late Gate Bit Synchronizer

M. K. Simon

IEEE Trans. Commun. Technol., Vol. COM-18, No. 5, pp. 589–596, October 1970

The steady-state phase noise performance of an absolute value type of early–late gate bit synchronizer is developed using the Fokker–Planck method. The results are compared with the per-

formance of two other commonly used bit synchronizer circuit topologies on the basis of either: (1) equal equivalent signal to noise in the loop bandwidth in the linear region, or (2) equal loop bandwidth at each input signal-to-noise ratio R_s. These comparisons are made as a function of R_s. In both cases, the absolute value type of early–late gate yields the best performance (in the sense of minimum phase noise) at every value of R_s.

S34 Optimization of the Performance of a Digital-Data-Transition Tracking Loop

M. K. Simon

IEEE Trans. Commun. Technol., Vol. COM-18, No. 5, pp. 686–689, October 1970

The steady-state behavior of a data-transition tracking loop, used as a bit synchronizer in a phase-coherent receiver, is considered. Optimization of mean-square phase noise and mean time to first cycle slip is performed when the average power of the reference cross-correlating signal is constrained. It is shown that by adjusting the quadrature channel gain along with the integration interval, a significant improvement in phase noise and cycle slip performances can be achieved over that system which integrates in the quadrature channel over the full symbol period. All the results are derived for a first-order loop filter merely to indicate the approach to the problem and the relative value of optimizing the system.

SJOGREN, W. L.

S35 Tracking System Analytic Calibration Activities for the *Mariner* Mars 1969 Mission

B. D. Mulhall, C. C. Chao, N. A. Mottinger, P. M. Muller, V. J. Ondrasik, W. L. Sjogren, K. L. Thuleen, and D. W. Trask

Technical Report 32-1499, November 15, 1970

For abstract, see Mulhall, B. D.

SKJERRE, L.

S36 Radio Science Support [by DSN, September–October 1970]

T. Sato, L. Skjerre, and D. Spitzmesser

The Deep Space Network, Space Programs Summary 37-66, Vol. II, pp. 151–153, November 30, 1970

For abstract, see Sato, T.

SMITH, H. J.

S37 High-Dispersion Spectroscopic Observations of Venus: IX. The Carbon Dioxide Bands at 12,030 and 12,177 Å

L. D. G. Young, R. A. J. Schorn, and H. J. Smith (University of Texas)

Icarus: Int. J. Sol. Sys., Vol. 13, No. 1, pp. 74–81, July 1970

For abstract, see Young, L. D. G.

SMITH, L. S.

S38 TOPS Attitude-Control Single-Axis Simulator True Position Encoder

W. C. Goss and L. S. Smith

Supporting Research and Advanced Development, Space Programs Summary 37-65, Vol. III, pp. 119–121, October 31, 1970

For abstract, see Goss, W. C.

SPITZMESSER, D.

S39 Radio Science Support [by DSN, September–October 1970]

T. Sato, L. Skjerre, and D. Spitzmesser

The Deep Space Network, Space Programs Summary 37-66, Vol. II, pp. 151–153, November 30, 1970

For abstract, see Sato, T.

STANTON, R. H.

S40 Approach Guidance Subsystem Development

R. H. Stanton

Supporting Research and Advanced Development, Space Programs Summary 37-65, Vol. III, pp. 107–111, October 31, 1970

An approach guidance sensor subsystem for multiplanet missions is being developed based on a satellite–star mapping concept. An on-board sensor provides maps of natural satellite motion referenced to fixed background stars which are then used to provide accurate trajectory estimates. Two separate approaches are being followed in developing this subsystem. The first, which uses

science cameras for all guidance measurements, is only briefly discussed. The main emphasis of this summary relates to the second approach, the development of a separate approach guidance sensor. The basic elements of a proposed sensor subsystem (optics, image intensifier, and image readout device) are briefly described. An important recent development is the inclusion of a channel plate image intensifier as a principal component of the system. Its effectiveness in solving the critical sensitivity and dynamic range problems is described, followed by a discussion of several alternate image readout devices.

STAPFER, G.

S41 Evaluation of a SNAP-19 TAGS Thermoelectric Generator

G. Stapfer

Supporting Research and Advanced Development,
Space Programs Summary 37-65, Vol. III, pp. 65–67,
October 31, 1970

The performance of a SNAP-19 (System for Nuclear Auxiliary Power 19) thermoelectric generator was evaluated, and the test results are discussed and analyzed in this article. The generator, SN-31, utilizes conventional lead telluride for the N-leg and a new improved material for the P-leg known as "TAGS." The results of tests to establish the electrical characteristic of the generator, as well as its ac impedance and thermal dynamic behavior, are presented. The degradation characteristic of the generator is shown, and a comparison is made with similar generators.

STARKEY, D. J.

S42 TOPS High-Gain Antenna

D. J. Starkey

Supporting Research and Advanced Development,
Space Programs Summary 37-66, Vol. III, pp. 157–159,
December 31, 1970

This article summarizes the design and development of the Thermoelectric Outer-Planet Spacecraft (TOPS) high-gain antenna. The main reflector for the TOPS high-gain antenna is 4.25 m in diameter, is unfurlable, and must have a surface accuracy of approximately 1 mm rms in order to meet X-band efficiency requirements. The concept embodies hinged radial ribs and a compliant mesh reflective surface. A mockup has been constructed and an engineering model is being developed.

STEINBACHER, R. H.

S43 *Surveyor* Final Reports—Introduction

L. D. Jaffe and R. H. Steinbacher

Icarus: Int. J. Sol. Sys., Vol. 12, No. 2, pp. 145–155, March 1970

For abstract, see Jaffe, L. D.

S44 *Surveyor* Final Report—Principal Scientific Results From the *Surveyor* Program

L. D. Jaffe, C. O. Alley (University of Maryland), S. A. Batterson (Langley Research Center), E. M. Christensen, S. E. Dwornik (NASA Headquarters), D. E. Gault (Ames Research Center), J. W. Lucas, D. O. Muhleman (California Institute of Technology), R. H. Norton, R. F. Scott (California Institute of Technology), E. M. Shoemaker (U.S. Geological Survey), R. H. Steinbacher, G. H. Sutton (University of Hawaii), and A. L. Turkevich (University of Chicago)

Icarus: Int. J. Sol. Sys., Vol. 12, No. 2, pp. 156–160, March 1970

For abstract, see Jaffe, L. D.

STELZRIED, C. T.

S45 The Quasi-Stationary Coronal Magnetic Field and Electron Density as Determined From a Faraday Rotation Experiment

C. T. Stelzried, G. S. Levy, T. Sato, W. V. T. Rusch (University of Southern California), J. E. Ohlson (University of Southern California), K. H. Schatten (Goddard Space Flight Center), and J. M. Wilcox (University of California, Berkeley)

Sol. Phys., Vol. 14, No. 2, pp. 440–456, October 1970

Pioneer VI was launched into a circumsolar orbit on December 16, 1965, and was occulted by the sun in the latter half of November 1968. During the occultation period, the 2292-MHz S-band telemetry carrier underwent Faraday rotation due to the interaction of this signal with the plasma and magnetic field in the solar corona. The NASA/JPL 210-ft-diameter antenna of the Deep Space Network near Barstow, California, was used for the measurement. The antenna feed was modified for automatic polarization tracking for this experiment.

The measurement results are interpreted with a theoretical model of the solar corona. This model consists of a modified

Allen–Baumbach electron density and a coronal magnetic field calculated from both Mount Wilson magnetograph observations using a source-surface model and field extrapolations from the *Explorer* 33 satellite magnetometer. The observations and the calculated rotation show general agreement with respect to magnitude, sense, and timing, suggesting that the use of the source-surface model and field extrapolations from 1 AU is a valid technique to obtain the magnetic field in the corona from 4 to 12 solar radii. Variations present can easily be ascribed to density enhancements known to be present in the corona. Longitudinal variations of the density in the corona cannot be obtained from coronagraph observations; thus, a purely radial variation was assumed. An improved fit to the Faraday rotation data is obtained with an equatorial electron density

$$N = 10^8\left(\frac{6000}{R^{10}} + \frac{0.002}{R^2}\right), \qquad 4 < R < 12$$

where R is in solar radii and N is in cm^{-3}.

STIMPSON, L. D.

S46 Revised Lunar Surface Thermal Characteristics Obtained From the *Surveyor V* Spacecraft

L. D. Stimpson and J. W. Lucas

J. Spacecraft Rockets, Vol. 7, No. 11, pp. 1317–1322, November 1970

Higher lunar surface temperatures have been obtained from *Surveyor* data than from Earth-based telescope measurements. In addition, temperatures derived from different sensors located on the *Surveyor* spacecraft were not entirely compatible. This paper presents the results of error analyses on the *Surveyor V* thermal data. In the compartments, heat conducted from the other faces is significant and is included in the latest calculations. Derived postsunset temperatures from solar panel data have total errors similar to those from the compartment thermal-sensor data. The actual temperature-sensor measurement inaccuracies, uncertainties in view factors, and conduction effects are the most significant sources of error. Other sources are uncertainties in internal heat loss, solar absorptance, and emissivity. Error bands for these factors are described. The overlapping of these error bands with each other and with the Earth-based results illustrates the degree of agreement of the data from the different sources. For postsunset, *Surveyor V* data previously had inferred a thermal parameter (γ), of about 400, whereas Earth-based measurements indicated $\gamma \simeq 850$. The latest compartment-based γ from *Surveyor V* is near 600, and from solar panel data it is near 1000.

STINNETT, W. G.

S47 DSN Command System Analysis Group

W. G. Stinnett

The Deep Space Network, Space Programs Summary 37-66, Vol. II, pp. 146–150, November 30, 1970

This article describes the functions of the Deep Space Network (DSN) Command System Analysis Group. Included are discussions on real-time functions of the group for support of DSN Command System operations and non-real-time analysis tasks. The key operational characteristics of the 1971 era DSN Command System are also given.

STIRN, R. J.

S48 Structural Damage in Lithium-Doped Silicon Solar Cells Produced by Neutron Irradiation

R. J. Stirn

Supporting Research and Advanced Development, Space Programs Summary 37-65, Vol. III, pp. 111–115, October 31, 1970

An investigation was undertaken to determine the size distribution, morphology, and structural characteristics of regions of lattice disorder which are produced by irradiating undoped and lithium-doped silicon solar cells with neutrons. The research was carried out entirely on the electron microscope using the techniques of surface replication, electron transmission, and electron diffraction. Evidence for the presence of precipitated metallic lithium was found in all samples. Crater defects thought to be associated with the space charge region around vacancy clusters were observed in all irradiated samples. The crater defect density was found to increase and the defect size was found to decrease with increasing irradiation dose and increasing lithium content. The crater defects were found to be stable at temperatures between 300 and 900°K. Significant annealing was only found in the undoped samples which were irradiated at the lowest doses.

S49 Investigation of Radiation Damage in Lithium-Diffused Silicon Solar Cells by Infrared Techniques

R. J. Stirn

Supporting Research and Advanced Development, Space Programs Summary 37-65, Vol. III, pp. 115–117, October 31, 1970

Research was undertaken to study the nature of electron radiation-induced defects in lithium-diffused silicon and their annealing characteristics using infrared photoconductivity and infrared absorption measurements. The background photoconductivity on unirradiated samples was 50 to 100 times smaller than for irradiated samples and no well-defined energy levels were detected. Levels in irradiated lithium-doped samples were observed at 0.28, 0.39, 0.64, and 0.82 eV from a band edge in oxygen-rich silicon, and at 0.34, 0.65, and 0.86 eV in oxygen-lean silicon. In addition, both types gave indication of strong contribution to the photoconductivity from a level (levels) less than 0.20 eV from a band edge. No levels corresponding to the divacancy or phosphorous-vacancy were detected. Annealing experiments showed that all levels anneal out by 450°C. In oxygen-lean silicon, a new level appears above 300°C at 0.92 eV. Identification of any of these levels with known defects, and correlation of the results with known degradation properties of irradiated silicon solar cells could not be made. An infrared absorption band was observed at 9.90 μ at 80°K in oxygen-rich silicon and is attributed to the $(OLi)^+$ complex. At irradiation doses of greater than about 10^{17} electrons/cm^2, the 9.9-μ band anneals out at 130°C and a new band at 13 μ appears, which in turn anneals at 200°C.

STIVER, R. A.

S50 Mark IIIA IBM 360/75 Computer Configuration

R. A. Stiver

The Deep Space Network, Space Programs Summary 37-66, Vol. II, pp. 71–75, November 30, 1970

Organizational aspects of the Mark IIIA IBM 360/75 computer configuration, including details of the memory and auxiliary storage, computation, and real-time input/output interface subsystems, are presented. The reference block diagram indicates interconnection between the subject subsystems and an overview of the related subsystems.

STRAND, L. D.

S51 Low-Pressure L^*-Combustion Limits

L. D. Strand

Supporting Research and Advanced Development, Space Programs Summary 37-66, Vol. III, pp. 179–180, December 31, 1970

Data was obtained on the effect of several propellant variables on the low-pressure/L^*-extinction limit. These variables included propellant binder, oxidizer coarseness, and the addition of oxamide, a coolant additive. The results did not support any simple correlation between the ease of extinguishment and propellant burning rate. Other complicating factors included the nature of the binder decomposition, transparency of the propellant to thermal radiation, and the mechanisms of burning rate catalysts and depressants.

STURMS, F. M., JR.

S52 Polynomial Expressions for Planetary Equators and Orbit Elements With Respect to the Mean 1950.0 Coordinate System

F. M. Sturms, Jr.

Technical Report 32-1508, January 15, 1971

Expressions are presented for the mean orbital elements of the nine planets with respect to the mean equinox and ecliptic of 1950.0. Also, expressions are presented for the right ascension and declination of the north pole of each of the nine planets with respect to the mean equinox and earth equator of 1950.0. The expressions are polynomials in time T measured in Julian centuries from the epoch January 1.0, 1950 E.T. The expressions are useful for coordinate transformations and approximate planetary ephemerides in astrodynamic computer programs.

SUTTON, G. H.

S53 *Surveyor* Final Report—Principal Scientific Results From the *Surveyor* Program

L. D. Jaffe, C. O. Alley (University of Maryland), S. A. Batterson (Langley Research Center), E. M. Christensen, S. E. Dwornik (NASA Headquarters), D. E. Gault (Ames Research Center), J. W. Lucas, D. O. Muhleman (California Institute of Technology), R. H. Norton, R. F. Scott (California Institute of Technology), E. M. Shoemaker (U.S. Geological Survey), R. H. Steinbacher, G. H. Sutton (University of Hawaii), and A. L. Turkevich (University of Chicago)

Icarus: Int. J. Sol. Sys., Vol. 12, No. 2, pp. 156–160, March 1970

For abstract, see Jaffe, L. D.

SYDNOR, R. L.

S54 Group Delay Measurements of Block IIIC Receiver–Exciter Modules

R. L. Sydnor and G. Thompson

The Deep Space Network, Space Programs Summary 37-66, Vol. II, pp. 27–28, November 30, 1970

To attain the ranging accuracy required by the Mark III Data System Development Plan, the Deep Space Instrumentation Facility receiver–exciter system must have a total group-delay stability of better than 10 ns. There is no verification that the present Block IIIC system meets this requirement. A measurement program has been started to determine the group-delay stability of the components of the receiver–exciter system. The measurement technique is described and test results are given for several system modules. A preliminary conclusion is that some components are much more critical than others with respect to group delay. Further measurement plans are outlined.

SZEJN, R.

S55 Optimization and Reliability Calculations for Multi-Thermionic-Converter Systems

R. Szejn and K. Shimada

Supporting Research and Advanced Development, Space Programs Summary 37-66, Vol. III, pp. 76–80, December 31, 1970

To realize an electric power system that is flyable for an extended space mission, the system reliability must be predicted and must be optimized to be compatible with mission length. Such a system is likely to have a large number of individual power generating devices that are connected in matrix configuration to meet the required power output and the redundancy necessary for a highly reliable system. In this article, approaches to optimization and reliability calculations for such power systems are presented along with an analysis of a sample system. The system is a three dimensional matrix of thermionic energy converters which are approximated by linear elements. The calculations are based on a linear systems analysis, combined with either a straightforward probability technique or a Monte Carlo technique. The latter method is successfully applied in optimizing the design of a 150-W thermionic generator system. This method is also applicable to practically all power systems, provided that they can be approximated by a linear model.

TAHERZADEH, M.

T01 Neutron Yield From (α, n) Reaction With O^{18} Isotope

M. Taherzadeh and M. A. Dore

Supporting Research and Advanced Development, Space Programs Summary 37-65, Vol. III, pp. 58–64, October 31, 1970

The neutron yield from the (α,n) reaction with oxygen is evaluated by integrating the reaction rate equation over all α-particle energies and all center of mass angles. The results indicate that for a PuO_2 fuel power source one should expect a total neutron yield of $(1.05 \pm 0.24) \times 10^4$ neutrons per gram of PuO_2 per second from the (α,n) reaction with oxygen. This result is compatible with the experimental value obtained for the same nuclear reaction.

TALBOT, T. D.

T02 DSN Progress Report for November–December 1970: Choice of Integrators for Use With a Variation-of-Parameters Formulation

T. D. Talbot and E. A. Rinderle

Technical Report 32-1526, Vol. I, pp. 117–121, February 15, 1971

In searching for better methods of computing the orbit of a satellite over many revolutions, a special perturbations theory using a variation-of-parameters formulation has been developed. As a prelude to obtaining valid comparisons with the Cowell technique currently in use, a study of various integrators was made in an effort to find the integrator best suited to a variation-of-parameters formulation. This study was initiated in response to suggestions that, for a given set of differential equations, there exists an optimum integrator. Three integrators were compared by the execution of two sets of test cases. The integrators were first compared in the predict-only mode and then in the predict–correct mode. The numerical results of these studies and the conclusions reached are presented in this article.

TAPPAN, R. W.

T03 Tau Ranging Subsystem Rebuild

R. W. Tappan

The Deep Space Network, Space Programs Summary 37-66, Vol. II, pp. 138–140, November 30, 1970

The tau planetary ranging equipment originally installed at DSS 14 (Mars Deep Space Station) has been redesigned and rebuilt to improve its operational and performance characteristics. This article discusses the significant improvements that have been incorporated into the equipment. The tau ranging subsystem has been functionally tested and re-installed at DSS 14 for use with the *Mariner* Mars 1971 mission.

TAUSWORTHE, R. C.

T04 DSN Progress Report for November–December 1970: A Second/Third-Order Hybrid Phase-Locked Receiver for Tracking Doppler Rates

R. C. Tausworthe

Technical Report 32-1526, Vol. I, pp. 42–45, February 15, 1971

This article describes a stable phase-locked receiver configuration for tracking frequency ramp signals. A usual second-order receiver is used for lockup; subsequently, a very simple modification is made to the loop filter, altering the loop to one of the third order. The altered loop then tracks the incoming signal with zero static phase error. The receiver bandwidth is practically unchanged; the damping factor lies in the region 0.5 and 0.707, and the design point is 12 dB in gain margin above instability.

T05 An Asymptotic Formula for the Mean Cycle-Slip Time of Second-Order Phase-Locked Loop With Frequency Offset

R. C. Tausworthe

The Deep Space Network, Space Programs Summary 37-66, Vol. II, pp. 42–48, November 30, 1970

Previous work has shown the mean time from lock to a slipped cycle of a second-order phase-locked loop is given by a certain double integral. Accurate numerical evaluation of this formula has proven extremely vexing because the difference between exponentially large quantities is involved. This article simplifies the formula to avert this problem, and then produces an asymptotic formula for the mean slip time that is surprisingly accurate even at low loop signal-to-noise ratios and moderate frequency offsets.

THOMPSON, G.

T06 Group Delay Measurements of Block IIIC Receiver–Exciter Modules

R. L. Sydnor and G. Thompson

The Deep Space Network, Space Programs Summary 37-66, Vol. II, pp. 27–28, November 30, 1970

For abstract, see Sydnor, R. L.

THULEEN, K. L.

T07 Tracking System Analytic Calibration Activities for the *Mariner* Mars 1969 Mission

B. D. Mulhall, C. C. Chao, N. A. Mottinger, P. M. Muller, V. J. Ondrasik, W. L. Sjogren, K. L. Thuleen, and D. W. Trask

Technical Report 32-1499, November 15, 1970

For abstract, see Mulhall, B. D.

TIMOR, U.

T08 Space Station Unified Communication: Efficiency of Biphase-Modulated Subcarriers, *N*-Channel Telemetry Systems

U. Timor

Supporting Research and Advanced Development, Space Programs Summary 37-65, Vol. III, pp. 27–30, October 31, 1970

The Manned Space Station high-rate links will have a multiplicity of channels. The efficiency of such N-channel digital coherent systems, where the data signals phase modulate the carrier with biphase-modulated subcarriers, is investigated. Two types of modulation are considered: linear binary phase-shift keying (BPSK) and interplex BPSK. For small N ($N \leq 4$), the interplex configuration is always superior. On the other hand the efficiency of the linear system is never below $36.8\% = e^{-1}$ no matter how large N is. However, for large N, the system to use is a concatenation of the two-channel interplex systems, which can be shown to be as efficient (theoretically 100%) as time-multiplex. Complete results, which show the efficiency of both systems for different power distributions in the N channels, are presented.

T09 Space Station Unified Communication: Equivalence of Time-Multiplex and PSK Signals for Digital Communication

U. Timor

Supporting Research and Advanced Development, Space Programs Summary 37-65, Vol. III, pp. 36–39, October 31, 1970

In comparing different techniques for multiplexing N binary data signals into a single channel such as would exist on the Manned

Space Station, time-division multiplexing is known to have a theoretical efficiency of 100% (neglecting sync power), and thus seems to outperform frequency-multiplexed subcarrier systems. In this article, it is shown that, using four-phase shift keying (PSK) of a squarewave subcarrier, an efficiency of 100% can be achieved. Thus, this scheme of PSK modulation is shown to be as efficient as time-division multiplexing. Therefore, the two seemingly different modulation schemes are, in effect, completely equivalent.

T10 Optimum Configurations for PSK/PM Systems

U. Timor

Supporting Research and Advanced Development,
Space Programs Summary 37-66, Vol. III, pp. 33–36,
December 31, 1970

The performance of N-channel phase-shift-keyed/phase-modulated (PSK/PM) digital communication systems is investigated. It is shown that for all possible power allocations to the data and RF channels either the Interplex scheme or the conventional modulation scheme is optimum (not necessarily unique). Therefore, to find the best performance achievable by PSK/PM systems, the investigation can be narrowed to these two schemes. Thus, a wide variety of multichannel multiplex schemes need not be developed.

TOM, H. Y.

T11 Investigation of Sterilizable Battery Separators [August–September 1970]

E. F. Cuddihy, D. E. Walmsley, J. Moacanin, and H. Y. Tom

Supporting Research and Advanced Development,
Space Programs Summary 37-65, Vol. III, pp. 171–176,
October 31, 1970

For abstract, see Cuddihy, E. F.

TOTH, L. R.

T12 Component Storage With Propellants

W. F. MacGlashan and L. R. Toth

Supporting Research and Advanced Development,
Space Programs Summary 37-65, Vol. III, p. 179,
October 31, 1970

For abstract, see MacGlashan, W. F.

T13 Material Compatibility [August–September 1970]

O. F. Keller and L. R. Toth

Supporting Research and Advanced Development, Space Programs Summary 37-65, Vol. III, pp. 180–181, October 31, 1970

For abstract, see Keller, O. F.

TRASK, D. W.

T14 Tracking System Analytic Calibration Activities for the *Mariner* Mars 1969 Mission

B. D. Mulhall, C. C. Chao, N. A. Mottinger, P. M. Muller, V. J. Ondrasik, W. L. Sjogren, K. L. Thuleen, and D. W. Trask

Technical Report 32-1499, November 15, 1970

For abstract, see Mulhall, B. D.

T15 DSN Progress Report for November–December 1970: DSN Inherent Accuracy Project

T. W. Hamilton and D. W. Trask

Technical Report 32-1526, Vol. I, pp. 11–13, February 15, 1971

For abstract, see Hamilton, T. W.

TRUSCELLO, V.

T16 Thermoelectric Generators for Deep Space Application

P. Rouklove and V. Truscello

Technical Report 32-1495, January 15, 1971

For abstract, see Rouklove, P.

TURKEVICH, A. L.

T17 *Surveyor* Final Report—Principal Scientific Results From the *Surveyor* Program

L. D. Jaffe, C. O. Alley (University of Maryland), S. A. Batterson (Langley Research Center), E. M. Christensen, S. E. Dwornik (NASA Headquarters), D. E. Gault (Ames Research Center), J. W. Lucas, D. O. Muhleman (California Institute of Technology), R. H. Norton, R. F. Scott (California Institute of Technology), E. M. Shoemaker (U.S. Geological Survey), R. H. Steinbacher, G. H. Sutton (University of Hawaii), and A. L. Turkevich (University of Chicago)

Icarus: Int. J. Sol. Sys., Vol. 12, No. 2, pp. 156–160, March 1970

For abstract, see Jaffe, L. D.

VOLKOFF, J. J.

V01 Discernibility of CRT Gray Shades

J. J. Volkoff

The Deep Space Network, Space Programs Summary 37-66, Vol. II, pp. 97–98, November 30, 1970

An experiment was performed to determine the luminances at which shades of gray produced on a cathode-ray tube (CRT) monitor are discerned. The experiment is described and the results are presented in terms of luminance difference required between gray shades as a function of luminance of the brighter shade.

WADA, B. K.

W01 Equivalent Spring-Mass System for Normal Modes

R. M. Bamford, B. K. Wada, and W. H. Gayman

Technical Memorandum 33-380, February 15, 1971

For abstract, see Bamford, R. M.

WAHLQUIST, H. D.

W02 Solution of Partial Differential Systems

F. B. Estabrook, B. K. Harrison (Brigham Young University), and H. D. Wahlquist

Supporting Research and Advanced Development, Space Programs Summary 37-66, Vol. III, p. 17, December 31, 1970

For abstract, see Estabrook, F. B.

WALMSLEY, D. E.

W03 Investigation of Sterilizable Battery Separators [August–September 1970]

E. F. Cuddihy, D. E. Walmsley, J. Moacanin, and H. Y. Tom

Supporting Research and Advanced Development, Space Programs Summary 37-65, Vol. III, pp. 171–176, October 31, 1970

For abstract, see Cuddihy, E. F.

WELLER, R. E.

W04 Block IV Receiver–Exciter Development

H. Donnelly, A. C. Shallbetter, and R. E. Weller

The Deep Space Network, Space Programs Summary 37-66, Vol. II, pp. 115–124, November 30, 1970

For abstract, see Donnelly, H.

WELLS, R. A.

W05 DSN Progress Report for November–December 1970: Diagnostics for the Mark IIIA Central Processing System: IBM 360/75 Computer On-Line Test Routines

R. A. Wells

Technical Report 32-1526, Vol. I, pp. 103–106, February 15, 1971

Described in this article is a family of real-time on-line diagnostics that was developed to check out all IBM-360/75-related components of the Space Flight Operations Facility Mark IIIA central processing system. Diagnostic requests are entered from a cathode-ray-tube display station, initiating concurrent tests of assorted user devices and communications links. A supervisory software monitor program coordinates execution and, where necessary, draws on the facilities of the JPL operating system in each IBM 360/75 computer.

WEN, L.

W06 Thermal Radiative Characteristics of Solar Arrays Determined by Calorimetric Techniques

L. Wen

Supporting Research and Advanced Development, Space Programs Summary 37-65, Vol. III, pp. 137–141, October 31, 1970

Effective solar absorptances and total hemispherical emittances of various types of solar cell modules were determined with calorimetric techniques. Sample specimens include five different modules, three painted surfaces, and two *Mariner* corrugated substrates. Emittances were measured at five temperature levels between −75 and 150°C.

WENGERT, R.

W07 High-Speed Data/Wide-Band Data Input/Output Assembly

R. Wengert, L. DeGennaro, and J. McInnis

The Deep Space Network, Space Programs Summary 37-66, Vol. II, pp. 133–136, November 30, 1970

The high-speed data/wide-band data (HSD/WBD) input/output assembly provides the interface and logic required for the bidirectional transfer of high-speed (4.8 kbits/s) and wide-band (50 kbits/s) information between the telemetry and command processor (TCP) computer and the HSD/WBD equipment in the Ground Communications Facility equipment. The former TCP high-speed data equipment provided a 2.4-kbit/s unbuffered send-only capability. Detailed functional descriptions of the modes of operations for the HSD/WBD input/output assembly are discussed in this article. The status of implementation at Deep Space Instrumentation Facility stations is also included.

WHITE, A. B.

W08 Optimal Methods for Computing the Incomplete Gamma and Related Functions

A. B. White

Supporting Research and Advanced Development, Space Programs Summary 37-65, Vol. III, pp. 3–11, October 31, 1970

Three methods of computing the incomplete gamma function are investigated: a zero-value marching algorithm, a power series technique, and a continued fraction method. The focus of each discussion is the development of techniques for computing sequences of the incomplete gamma function correct to any desired absolute accuracy. Miscellaneous properties of the incomplete gamma are also discussed.

WHITE, N.

W09 The Critical Problem and Coding Theory

N. White

Supporting Research and Advanced Development, Space Programs Summary 37-66, Vol. III, pp. 36–42, December 31, 1970

This article investigates in detail the interesting fact that the critical problem of combinatorial geometry contains, as a special

case, the problem of determining the largest dimension possible for a linear code over $GF(q)$, the finite field of order q, of fixed length and minimum distance. Following an introduction to the critical problem and its relationship to coding theory, the critical problem for B_2^n, $q = 2$; the critical problem for B_w^n, $w \geq 3, q = 2$; recursion for $p(\lambda; B_3^n)$, and values for p are discussed.

WICK, M. R.

W10 Programmed Oscillator Development

M. R. Wick

The Deep Space Network, Space Programs Summary 37-66, Vol. II, pp. 127–132, November 30, 1970

Programmed oscillators have been under development over the past several years for use in deep space communications, radar astronomy, and most recently in the time-synchronization transmitter of the Deep Space Network (DSN). This article describes one phase of the development activity of programmed oscillators for possible application in the DSN. The particular technique described utilizes a Dana digiphase synthesizer that is remotely and digitally controlled. A brief description of the digital control is also given.

WILCOX, J. M.

W11 The Quasi-Stationary Coronal Magnetic Field and Electron Density as Determined From a Faraday Rotation Experiment

C. T. Stelzried, G. S. Levy, T. Sato, W. V. T. Rusch (University of Southern California), J. E. Ohlson (University of Southern California), K. H. Schatten (Goddard Space Flight Center), and J. M. Wilcox (University of California, Berkeley)

Sol. Phys., Vol. 14, No. 2, pp. 440–456, October 1970

For abstract, see Stelzried, C. T.

WILLEMS, A. M.

W12 Simulation Center Hardware Development—Programmed Input/Output Serial Data Generators and Receivers

A. M. Willems

The Deep Space Network, Space Programs Summary 37-66, Vol. II, pp. 70–71, November 30, 1970

The EMR 6050 computer in the Simulation Center receives from and outputs to the Ground Communications Facility serial data

streams. These data streams comprise simulated tracking, telemetry, command, monitor, and operations control data in formats identical to mission data. The EMR 6050 processes these data in parallel format, thus requiring conversions to and from serial format. The programmed input/output serial data generators and receivers that perform this function are described in this article.

WILLIAMS, H. E.

W13 Boundary Layer Equations of a Heated Constrained Spherical Shell

H. E. Williams (Harvey Mudd College)

Supporting Research and Advanced Development,
Space Programs Summary 37-66, Vol. III, pp. 136–140,
December 31, 1970

The general equations governing the nonlinear, thermoelastic behavior of thin shells of revolution are simplified by an order of magnitude analysis to study boundary layer development in spherical shells. The range of thermal strain studied produces transverse deflections comparable with the shell thickness. The boundary layer equations are developed first for a general asymmetric temperature rise (constant through the shell thickness) and then applied to the case of a uniformly heated, shallow spherical shell. The resulting equations are linear in the stress–displacement variables. However, as the in-plane displacements are nonlinearly related to the slope of the transverse displacement, the temperature dependance of the in-plane displacements is nonlinear. Finally, it is shown that the equations derived for shallow, spherical shells also apply to ellipsoidal shells of revolution.

W14 Derivation of the Equations Governing Heated Shallow Shells of Revolution

H. E. Williams (Harvey Mudd College)

Supporting Research and Advanced Development,
Space Programs Summary 37-66, Vol. III, pp. 141–144,
December 31, 1970

The general equations derived earlier by the author are shown to contain Marguerrés equations when simplified by an order of magnitude analysis. The range of thermal strain studied is comparable to that sufficient to cause buckling of a flat, circular plate of the same thickness and span. It is assumed further that a boundary layer does not develop and stress–displacement vari-

ables vary significantly over lengths comparable with the span of the shell. Although the development is applied to a spherical shell, it can be shown that the equations also apply to shallow, ellipsoidal shells of revolution.

WILLIAMSON, R. E.

W15 Automated Test Techniques for Guidance and Control Subsystems

R. E. Williamson

Supporting Research and Advanced Development, Space Programs Summary 37-66, Vol. III, pp. 90–91, December 31, 1970

The complexity of the long-life outer-planet spacecraft is such that automated testing will be required. This article describes the development of guidance and control automated support equipment technology which is in process to meet the requirements of future planetary missions.

WINKELSTEIN, R.

W16 DSN Progress Report for November–December 1970: Digital Modulator

R. Winkelstein

Technical Report 32-1526, Vol. I, pp. 63–65, February 15, 1971

Utilization of the increased capability of the Mars Deep Space Station (DSS 14) transmitter and antenna for planetary radar transmission has been made possible by the design, construction, and installation of a digital modulator at DSS 14. As described in this article, this device reshapes the digital modulating waveform generated at the Venus Deep Space Station (DSS 13) and received over the microwave link at DSS 14. The digital modulator output is an accurately adjustable 2-level waveform used to biphase-modulate the transmitter frequency. During precalibration setup, the digital modulator provides selectable frequency square waves used in correctly adjusting the waveform amplitude to obtain carrier suppression greater than 40 dB. The capability that this technique provides has been demonstrated in planetary radar experiments. By this method, one station's processor can be used to generate commands to be sent to a spacecraft from another station at the same complex, thus increasing the reliability of the Deep Space Network (DSN) command system.

WINN, F. B.

W17 **DSN Progress Report for November–December 1970: Refractivity Influence on DSS Doppler Data**

F. B. Winn and R. K. Leavitt

Technical Report 32-1526, Vol. I, pp. 31–41, February 15, 1971

As described in this article, doppler data from deep space missions show terrestrial media contamination influences even after least-square fitting. Cross-correlation between solution parameters and the media-induced errors is large enough to adversely affect parameter least-square adjustments. When a scale factor for Cain's tropospheric refractivity profile is included in the parameter list, the media-induced observed-minus-computed (O − C) structures do not appear above 15-deg elevation. When the scale factor is not included, O − C structures commence to appear at ~25-deg elevation.

WONG, S. K.

W18 **The *Mariner VI* and *VII* Flight Paths and Their Determination From Tracking Data**

H. J. Gordon, D. W. Curkendall, D. A. O'Handley, N. A. Mottinger, P. M. Muller, C. C. Chao, B. D. Mulhall, V. J. Ondrasik, S. K. Wong, S. J. Reinbold, J. W. Zielenback, J. K. Campbell, R. T. Mitchell, J. E. Ball, W. G. Breckenridge, T. C. Duxbury, and R. E. Koch

Technical Memorandum 33-469, December 1, 1970

For abstract, see Gordon, H. J.

WOO, K.

W19 **Spacecraft Antenna Research: Further RF Study of Reflector Surface Materials for Spacecraft Antennas**

K. Woo and T. Y. Otoshi

Supporting Research and Advanced Development, Space Programs Summary 37-65, Vol. III, pp. 47–52, October 31, 1970

A computerized network analyzer technique permitting rapid measurement of RF loss and phase characteristics of reflector surface materials for spacecraft antennas is described. The RF reflectivity losses at 8448 MHz of gold-plated Chromel-R mesh,

Paliney-7 mesh, silver-plated nylon mesh, perforated stainless steel sheet, perforated aluminum sheet, and perforated copper-clad glass epoxy laminate measured by the network analyzer method are presented.

W20 Spacecraft Antenna Research: S/X-Band High-Gain Antenna Feed for Thermoelectric Outer-Planet Spacecraft

K. Woo

Supporting Research and Advanced Development, Space Programs Summary 37-65, Vol. III, pp. 52–57, October 31, 1970

A high-gain antenna feed has been developed for the Thermoelectric Outer-Planet Spacecraft. The feed is designed to operate with linearly polarized signals and is capable of: (1) transmitting telemetry at both 8448 and 2295 MHz, (2) receiving commands at 2115 MHz, and (3) angle-tracking at 2115 MHz. Test results show that the feed provides high efficiency at all operating frequencies and good monopulse tracking capability.

YANG, J.-N.

Y01 Optimum Pressure Vessel Design Based on Fracture Mechanics and Reliability Criteria

E. Heer and J.-N. Yang

Technical Memorandum 33-470, February 1, 1970

For abstract, see Heer, E.

Y02 Optimization of Space Antenna Structures

E. Heer and J.-N. Yang

Technical Memorandum 33-472, March 15, 1971

For abstract, see Heer, E.

Y03 Creep Failure of Randomly Excited Structures

J.-N. Yang

Supporting Research and Advanced Development, Space Programs Summary 37-66, Vol. III, pp. 120–128, December 31, 1970

A method is developed for the prediction of creep failure of structures under random excitations. The fracture mechanics

concept and the cumulative flaw growth hypothesis have been employed to obtain the statistical characteristics of the relative flaw growth of structures under random loadings. The probability of creep failure is evaluated using the principle of maximum entropy. Two numerical examples are used to illustrate the general results.

Y04 Reliability of Randomly Excited Structures

J.-N. Yang and E. Heer

Supporting Research and Advanced Development, Space Programs Summary 37-66, Vol. III, pp. 128–136, December 31, 1970

A method is developed to predict the reliability of structures under stationary random excitations. The present approach takes into account the interaction of catastrophic failure modes and fatigue failure modes as well as the statistical variation of the material strength. Fracture mechanics and extreme point processes are employed throughout the formulation. It is demonstrated that neglecting the interactions of failure modes, or disregarding the statistical dispersion of the material strength, results in an unconservative reliability estimate.

YASUI, R. K.

Y05 Effects of High-Temperature, High-Humidity Environment on Silicon Solar Cell Contacts

R. K. Yasui and P. A. Berman

Technical Report 32-1520, February 15, 1971

The electrical and mechanical characteristics of various solar cell contact systems after exposure to a high-temperature, high-humidity environment were investigated at the Jet Propulsion Laboratory. The results are discussed. An unexpected failure mode involved degradation of the silicon monoxide antireflective coating after environmental exposure. Significant degradation of electrical characteristics was observed in cells having palladium-containing Ti–Ag contacts, and differences in contact structure and composition were noted between different manufacturers. Non-palladium-containing Ti–Ag contacts on lithium-doped cells showed a surprising degree of stability. In general, the most stable contact system, electrically and mechanically, was the solder-coated, Ti–Ag system used on the *Mariner* Mars 1969 solar cells.

YEATES, C. M.

Y06 Experimental Study of Magnetic Flux Transfer at the Hyperbolic Neutral Point

A. Bratenahl and C. M. Yeates

Phys. Fluids, Vol. 13, No. 11, pp. 2696–2709, November 1970

For abstract, see Bratenahl, A.

YEN, S. P. S.

Y07 Energy Transfer in Bipyridilium (Paraquat) Salts

A. Rembaum, V. Hadek, and S. P. S. Yen

Supporting Research and Advanced Development, Space Programs Summary 37-66, Vol. III, pp. 189–191, December 31, 1970

For abstract, see Rembaum, A.

YOUNG, A. T.

Y08 Saturation of Scintillation

A. T. Young

J. Opt. Soc. Am., Vol. 60, No. 11, pp. 1495–1500, November 1970

Recent observations of stellar scintillation provide new evidence that atmospheric dispersion alone is not sufficient to cause the saturation observed at large zenith angles. Saturation is produced by lateral spreading of the (initially collimated) light in traversing the turbulent atmosphere—a phenomenon called seeing by astronomers, or multiple scattering by optical physicists. The magnitude of this effect, as estimated from stellar scintillation data, agrees well with the minimum resolution predicted by Fried and by Hulett and is correlated as expected with the strength of scintillation in the zenith. The observational data, the theory, comparisons of observation and theory and with earlier results, and saturation in other scintillation data are discussed.

Y09 Improved Constants for the 7820 Å and 7883 Å Bands of CO_2

L. D. G. Young, A. T. Young, and R. A. Schorn

J. Quant. Spectrosc. Radiat. Transfer, Vol. 10, No. 12, pp. 1291–1300, December 1970

For abstract, see Young, L. D. G.

Y10 Improved Solar Wavelengths Between 7780 and 7925 Å

A. T. Young and R. A. Schorn

Sol. Phys., Vol. 15, No. 1, pp. 97–101, November 1970

By utilizing the known rotational constants for the 7820 and 7883 Å CO_2 bands, the authors were able to derive substantially improved wavelengths for solar lines in the 7780–7925 Å region. It seems unlikely that any of the values obtained (with the exceptions that are noted) is in error by as much as 0.010 Å, and the results are believed to represent a substantial improvement over the catalog values for many of the lines.

YOUNG, L. D. G.

Y11 High-Dispersion Spectroscopic Observations of Venus: IX. The Carbon Dioxide Bands at 12,030 and 12,177 Å

L. D. G. Young, R. A. J. Schorn, and H. J. Smith (University of Texas)

Icarus: Int. J. Sol. Sys., Vol. 13, No. 1, pp. 74–81, July 1970

Observations of the 12,030- and 12,177-Å bands of carbon dioxide in the spectrum of Venus were made from March through May 1967. The 10 best spectra were used to derive rotational temperatures. Two methods were used. A linear-least-squares fit to a square-root absorption law yielded an average rotational temperature of 238 ± 5 °K, while a curve-of-growth technique gave an average rotational temperature of 236 ± 5 °K. The rotational temperatures showed no significant variation with the phase angle, i, of Venus for our restricted range of $49 \leq i$, deg ≤ 63.

Y12 Interpretation of High-Resolution Spectra of Venus: II. The $(102\text{–}000)_{II}$ Band of $^{12}C^{16}O^{18}O$ at 1.71 Microns

L. G. Young

Icarus: Int. J. Sol. Sys., Vol. 13, No. 2, pp. 270–275, September 1970

High-resolution spectra obtained by Pierre and Janine Connes in the region of 1.7 microns have been used to obtain a curve of growth for the $(102\text{–}000)_{II}$ band of the $^{12}C^{16}O^{18}O$ isotope of carbon dioxide. Several methods of data reduction have been employed. Assuming a constant rotational line half-width, we find a rotational temperature for Venus of $T_{rot} = 242° \pm 2°K$ in agreement with our previous results. When a variable line half-width is used, the rotational temperature is increased to $249° \pm 3°K$.

Y13 Improved Constants for the 7820 Å and 7883 Å Bands of CO_2

L. D. G. Young, A. T. Young, and R. A. Schorn

J. Quant. Spectrosc. Radiat. Transfer, Vol. 10, No. 12, pp. 1291–1300, December 1970

High-dispersion spectra of Venus are used in obtaining line positions and band constants for the $(105)_I$ and $(105)_{II}$ bands of CO_2. An improved method of analysis is used to obtain very accurate results. Assuming $B'' = 0.390218$ and $D'' = 13.3 \times 10^{-8}$ for the ground state, the following values are obtained:

Constant	Value for 7820-Å band	Value for 7883-Å band
ω_0, cm^{-1}	12774.727 ±0.002	12672.274 ±0.004
B'	0.374540 ±0.000006	0.375657 ±0.000014
D'	10.9×10^{-8} ±0.4	17.2×10^{-8} ±1.7

The values for ω_0 and B' are at least an order of magnitude more accurate than those given by Herzberg and Herzberg in 1953, and the D' values are new.

YOUNGBERG, C. L.

Y14 Holographic Study of Operating Compact-Arc Lamp

C. G. Miller and C. L. Youngberg

Supporting Research and Advanced Development, Space Programs Summary 37-66, Vol. III, pp. 171–174, December 31, 1970

For abstract, see Miller, C. G.

ZANDELL, C.

Z01 DSN Progress Report for November–December 1970: IBM 360/75 Computer Time Interface

C. Zandell

Technical Report 32-1526, Vol. I, pp. 107–109, February 15, 1971

The IBM 360/75 computer time interface and the capabilities of two custom-feature modifications of the IBM 360/75 are described. The modified IBM 360/75 accepts signals from an existing time reference, provides GMT with 10-μs resolution, includes an interval timer, and provides programmable interrupts.

Z02 **DSN Progress Report for November–December 1970: IBM 360/75–Univac 1108 Computer Interface**

C. Zandell

Technical Report 32-1526, Vol. I, pp. 110–112, February 15, 1971

In the functional design of the Space Flight Operations Facility (SFOF) for the 1970–1972 era, a capability for interfacing the central processing system with the scientific computing facility will exist. This interface is required to implement the transfer of orbital and trajectory data between programs in the IBM 360/75 and the Univac 1108 computers for the *Mariner* Mars 1971 and *Pioneer F* missions. This article describes the interface design which provides a method of serial synchronous communication for short distances without the use of modems. Reducing the total resistance between the current mode drivers and receivers makes transmission lengths of 400 ft possible. External timing replaces the modem function, allowing the direct connection of serial synchronous devices.

ZIELENBACK, J. W.

Z03 **The *Mariner VI* and *VII* Flight Paths and Their Determination From Tracking Data**

H. J. Gordon, D. W. Curkendall, D. A. O'Handley, N. A. Mottinger, P. M. Muller, C. C. Chao, B. D. Mulhall, V. J. Ondrasik, S. K. Wong, S. J. Reinbold, J. W. Zielenback, J. K. Campbell, R. T. Mitchell, J. E. Ball, W. G. Breckenridge, T. C. Duxbury, and R. E. Koch

Technical Memorandum 33-469, December 1, 1970

For abstract, see Gordon, H. J.

ZOHAR, S.

Z04 **DSN Progress Report for November–December 1970: Matched Filters for Binary Signals**

S. Zohar

Technical Report 32-1526, Vol. I, pp. 52–62, February 15, 1971

Matched filters for the optimal high-speed detection of binary signals are designed, and their performance as a function of their complexity is explored. The range of filters designed extends

from a 2-element filter whose performance is about 0.7 dB below the ideal filter up to a 20-element filter with a degradation of about 0.1 dB.

ZYGIELBAUM, A. I.

Z05 DSN Progress Report for November–December 1970: Probing the Solar Plasma With *Mariner* Radio Metric Data, Preliminary Results

P. F. MacDoran, P. S. Callahan, and A. I. Zygielbaum

Technical Report 32-1526, Vol. I, pp. 14–21, February 15, 1971

For abstract, see MacDoran, P. F.

Subject Index

Publication Index

Technical Reports

DSN Progress Report for November–December 1970 (Technical Report 32-1526, Vol. I)

Technical Memorandums

Space Programs Summary 37-65, Vol. III

Space Programs Summary 37-66, Vol. I

Space Programs Summary 37-66, Vol. II

Space Programs Summary 37-66, Vol. III

Open Literature Reporting

NASA — JPL — Coml., L.A., Calif.